N° d'ordre : 40268

THESE

présentée à
Université Lille I
Ecole Doctorale des Sciences de la Matière et du Rayonnement

pour obtenir le grade de
Docteur
Spécialité : Molécules et Matière Condensée
par

Chanapa KONGMARK

De la Genèse Suivie par Techniques *In-situ* à l'Utilisation en Réacteur Catalytique à Membrane Dense : Application au Catalyseur Molybdate de Bismuth

(Genesis of Bismuth Molybdenum Oxide Catalyst followed by *In-situ* Techniques and its Use in Catalytic Dense Membrane Reactor)

Soutenue le 7 Mai 2010 devant la commission d'examen :

Rapporteurs	
Philippe Lacorre	Directeur de recherche, Université du Maine
Jean-Marc Millet	Directeur de recherche, Université Claude Bernard Lyon I
Examinateurs	
François Beson-Verduraz	Professeur, Université Paris VII
Gopinathan Sankar	Professeur, University College London
Directeurs de thèses	
Rose-Noëlle Vannier	Professeur, Ecole Nationale Supérieure de Chimie de Lille
Elisabeth Bordes-Richard	Professeur, Ecole Nationale Supérieure de Chimie de Lille
Axel Löfberg	Chargé de recherche, Université Lille I
Caroline Pirovano	Maître de conférences, Ecole Nationale Supérieure de Chimie de Lille

Remerciements

Je tiens à exprimer ma profonde gratitude à ma directrice de thèse Rose-Noëlle Vannier, Professeur à l'ENSCL (alias chef N°1), pour sa patience, ses conseils et son soutien durant mes années de master recherche et de thèse à l'Université de Lille 1. J'ai eu l'opportunité de travailler avec elle et de partager son optimisme, son enthousiasme et sa joie pour la recherche. Elle m'a fait découvrir le monde de la recherche et de la science.

J'adresse mes sincères remerciements à ma co-directrice de thèse Elisabeth Bordes-Richard, Professeur à l'ENSCL (alias chef N°2), pour sa grande culture en catalyse et sa bonne plume, un grand merci particulièrement pour ses corrections de thèse et articles.

Je tiens à remercier également Axel Löfberg (Chef N°3), chargé de recherche à CNRS, pour son savoir et sa patience. Ses explications très utiles m'ont permis de mieux comprendre la catalyse.

Je n'oublie pas non plus mon chef N°4, Caroline Pirovano, maître de conférences à L'ENSCL, pour sa patience et son aide pour les parties synthèse et catalyse expérimentale.

J'adresse toute ma gratitude à François Beson-Verduraz, Professeur, Université Paris VII, qui m'a fait l'honneur de présider ce jury. Je tiens également à remercier M. Philippe Lacorre, Directeur de recherche à l'Université du Maine et M. Jean-Marc Millet, Directeur de recherche à l'UCBL qui ont accepté d'être rapporteur de ce travail.

J'exprime également ma gratitude aux spécialistes en spectroscopie, Annick Rubens, Professeur à Polythech'Lille et Sylvain Cristol, maître de conférences à l'Université de Lille 1, pour leur savoir en spectroscopie Raman et spectrométrie d'absorption des rayons X ainsi que pour leur aide. Je suis très reconnaissante de m'avoir consacré beaucoup de leur temps.

Mes sincères remerciements à mes collaborateurs durant mes années de recherche :

- Gopinathan Sankar, Professeur à l'University College London, qui m'a beaucoup appris par le travail sur le grand instrument (Synchrotron).

- Zhen Qian, Professeur à l'Université de Shangai, qui nous a permis d'élaborer des membranes tubulaires. Sa patience et sa ténacité viennent à bout de tous les problèmes. En plus, grâce à sa générosité et son accueil, j'ai eu un séjour inoubliable à Shangai (délicieuse fondue chinoise et la soirée de Noëlle).
- Professeur Franciszek Krok, Professeur Rózef R. Dygas et Dr. Marcin Malys à l'Université Technique de Varsovie, pour leur chaleureux accueil et pour toutes les compétences sur la spectroscopie d'impédance qu'ils m'ont transmises.

Je remercie aussi tous ceux sans qui ce travail n'aurait pu être réalisé, en commençant par mes deux stagiaires : Lucile Gouzerh pour l'application des membranes denses et Rachel Coulter pour la synthèse de Bi_2MoO_6 ; Nora Djelal qui a fait des belles images de microscopique électronique et des mesures d'analyses thermiques. Merci à Laurence Burylo pour les mesures de diffraction des rayons X ainsi que Dr. Pascal Roussel pour des conseils très utiles pour l'analyse DRX. Un grand merci au Prof. Marielle Huvé pour toutes les analyses de diffraction électronique, à David Kho pour l'optimisation du circuit électronique ajouté au réacteur catalytique, à Olivier Gardoll pour la mesure de BET et à Martine Frère pour les mesures XPS. Merci également à Julien Trebosc pour l'apprentissage du program Matlab et à Edouard Capoen pour le montage de mesure de spectroscopie d'impédance et de semi-perméabilité. J'adresse également un grand merci à Maxence Vandewalle, Véronique Alaimo, Jérémy Maton, Claudine Devynck et tous les membres du laboratoire dont les diverses compétences m'ont permis d'effectuer ma thèse dans de très bonnes conditions.

Je n'oublie pas de remercier tous mes collègues et amis thésards : Jean François (JF), Alex (le chauve), Zhen (le petit chinois), Dr. Jérome (le moyen), Rudy (Benni), Aurélien (le gros sac), Nico, Nina, Dr. Bingwen, Dr. Ghislaine et Dr. Olfa avec qui j'ai partagé durant ces cinq années mon bureau, un bout de paillasse, des discussions scientifiques ou non et des bières de ch'Nord.

J'adresse également mes remerciements sincères à mes enseignants de la formation MST : Prof. B. Mutel, Prof. P. Supiot, Dr. F. Langrand, Dr. C. Vivien et Dr. M. C. Dhamelincourt pour leur formation pluridisciplinaire très intense qui m'ont conduit à ne pas avoir peur d'étudier ou de travailler dans différents domaines, 'we can do anything if we really want to'.

Je tiens à exprimer ma profonde gratitude au Prof. M. Torikachvili et mon collègue Matt Steiger qui m'ont donné l'opportunité de connaître la recherche en Sciences des Matériaux au SDSU pendant mon stage de MST, malgré ma modeste formation dans ce domaine. Je voudrais les remercier pour m'avoir appris la base des Sciences des Matériaux, de la recherche et le travail en équipe. Un grand merci également pour leur infaillible patience, leur encouragement et pour croire toujours en moi.

Je remercie également ceux qui ont partagé avec moi cette vie étudiante en France, les bons moments qu'on a partagé restera encore dans mon souvenir même si chacun de nous a suivi un chemin différent: Véronique, Luïc, David, Noppol, Aek, P'Un, P'Noon, Anne-Laure, Phylarsay, Gaëlla, Manu,…

Je remercie très chaleureusement mes amis : Elodie, Aurélie, Filipe, Clément, François, Christian, Paul, Constant, Jing, Rong, Vladimir, Martin, Sit, P'Lek, Tah, Kong, Koy, Niki, Tou, Choochart avec qui j'ai passé des bonnes soirées fêtardes, bourrées, raclettes, à dégustation internationale,…

Je tiens à remercier en particulier Sofia pour son soutien, ses conseils, son humour et son énergie inépuisable qui m'a fait oublier le stress de la fin de thèse et qui m'a fait apprécier ma dernière année en France.

Je remercie vivement mes grandes cuisinières : Flo et Ji qui m'ont dépannée plusieurs repas durant mes années études, sans elles je n'aurais pas pu survivre. Leur écoute, leur patience et leur compréhension sont redoutables.

Un grand merci tout particulièrement à mon ancien colocataire Sudarat Buddhapong, qui est toujours là pour m'aider, dans les bons et les mauvais moments de ma vie. 'Voici, j'ai accompli ma promesse, je vais finir ma thèse en science cette année. A toi, tu vas finir ta thèse en linguistique aussi.'

Je tiens à exprimer ma plus profonde gratitude à mes parents qui m'ont donné tout ce que les parents peuvent donner à leur fille : l'éducation, l'amour, l'encouragement et la compréhension qui fait de moi ce que je suis aujourd'hui. Je remercie ma famille : mes grandes mères, ma tante, mon oncle, mon frère et ma sœur et les autres qui sont toujours là pour me donner du réconfort quand je suis désespérée et je ne veux plus rien. Malgré les longues distances qui nous séparent, ils sont toujours là pour moi.

A ma grande mère, je t'aime.

Résumé

Les molybdates de bismuth présentent un grand intérêt en catalyse d'oxydation sélective du propène. Leurs mécanismes de formation ont fait l'objet de nombreuses études mais leur compréhension reste encore incomplète.

Dans un premier temps, la formation de γ-Bi_2MoO_6 au cours de sa synthèse par voie hydrothermale a été suivie *in situ* par diffraction X combinée à la spectrométrie d'absorption des rayons X (XAS) et à la diffusion Raman. Les mesures ont été réalisées au synchrotron à l'ESRF. Des informations sur la cinétique de réaction ont pu être déduites des données *in-situ*, elles ont été complétées par des analyses physico-chimiques *ex-situ*. L'étude montre que le catalyseur est généré selon un mécanisme en deux étapes, passant par la formation d'un molybdate de bismuth de structure proche de la fluorine à partir de laquelle se développent les cristaux lamellaires de γ-Bi_2MoO_6.

Ce catalyseur a ensuite été utilisé en mode découplage redox dans l'oxydation du propène à l'aide d'un Réacteur Catalytique à Membrane Dense (RCMD) dont le principe repose sur une membrane céramique dense, conductrice par ions oxydes O^{2-}, qui sépare de façon étanche deux compartiments alimentés respectivement par l'hydrocarbure et l'air. La composition $Bi_{25.75}Mo_{10}O_{68.625}$ a été retenue pour la membrane. L'étude montre que l'activités catalytique de la membrane seule ou avec le catalyseur (γ-Bi_2MoO_6) déposé à sa surface peut être modulée par l'application d'un courant électrique. L'apport en oxygène est suffisant pour permettre un travail en continu du catalyseur γ-Bi_2MoO_6 qui devrait être ré-oxydé par l'air co-alimenté avec le propène dans un réacteur classique.

Mots clés : Catalyseurs au Molybdène, Synchrotron, XANES, Spectroscopie Raman, Diffraction de Rayons X, Réacteur à Membrane, Propène-Oxydation, Electrocatalyse.

Abstract

Bismuth molybdates have drawn significant research interest because of their catalytic properties for propylene oxidation. Despite several studies dealing with the mechanism of their formation, uncertainties remain.

The genesis of γ-Bi_2MoO_6 under hydrothermal conditions was first elucidated by an *in-situ* study combining High-Resolution Powder Diffraction (HRPD) / X-ray Absorption Spectroscopy (XAS) / Raman Scattering. Experiments were carried out at the European Synchrotron Radiation Facility. The informations on the two-step kinetics of reaction which were obtained by these experiments were completed by additional *ex-situ* characterizations. It was shown that the catalyst is formed via a bismuth molybdate of fluorite structure acting as a template for the layered γ-Bi_2MoO_6 crystals to be nucleated.

In the second part, the catalytic properties of γ-Bi_2MoO_6 were studied in a the Catalytic Dense Membrane Reactor CDMR in which the reduction and reoxidation of catalyst were physically separated (redox decoupling). $Bi_{25.75}Mo_{10}O_{68.625}$, known as a good oxide ion conductor, was used as the dense membrane, separating two compartments, one containing air and the other containing propylene to be oxidized selectively. The study has demonstrated that the catalytic activity of the γ-Bi_2MoO_6 and of the $Bi_{25.75}Mo_{10}O_{68.625}$ dense membrane itself was modified by applying an electrical bias. In contrast to conventional reactors in which γ-Bi_2MoO_6 must be reoxidized by air cofed with propylene, in a CDMR the oxygen supply is high enough for γ-Bi_2MoO_6 to operate continuously.

Keywords: Molybdenum Catalysts, Synchrotron, XANES, Raman spectroscopy, X-ray Diffraction, Membrane Reactor, Propene-Oxidation, Electrocatalysis.

Introduction

Acrolein has been commercially produced since 1938. In 1995, the worldwide refined acrolein capacity was about 113 Kton/year. Acrolein is utilized in the manufacture of organic compounds such as glycerin, plastics, polymethane, polyester resins, D,L-methionine (which is used as an animal food additive), glutaraldehyde, allyl compounds, acrylic acid, acrylates, perfumes and other esters [1]. It is also widely known as a biocide in oil wells and liquid petrochemical fuel, as an herbicide for the control of algae and weeds in the irrigation canals, as a slimicide in the paper industry, and to enter in the composition of military tear gas mixture [2]. However, the largest single use of acrolein is as an unisolated intermediate in the production of acrylic acid.

Acrolein is naturally produced from heating of cooking oils, combustion of wood and tobacco and automobile end diesel exhausts [3]. For industrial applications, acrolein was first commercially produced in the 1930s through the vapor-phase condensation of acetaldehyde and formaldehyde [1, 4]. Since the 1940s, the partial oxidation of propylene was strongly developed and became the primary method used for the acrolein production till today.

The heterogeneous partial oxidation of propylene started to be considerably developed after Hearne *et al.* [5] reported, in 1948, that using cuprous oxide catalyst led to acrolein with a yield of about 50%. An extensive research was later carried out in order to improve the catalyst performance. In the 1950s, Idol [6] and Callahan *et al.* [7] reported that bismuth molybdate catalysts were far more efficient than cuprous oxide. They reported as well that the bismuth molybdate catalysts were active for the ammoxidation of propylene to acrylonitrile and the oxidative hydrogenation of butene to butadiene. The bismuth molybdate catalysts were commercially used by Standard Oil of Ohio Company (SOHIO) and the vapor-phase oxidation and ammoxidation processes are now utilized worldwide.

Significantly higher yields of acrolein (acrylonitrile) were later obtained upon inclusion of other elements (Fe, Co, Ni, K, P, Si,…) giving rise to the so-called MultiComponent Bismuth Molybdates catalysts [8]. During calcination, the added transition metals are converted to metallic molybdates (mostly $MMoO_4$, M = Fe, Co, Ni, as well as

$M_2Mo_3O_{12}$, M = Bi, Fe). The synergistic effect observed in terms of the large increase of acrolein yield is related to coherent interfaces between the structurally parent molybdates [9]. Because the lattice misfit between the lattices is low, the energy barrier at grain boundaries between crystallites is low, so that the Mo^{6+}/Mo^{5+} redox couple in a bismuth molybdate can be modified by the Fe^{3+}/Fe^{2+} couple in iron molybdate at the boundary. The result is that the additional phases are responsible not only for improving the stability against over reduction but also for increasing the O^{2-} oxygen reservoir and for assisting the reoxidation step of the redox mechanism [10, 11, 12].

Coming back to the more simple Bi-Mo-O catalytic system, the catalytic activity studies of the three well known parent bismuth molybdates called α-$Bi_2Mo_3O_{12}$, β-$Bi_2Mo_2O_9$, and γ-Bi_2MoO_6, were not in accordance. For example, Grasselli *et al.* [13] and Beres *et al.* [14] found that the activity/selectivity decreases along $\beta > \alpha > \gamma$ series, but Batist *et al.* [15] showed that the γ-phase is as active as α, whereas Cullis *et al.* [16] observed the $\alpha > \beta > \gamma$ order of activity. The protocol of preparation, the calcination [17] and the catalytic operating conditions are certainly responsible for these differences [18].

The partial oxidation of propylene to form acrolein relies on the well known Mars Van Krevelen mechanism [19] in which two redox steps are involved: the catalyst is first reduced to oxidize the reactant and in the second step the catalyst is reoxidized. To increase the selectivity to the desired product, a redox-decoupling operation which is based on the separation of the reduction and reoxidation steps in a redox mechanism was proposed. This redox-decoupling concept was achieved in the DuPont process for the production of maleic anhydride by mild oxidation of *n*-butane [20]: the catalyst reacts with *n*-butane in one reactor and is conveyed to another reactor to be regenerated. Another set-up which can be proposed for the redox-decoupling is the Catalytic Dense Membrane Reactor (CDMR) [21].

The principle of CDMR is based on a ceramic membrane which allows oxygen diffusion at high temperature. The membrane is placed between two compartments, one containing air and another filled with hydrocarbon. Thanks to this oxide ion conductive membrane, one can expect to combine the selective oxidation at the hydrocarbon side by O^{2-} species with the *in-situ* reoxidation of the catalyst by means of controlled diffusion of O^{2-} species through the membrane. The first experiments led with substituted bismuth oxides [21, 22], BIMEVOX materials which exhibit higher ion oxide conductivity than yttria-zirconia at lower temperature, were extensively investigated in our laboratory [23, 24].

Interestingly, there is a good oxide ion conductor in the Bi_2O_3-MoO_3 phase diagram, ε solid solution observed for $25.75 \leq Bi/Mo \leq 27.75$, composition which is located close to that of Bi_2MoO_6 [25]. This material is a good candidate as a membrane for CDMR. Moreover, according to our knowledge, there is no report on its catalytic properties. One can also consider that, the combination of a membrane of ε like $Bi_{25.75}Mo_{10}O_{68.625}$ with γ-Bi_2MoO_6 deposited on its surface should lead to interesting catalytic properties.

Despite the fact that multicomponent molybdates are commercially used as catalysts in oxidation of propylene, the bismuth molybdate structures are still believed to play the main role in the catalytic activity. It has been shown in the case of MoO_3 and V_2O_5 during the oxidation of methanol [26, 27], and of $(VO)_2P_2O_7$ [28, 29] during oxidation of *n*-butane, that the crystallinity, size and morphology of the particles exert a significant influence on their catalytic properties. In turn, these properties depend on the chosen method of synthesis as well as the operating parameters during calcination step. In the meantime, the interest of a study on the synthesis of γ-Bi_2MoO_6 has been brought to our attention. Since γ-Bi_2MoO_6 exhibits an irreversible phase transition near 610°C in a high-temperature polymorph which is not catalytically active, the methods of preparation at low temperature are favourable, particularly the hydrothermal synthesis by which well crystallised materials can be obtained. Although there have been several reports on its synthesis, including by hydrothermal synthesis [30, 31, 32, 33], the formation of the γ-Bi_2MoO_6 catalyst is not yet fully understood.

Therefore we have undertaken a study to understand the genesis of the γ-Bi_2MoO_6 catalyst and to demonstrate that this catalyst and its parent phases like ε could be shaped and used as ceramic membrane for the Catalytic Dense Membrane Reactor.

The work is presented in four chapters. First, the background knowledge related to selective oxidation catalysis, the possibility to operate the catalyst by redox-decoupling application, particularly the Catalytic Dense Membrane Reactor is established, and the main properties of phases in the Bi_2O_3-MoO_3 diagram are described. The second chapter deals with the genesis of γ-Bi_2MoO_6 under hydrothermal conditions which was studied by *in-situ* techniques combining high resolution X-ray diffraction, XANES and Raman Scattering. In order to complete this study and to get enough information to be able to propose a mechanism of formation, *ex-situ* characterizations were performed, of which results will be presented in the third chapter. Finally, the experiments using a Catalytic Dense Membrane Reactor based on bismuth molybdenum oxides shaped as membrane and catalyst like $Bi_{25.75}Mo_{10}O_{68.625}$ and γ-Bi_2MoO_6 will be described in the fourth chapter, before the final conclusion.

References

[1] K. Weissermel and H.-J. Arpe, *Industrial Organic Chemistry*, Wiley-VCH, 2000.

[2] L. Fishbein, *Potential industrial Carcinogens and Mutagens*, Elsevier, 1979.

[3] ed. J. D. Spengler, J. M. Sarmet, and J. F. McCarthy, *In Door Air Quality Handbook*, McGraw-Hill, 2001.

[4] W. G. Etzkorn, S. E. Pedersen, and T. E. Snead, *Acrolein and Derivatives*, John Wiley & Sons, Inc.

[5] G. W. Hearne, E. Cerrito, and M. L. Adams, Production of unsaturated carbonylic compounds, 1948.

[6] J. D. Idol, Process for the manufacture of acrylonitrile, 1959.

[7] J. L. Callahan, R. W. Foreman, and F. Veatch, Process for the oxidation of olefins, 1960.

[8] G. Yamaguchi and S. Takenaka, Process for the oxidation of olefins to aldehydes and acids, 1969.

[9] P. Courtine and E. Bordes in *Stud. Surf. Sci. Catal.*, ed. R. Grasselli, S. Oyama, A. Gaffney, and J. Lyons, Vol. 110; 1997; pp. 177–184.

[10] J. F. Brazdil, D. D. Suresh, and R. K. Grasselli, *J. Catal.*, 1980, **66**, 347–367.

[11] D. H. He, W. Ueda, and Y. Moro-Oka, *Catal. lett.*, 1992, **12**, 35–44.

[12] H. Ponceblanc, J. M. M. Millet, G. Coudurier, and J. C. Védrine; 1992; p. 262.

[13] R. K. Grasselli, J. D. Burrington, and J. F. Brazdil, *J. Chem. Soc., Faraday Disc.*, 1982, **72**, 203–223.

[14] J. Beres, A. Janik, and J. Wasilewski, *J. Catal.*, 1969, **15**, 101–105.

[15] P. A. Batist, A. H. W. M. D. Kinderen, Y. Leeuwenburgh, F. A. M. G. Metz, and G. C. Schuit, *J. Catal.*, 1968, **12**, 45–60.

[16] C. F. Cullis and D. J. Hucknall in *Catalysis, Selective Oxidation of Hydrocarbons*, ed. G. C. Bonds and G. Webb; The Royal Society of Chemistry, London, 1982; p. 273–307.

[17] W. J. M. van Well, N. C. S. M. T. Le, S. Hoste, and P. Stoltze, *J. Mol. Catal. A: Chem.*, 2006, **256**, 1–8.

[18] G. W. Keulks, L. D. Krenzke, and T. M. Notermann, *Adv. Catal.*, 1978, **27**, 183–225.

[19] P. Mars and D. van Krevelen, *Chem. Eng. Sci.*, 1954, **3**, 41–59.

[20] R. M. Contractor, Improved vapor phase catalytic oxidation of butane to maleic anhydride, 1987.

[21] S. Azgui, F. Guillaume, B. Taouk, and E. Bordes, *Catal. Today*, 1995, **25**, 291–296.

[22] C. Courson, B. Taouk, and E. Bordes, *Catal. lett.*, 2000, **66**, 129–138.

[23] G. Mairesse, *C.R. Acad. Sci. Paris, Ser. IIc*, 1999, **2**, 651–660.

[24] A. Löfberg, S. Boujmiai, E. Capoen, M. C. Steil, C. Pirovano, R. N. Vannier, G. Mairesse, and E. Bordes-Richard, *Catal. Today*, 2004, **91-92**, 79–83.

[25] R. N. Vannier, G. Mairesse, F. Abraham, and G. Nowogrocki, *J. Solid State Chem.*, 1996, **122**, 394–406.

[26] J. C. Volta and J. L. Portefaix, *App. Catal.*, 1985, **18**, 1–32.

[27] J. M. Tatibouet, J. E. Germain, and J. C. Volta, *J. Catal.*, 1983, **82**, 240–244.

[28] E. Kestemann, M. Merzouki, B. Taouk, E. Bordes, and R. Contractor In ed. G. Poncelet, J. Martens, B. Delman, P. A. Jacobs, and P. Grange, *Preparation of catalysts VI, Stud. Surf. Sci. Catal.*, Vol. 91, pp. 707–716, 1995.

[29] N. Duvauchelle and E. Bordes, *Catal. Lett.*, 1999, **57**, 81–88.

[30] A. Beale and G. Sankar, *Nucl. Instr. and Meth. Phys. Res. B*, 2003, **199**, 504–508.

[31] A. M. Beale and G. Sankar, *Chem. Matter*, 2003, **15**, 146–153.

[32] A. M. Beale, M. T. Le, S. Hoste, and G. Sankar, *Solid State Sci.*, 2005, **7**, 1141–1148.

[33] A. M. Beale, L. M. Reuilly, and G. Sankar, *Appl. Catal. A: Gen.*, 2007, **325**, 290–295.

Summary

CHAPTER 1: AIM, BACKGROUND AND KEY CONCEPTS

CHAPTER 2: IN-SITU STUDY OF γ-Bi_2MoO_6 HYDROTHERMAL SYNTHESIS BY COMBINING HRPD, XANES AND RAMAN SCATTERING

CHAPTER 3: EX-SITU STUDY OF γ-Bi_2MoO_6 HYDROTHERMAL SYNTHESIS

CHAPTER 4: CATALYTIC DENSE MEMBRANE REACTOR

CHAPTER 1

Aim, Background and Key Concepts

SUMMARY OF CHAPTER 1

Chapter 1

Aim, Background and Key Concepts

1. INTRODUCTION TO SELECTIVE OXIDATION CATALYSIS

An intimate relationship exists between petroleum and chemical industries since about 85% of the primary organic chemical products are today derived from petroleum and natural gas sources. The majority of petroleum utilization (about 90-92%) is for energy production via total combustion to CO_2 and water. In contrast to this, oxidation reactions in chemical industries are required to be much more selective, using catalysts to decrease the activation energy for the selected process and to provide a facile path by which useful products can form. Such a class of important processes is selective oxidation by heterogeneous catalysis which represents more than 25% of catalytic processes in the modern chemical industry.

One of the most important applications of selective oxidation catalysis is the functionalization of hydrocarbons. Today, catalytic oxidation is the basis for the synthesis of a large part of the monomers or modifiers used for the production of fibers and plastic. The major industrial applications of catalytic oxidation of hydrocarbons for the synthesis of monomers are listed in Table 1.1. These data illustrate some major limitations in catalytic oxidation: few reactions attain total conversion with very high selectivity to product, none of the reaction runs at maximum selectivity due to the formation of undesired by-products, processes can generate co-products which are not always economically interesting, and some raw materials and products are suspected to be toxic.

The petrochemical technologies today are considered as mature. However, owing to the large production of kilotons or more per year, any increase of selectivity by some percentage points may increase considerably profit margins. This is the reason why the improvement of the catalyst performance and processes is still demanded by industries. The product cost is not the only one factor to improve. The high product purity, energy economics and the friendly environmental process are all expected from technological innovations in catalytic oxidation processes.

Table 1.1 Major industrial applications of catalytic oxidation for the synthesis of monomers [1].

Reactant	Products/coproduct	catalyst	Conversion (%)	Selectivity (%)
Methanol/air	Formaldehyde	Heterogeneous	99	94
n-Butane/air	Maleic anhydride	Heterogeneous	70-80	65-70
Benzene/air	Maleic anhydride	Heterogeneous	98	75
o-Xylene/air	Phthalic anhydride	Heterogeneous	100	79
Naphthalene/air	Phthalic anhydride	Heterogeneous	100	84
Propylene/air/NH_3	Acrylonitrile	Heterogeneous	97-99	73-82
Propylene/air	Acrolein	Heterogeneous	> 90	80-85
Acrolein/air	Acrylic acide	Heterogeneous	> 95	90-95
Isobutene/air	Methacrolein	Heterogeneous	> 97	85-90
Methacrolein/air	Methacrylic acid	Heterogeneous	70-75	80-90
Ethene/O_2	Ethene oxide	Heterogeneous	90	80
Ethene/air/HCl	1, 2-Dichloroethane	Heterogeneous	> 95	>95
Ethene/O_2/HCl	1, 2-Dichloroethane	Heterogeneous	> 95[a]	>97
Propene/hydroperoxide	Epoxide/alcohol	Homogeneous	10	90
p-Xylene/air	Terephthalic acid	Homogeneous	90	85-90
Cumene/air	Phenol/acetone	Homogeneous	35-40	90
Cyclohexane/air	Cyclohexanone	Homogeneous	5-15	85-90
Cyclohexanone/HNO_3	Adipic acid	Homogeneous	> 95	92-96
Cyclohexanone/NH_2OH/ H_2SO_4	Cyclohexanone oxime, $(NH_4)_2SO_4$	Homogeneous	100	>98
Ethylene/acetic acid/air	Vinyl Acetate	Homogeneous	20-35	98-99

[a] when the ethene/O_2/HCl ratio is close to stoichiometry; otherwise, the conversion per pass depends on the ethene excess.

1.1. Selective oxidation of light hydrocarbons

The selective oxidation of light hydrocarbons is one of the most attractive and challenging process due to its high potential as feedstock for providing more useful chemical products. This process has been intensively studied over the last decades. The major partial oxidations of light hydrocarbons are presented in Table 1.2. Most of these results are obtained using conventional reactor (fixed bed or fluidized bed reactors) [2].

Table 1.2 The major partial oxidations of light hydrocarbons

Reaction	**Reactant**	**Product**	**Catalyst**	**Maximum yield (mol%)**	**Ref.**
Oxidative Coupling	Methane	Ethane + Ethylene	Li/MgO	25	[3]
	Propene	Hexadiene+benzene	Bi(Me)O	10	[4]
ODH (Oxidative dehydrogenation)	Ethane	Ethylene	V/MgO+oxide	58	[5]
	Propane	Propene	V/MgO+oxide	18	[6]
	n-Butane	Butene Butadiene	Metal Molybdates	38	[7, 8]
Oxidation	Methane	CO + H_2	Pt, Ni	95	[9]
		Formaldehyde	MoSnPO	16	[10]
	Ethylene	Ethylene oxide	Ag/Al_2O_3	8	[11]
		Acetaldehyde + Acetic acid	V_2O_5 + $PdCl_2$	50	[12]
	Ethane	Acetic acid	MoVNbO	10	[13, 14]
	Propene	Acrolein	BiMoFeCoO	95	[1, 15]
	Propane	Acrylic acid	MoVNbTeO	8	[16]
	n-Butane	Maleic Anhydride	$(VO)_2P_2O_7$	70	[17]

1.2. Partial oxidation of propylene to acrolein

The selective oxidation of propylene to acrolein follows the reaction equation below:

$$CH_3CH{=}CH_2 + O_2 \rightarrow CH_2{=}CHCHO + H_2O \qquad (1.1)$$

The thermodynamic parameters of the formation of acrolein and other propylene oxidation products are given in Table 1.3. It is noteworthy that the formation of the side-products (such as CO_2 and CO) is more thermodynamically favorable than that of acrolein, hence, the use of a catalyst is extremely important to optimize the formation of acrolein.

Table 1.3 Themodynamic data of the propylene oxidations [15].

Reactions	$\Delta G°_{427°C}$ (kcal/mol)
$C_3H_6(g) + 4.5O_2(g) \rightarrow 3CO_2(g) + 3H_2O(l)$	-463.86
$C_3H_6(g) + 3O_2(g) \rightarrow 3CO(g) + 3H_2O(l)$	-304.95
$C_3H_6(g) + 1.5O_2(g) \rightarrow C_3H_4O_2(g) + H_2O(l)$	-131.42
$C_3H_6(g) + O_2(g) \rightarrow C_3H_4O(g) + H_2O(l)$	-80.82

Mechanism of selective oxidation of propylene on bismuth molybdenum oxide catalysts has been extensively investigated [18]. Several models have been proposed but the most widely accepted is the concept of 'dual site' proposed by Burrington *et al*. [19]. The adsorption studies using allyl radicals or allyl alcohol revealed that the reaction involves both bismuth oxide and molybdenum oxide sites. The detailed reaction mechanism of propylene oxidation into acrolein over bismuth molybdate catalysts is illustrated in Fig. 1.1. The initial chemisorption occurs on coordinately unsaturated Mo(VI) centers (1), followed by H-abstraction by an oxygen atom associated with bismuth to form a π-allyl complex (2), which then undergoes C-O bond formation, resulting in a σ-O-allyl molybdate (3). The acrolein precursor and Mo(V/VI) esters are then formed from allyl alcohol and bismuth molybdate. Lattice oxygen removed from the catalyst during the oxidation of propylene to acrolein must be replenished by gaseous oxygen in order to reconstitute the active site (1) and complete the redox cycle [15].

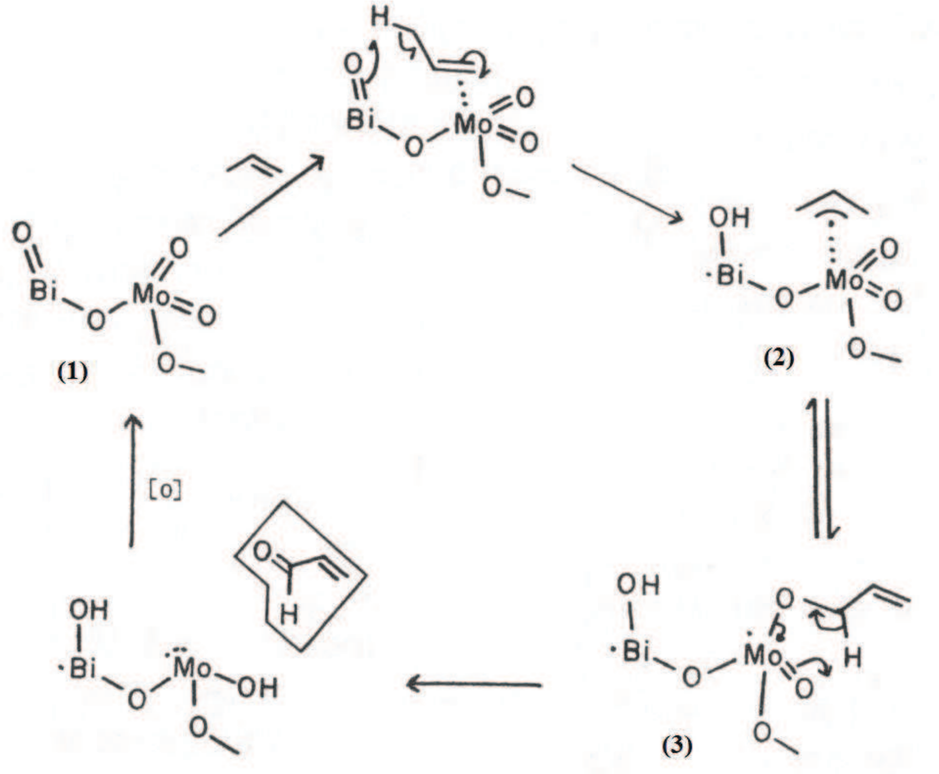

Fig. 1.1 Mechanism proposed for the selective oxidation of propylene on bismuth molybdate catalysts [19].

1.3. Mars and van Krevelen mechanism and redox-decoupling operation

In general, the selective oxidation of hydrocarbons on a metal oxide catalyst proceeds by the redox mechanism proposed by Mars and van Krevelen [20]:

$$\underset{\text{Reactant}}{[RCH_n]} + \underset{\text{Catalyst(Ox)}}{K\mathbf{O}} \rightarrow \underset{\text{Products}}{[RC\text{-}\mathbf{O}] + H_2\mathbf{O}} + \underset{\text{Catalyst(Red)}}{K} \qquad (1.2)$$

$$\underset{\text{Catalyst(Red)}}{K + O_2} \rightarrow \underset{\text{Catalyst(Ox)}}{K\mathbf{O}} \qquad (1.3)$$

This mechanism relies on the direct participation of oxygen ions O^{2-} of the oxide catalyst in the reaction products. It occurs in two steps. The reactant $[RCH_n]$ first reacts on the catalyst surface which is in its oxidized form (KO) to form the products of the selective oxidation reaction. Meanwhile the metallic cation is reduced and oxygen vacancies are formed on the surface. The reduced catalyst (K) is then reoxidized by the gaseous oxygen, which is cofed with the reactant, to restore the original oxidation state of the metallic cation with refilled vacancies. This reoxidized catalyst can subsequently react with a new molecule of reactant $[RCH_n]$ again.

However, it often happens that the formed products are more reactive than the reactants, resulting in a non negligible part of complete oxidation to CO_2. This is particularly the case when alkanes are the chosen reactant. The reactant itself may also be directly oxidized to CO_2 by O_2. The formation of CO_2 can also be promoted during the second step, the reoxidation of catalyst by gaseous dioxygen, which proceeds on the surface along:

$$O_2 \rightarrow O_2^{2-} \rightarrow O_2^{-} \rightarrow 2O^{-} \rightarrow 2O^{2-}$$

Peroxide and other electrophilic species are known to lead to complete oxidation while only O^{2-} oxide ions are selective.

Therefore to increase selectivity one technique would be to oxidize the reactant by means of the O^{2-} ions only, by suppressing the co-fed dioxygen in the first step of redox mechanism. In other words, following the mechanistic scheme, the reaction could be operated in two separated steps, which was called "redox decoupling".

This redox-decoupling concept was achieved in the DuPont process for the production of maleic anhydride by mild oxidation of *n*-butane [21]. Mimicking the FCC (Fluid Catalytic Cracking of petroleum charges) continuous process in which the catalyst reacts in one reactor and is conveyed (after separation of products) to another reactor to be regenerated, *n*-butane was oxidized in a ***Circulating Fluidized Bed Reactor*** (CFBR) in two reactors, one for the reaction, the other for reoxidation of the catalyst (Fig. 1.2). The particles of $(VO)_2P_2O_7$, the vanadium/phosphorus oxide catalyst, were pneumatically carried by the gas stream containing *n*-butane in the "riser reactor" where the *n*-butane was oxidized by the lattice oxygen of the catalyst to form mainly maleic anhydride. At the top of the riser, the reduced catalyst was separated from the gas effluent in a cyclone and fell into a fluidized bed reactor where it was reoxidized with air before being recycled to the riser.

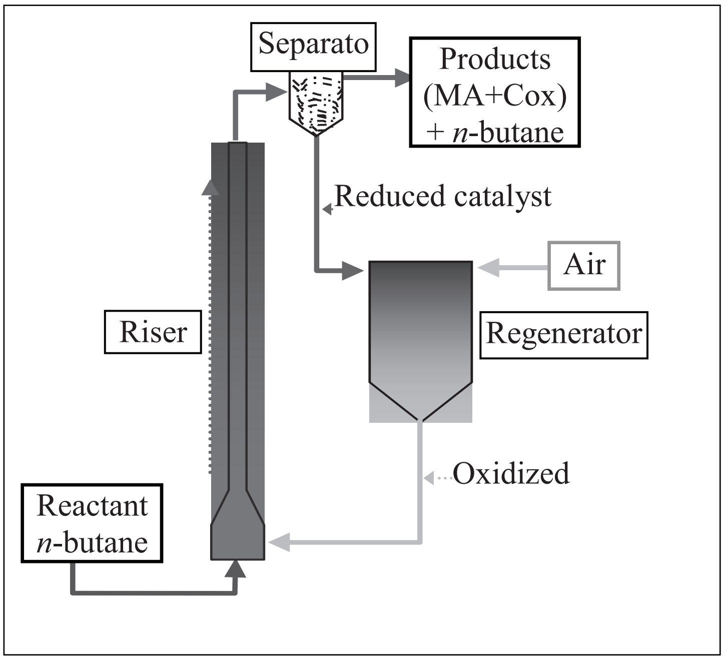

Fig. 1.2 The circulating fluidized bed reactor (CFBR).

This process was commercialized in 1996 in Gijon, Spain. However, due to various operational problems the plant was closed in 2004. Arco (Atlantic Richfield Company) developed this concept for oxidative coupling of methane as well [22] and Arkema issued patents to oxidize propylene directly to acrylic acid.

The CFBR is a way to decouple the redox mechanism in space by using two reactors. Another means is to use membrane reactors, in which the two compartments separated by a catalytic membrane are fed separately by the hydrocarbon and by air, which will be described below. This decoupling may also be achieved along time, by alternating periods of reduction (oxidation of reactant) with periods or reoxidation of catalyst. This is the case of ***Periodic feed Reactors, and Pulse feed Reactors***. The difference is small and is mainly related to the duration and analysis mode (very short time and integral analysis for pulse, vs. longer times and continuous analysis for periodic reactor). In these fixed reactors, the periodic operation consists of feeding alternately the reactor by the reactant (hydrocarbon) and the oxidant (air or oxygen), that is in two extreme conditions: oxidizing and reducing atmospheres. More particularly, the capacity of the solid to provide (selective) O^{2-} oxide ions, the so-called "oxocapacity", can be studied as a function of operating parameters (the partial pressure of reactants, contact time, duration, temperature, etc.) This tool is very useful to elucidate the reaction mechanism in laboratories but cannot be used at industrial scale due to low capacity of production.

2. MEMBRANE REACTORS

Other examples of redox-decoupling operation are the ***Catalytic (Dense) Membrane Reactors***. The main advantage of the membrane utilization is that it combines reaction and separation in a single unit [23]. Obviously, the concept of membrane reactor is far from being new. A number of important membrane processes were initially developed in biological systems, giving rise to ***organic membranes***. However, most of the catalytic industrial processes which operate at high temperature and in hazardous conditions require inorganic membranes, or at least polymer membranes which are stable enough like ®Nafion in protonic fuel cells [24]. The availability of inorganic membranes in the application market pushed forward the accelerated development of membrane reactors in the last decades, beginning by SOFCs (Solid Oxide Fuel Cells) [25] and COG (Ceramic Oxygen Generators). Though the potential of membrane reactors has been widely demonstrated at laboratory scale for petrochemical applications, e.g., the direct and oxidative dehydrogenation of hydrocarbons [5, 6], this concept is still rarely applied at the industrial scale [26]. Indeed, the principal limitation of the development of membrane reactors is the membrane itself. The optimization of the existing membranes and the discovery of new materials are still necessary for the use of membranes in industrial applications.

2.1. Types of membranes

Based on the structure of membranes and on the mechanism of transport of chemical species through them, two categories of ***inorganic membranes*** are considered, the ***porous*** and ***dense membranes*** [26]. ***Dense membranes*** themselves differ if made of metal or behaving as solid electrolyte. Apart from their permselectivity and reactivity, one of the main characteristics of these membranes is their permeability which determines the capacity of the membrane. It is especially dependent of the thickness and the dense or porous texture of the membranes which determine the transport mechanism.

In catalytic applications, the ***porous membranes*** (Fig. 1.3) are used as supports of catalysts. This type of membrane acts as both a catalyst and a separator between the reactants, that may be dioxygen (O_2) and the hydrocarbon in oxidation reactions. They offer a high permeability which allows a high O_2 supply to the catalytic active sites in the whole membrane. This characteristic is potentially interesting for increasing the conversion rates. The most appropriate membranes are micro and mesoporous, with pore diameters less than 50 nm, which allows a good mixing between reactants and catalyst surface. However, (retro)diffusion of other species than O_2 may occur and these membranes are not completely oxygen permselective. Such a disadvantage excludes the use of these membranes for example in the syngas (CO, H_2) production.

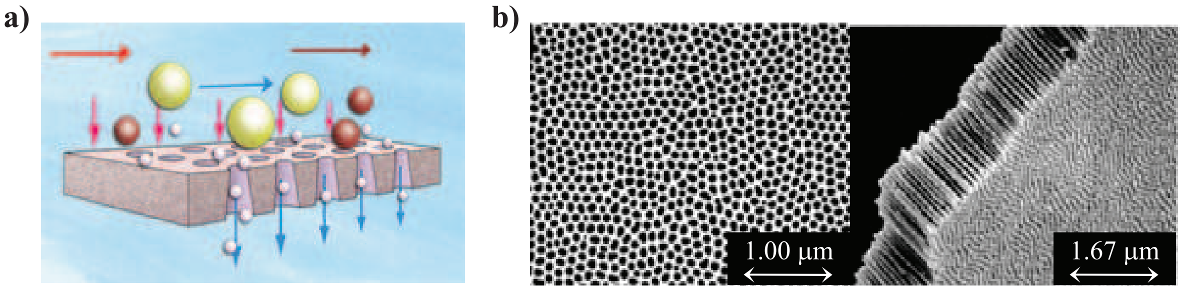

Fig. 1.3 a) Schematic illustration and b) Scanning electron micrographs of a nanosized porous alumina membrane [27].

On the contrary, dense membranes are known for their high permselectivity. When they are metallic, the gas transport inside follows the solution-diffusion mechanism. For instance, palladium is preferred for their permselectivity to H_2 while the silver membranes are generally used for their permselectivity to O_2. However, the latter cannot be employed durably under an oxidizing atmosphere at high temperatures. An extensive research has been carried out for the utilization of dense membranes for the reaction using O_2 like in oxidation and dehydrogenation reactions. When the dense membranes are protonic or oxide ion conducting they are used as electrolytes in various applications including Solid Oxide Fuel Cell (SOFC), oxygen sensors, oxygen separators. Restricting to ceramic membranes, the materials behave as ***pure ionic conductors*** or as ***mixed ionic and electronic conductors*** (MIEC). Most ceramic membranes used with success in catalytic membrane reactors in hydrocarbon oxidation belong to the MIEC category. An example is the brownmillerites used in the methane reforming to syngas [28].

2.2. Catalytic Dense Membrane Reactor (CDMR) applications

The concept of CDMR theoretically offers the possibility to avoid the direct reaction between dioxygen gas phase and the hydrocarbon that may lead to its total oxidation [4, 29]. The catalytic dense membrane separates two compartments, the first is fed by the (diluted) hydrocarbon on the reactant side and the second is fed by diluted oxygen on the oxidizing side. At the high oxygen partial pressure side (HOP), O_2 is reduced into O^{2-} species, which diffuse through the membrane towards the low oxygen partial pressure side (LOP). Therefore the driving force of O^{2-} diffusion in CDMRs depends on the types of membrane material. It can be the gradient of oxygen partial pressure between the two sides of the membrane for a MIEC or the difference in electrical potential between two electrodes applied by means of an external electric circuit for a pure ionic conductor. The expected reactions are:

- Reduction of dioxygen at HOP : $O_2 + 4e^- \rightarrow 2O^{2-}$ (1.4)

- Oxidation of hydrocarbon by O^{2-} coming by diffusion through the membrane at LOP :

$$[RCH_n] + O^{2-} \rightarrow [RC\text{-}O] + H_2O + 2e^- \quad (1.5)$$

It must be noticed that when O^{2-} arrives at LOP surface, it may be oxidized back to form gaseous O_2 by the reverse reaction (Eq. 1.4). This phenomenon corresponds to the semi-permeability to O_2 of the material. Otherwise, O^{2-} may preferably react selectively with the hydrocarbon (Eq. 1.5). These processes are illustrated in Fig. 1.4 for pure ionic conductor and for MIEC.

To be used in CDMR, the dense oxide ion conductive membrane must display a high ionic conductivity, and must be stable but catalytically active in the reaction conditions. In this concept, the dense membrane has two roles: it provides the oxygen needed for the reaction and acts as the catalyst. If the catalytic activity of the membrane is not good enough, a catalyst can be deposited on the membrane surface to enhance its catalytic activity.

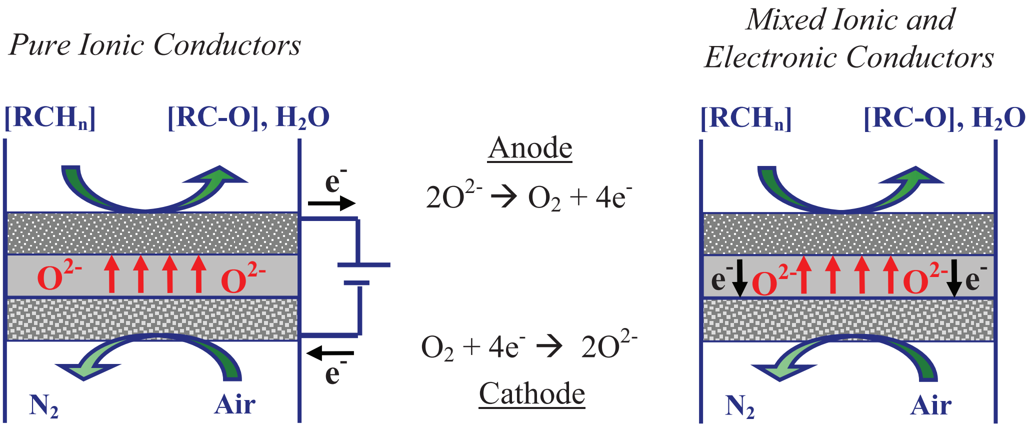

Fig. 1.4 The pure ionic conductors (left) and the mixed ionic and electronic conductors (MIEC) (right).

a) Mixed Ionic Electronic Conductors

The crystal structures of MIEC are numerous: substituted fluorite (e.g. Ti-YSZ [30]), perovskite (e.g. $La_{1-x}Sr_xCo_{1-y}Fe_yO_{3-d}$ [31]), brownmillerite (e.g. $Sr_2Fe_2O_5$, $Ca_2Fe_2O_5$ [28]), Aurivillus-type (e.g. BiMeVOX [32]), etc. The oxygen transfer in these materials can be achieved without a current supply due to their intrinsic electric conductivity, but membrane need to operate at high temperature to have sufficient electric and ionic conductivity. A good oxygen permeation rate is strongly dependent on the ionic conductivity (for O^{2-} oxide ion diffusion) and also on the electronic conductivity (for electronic diffusion and for ensuring the reduction of O_2). Besides, the oxygen surface exchange can also limit the oxygen permeation flux. When the oxygen transfer is not limited at the surface, the oxygen permeation flux is given by Wagner equation:

$$J_{O_2} = \frac{RT}{(4F)^2 L} \frac{\sigma_e \sigma_i}{\sigma_e + \sigma_i} \ln \frac{P_{O_2}^{'}}{P_{O_2}^{''}} \qquad (1.6)$$

where L is the thickness of the membrane, σ_e and σ_i are the electronic and ionic conductivity, P'_{O2} and P''_{O2} are the oxygen partial pressures in the two sides of the membrane reactor, R is the gas constant (8,314 $J.k^{-1}.mol^{-1}$), T is the temperature in Kelvin and F is the Faraday constant (96500 C/mol). The $\frac{\sigma_e \sigma_i}{\sigma_e + \sigma_i}$ ratio is known as the ambipolar conductivity, σ_{ambi}.

The ***mixed-conducting dense ceramic membranes*** are generally applied for the high temperature catalytic reactions such as the methane conversion to synthesis gas, methane oxidative coupling, etc. Recently, Eltron Research Inc. has developed this concept for selective oxidation of methane to synthesis gas. The potential of these membranes has been widely demonstrated. Although they often play the role of catalysts (e.g. $La_{0.3}Bi_{1.7}O_3$ [33]), they are sometimes covered with a specific catalyst layer. An increase of 60% of the conversion of methane was obtained with a layer of Ni/Al_2O_3 on the surface of a perovskite membrane [31]. However, the number of potential applications is limited by the low oxygen diffusion through membrane at low temperatures, typically below 700°C.

Other examples of ***mixed-conducting dense ceramic membranes*** are BIMEVOX materials, based on the γ-$Bi_4V_2O_{11}$ structure in which V is partially substituted by ME = Co, Cu, Ta, Ni, which were extensively studied at UCCS for the temperature range of 550-750°C [34, 35, 36, 37, 38, 39, 40]. Their catalytic properties in the oxidation of light hydrocarbons, such as methane, ethane, propane and propylene, were examined in terms of, (i) active sites on polished or unpolished surfaces, (ii) operating conditions (T, pO_2 in the high partial pressure compartment), which determine the selectivity, either to mild oxidation products (acrolein, hexadiene, CO) or to partial oxidation product (CO, H_2), and, (iii) nature of ME cations and relative properties. Although BIMEVOX membranes exhibit very low semi-permeability to oxygen because of a low oxygen transfer coefficient at the surface [41], this property leads to strong polarization of the membranes which contributed to their good stability, even at low pressure side of the membrane.

b) ***Pure ionic conductors***

The structure of most pure ionic conductors is fluorite-type, like ZrO_2, CeO_2 or Bi_2O_3 stabilized by Y, Mg, Er or Ca. Because of their poor electronic conductivity, the electroneutrality of the oxide is assured by an external electronic circuit when used in CDM-type reactors. The driving force in this process is the difference in electrical potential between two electrodes applied by the current generator. The oxygen flux J_{O2} ($cm^{-3}.min^{-1}$) is proportional to the intensity of the current applied. The theoretical oxygen flux can be calculated by:

$$J_{O_2} = \frac{V_m \times I}{4F} \tag{1.7}$$

where V_m is the molar volume (24056 mL/mol at 20°C), I is the current applied (A) and F is the Faraday constant (96500 C/mol). For example, when the faradic yield is 100%, a 1 $A.cm^{-2}$ applied current density can generate an oxygen flux of about 3.74 $cm^{-3}.cm^{-2}.min^{-1}$.

The reactors using this process are called ***electrochemical membrane reactors*** or ***Solid-Electrolyte Membrane Reactors*** (SEMR). Almost solid electrolytes employed are yttria-stabilized zirconia (YSZ) but the material used as a porous anode is chosen as a function of catalytic reactions or desired products. In general, it is a metal, e.g. Ag [42], Au [43], Ni [44], Pd [45], Pt [46] or Rh [47], which is known for its high catalytic activity in certain specific oxidation reactions [48]. The main advantage is the possibility to control the O_2 flux diffusing through the membrane by the imposed electric current. This allows oxygen diffusion at low temperatures which is the limitation of MIEC ceramic membranes. With such reactors, it is possible to perform low temperature catalytic reactions, for example the oxidation of alkanes and alkenes, the reactions $C_2H_6, O_2 \rightarrow CH_3CHO, CO, CO_2, H_2O$ [43], $C_2H_4, O_2 \rightarrow CO_2, H_2O$ [49] and $C_3H_8, O_2 \rightarrow C_3H_6, CO, H_2O$ [32], etc.

2.3. Applications to the partial oxidation of propylene to acrolein

The partial oxidation of propylene to acrolein using an electrochemical membrane reactor has been the matter of considerable attention by the group of Hayakawa and Takehira in the 80's. The primary goal of these studies was to examine if acrolein could be produced at selectivity higher than that achieved in conventional fixed bed reactors (ca. 85% at 95% conversion). The electrocatalytic formation of acrolein was studied with various metal and metallic oxide electrodes, with or without metal oxide catalyst on the membrane surface, [50, 51, 52, 53, 54, 55, 56]. For example in 1986, Hayakawa et *al*. [50] demonstrated the production of acrolein from propylene by oxygen species generated electrochemically on an inert gold film via yttria-stabilized zirconia at 450°C. Later, the reactivity and selectivity of Bi_2O_3, MoO_3, as well as the three well known bismuth molybdate catalysts (α-$Bi_2Mo_3O_{12}$, β-$Bi_2Mo_2O_9$, γ-Bi_2MoO_6), all deposited on a gold anode were evidenced [51, 52, 53]. Among these catalysts, MoO_3 showed the highest activity for propylene oxidation to acrolein. Its activity was up to 600 times higher than that obtained with the same catalyst using a mixed-gas flow reactor. From these results, it was suggested that oxygen species bound to molybdenum metal possess a definite role for both hydrogen abstraction from propylene and oxygen insertion into the allylic intermediate under a sufficient oxygen supply. On the other hand, the measured oxygen permeation through a Bi_2O_3 film suggested that the bismuth species is effective for O_2 incorporation into the catalyst and also for the transportation of oxide ions through the catalyst [53].

In order to achieve higher oxygen permeation fluxes at lower temperatures (350-450°C), $(CeO_2)_{0.8}(SmO_{1.5})_{0.2}$ was later employed as a membrane instead of YSZ [54, 55, 56]. The formation rate of acrolein increased linearly with increasing current density. However, the addition of oxygen to the propylene-mixed gas at the low oxygen partial pressure side did not affect the acrolein production. Consequently, it was suggested that propylene was oxidized to acrolein by the oxygen species produced electrochemically at the triple phase boundary (TPB) of the gold-electrolyte-gas phase.

Although interesting results were obtained, there have been little studies on this thematic. There is still no report on the combination of bismuth molybdate membrane and catalysts for the CDMR applications.

3. MATERIALS FOR CDMR: Bi_2O_3-MoO_3 PHASE DIAGRAM

Looking at the binary Bi_2O_3-MoO_3 system and the properties of some compounds (Fig. 1.5 and Fig. 1.6) gives a new incentive for optimization of catalytic membrane reactors, because the materials used as a membrane and a catalyst can belong to the same binary system. The combination of one of the well-known active (α, β, γ-bismuth molybdates) catalysts for the partial oxidation of propylene to acrolein with a bismuth molybdate membrane exhibiting high ionic conductivity at low temperature is expected to give an efficient system for a catalytic dense membrane reactor.

The binary Bi_2O_3-MoO_3 system is particularly rich in phases known for their catalytic properties or their oxide ion conductivity. Most of the early investigations in the 70's dealt with the three phases with Bi/Mo ≤ 2: α-$Bi_2Mo_3O_{12}$, β-$Bi_2Mo_2O_9$ and γ-Bi_2MoO_6 which exhibited catalytic properties in the partial oxidation of propylene to acrolein (Fig. 1.5) [44]. On the bismuth-rich side, several compounds with Bi/Mo > 2 have recently been identified in the past few years (Fig. 1.6). They can be described as molybdenum doped δ-Bi_2O_3 related structures which are known for their good oxide ion conductivities.

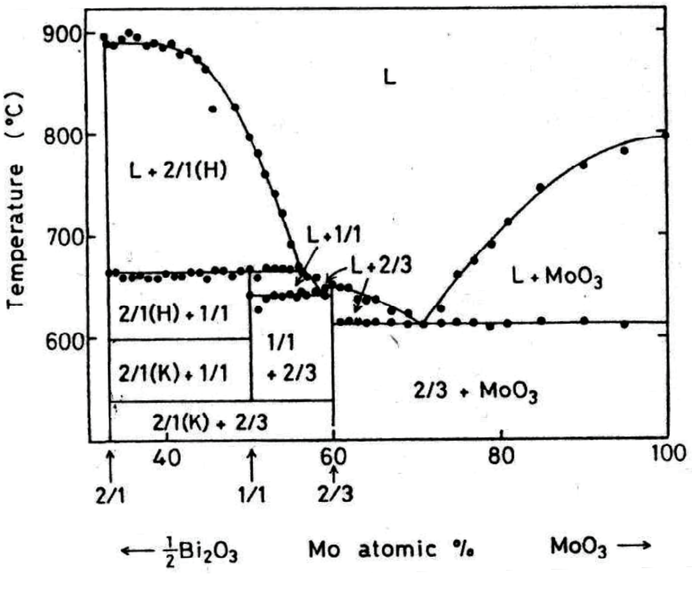

Fig. 1.5 Partial phase diagram of the system Bi_2O_3-MoO_3 adapted from Egashira *et al* [57]. 2/3 is α-$Bi_2Mo_3O_{12}$; 1/1 is β-$Bi_2Mo_2O_9$; 2/1(K) is γ'-Bi_2MoO_6 (low temperature form); 2/1(H) is γ''-Bi_2MoO_6 (high temperature form).

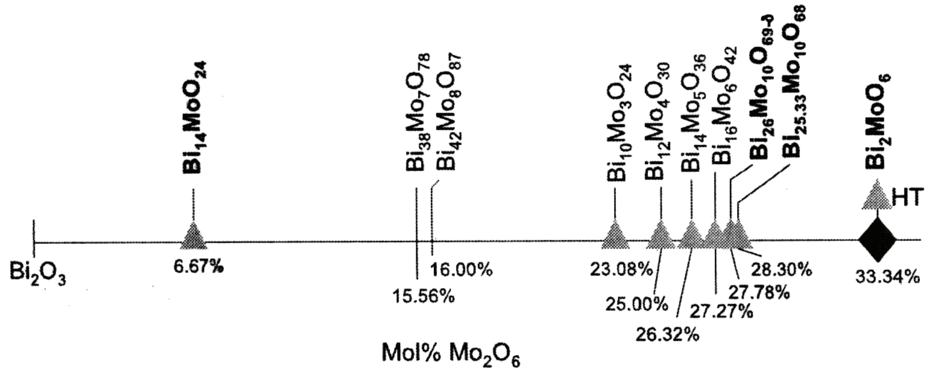

Fig. 1.6 Partial phase diagram of the pseudo-binary Bi_2O_3-MoO_3 system (adapted from Sharma *et al* [58]).

Among these compounds, the solid solution called ε which is located around the parent compound $Bi_{26}Mo_{10}O_{69}$ was extensively studied at UCCS [59, 60]. It is a pure oxide ion conductor which could be used as an oxide ion membrane at low temperatures since its conductivity has been demonstrated to be higher than that of YSZ at low temperatures. With the aim to develop a bismuth-molydate Catalytic Dense Membrane Reactor, the upper limit of the solid solution $Bi_{25.75}Mo_{10}O_{68.625}$, was chosen for the membrane. Since only molybdenum rich compositions were shown to have catalytic properties, to avoid any risk of phase evolution, γ-Bi_2MoO_6 was selected as the catalyst to be deposited on the membrane surface, in order to increase the catalytic activity in the membrane reactor.

3.1. $Bi_{26}Mo_{10}O_{69}$ and its solid solution ε as a membrane

3.1.1. Crystal structure and polymorphism

The $Bi_{26}Mo_{10}O_{69}$ was possibly first identified in 1971 by Erman *et al.* [61] who described it as a phase formulated ~$1.4Bi_2O_3$-MoO_3, having a solid solubility. Later Miyazawa *et al.* [62] obtained large single crystals from congruent melt with the composition of $3Bi_2O_3$-$2MoO_3$ despite of a chemical analysis yielding Bi/Mo ~ 2.6. The existence of a solid solution extending around the $1.3Bi_2O_3$-MoO_3 composition was later confirmed by Chen and Smith [63]. They found that the symmetry of the monoclinic crystal structure was $P2_1/m$ or $P2_1$, with unit cell parameters a = 24.723(3), b = 5.804(1), c = 11.799(3) Å and β = 102.76(2)°, rather than a $P2/c$ monoclinic with unit cell parameters, a = 24.786, b = 5.805, c = 23.527 Å and β = 102.93° as reported by Miyazawa *et al.* [62].

The crystal structure of $Bi_{26}Mo_{10}O_{69}$ (Fig. 1.7) was accurately solved in 1996 by Vannier *et al.* [59]. The single crystal X-ray diffraction studies revealed a monoclinic crystal structure in *P*2/c with a = 11.742(8), b = 5.800(7), c = 24.77(5) Å, β = 102.94(6)° and Z = 1; its atomic coordinates are given in Table 1.4.

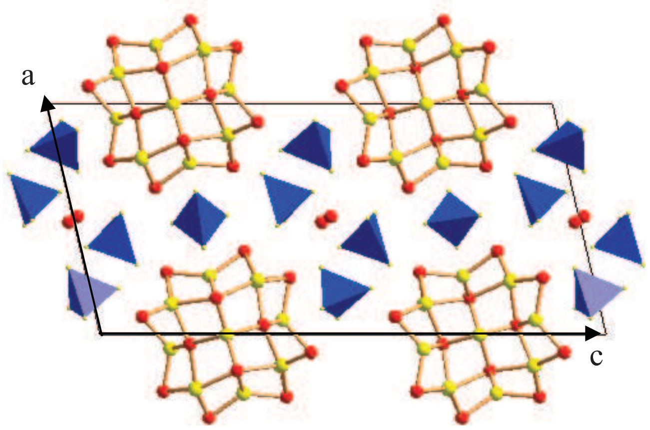

Fig. 1.7 The crystal structure of $Bi_{26}Mo_{10}O_{69}$ structure projected along the *b* axis (Bi red, O yellow and [MoO_4] in blue tetrahedral).

The $Bi_{26}Mo_{10}O_{69}$ structure can be described as a fluorite related structure. It consists of rose-shaped $[Bi_{12}O_{14}]^{8+}$ columns, containing typically Bi^{III}-oxygen arrangements, which run parallel along the [010] axis and are surrounded by isolated $[MoO_4^{2-}]$ tetrahedra.

The bismuth coordination within the rose-shaped $[Bi_{12}O_{14}]^{8+}$ networks, Bi(1)-(6) surrounded by O(1)-(8) atoms, appears irregular. They have a large variation of Bi-O length (2.10(3)-3.06(3) Å) and most bismuth atoms are surrounded by two or three oxygen atoms with short Bi-O bond lengths (< 2.4 Å). Such short Bi-O bonds can be accounted for the stereochemical active $6s^2$ lone pair of Bi atoms. An isolated Bi(7) atom is coordinated with 8 O atoms and surrounded by MoO_4 tetrahedra of Mo(1) and Mo(2) type atoms. The Mo(3) type of MoO_4 tetrahedra are not involved in the Bi(7) coordination, they are only shared by the two rose-shaped $[Bi_{12}O_{14}]^{8+}$ columns. The local environment of these three isolated molybdate groups is tetrahedrally distorted. However, the structure determination of $Bi_{26}Mo_{10}O_{69}$ by single X-ray diffraction led to the crystallographic formula: $[Bi_{12}O_{14}](MoO_4, Bi)(MoO_4)_4$, i.e. $Bi_{26}Mo_{10}O_{68}$ instead of $Bi_{26}Mo_{10}O_{69}$. The existence of additional oxygen was not revealed by X-ray diffraction technique. Moreover, the solid solution of this phase, called ε , was found in the range of approximately $2.575 \leq Bi/Mo \leq 2.775$ by the solid state synthesis using stoichiometric amounts of Bi_2O_3 and MoO_3.

Table 1.4 The structure model of $Bi_{26}Mo_{10}O_{69}$ proposed by Vannier *et al.* [59].

$Bi_{26}Mo_{10}O_{69}$
Space Group: *P*2_1/c: =17.742(8), b=5.800(7), c=24.77(5) Å, β= 102.94(6)° and Z=1

Atom	Site	x	y	z	Biso (Å^2)	occupation
Bi1	(4g)	0.04101(8)	0.4163(2)	0.32690(5)	0.99(3)	1
Bi2	(4g)	0.15779(8)	0.9151(2)	0.24587(5)	1.06(3)	1
Bi3	(4g)	0.24670(8)	0.0113(2)	0.40065(4)	1.20(3)	1
Bi4	(4g)	0.36084(8)	0.5026(2)	0.32328(5)	1.19(3)	1
Bi5	(4g)	0.26942(7)	0.5034(2)	0.16025(5)	1.07(3)	1
Bi6	(4g)	0.07778(7)	0.0081(2)	0.09138(4)	1.03(3)	1
Bi7	(4g)	0.5120(7)	0.478(2)	0.0101(2)	3.5(2)	0.5
Mo1	(4g)	0.4180(2)	0.9955(5)	0.0775(2)	1.54(6)	1
Mo2	(4g)	0.8317(3)	0.5160(5)	0.0108(2)	2.06(7)	1
Mo3	(2f)	0.5	0.0078(8)	0.25	1.83(9)	1
O1	(2e)	0	0.727(4)	0.25	0.9(4)	1
O2	(4g)	0.136(2)	0.261(3)	0.1582(8)	1.3(3)	1
O3	(4g)	0.132(2)	0.755(4)	0.1539(9)	1.7(4)	1
O4	(4g)	0.238(2)	0.769(3)	0.3362(8)	1.4(4)	1
O5	(4g)	0.255(2)	0.589(4)	0.2440(8)	1.6(3)	1
O6	(4g)	0.063(2)	0.066(3)	0.3674(8)	1.3(3)	1
O7	(2e)	0	0.239(5)	0.25	1.4(5)	1
O8	(4g)	0.230(2)	0.269(4)	0.3350(9)	1.7(4)	1
O9	(4g)	0.506(3)	0.735(8)	0.082(2)	9.0(1)	1
O10	(4g)	0.379(4)	0.106(9)	0.013(3)	11.0(2)	1
O11	(4g)	0.302(4)	0.976(8)	0.105(2)	9.0(2)	1
O12	(4g)	0.528(4)	0.205(9)	0.099(3)	12.0(2)	1
O13	(4g)	0.929(3)	0.303(8)	0.023(2)	9.0(1)	1
O14	(4g)	0.800(3)	0.552(6)	0.942(2)	6.0(7)	1
O15	(4g)	0.888(3)	0.755(6)	0.049(2)	6.7(8)	1
O16	(4g)	0.710(3)	0.433(6)	0.032(2)	6.9(8)	1
O17	(4g)	0.378(2)	0.166(5)	0.245(2)	4.3(5)	1
O18	(4g)	0.482(4)	0.820(9)	0.194(3)	11.0(2)	1
O19	(4*)					0.25

This structural study and the limits of the solid solution in the Bi_2O_3-MoO_3 binary diagram were later supported by Buttrey *et al*. [64]. These authors solved the $Bi_{26}Mo_{10}O_{69}$ structure from neutron diffraction data, and they suggested the existence of an interstitial oxide for the additional oxygen O(19), to explain the oxygen stoichiometry. Nevertheless, their model led to a short O-O bond length of 1.62 or 2.11 Å due to constrain used in the refinement. Enjalbert *et al*. confirmed the basic structural features proposed by Vannier *et al*. [59] as well and later published the structure of isotypic compounds which are $PbBi_{12}Mo_5O_{34}$

[65] and $Bi_{13}Mo_4VO_{34}$ [66]. However they disagreed on the interpretation of nonstoichiometry and proposed another solid solubility range of $2.86 \leq Bi/Mo \leq 3.5$ which was based on the existence of $Bi_6Mo_2O_{15}$ compound reported earlier by Miyazawa *et al.* [62]. Later, Enjalbert team [67] proposed a new range of solid solubility: $2.534 \leq Bi/Mo \leq 3.5$ which includes the first solid solution range proposed by Vannier *et al.* [59]. However, it is uncertain whether the limit of this solid solution would be up to Bi/Mo = 3.5 because it is not supported by experimental results.

Vannier *et al* [60] later redetermined the crystal structure of this solid solution from neutron diffraction data collected on the Bi/Mo 2.75 composition. There was no significant change in the structure. Based on a comparison with the fluorite structure, an O(19) site was introduced in the model and its surrounding exhibits no physical unacceptable characteristics. Differential Scanning Calorimetry (DSC) and high temperature X-ray diffraction experiments were carried out by Vannier *et al.* [59] and revealed that a reversible phase transition between a low temperature form with triclinic symmetry and a high temperature form with monoclinic symmetry occurs at about 310°C. These two polymorphs appear very similar, the only difference is the symmetry. For the range $2.575 \leq Bi/Mo \leq 2.775$ of solid solubility, the symmetry is triclinic at room temperature; an increase of the bismuth content leads to the stabilization of the monoclinic phase at room temperature for $Bi/Mo \geq 2.75$.

3.1.2. Physical and electrical properties

$Bi_{26}Mo_{10}O_{69}$ and its solid solution ε were demonstrated to exhibit high oxide ion conductivity at low temperature [59, 60, 68]. The conductivity (σ) value of $Bi_{25.75}Mo_{10}O_{68.625}$ is about $1.5.10^{-2}$ $S.cm^{-2}$ at 500°C which is rather high compared with that of the well-known solid electrolyte YSZ at the same temperature ($\sigma = 1.10^{-2}$ $S.cm^{-2}$). It is worth noting that the ionic conductivity of $Bi_{25.75}Mo_{10}O_{68.625}$ is higher than that of $Bi_{26}Mo_{10}O_{69}$ which is probably due to a higher abundance of interstitial O atoms or of O vacancies in $Bi_{25.75}Mo_{10}O_{68.625}$ structure.

Vannier *et al* [60] described three types of oxide ion conductors in the molybdenum doped δ-Bi_2O_3 related structures: three-, two- and monodimensional. The three-dimensional conduction occurs in the fluorite type structure δ-Bi_2O_3 that can be stabilized by numerous appropriated dopants [69, 25] and where oxide ions can move through the lattice without direction constraints. The two-dimensional conduction is found in layered structures such as γ-Bi_2MoO_6 Aurrivillius phase [70] and the related BIMEVOX compounds [71] where oxide ions can move along 2D-planes. The first example of monodimensional type conductor is provided by $Bi_{26}Mo_{10}O_{69}$. From neutron diffraction study, two types of O atoms are distinguished in this structure: those of the $[Bi_{12}O_{14}]^{8+}$ columns and those of Mo surroundings, the latter are likely responsible for the oxide anionic conductivity because of their high thermal parameters [60]. This idea was later supported by NMR study [72]. Moreover, measurements of conductivity under variable oxygen partial pressure clearly indicated that these materials can be considered as pure oxide ionic conductors with negligible electronic semiconducting contribution within the range of temperature and oxygen partial pressure studied (719-790°C and 1 - ~10^{-6} atm).

The electrochemical stability of the material plays also an important role for the future applications such as fuel cells or CDMR. The electrochemical stability of $Bi_{26}Mo_{10}O_{69}$-based materials was studied on micro samples by voltametry [73, 74]. These results show a stability limit located approximately at 100 mV which is higher than that of BIMEVOX. This limit is probably related to the reduction of Mo(VI) to Mo(IV) and Bi(III) to Bi(0), unfortunately the second redox process is not reversible. This disadvantage prevents the application of these materials in Solid Oxide Fuel Cell but being more stable than BIMEVOX, they can be a promising membrane for CDMR applications. Although, their catalytic activity is not proven yet, the choice of the upper limit of the ε solid solution, $Bi_{25.75}Mo_{10}O_{68.625}$, should prevent any evolution of the chemical composition during the catalytic test.

3.2. γ-Bi_2MoO_6 as a catalyst

3.2.1. Crystal structures of γ-Bi_2MoO_6

The crystal structure of γ-Bi_2MoO_6, with the mineral name koechlinite, was first determined by Zemann [75] in 1956, using powder X-ray diffraction. It was first described in *C*mca orthorhombic symmetry, with lattice parameters: a = 5.50(2), b = 16.24(6), c = 5.49(2) Å and Z = 4. This structure model was later abandoned in 1982 for a *P*bca space group [76] and ruled out by Van den Elzen and Rieck [77]. These authors showed that its linear absorption coefficient [75] was too high and that the *C*mca space group did not allow a proper refinement for X-ray data collected from a natural single crystal of koechlinite. They proposed the space group *P*ca2_1 with cell parameters: a = 5.487(2), b = 16.226(6), c = 5.506(2) Å and Z = 4. However, the nearest O-O distance in this model, only 2.2 Å, is too short, showing an unrealistic physical feature. According to the effective ionic radii of oxygen, the shortest distance allowable for two unbonded oxygen is about 2.4 Å [78].

The structural models proposed by Van den Elzen and Rieck [77] and Pertlik and Zemann [76] show a good agreement for the positions of the heavy atoms, only the oxygen arrangements are different for the different space groups. The conventional X-ray diffraction usually shows the difficulty of locating oxygen ions in the presence of strong scatterers such as bismuth or molybdenum ions. Using neutron diffraction technique, in which the oxygen (scattering length b = 0.581×10^{-12} cm) scatters as well as bismuth (b = 0.853×10^{-12} cm) and molybdenum (b = 0.853×10^{-12} cm) [70], the oxygen positions in koechlinite can be determined without ambiguity. In 1982, the neutron diffraction study of γ-Bi_2MoO_6 was carried out independently by Teller *et al.* [79] and Theobald *et al.* [70], using time of flight and monochromated neutrons, respectively. They clarify the controversy over the space group symmetry. Both obtained the same result within experimental error for *P*ca2_1 space group as proposed early [77], despite a typographical error in the abstract of the paper by Teller *et al.* [79] indicating *P*na2_1.

The shortest O-O distance of about 2.55 Å is now acceptable and the non centro-symmetric space group *P*ca2_1 is compatible with the ferroelectric properties reported by Ismailzade et al. [80]. The structure model proposed by Theobald *et al.* [70] is given in Table 1.5. It will be used later in our XRD refinement studies.

The structure model of γ-Bi_2MoO_6 developed by Theobald *et al.* [70] and Teller *et al.* [79] was described as an Aurivillius structure [81] which is built up, with a perovskite arrangement, by the infinite $[Bi_2O_2^{2+}]_n$ layers separated by the infinite layers of distorted corner-sharing MoO_6 octahedra: $[MoO_4^{2-}]_n$, perpendicular to the [010] direction. Three types of oxygen atoms are distinguished:

- First type: O(2) and O(3) are entirely contained in the $[Bi_2O_2^{2+}]_n$ layers, bridging four metal atoms.
- Second type: O(4) and O(5) are within the MoO_6 octahedral layers, $[MoO_4^{2-}]_n$, bridging only two Mo atoms in the plane perpendicular to the y direction.

- Third type: O(1) and O(6) are two apex ions of the MoO_6 octahedra, pointing towards two $[Bi_2O_2^{2+}]_n$ layers, one above and one below. Each oxygen atom is bonded to one Mo and two Bi atoms.

Table 1.5 The structure model of γ-Bi_2MoO_6 proposed by Theobald *et al.* [70].

γ-Bi_2MoO_6

Space Group: $Pca2_1$: a=5.487(2), b=16.226(6), c=5.506(2) Å and Z=4

atom	site	X	y	z	Biso (Å^2)	occupation
Bi1	(4a)	0.519(1)	0.4231(4)	0.983(2)	0.15(11)	1
Bi2	(4a)	0.483(1)	0.0786(5)	0.989(2)	0.86(16)	1
Mo1	(4a)	0.001(2)	0.2479(6)	0	0.94(7)	1
O1	(4a)	0.049(2)	0.1428(6)	0.091(2)	1.04(19)	1
O2	(4a)	0.259(1)	0.9956(5)	0.271(2)	0.39(15)	1
O3	(4a)	0.242(2)	0.5048(5)	0.272(2)	0.97(18)	1
O4	(4a)	0.698(2)	0.2297(5)	0.251(2)	1.06(14)	1
O5	(4a)	0.207(2)	0.2624(6)	0.360(2)	1.84(15)	1
O6	(4a)	0.572(2)	0.3602(9)	0.575(2)	2.19(34)	1

According to Theobald *et al.* [70], the octahedra in this structure are not only distorted but also folded each other, as demonstrated by the shift of the O(1) and O(6) in the opposite direction in Fig. 1.8. For the distortion of octahedra, it appears that the Mo atom is shifted towards one of the O(4)-O(5) edges, about 0.357 Å away from the center of the octahedron and the distance from the Mo atom to the equatorial plane is 0.039(3) Å. So the symmetry around Mo is plausibly C_{2v} rather than C_{3v} or C_{4v}. Consequently, 4 distances (1.78-1.91 Å) are much shorter than 2 others (2.18-2.30 Å), so that the Mo-O coordination can be described as tetrahedral as well. This observation was later supported by Antonio *et al* [82] who carried out an X-ray absorption spectroscopy (XAS) analysis to determine the local environment of Bi^{3+} and Mo^{6+}. In addition, the Bi^{3+} was found to be asymmetrically surrounded by six O^{2-}. Using transmission electron microscopy, Buttrey *et al* [83] revealed the presence of incommensurate in-plane modulations in the γ-Bi_2MoO_6 structure, giving the (4/7, 0, 2/7) superstructure reflections.

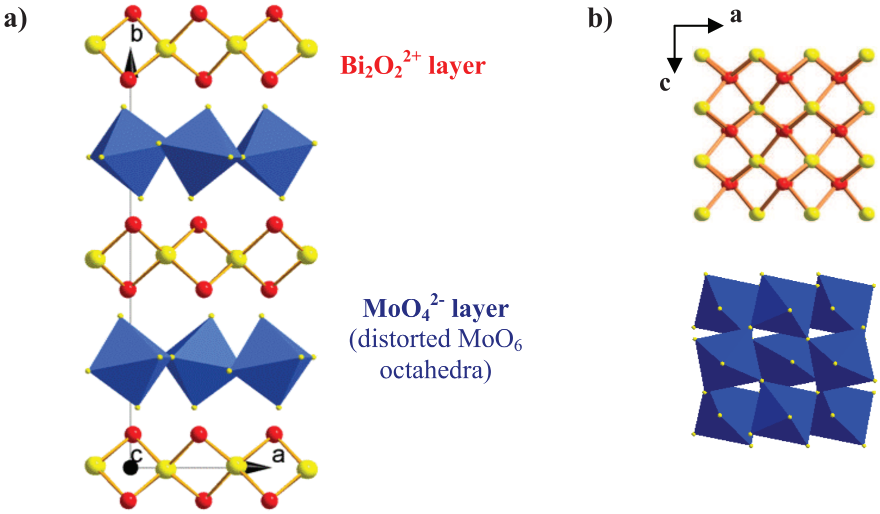

Fig. 1.8 a) The γ-Bi_2MoO_6 structure in the projection along the *c* axis and b) Two different type layers: $Bi_2O_2^{2+}$ and MoO_4^{2-} layers are found perpendicular to the *b* axis.

3.2.2. Polymorphism of γ-Bi_2MoO_6

Unlike α-$Bi_2Mo_3O_{12}$ and β-$Bi_2Mo_2O_9$, Bi_2MoO_6 has three polymorphs: γ, γ'', and γ' corresponding to the low-, intermediate- and high-temperature phases, respectively. The structure just discussed is the low-temperature polymorph γ, which is stable only in a limited domain of temperature. The phase transitions of Bi_2MoO_6 have been the subject of considerable attention and were studied by several techniques such as DTA [84], Raman spectroscopy [85, 86], X-ray absorption spectroscopy (XAS) [87], high-resolution neutron and synchrotron powder diffraction [83].

The phase transition of Bi_2MoO_6 takes place in two steps. The incommensurate γ-Bi_2MoO_6 first transforms to a commensurate form, γ''-Bi_2MoO_6, around 840 K and then to a fluorite related high temperature γ'-Bi_2MoO_6 polymorph near 877 K [83]. The first phase transition is reversible whereas the second one is irreversible. Consequently, caution should be taken for the preparation of γ-Bi_2MoO_6 since only γ polymorph is active for partial oxidation of propylene to acrolein.

The structure of γ''-Bi_2MoO_6 was found to be very similar to the γ-Bi_2MoO_6; the only difference is the absence of commensurate modulation in the structure. Interestingly, the high temperature form γ'-Bi_2MoO_6 (Fig. 1.9) is the only one of the three polymorphs that has a fluorite derived structure, similar to α-$Bi_2Mo_3O_{12}$ and β-$Bi_2Mo_2O_9$ phase, but without vacant metal sites.

Several studies were carried out in order to evidence this particular polymorph structure of Bi_2MoO_6.

An accurate crystal structure of γ'-Bi_2MoO_6 was achieved in 1994 by Buttrey *et al.* [88] who performed single crystal X-ray diffraction and powder neutron diffraction measurements to precisely localize the cation and oxygen sites in the structure. The structure was found in $P2_1/c$ monoclinic symmetry with unit cell parameters, a = 17.2627(1), b = 22.4296(2), c = 5.58489(5) Å, β = 90.4974(6)° and Z = 16; its atomic positions are given in Table 1.6. In agreement with the previous model proposed by Van den Elzen *et al.* [89], Buttrey *et al.* [90] and Watanabe *et al.* [91], the cation distribution in this structure forms a fluorite-related supercell without vacant metal site, with infinite 'Latin cross-shaped' channels of bismuth polyhedra along the [001] direction, surrounded by Mo tetrahedra.

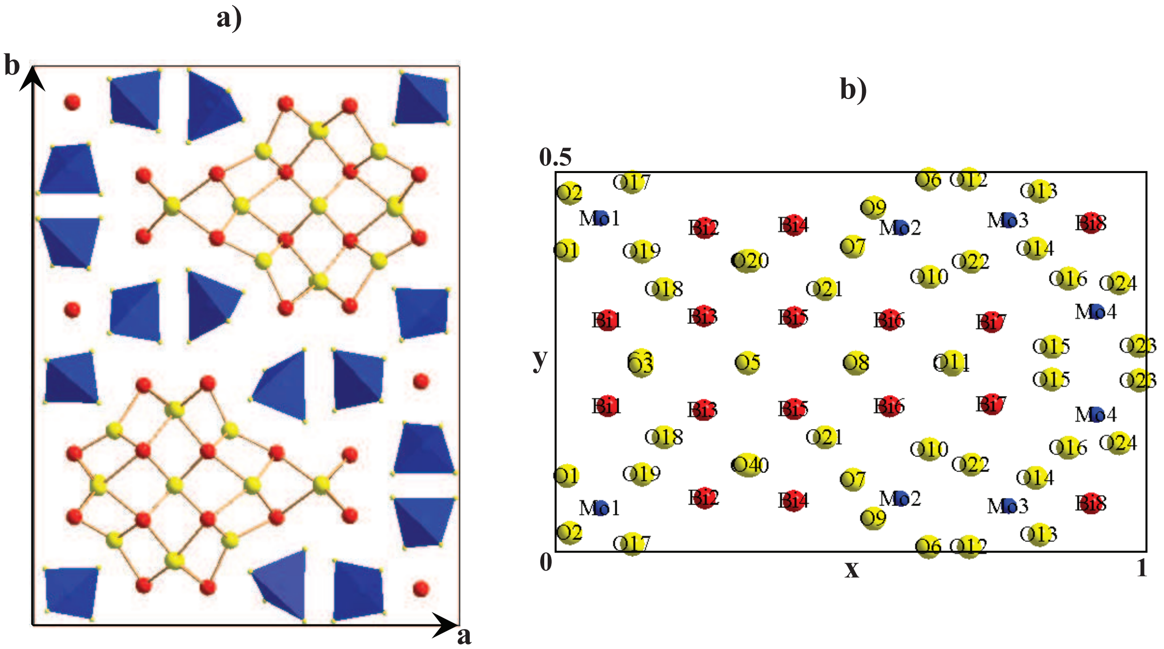

Fig. 1.9 a) The high temperature polymorph γ'-Bi_2MoO_6 structure in the projection along the *c* axis and b) its atom map in half-unit cell.

Table 1.6 The structure model of γ'-Bi_2MoO_6 proposed by Buttrey *et al* [88].

γ'-Bi_2MoO_6

Space Group: $P2_1/c$: =17.2627(1), b=22.4296(2), c=5.58489(5) Å, β= 90.4974(6)° and Z=16

Atom	site	x	y	z	Biso (Å^2)	occupation
Bi1	(4e)	0.0950(3)	0.1934(2)	0.003(1)	0.247(3)	1
Bi2	(4e)	0.2581(3)	0.0713(2)	0.018(1)	0.247(3)	1
Bi3	(4e)	0.2566(3)	0.1877(3)	0.424(1)	0.247(3)	1
Bi4	(4e)	0.4084(3)	0.0676(2)	0.504(1)	0.247(3)	1
Bi5	(4e)	0.4089(3)	0.1891(2)	0.934(1)	0.247(3)	1
Bi6	(4e)	0.5701(3)	0.1927(2)	0.520(1)	0.247(3)	1
Bi7	(4e)	0.7423(3)	0.1956(2)	0.997(1)	0.247(3)	1
Bi8	(4e)	0.9094(3)	0.0643(2)	0.018(1)	0.247(3)	1
Mo1	(4e)	0.0831(5)	0.0580(3)	0.495(1)	1.16(1)	1
Mo2	(4e)	0.5888(5)	0.0708(3)	0.011(1)	1.16(1)	1
Mo3	(4e)	0.7704(4)	0.0611(4)	0.498(1)	1.16(1)	1
Mo4	(4e)	0.9185(5)	0.1818(3)	0.511(1)	1.16(1)	1
O1	(4e)	0.0265(5)	0.1009(4)	0.309(1)	0.519(1)	1
O2	(4e)	0.0311(4)	0.0252(4)	0.733(1)	0.519(1)	1
O3	(4e)	0.1516(5)	0.2463(4)	0.751(1)	0.519(1)	1
O4	(4e)	0.3276(5)	0.1152(3)	0.754(1)	0.519(1)	1
O5	(4e)	0.3309(5)	0.2501(4)	0.754(1)	0.519(1)	1
O6	(4e)	0.6354(5)	0.0066(3)	0.125(1)	0.519(1)	1
O7	(4e)	0.5081(5)	0.0959(4)	0.199(1)	0.519(1)	1
O8	(4e)	0.5133(5)	0.2508(4)	0.769(1)	0.519(1)	1
O9	(4e)	0.5431(5)	0.0442(4)	0.739(1)	0.519(1)	1
O10	(4e)	0.6372(5)	0.1360(3)	0.917(1)	0.519(1)	1
O11	(4e)	0.6754(5)	0.2482(4)	0.242(1)	0.519(1)	1
O12	(4e)	0.7037(5)	0.0066(4)	0.624(1)	0.519(1)	1
O13	(4e)	0.8226(5)	0.0227(3)	0.270(1)	0.519(1)	1
O14	(4e)	0.8159(5)	0.0984(4)	0.765(1)	0.519(1)	1
O15	(4e)	0.8432(5)	0.2285(4)	0.616(1)	0.519(1)	1
O16	(4e)	0.8710(5)	0.1380(3)	0.286(1)	0.519(1)	1
O17	(4e)	0.1363(5)	0.0104(4)	0.280(1)	0.519(1)	1
O18	(4e)	0.1897(4)	0.1520(4)	0.102(1)	0.519(1)	1
O19	(4e)	0.1526(5)	0.1026(4)	0.625(1)	0.519(1)	1
O20	(4e)	0.3349(5)	0.1148(3)	0.258(1)	0.519(1)	1
O21	(4e)	0.4610(5)	0.1518(4)	0.600(1)	0.519(1)	1
O22	(4e)	0.7076(5)	0.1158(4)	0.370(1)	0.519(1)	1
O23	(4e)	0.9901(5)	0.2273(4)	0.390(1)	0.519(1)	1
O24	(4e)	0.9562(2)	0.1440(4)	0.775(1)	0.519(1)	1

The crystal structure of γ'-Bi_2MoO_6 is suggested to be similar to that of β-$Bi_2Mo_2O_9$ [88, 90, 91], where the isolated MoO_4 tetrahedra of Mo(1), Mo(3) and Mo(4) form square tunnels enclosing a single column of Bi^{3+} sites. These square tunnels are arranged as pairs and are further surrounded by $Mo(2)O_4$ tetrahedra. The local environment of Mo atoms is nearly regular tetrahedral with a variation in Mo-O distance (1.718(12)-1.871(12) Å) and O-Mo-O bond angles (102.33(59)° - 124.75(51)°) [88]. According to Buttrey *et al.* [88], the coordination environments of the bismuth atoms within the 'Latin cross-shaped' channels: Bi(1) - Bi(7) are irregular with wide variations in Bi-O distance (2.082(11)-3.108(11) Å) and O-Bi-O bond angles (71.28(32)° - 98.36(39)°); most of them are surrounded by two or three oxygen atoms with short Bi-O bond lengths (~2.15 Å). The lone pairs of 'Latin cross-shaped' channels of bismuth oxide appear to be directed away from its channels axis. For the Bi(8), which is enclosed in the square tunnels of MoO_4 tetrahedra, it is in a nearly regular fluorite environment with one marginally distance and seven intermediate bond length of oxygen neighbors.

Interestingly, it was found that γ'-Bi_2MoO_6 and β-$Bi_2Mo_2O_9$ have strikingly similar features: common florite-type cation arrangement, similarities in channel structures, lone electron pair orientation, site potential, valence sum, etc. In addition, γ'-Bi_2MoO_6 also adopts a similar structure to that of the ε solid solution in which the rose-shaped [$Bi_{12}O_{14}$] columns are very alike to the latin cross shape of γ'-Bi_2MoO_6. More recently, Vila et *al*. [92, 93, 94, 95, 96] showed evidence of the low-temperature forms corresponding to the ε solid solution. These forms exhibit layered structural features common to the layered γ-Bi_2MoO_6.

4. CONCLUSION

The Bi_2O_3-MoO_3 phase diagram appears to be an ideal system for the development of a Catalytic Dense Membrane reactor all made with bismuth molybdenum oxides since they display both good oxide ion conductivity and catalytic properties. To allow a good stability of the catalyst and the membrane at interface, $Bi_{25.75}Mo_{10}O_{68.625}$ composition was chosen for the membrane and γ-Bi_2MoO_6 for the catalyst. Although there have been several studies on the γ-Bi_2MoO_6 synthesis, the formation of this catalyst is not yet fully understood. By means of *in-situ* characterization techniques, it will be studied in the next chapter.

References

[1] G. Centi, F. Cavani, and F. Trifiro, *Selective Oxidation by Heterogeneous Catalysis*, Kluwer Academic/Plenum, 2001.

[2] E. Bordes-Richard, *L'Actualité chimique*, 2002, **mai-juin**, 38–44.

[3] N. Aishah, S. Amin, and S. E. Pheng, *Chem. Eng. J.*, 2006, **116**, 187–195.

[4] R. D. Cosimo, J. D. Burrington, and R. K. Grasselli, *J. Catal.*, 1986, **102**, 234–239.

[5] M. Rebeilleau-Dassonneville, S. Rosini, A. C. van Veen, D. Farrusseng, and C. Mirodatos, *Catal. Today*, 2005, **104**, 131–137.

[6] R. Ramos, M. Menéndez, and J. Santamaría, *Catal. Today*, 2000, **56**, 239–245.

[7] E. Santacesaria, M. Cozzolino, M. D. Serio, A. M. Venezia, and R. Tessera, *Appl. Catal. A: Gen.*, 2004, **270**, 177–192.

[8] L. M. Madeira, J. M. Herrmann, J. Disdier, M. F. Portela, and F. G. Freirec, *Appl. Catal. A: Gen.*, 2002, **235**, 1–10.

[9] P. Corbo and F. Migliardini, *Int. J. Hydrogen Energy*, 2007, **32**, 55–56.

[10] S. Pei, B. Yue, L. Qian, S. Yan, J. Cheng, Y. Zhou, S. Xie, and H. He, *Appl. Catal. A: Gen.*, 2007, **329**, 148–155.

[11] Y.-C. Kim, N.-C. Park, J.-S. Shin, S. R. Lee, Y. J. Lee, and D. J. Moon, *Catal. Today*, 2003, **87**, 153–162.

[12] E. van der Heide, M. Zwinkels, A. Gerritsen, and J. Scholten, *Appl. Catal. A: Gen.*, 1992, **86**, 181–198.

[13] D. Montolio-Rodrigueza, D. Linkeb, and P. Linke, *Chem. Eng. Sci.*, 2007, **62**, 5602–5608.

[14] M. Roussel, M. Bouchard, E. Bordes-Richard, K. Karim, and S. Al-Sayari, *Catal. Today*, 2005, **99**, 77–87.

[15] R. K. Grasselli and J. D. Burrington, *Adv. Catal.*, 1981, **30**, 133–163.

[16] P. Botella, P. Concepcion, J. L. Nieto, and Y. Moreno, *Catal. Today*, 2005, **99**, 51–57.

[17] A. M. D. de Farias, W. de A. Gonzalez, P. G. P. de Oliveira, J.-G. Eon, J.-M. Herrmann, M. Aouine, S. Loridant, and J.-C. Volta, *J. Catal.*, 2002, **208**, 238–246.

[18] H. Fansuri *Catalytic partial oxidationof propylene to acrolein: the crystal structure, reaction mechanism and kinetics* PhD thesis, Curtin University of Technology, 2005.

[19] J. D. Burrington, C. T. Kartisek, and R. K. Grasselli, *J. Catal.*, 1980, **63**, 235–254.

[20] P. Mars and D. van Krevelen, *Chem. Eng. Sci.*, 1954, **3**, 41–59.

[21] R. M. Contractor, Improved vapor phase catalytic oxidation of butane to maleic anhydride, 1987.

[22] C. A. Jones, J. J. Leonard, and J. A. Sofranko, Methane conversion, 1984.

[23] T. T. Tsotsis, A. M. Champagnie, R. G. Minet, and H.-G. Liu, *Computer Aided Design of Catalysts*, Marcel Dekker, 1993.

[24] W. G. Grot, Laminates of support material and fluorinated polymer containing pendant side chains containing sulfonyl groups., 1973.

[25] A. M. Azad, S. Larose, and S. A. Akbar, *J. Mater. Sci.*, 1994, **29**, 4135–4151.

[26] G. Saracco and V. Specchia, *Catal. Rev.-Sci. Eng.*, 1994, **36**, 305–384.

[27] M. Kang, S. Yu, N. Li, and C. R. Martin, *Small*, 2005, **1**, 69–72.

[28] H. J. M. Bouwmeester, *Catal. Today*, 2003, **82**, 141–150.

[29] C. Courson, B. Taouk, and E. Bordes, *Catal. lett.*, 2000, **66**, 129–138.

[30] E. A. Hazbun, Ceramic membrane and use thereof for hydrocarbon conversion, 1989.

[31] Y. H. Ma, *MRS bulletin*, 1999, **24**, 46.

[32] H. Bodet, A. Löfberg, C. Pirovano, M. Steil, R. Vannier, and E. Bordes-Richard, *Catal. Today*, 2009, **141**, 260–263.

[33] Y. Lu, A. G. Dixon, W. R. Moser, and Y. H. Ma, *Oxidative coupling of methane using an oxygen permeable dense membrane reactor*, Proc. 3th International Conference on Catalysis in Membrane Reactors, 1998.

[34] A. Löfberg, S. Boujmiai, E. Capoen, M. C. Steil, C. Pirovano, R. N. Vannier, G. Mairesse, and E. Bordes-Richard, *Catal. Today*, 2004, **91-92**, 79–83.

[35] A. Chetouani, B. Taouk, and E. Bordes-Richard, *Catal. Today*, 2004, **91-92C**, 75–79.

[36] A. Lofberg, H. Bodet, C. Pirovano, R. Vannier, M. Steil, and E. Bordes-Richard, *Catal. Today*, 2006, **112**, 8–11.

[37] C. Pirovano, A. Lofberg, H. Bodet, E. Bordes-Richard, M. Steil, and R. Vannier, *Solid State Ionics*, 2006, **177**, 2241–2244.

[38] A. Löfberg, H. Bodet, C. Pirovano, M. Steil, R.-N. Vannier, and E. Bordes-Richard, *Catal. Today*, 2006, **117**, 168–173.

[39] A. Löfberg, H. Bode, C. Pirovano, M. Steil, R. Vannier, and E. B. Richard, *Catal. Today*, 2006, **118**, 223–227.

[40] A. Löfberg, C. Pirovano, R.-N. Vannier, and E. Bordes-Richard, *Topics Catal.*, 2006, **38**, 169–179.

[41] E. Capoen, M. Steil, G. Nowogrock, M. Malys, C. Pirovano, A. Lofberg, E. Bordes-Richard, J. Boivin, G. Mairesse, and R. Vannier, *Solid State Ionics*, 2006, **177**, 483–488.

[42] S. Bebelis and C. G. Vayenas, *J. Catal.*, 1992, **138**, 588–610.

[43] S. Hamakawa, K. Sato, T. Hayakawa, A. P. E. York, T. Tsunoda, K. Suzuki, M. Shimizu, and K. Takehira, *J. Electrochem. Soc.*, 1997, **144**, 1–5.

[44] S. Hamakawa, T. Hayakawa, K. Suzuki, K. Murata, K. Takehira, S. Yoshino, J. Nakamura, and T. Uchijima, *Solid State Ionics*, 2000, **136-137**, 761–766.

[45] S. Hamakawa, M. Koizumi, K. Sato, J. Nakamura, T. Uchijima, K. Murata, T. Hayakawa, and K. Takehira, *Catal. Lett.*, 1998, **52**, 191–197.

[46] C. G. Vayenas and S. Neophytides, *J. Catal.*, 1991, **127**, 645–664.

[47] S. Hamakawa, T. Hayakawa, K. Suzuki, R.Shiozaki, and K. Takehira, *DENKI KAGAKU*, 1997, **65**, 1049–1056.

[48] T. J. Mazanec, T. L. Cable, and J. J. G. Frye, Process for the electrocatalytic conversion of light hydrocarbons to synthesis gas, 1988.

[49] J. Nicole and C. Comninellis, *J. Appl. Electrochem.*, 1998, **28**, 223–226.

[50] T. Hayakawa, T. Tsunoda, H. Orita, T. Kameyama, H. Takahashi, K. Takehira, and K. Fukuda, *J. Chem. Soc., Chem. Commun.*, 1986, pp. 961–962.

[51] T. Hayakawa, T. Tsunoda, H. Orita, T. Kameyama, H. Takahashi, K. Fukuda, and K. Takehira, *J. Chem. Soc., Chem. Commun.*, 1987, pp. 780–782.

[52] T. Tsunoda, T. Hayakawa, Y. Imai, T. Kameyama, K. Takehira, and K. Fukuda, *Catal. Today*, 1995, **25**, 371–376.

[53] T. Tsunoda, T. Hayakawa, T. Kameyama, K. Fukuda, and K. Takehira, *J. Chem. Soc., Faraday Trans.*, 1995, **91**, 1117–1124.

[54] S. Hamakawa, T. Hayakawa, H. Yasuda, K. Suzuki, M. Shimizu, and K. Takehira, *J. Electrochem. Soc.*, 1995, **142**, L159–L160.

[55] S. Hamakawa, T. Hayakawa, A. P. E. York, T. Tsunoda, Y. S. Yoon, K. Suzuki, M. Shimizu, and K. Takehira, *J. Electrochem. Soc.*, 1996, **143**, 1264–1268.

[56] S. Hamakawa, T. Hayakawa, T. Tsunoda, K. Suzuki, K. Murata, and K. Takehira, *Electrochem. Solid-State Lett.*, 1998, **1**, 220–221.

[57] M. Egashira, K. Matsuo, S. Kagawa, and T. Seiyama, *J. Catal.*, 1979, **58**, 409–418.

[58] N. Sharma, R. B. Macquart, M. Christensen, M. Avdeev, Y.-S. Chen, and C. D. Ling, *J. Solid State Chem.*, 2009, **182**, 1312–1318.

[59] R. N. Vannier, G. Mairesse, F. Abraham, and G. Nowogrocki, *J. Solid State Chem.*, 1996, **122**, 394–406.

[60] R. N. Vannier, F. Abraham, G. Nowogrocki, and G. Mairesse, *J. Solid State Chem.*, 1999, **142**, 294–304.

[61] L. Y. Erman, E. L. Galpérin, and B. P. Soboler, *Russ. J. Inorg. Chem. (Engl. Transl.)*, 1971, **16**, 258.

[62] S. Miyazawa, A. Kawana, H. Koizumi, and H. Iwasaki, *Mater. Res. Bull.*, 1974, **9**, 41–51.

[63] T. Chen and G. S. Smith, *J. Solid State Chem.*, 1975, **13**, 288–297.

[64] D. J. Buttrey, T. Vogt, G. P. A. Yap, and A. L. Rheingold, *Mater. Res. Bull.*, 1997, **32**, 947–962.

[65] R. Enjalbert, G. Hasselmann, and J. Galy, *Acta Crystallogr.*, 1997, **53**, 269–272.

[66] R. Enjalbert, G. Hasselmann, and J. Galy, *J. Solid State Chem.*, 1997, **131**, 236–245.

[67] J. Galy, R. Enjalbert, P. Rozier, and P. Millet, *Solid State Sci.*, 2003, **5**, 165–174.

[68] F. C. Fonseca, M. C. Steil, R. N. Vannier, G. Mairesse, and R. Muccillo, *Solid State Ionics*, 2001, **140**, 161–171.

[69] P. Shuk, H. D. Wiemhöfer, U. Guth, W. Göpel, and M. Greenblatt, *Solid State Ionics*, 1996, **89**, 179–196.

[70] F. Theobald, A. Laarif, and A. W. Hewat, *Ferroelectrics*, 1984, **56**, 219–237.

[71] F. Abraham, J. Boivin, G. Mairesse, and G. Nowogrocki, *Solid State Ionics*, 1990, **40-41**, 934–937.

[72] L. Holmes, L. Peng, I. Heinmaa, L. A. O'Dell, M. E. Smith, R.-N. Vannier, and C. P. Grey, *Chem. Mater.*, 2008, **20**, 3638–3648.

[73] G. Fafilek and P. Kurek, *Solid State Ionics*, 2003, **157**, 171–176.

[74] M. Malys, G. Fafilek, C. Pirovano, and R. N. Vannier, *Solid State Ionics*, 2005, **176**, 1769–1773.

[75] J. Zemann, *Beitr. Miner. Petrogr.*, 1956, **5**, 139–145.

[76] F. Pertlik and J. Zemann, *Fortschr. Mineral.*, 1982, **60**, 162–163.

[77] A. F. van den Elzen and G. Rieck, *Acta. Cryst.*, 1973, **B29**, 2436–2438.

[78] R. D. Shannon and C. T. Prewitt, *Acta Cryst.*, 1969, **B25**, 925–946.

[79] R. G. Teller, J. F. Brazdil, R. K. Grasselli, and J. D. Jorgensen, *Acta Cryst.*, 1984, **C40**, 2001–2005.

[80] I. H. Ismailzade, I. M. Aliyev, R. M. Ismailov, A. I. Alekberov, and D. A. Rzayev, *Ferroelectrics*, 1979, **22**, 853–854.

[81] B. Aurivillius, *Arkiv*, 1952, **5**, 39–47.

[82] M. Antonio, R. Teller, D. Sandstrom, M. Mehicic, and J. Brazdil, *J. Phys. Chem.*, 1988, **92**, 2939–2944.

[83] D. J. Buttrey, T. Vogt, and B. D. White, *J. Solid State Chem.*, 2000, **155**, 206–215.

[84] H. Kodama and A. Watanabe, *J. Solid State Chem.*, 1985, **56**, 225–229.

[85] P. Gaucher, V. Ernst, and P. Courtine, *J. Solid State Chem.*, 1983, **47**, 47–52.

[86] R. Murugan, R. Gangadharan, J. Kalaiselvi, S. Sukumar, B. Palanivel, and S. Mohan, *J. Phys.: Condens. Matter*, 2002, **14**, 4001–4010.

[87] G. Sankar, M. A. Roberts, J. M. Thomas, G. U. Kulkarni, N. Rangavittal, and C. N. R. Rao, *J. Solid State Chem.*, 1995, **119**, 210–215.

[88] D. J. Buttrey, T. Vogt, U. Wildgruber, and W. R. Robinson, *J. Solid State Chem.*, 1994, **111**, 118–127.

[89] A. F. van den Elzen, L. Boon, and R. Metselaar, *Solid State Chemistry*, Elsevier, 1982.

[90] D. J. Buttrey, D. A. Jefferson, and J. M. Thomas, *Philos. Mag. A*, 1986, **53**, 897–906.

[91] A. Watanabe, S. Horiuchi, and H. Kodama, *J. Solid State Chem.*, 1987, **67**, 333–339.

[92] E. Vila, J. M. Rojo, J. E. Iglesias, and A. Castro, *Chem. Mater.*, 2004, **16**, 1732–1739.

[93] E. Vila, J. E. Iglesias, J. Galy, and A. Castro, *Solid State Sci.*, 2005, **7**, 1369–1376.

[94] E. Vila, A. R. Landa-Canovas, J. Galy, J. E. Iglesias, and A. Castro, *J. Solid State Chem.*, 2007, **180**, 661–669.

[95] J. Galy, J. Hernandez-Velasco, A. R. Landa-Canovas, E. Vila, and A. Castro, *J. Solid State Chem.*, 2009, **182**, 1177–1187.

[96] A. R. Landa-Canovas, E. Vila, J. Hernandez-Velasco, J. Galy, and A. Castro, *Acta Cryst. B*, 2009, **65**, 458–466.

CHAPTER 2

In-Situ Study of γ-Bi_2MoO_6 Hydrothermal Synthesis by Combining HRPD, XANES and Raman Scattering

SUMMARY OF CHAPTER 2

Chapter 2

In-Situ Study of γ-Bi_2MoO_6 Hydrothermal Synthesis by Combining HRPD, XANES and Raman Scattering

1. INTRODUCTION

Over the years bismuth molybdate catalysts have been prepared by varying the methods (wet chemistry or solid state synthesis) in order to improve the purity, surface acidity, surface area, crystallinity and morphology of the catalyst particles which exert a significant influence on their catalytic properties [1, 2, 3]. Conventional methods of preparation by solid-state reactions [4] and wet chemistry (e.g. co-precipitation methods) [5] were first used. They provide a surface area of approximately 1-2m^2/g. Other novel methods such as sol-gel and spray-drying methods were recently demonstrated to increase the catalyst surface area up to 5.4 m^2/g and 17 m^2/g respectively, leading to an increase of catalytic activity [6]. However, these protocols require the use of organic additives that may cause environmental problem when burning off organic substances. Most wet chemistry techniques necessitate a calcination step at *ca.* 400-700°C to obtain the final crystalline material of which the purity, morphology, surface texture, and grain shape of synthesized material are not easily controlled. More particularly, the phase transition from γ-Bi_2MoO_6 to inactive phase γ'-Bi_2MoO_6 can occur during this heating process.

In order to overcome this difficulty, hydrothermal methods were applied to synthesize γ-Bi_2MoO_6 under mild conditions, at temperatures below 200°C [7, 8, 9]. Such promising methods are well known to generate highly crystalline products, with high purity, narrow size distribution, and low aggregation of particles [7]. A pure γ-Bi_2MoO_6 catalyst with a quite high surface area of *ca.* 10m^2/g was first obtained [8].

Aiming at optimizing the conditions of production of γ-Bi_2MoO_6 catalyst by controlling the crystal growth, determining and minimizing any intermediate phases formed during the synthesis process, *in-situ* characterizations were performed to follow the catalyst formation during synthesis.

This work was intended to complete and to extend the work carried out by Beale et *al*. [8, 10, 11] who used the combination of EDXRD (Energy dispersive X-ray diffraction) and XAS techniques to study *in-situ* the kinetics of crystallisation of the γ-Bi_2MoO_6 phase under hydrothermal conditions in the temperature range from 110 to 150°C. XAS techniques revealed changes in the coordination of Mo(VI) ions whereas EDXRD gave information on the solid crystallinity. An intermediate compound (possibly an intermediate layer structure) was evidenced but at that time, it was not possible to precisely determine its nature and structure, nor the structural modifications that take place during the growth process.

Another *ex-situ* study of crystallization mechanism at 180°C, using XRD, TEM and Raman spectroscopy, carried out by Li et *al*. [12] could not show any intermediate phase. This was likely due to the fast reaction especially during the intermediate state which is difficult to observe in the time resolution of about 1h while the use of different reactant sources can not be neglected. In this *ex-situ* study, only the synthesis time to obtain a pure final γ-Bi_2MoO_6 phase was optimised, while the transformation of Mo coordination during the formation of bismuth molybdate was ignored.

It was therefore challenging to elucidate how the crystallites grow and the layered structure of γ-Bi_2MoO_6 forms under hydrothermal conditions in real time. In the present work, an *in-situ* study combining High-resolution powder diffraction (HRPD)/ X-ray Absorption Spectroscopy (XAS)/ Raman experiments was performed. By combination of these techniques, it is possible to obtain information on both short-range and extended-range structural changes.

2. CHARACTERIZATION TECHNIQUES

Extended range structural information will be obtained from HRPD. Using high quality and high resolution powder diffraction data, the crystal structure can be investigated during phase transition or transformations. In contrast, XAS and Raman scattering will provide information on the local surrounding of molybdenum.

Raman Scattering is known as a powerful tool for qualitative analysis. It is very sensitive to the molecular environments, which can help to identify several compounds: crystalline phases, amorphous phases, solid, liquid or gas, all at once.

On the other hand, XAS techniques allow both a qualitative and quantitative analysis of the local environment around an absorbing element; providing coordination numbers, radial locations and atomic type differentiation. This study was completed by *ex-situ* characterizations to fully understand the crystal growth of γ-Bi_2MoO_6 catalyst.

Experiments were carried out on the Swiss-Norwegian beamline (SNBL) at the European Synchrotron Radiation Facilities (ESRF) in Grenoble, France (Fig. 2.1).

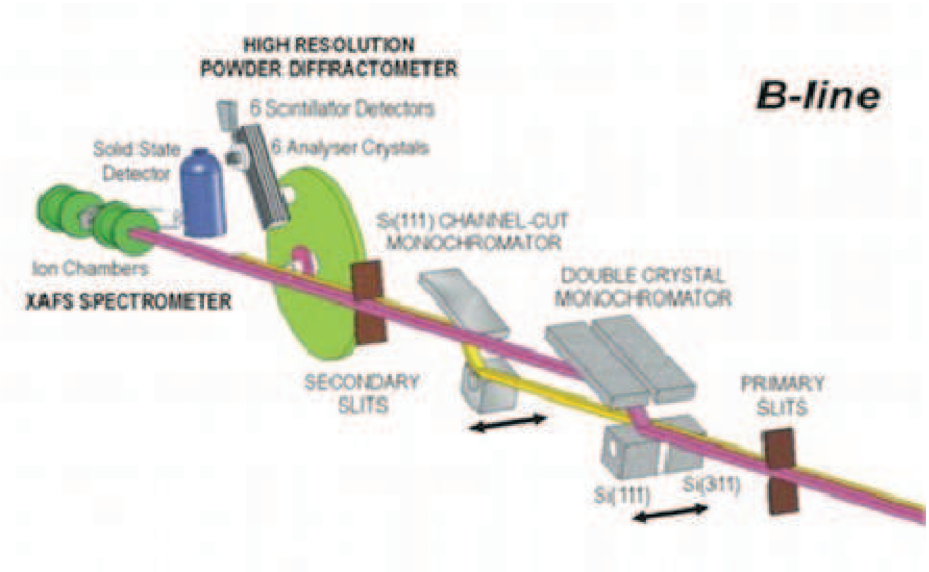

Fig. 2.1 Schematic layout of the Swiss-Norwegian beamline B (SNBL) at ESRF

The hydrothermal syntheses of γ-Bi_2MoO_6 were followed sequentially by High-resolution X-ray diffraction (HRPD) and X-ray absorption and simultaneously by Raman spectroscopy.

2.1. High Resolution X-ray Diffraction (HRPD)

Although the Energy Dispersive X-Ray Diffraction (EDXRD) is occasionally used to identify crystalline phases during reaction because of the short acquisition time [8, 11], this technique is inappropriate for structure determination. EDXRD provides only a short range of 2θ or d-spacing data that prevents full use of the available information to refine structural parameters or crystallite size. In contrast, High-Resolution X-ray Diffraction (HRPD) is an essential technique for phase identification, crystal structure refinement and crystallite morphology study. It is developed from a standard X-ray diffraction to obtain high resolution data with a short collection time.

2.1.1. Introduction to XRD refinement

The X-ray diffraction of powder samples results in a pattern characterized by reflections of given intensity at certain positions. The height, width and position of these peaks can be used to determine many characteristics of the material structure. The positions corresponding to lattice spacing and the relative intensity of the reflections are indicative of crystalline structures, providing a *fingerprint* of the materials. The phase identification can be first performed by comparison of the diffraction pattern to a database such as the Powder Diffraction File (PDF) of the International Centre for Diffraction Data.

2.1.2. The Rietveld method

The crystal structure of known materials can be refined by using the *Rietveld method*. A crystal structure, together with instrumental and microstructural information is used to generate a theoretical diffraction pattern that can be compared to the measured profile. The profile can be modeled using the calculated counts y_i^{calc} at the i^th^ step of 2θ by summing the contribution from neighboring Bragg reflection plus the background:

$$y_i^{calc} = y_i^b + \sum_\phi S_\phi \sum_h j_{\phi,h} \cdot Lp_{\phi,h} \cdot P_{\phi,h_i} \cdot A_{\phi,h} \cdot \left|F_{\phi,h}\right|^2 \cdot \Omega_{i,\phi,h} \tag{2.1}$$

where y_i^b is the background intensity,

S_ϕ is the scale factor of the phase ϕ,

$j_{\phi,h}$ is the multiplicity factor of the h^th^ reflection,

$Lp_{\phi,h}$ is the Lorentz-polarization factor,

$P_{\phi,h}$ is the preferred orientation function,

$A_{\phi,h}$ is the absorption correction,

$F_{\phi,h}$ is the structure factor,

$\Omega_{i,\phi,h}$ is the reflection profile function that models both instrumental and sample effects.

This technique uses a least squares approach to minimize a function χ^2 that represents the difference between the calculated y_i^{calc} and observed y_i^{obs} intensities at equal angular intervals by adjusting model parameters.

$$\chi^2 = \sum_{i=1}^{n} w_i \left\{ y_i^{obs} - y_i^{calc} \right\}^2 \tag{2.2}$$

with $w_i = \dfrac{1}{\sigma_i^2}$, where σ_i^2 is the variance of the observed intensity y_i^{obs}.

2.1.3. The microstructure effects

The Full Width at Half Maximum (FWHM) of a powder diffraction reflection is influenced by several factors including instrumental factors, the presence of defects and microstructural effects i.e., strain and size effects.

Since the FWHM can be described as the convolution of the instrumental resolution and the sample effect, the microstructure effects can be separated from other factors by using the combination of the *Rietveld method* with the instrumental resolution function. The instrumental resolution function can be deduced from the diffraction pattern of LaB_6 used as a standard [13] or from the instrumental profile that the FWHM (H) can be modelled using the ralationship proposed by Caglioti *et al*. [14]:

$$H^2 = U \cdot \tan^2\theta + V \cdot \tan\theta + W \tag{2.3}$$

The Caglioti U, V and W parameters depend on the instrumental setup.

Once the instrumental resolution function is known, it is therefore possible to determine the size and strain contribution for each reflection. As the strain effect was insignificant in our study, we shall focus only on the size effect in the following.

The intrinsic profile of a particular reflection due to size effect has an integral breadth β_s which is formally defined as the integral of the peak profile divided by the peak height. For an isotropic size broadening, the averaged apparent size of the crystallites $\langle D \rangle_V$ in the direction normal to the scattering planes is defined from the Scherrer formula:

$$\langle D \rangle_V = \frac{\lambda}{\beta_S \cos\theta} \tag{2.4}$$

For an anisotropic size broadening, using the Scherrer formula, the size broadening can be written as a linear combination of spherical harmonics (SPH):

$$\beta_{hkl} = \frac{\lambda}{D_{hkl}\cos\theta} = \frac{\lambda}{\cos\theta}\sum_{ijp} a_{ijp} Y_{ijp}(\Theta_{hkl}, \Phi_{hkl}) \tag{2.5}$$

where β_{hkl} is the size contribution to the integral breadth of the reflection hkl

$Y_{ijp}(\Theta_{hkl}, \Phi_{hkl})$ is the real spherical harmonics with normalization [15], the maximum |Y| is 1, represented as a density map of electrons on the surface of the unit sphere in the direction (Θ_{hkl}, Φ_{hkl}). This function is based on the Legendre polynomials, where *i* and *j* are quantum numbers that $0 \le j \le i$. The Φ_{hkl} variance depends on the parity *p*; for even parity (p = 1), the function is *cosine* and for odd parity (p = -1), the function is *sine*.

After refinements of the coefficients a_{ijp}, the apparent size will be then calculated along each reciprocal lattice vector.

2.2. X-ray Absorption Spectroscopy (XAS)

In general, when X-rays or electromagnetic radiation interacts with the sample, the radiation is scattered, transmitted or absorbed. The dominant process in the X-ray absorption at photon energies below 100 keV is the photoelectric effect, by which the photon is absorbed, transferring its energy to the ejected photoelectron. When the sample absorbs X-rays, the linear absorption coefficient μ can be obtained from the Beer-Lambert law.

$$\mu x = ln(I_0/I) \tag{2.6}$$

where I_0 and I are the intensities of the incident and transmitted radiation respectively and x is the path length of the absorbing sample.

This X-ray absorption coefficient μ for photoelectric effect decreases smoothly with increasing photon energy. However, when the photon energy reaches one of the deep inner-shell ionization energies of the atom, the absorption increases drastically, giving rise to a so-called *absorption edge*, as shown in Fig. 2.2(a). For example, a K-edge corresponds to removal of a K-shell (1s) electron to a continuum state, to produce a photoelectron. When the photoelectron travels outward from the absorbed atoms, the same wave is scattered by the neighbouring atoms, as illustrated in Fig. 2.2(b). The phase and amplitude of the backscattered wave are dependent on the type of atom and the distance of the backscattering atoms from the central atom. Thus, the spectrum giving the absorbance in function of the incident photons energy is not only characterized by its edge but also by the modulated part. These modulations are linked to the number of neighbouring atoms and their distance from the absorbing atom. Therefore, it is possible to determine the chemical environment of the absorbing atom by analysing XAS data.

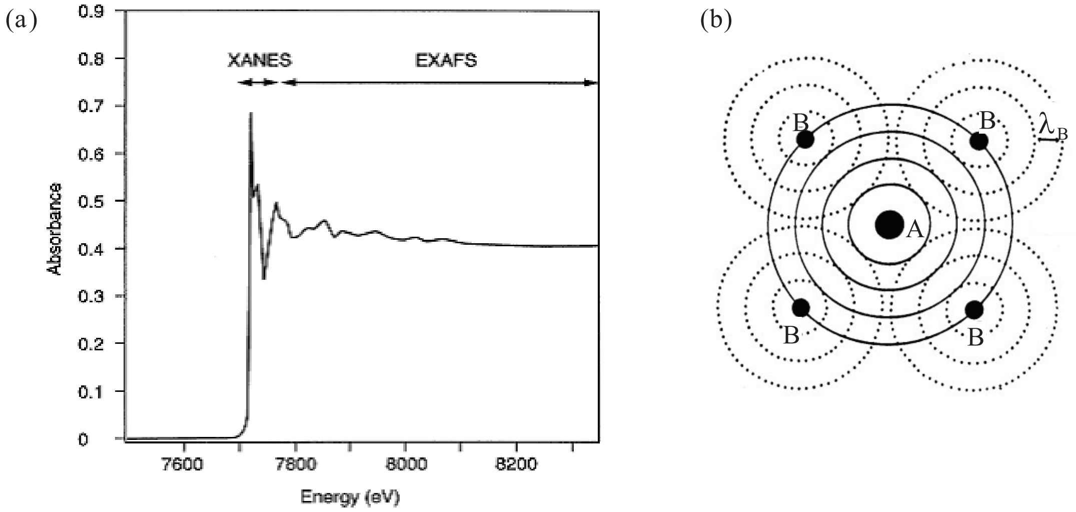

Fig. 2.2 a) Schematic XAS representation of an absorption edge of the absorbing atom. b) Interference between scattered photoelectrons in a crystalline material.

An XAS spectrum consists of 3 regions, as presented in Fig. 2.2(a):

1) *Pre-edge*, where the incident energy is less than the edge energy. The features in the pre-edge region are usually due to the core-shell electron being promoted to unoccupied orbitals, such as 5p or 5d.

2) *X-ray absorption near edge structure* (XANES), observed in the edge energy region extending over the range of about 100 eV. This signal can be used to determine the average oxidation state and the coordination environment of the element in the sample.

3) *Extended X-ray absorption fine structure* (EXAFS), observed after the absorption edge at higher energy (*ca.* 100-1000 eV) that corresponds to oscillation signal related to backscattered wave, as previously mentioned.

Due to the limitation of acquisition time, our present study focused on XANES analysis to determine the coordination environment of the metal atoms in the sample.

2.3. Raman Scattering

Raman scattering is a promising technique for following the change in the chemical environment of metal oxide structures or molecular species during the course of the reaction. From the fact that Raman bands generally reflect the bond lengths, bond strengths, as well as the overall symmetry of molecules, a particular Raman spectrum can be used as a *fingerprint* to identify each molecular species that is present in any state: gas, solution or solid (whether in crystalline or amorphous phase).

The Raman scattering process relies on inelastic scattering of monochromatic and coherent light, known as incident electromagnetic radiation

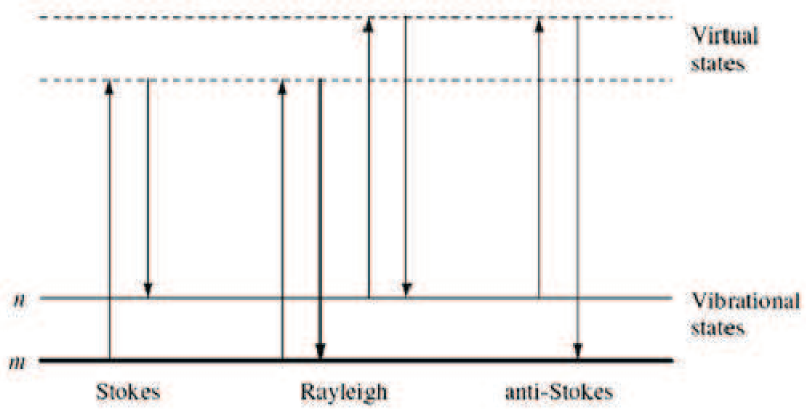

Fig. 2.3 Transitions for scattering process: *Rayleigh*, *Stokes* and *anti-Stokes scattering* [16].

When the excitation energy is equal to the vibration energy, a quantum of radiation may be absorbed or emitted. These phenomena are known as *infrared absorption* and *stimulated emission*, respectively. Whereas a *scattering process* generally occurs when the excitation energy is much higher than the vibration energy (Fig. 2.3). With an excited light quantum, a molecule will be excited to a virtual state, and relax to an excited state by emitting a secondary light quantum of the same or different energy. Generally, the exciting light quanta are elastically scattered giving rise to the so-called *Rayleigh scattering*. The inelastic scattering called *Raman scattering* was also observed but with more than a million times less probability than *Rayleigh scattering*. The inelastic interaction of a primary light quantum with a molecule in the vibrational ground state gives *Stokes lines*, a secondary light quantum of lower energy (or frequency). If a molecule is not in its ground state, the interaction of a primary light quantum may produce a secondary light quantum of higher energy, giving *anti-Stokes lines.* Since the intensity of the Rayleigh is several orders of magnitude higher than that of the Raman lines, the use of an intense monochromatic and coherent light, *i.e.* the ultraviolet, visible or near infrared lasers as the exciting sources is necessary.

According to the classical theory, Raman scattering can be explained as follows: the electric field strength (*E*) of an electromagnetic wave (laser beam) fluctuates with time (t) and can be described by:

$$E = E_0 cos 2\pi v_0 t \qquad (2.7)$$

where E_0 is the vibration amplitude and v_0 is the frequency of the laser.

When a molecule is exposed to an electric field, electrons and nuclei are forced to move in opposite direction. An electric dipole *P* is induced:

$$\vec{P} = \alpha \vec{E} \qquad (2.8)$$

Here α is the proportionality constant, called polarizability.

It is known that the electric pole moment *P* is related to the vibrational energy. If the molecule is vibrating with a frequency v_m, the nuclear displacement *q* or the so-called *normal coordinate* can be written:

$$q = q_0 cos 2\pi v_m t \qquad (2.9)$$

where q_0 is the vibrational amplitude.

For small amplitude of vibration, α is a linear function of *q*. Thus we can write:

$$\alpha = \alpha_0 + \left(\frac{\partial \alpha}{\partial q}\right)_0 q + ... \qquad (2.10)$$

Combining (2.8), (2.9) and (2.10), we obtain:

$$p = \alpha_0 E_0 \cos(2\pi \upsilon_0 t) + \frac{1}{2}\left(\frac{\partial \alpha}{\partial q}\right)_0 q_0 E_0 \left[\cos\{2\pi(\upsilon_0 + \upsilon_m)t\} + \cos\{2\pi(\upsilon_0 - \upsilon_m)t\}\right] \qquad (2.11)$$

According to the classical theory, the first term represents *Rayleigh scattering*, the second and third terms correspond to *anti-Stokes* and *Stokes lines*, respectively. A vibration can be observed in a Raman spectrum only if the rate of change of polarizability (α) with the vibration is not zero.

$$\left(\frac{\partial \alpha}{\partial q}\right) \neq 0 \qquad (2.12)$$

If the symmetry of a molecule is such that this condition is fulfilled, then the transition is allowed, it is called *Raman active*; if it is not fulfilled, the transition is forbidden, this is called *Raman inactive*.

3. *IN-SITU* EXPERIMENTS

3.1. Preparation of γ-Bi_2MoO_6 by hydrothermal route

According to the procedure described by Beale and Sankar [10], two solutions, A: 2.32 g of Bi_2O_3 (Riedel-de-Haën, 99.5%) dissolved in 5.8 ml 65% (wt/wt) HNO_3 and B: 0.88 g of $(NH_4)_6Mo_7O_{24}\bullet 4H_2O$ (Janssen Chimica, 99%) dissolved in 5.6 ml 28% (wt/wt) ammonia were prepared. The solution B was slowly added into the solution A. The pH of this mixture was adjusted to be higher than 6 before loading about 1 cm^3 into the specially designed hydrothermal synthesis cell (Fig. 2.4). This cell was then introduced into a pre-heated block just before starting measurements. The experiments were carried out at three temperatures: 160, 170 and 180°C.

3.2. Instrumental descriptions and operating conditions

3.2.1. High-Resolution Powder Diffractometer

The HRPD data were collected with the standard BM1B setup equipped with an X-ray detector consisting of six independent counting chains, each made of a Si111 analyzer crystal and a NaI scintillation counter, resulting in an intrinsic resolution (FWHM) of approximately 0.01° at wavelength of 1 Å.

3.2.2. XAS

A water-cooled Si (111) channel cut monochromator was used to tune the incident X-ray beam to the desired energies. X-ray absorption spectra were collected over the photoemission ranges of Mo K-edges by a Vortex-EM silicon drift X-ray fluorescence detector, a 50mm^2 active area single element detector with Xia digital electronics.

3.2.3. Raman Spectrometer

A standard Raman RP10 probe with long distance objective was added to the experimental setup. It was connected to a dispersive InVia Renishaw spectrophotometer by optical fibers [17]. The 532 nm laser line was focused on the sample using a video camera on a RP20V probe head with a final optimization by cyclic fast acquisitions of the Raman spectrum. The 1200 lines/mm grating calibration was systematically controlled by checking the position of the Raman line of a Si standard at 520 cm^{-1}. Therefore, the standard microscope lens on the RP20V was replaced by a long-distance optical expander allowing a long working distance of 150 mm between sample and the probe and a gain of space for *in-situ* auxilliary equipment.

3.3. *In-Situ* experimental setup

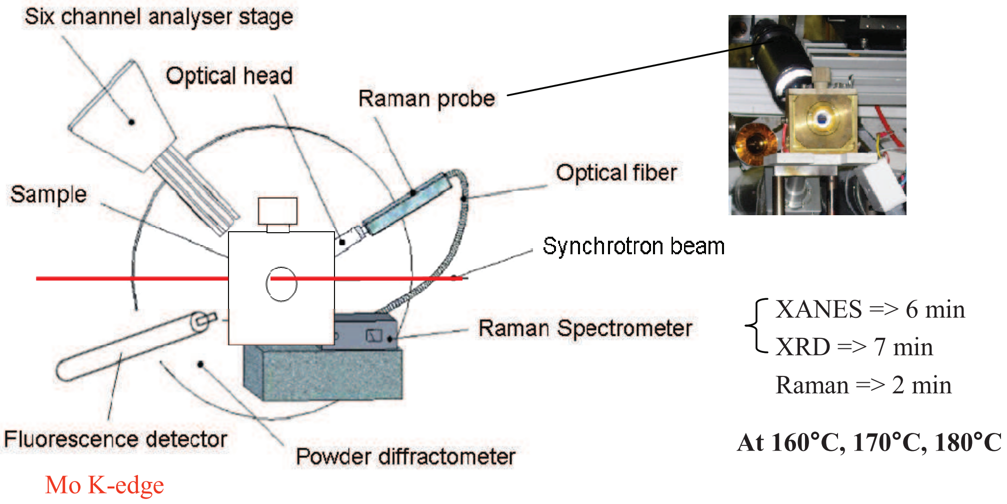

XANES => 6 min
XRD => 7 min
Raman => 2 min

At 160°C, 170°C, 180°C

Fig. 2.4 Schematic of the experimental setup available at ESRF

The reactions were followed sequentially by XANES / HRPD and simultaneously by Raman spectroscopy. The Mo K-edge XANES data were collected over 6 minutes at the Molybdenum K-edge. The energy step and counting times were adjusted to improve the spectral resolution with a 0.7eV step near the edges, and a 3-10 eV step beyond the edges with an integration time of 1 s per step. The total XANES collection time including dead times was 378 sec (about 6 min). HRPD patterns were collected at 0.49995 Å wavelength in the 8.001° - 17.514° 2θ domain with a step of 0.003° and 150 ms/step counting time. The total duration for the collection of a pattern was 475 s, almost 7 min. Since XAS techniques require a change of the beam energy, it was not possible to carry out XANES and HRPD at the same time. XANES spectra and HRPD patterns were therefore collected alternately every 13 minutes. Raman spectra were recorded in the 100-1200 cm^{-1} range for 132 s with a laser power of 70 mWatt. XANES data were processed using the Athena software [18], which is based on the IFEFFIT program suite [19]. A linear combination fitting analysis was carried out on the normalised XANES to determine the relative contribution of each coordination type of Mo(VI) during the reaction. Labspec program was used to normalise and determine the surface area of Raman Spectra. X-ray diffraction data were refined with the Fullprof suite [20]. The Thompson-Cox-Hastings pseudo-Voigt profile function was used [21]. The resolution of the instrument was deduced from a LaB_6 [13] XRD diagram.

4. RESULTS AND DISCUSSION

Mo K-edge XANES, stacked XRD patterns and stacked plots of Raman spectra during the hydrothermal reaction at 160, 170 and 180°C, are given in Fig. 2.5-2.7, 2.8-2.10 and 2.11-2.13, respectively. All these techniques revealed that a transformation occurs after about 33.8, 30.0 and 22.8 minutes of reaction at 160, 170 and 180°C, respectively.

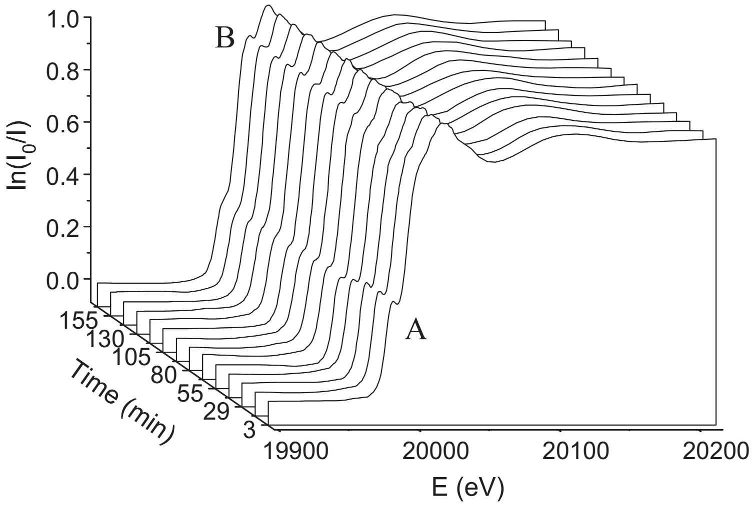

Fig. 2.5 Mo K-edge XANES spectra collected at 160°C. The features marked A and B are characteristic of Mo(VI) in tetrahedral and octahedral environment respectively.

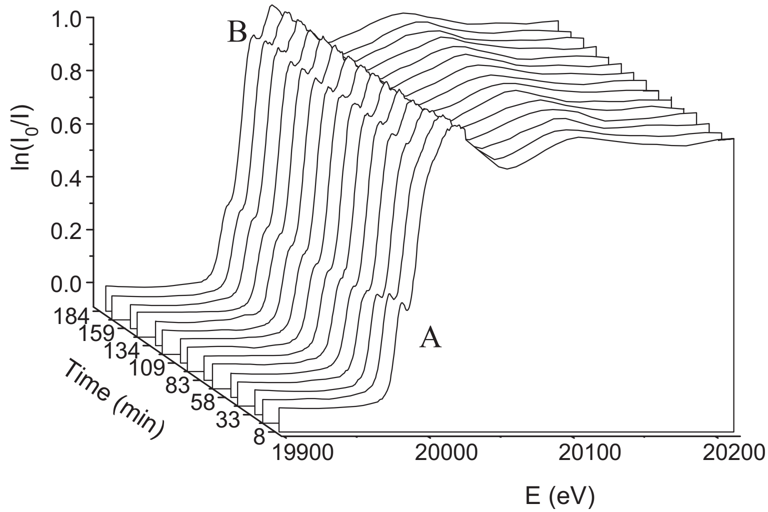

Fig. 2.6 Mo K-edge XANES spectra collected at 170°C. The features marked A and B are characteristic of Mo(VI) in tetrahedral and octahedral environment respectively.

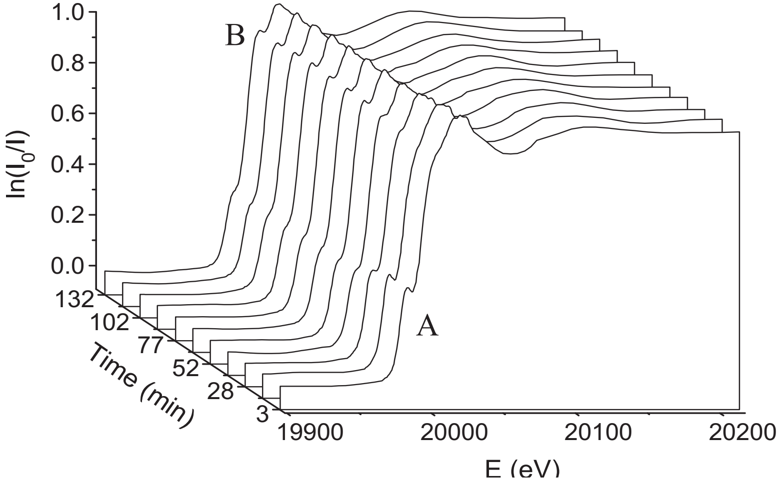

Fig. 2.7 Mo K-edge XANES spectra collected at 180°C. The features marked A and B are characteristic of Mo(VI) in tetrahedral and octahedral environment respectively.

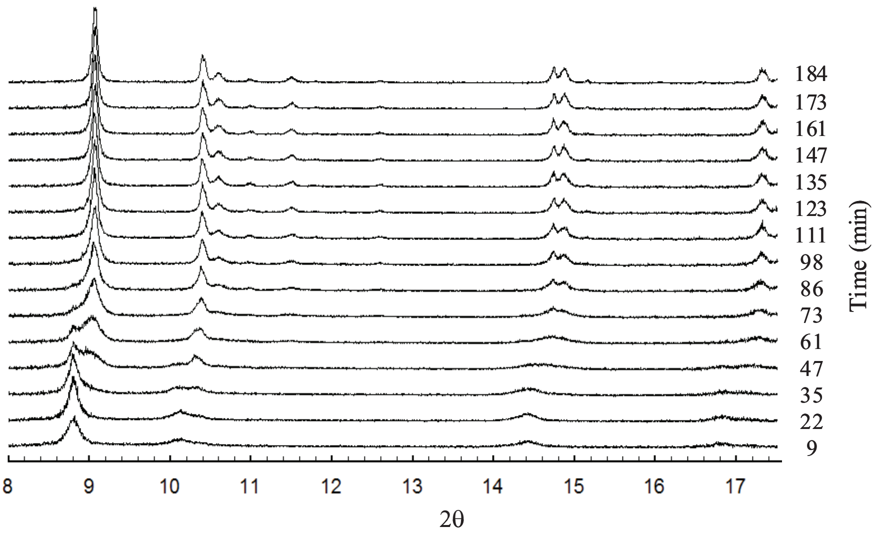

Fig. 2.8 *In-situ* XRD patterns collected during the hydrothermal synthesis of γ-Bi_2MoO_6 at 160°C.

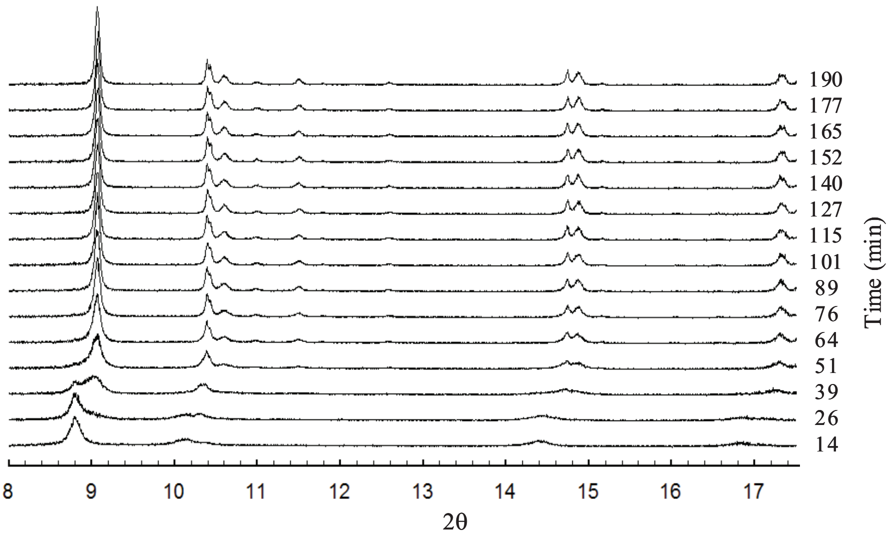

Fig. 2.9 *In-situ* XRD patterns collected during the hydrothermal synthesis of γ-Bi_2MoO_6 at 170°C.

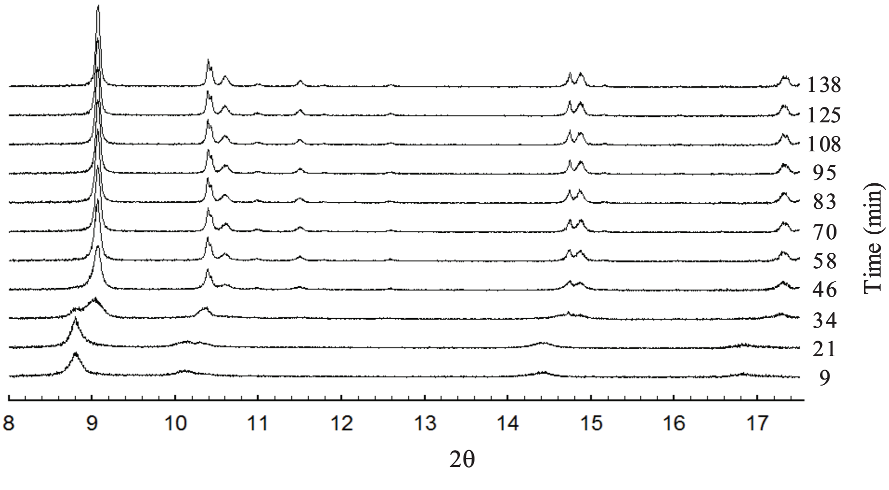

Fig. 2.10 *In-situ* XRD patterns collected during the hydrothermal synthesis of γ-Bi_2MoO_6 at 180°C.

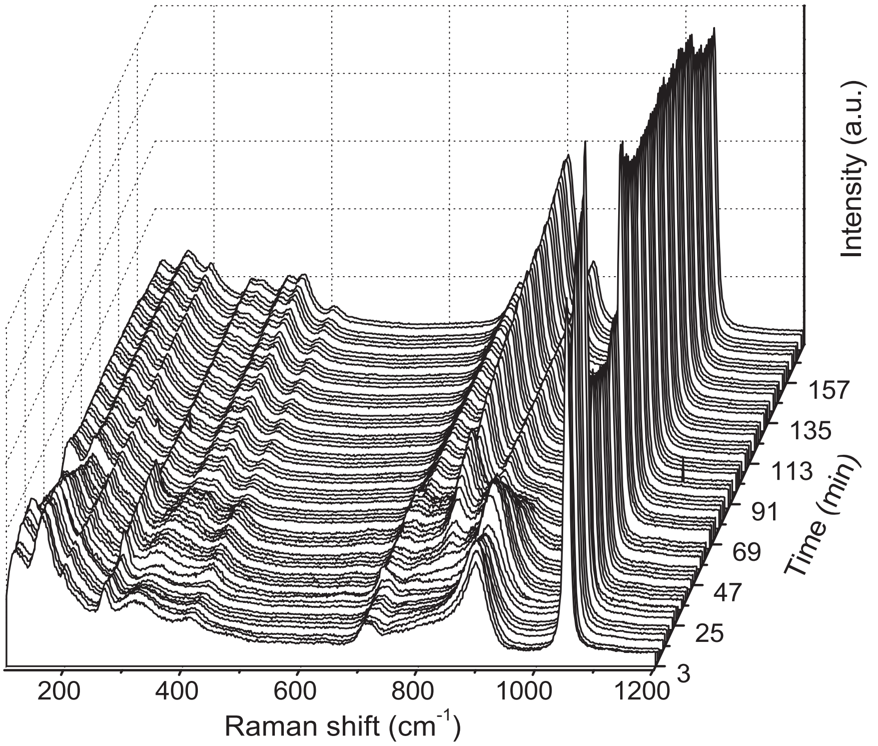

Fig. 2.11 Raman spectra collected during the hydrothermal synthesis of γ-Bi_2MoO_6 at 160°C.

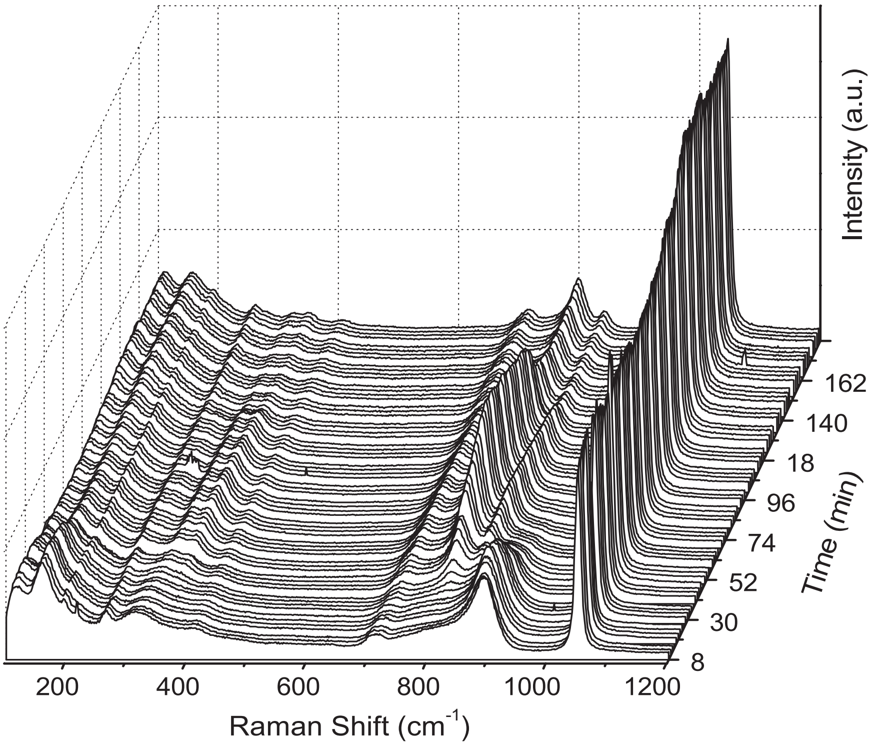

Fig. 2.12 Raman spectra collected during the hydrothermal synthesis of γ-Bi_2MoO_6 at 170°C.

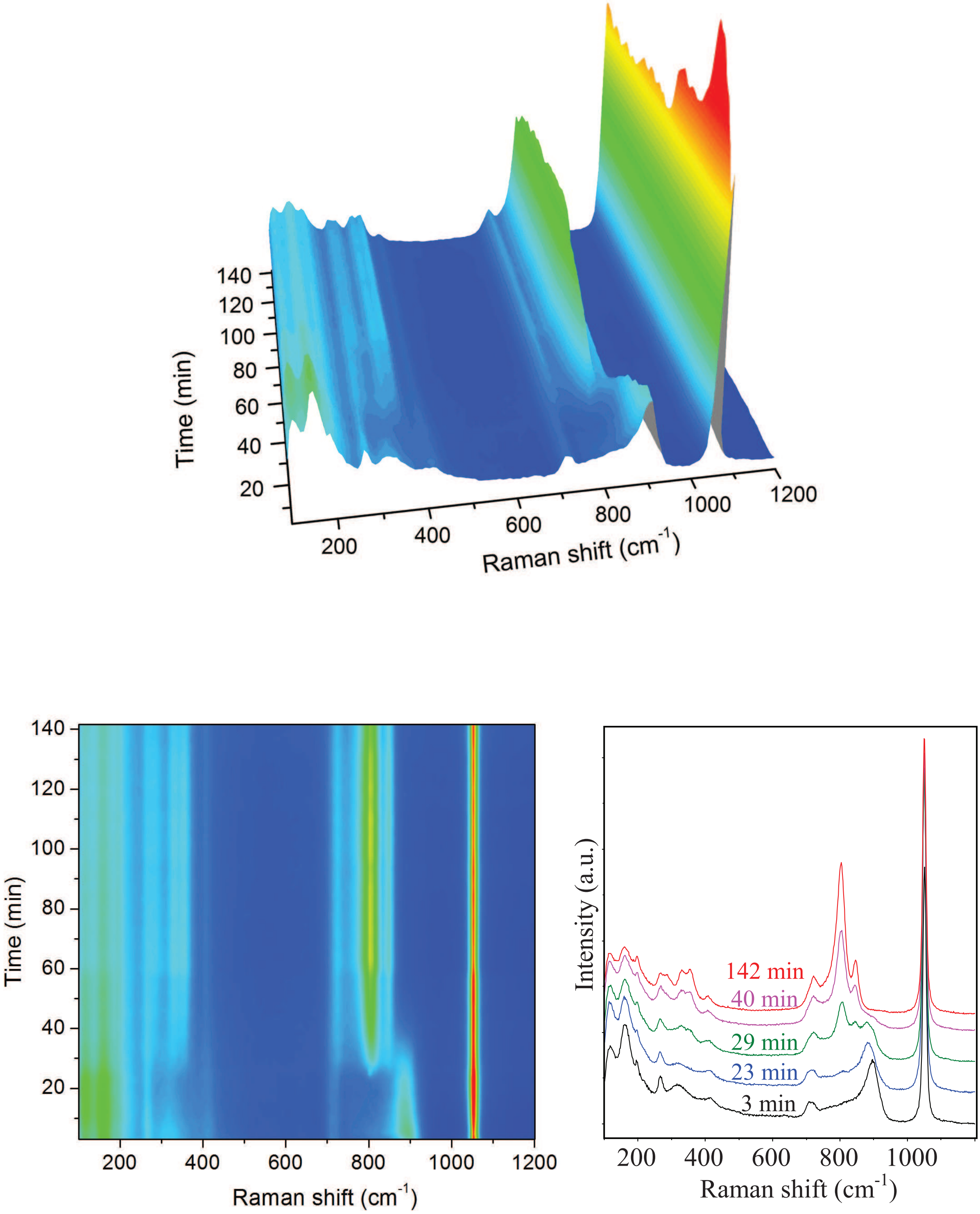

Fig. 2.13 Raman spectra collected during the hydrothermal synthesis of γ-Bi_2MoO_6 at 180°C.

All data allow comparing the rate of reaction or the changes during the reaction observed for XANES, Raman scattering and XRD techniques. However, the figures will be discussed according to the short- or long-range environment revealed by each technique.

4.1. Short-range environment: XANES

XANES evolution is consistent with a previous study performed on the same system but at lower temperatures of 120°C and 130°C [8, 11]. It is characterized by two features labelled A and B in Fig. 2.5 which respectively decreases and increases, after *ca.* 40 minutes at 160°C. The intensities of the *pre-edge* peak and the *post-edge* peak are known to be signatures of the coordination environment of Mo(VI) compounds. It is well-known that a very distinctive *pre-edge* feature appears in XANES spectra for the compounds containing transition-metal ions in non-centrosymmetric sites. Transitions such as 1s-3d and 1s-4d, which are forbidden by the selection rules, become allowed in systems without inversion symmetry when the d-orbitals mix with the surrounding p-orbitals [22] and [23].

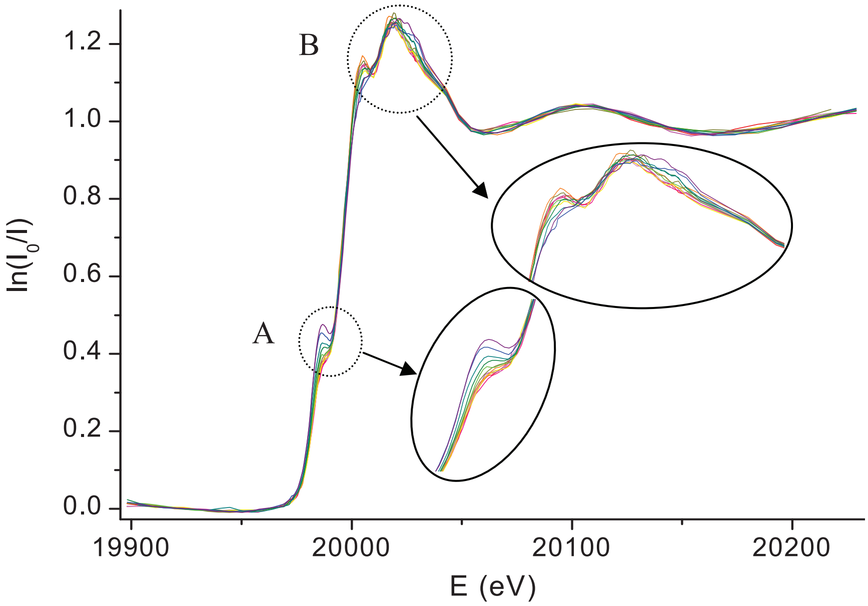

Fig. 2.14 Mo K-edge XANES spectra collected at 160°C showing isosbestic points. The features marked A and B are characteristic of Mo(VI) in tetrahedral and octahedral environment, respectively.

In Fig. 2.5, the XANES spectra of the initial gel precursor display a strong *pre-edge* peak at *ca.* 19987eV (labelled A) and a weak shoulder on the top of the edge at which suggests that non-centrosymmetric tetrahedral MoO_4^{2-} species are present in the system [24]. The decreasing intensity of the *pre-edge* peak and the increasing intensity of shoulder on the top of the edge at *ca.* 20006eV (labelled B) account for conversion of tetrahedral to octahedral coordination around molybdenum during the course of the reaction.

Moreover, isosbestic points found in XANES spectra during the chemical reaction (in Fig. 2.14) would indicate that the two chemical species: MoO_4^{2-} and MoO_6 have identical molar absorption coefficients, which remain constant as the reaction proceeds. The stability of isosbestic points shows that this reaction is probably a direct transformation from MoO_4^{2-} to MoO_6 species.

4.2. Short-range environment: Raman Scattering

Raman scattering confirms these molybdenum coordinations with new insight and additional information on the local environments of bismuth ions.

4.2.1. Literature reviews of γ-Bi_2MoO_6 Raman spectra

There have been extensive articles published on Mo local environment studied by Raman scattering. For bismuth molybdates, it is assumed that bands observed below 400 cm^{-1} are assigned to bending, wagging, translational and librational motions of the different species in the crystal whereas bands observed above 600 cm^{-1} are assigned to stretching motions of Mo-O bond.

Although, the Raman spectrum of γ-Bi_2MoO_6 form (koechlinite structure) stable at room temperature has been investigated, the assignment of vibrational modes is not yet clear. It is usually compared to the spectrum of Bi_2WO_6, an isomorph to Bi_2MoO_6. Their structures belongs to the Aurivillius family, with general formula: $(Bi_2O_2)(A_{n-1}B_nO_{3n+1})$, where n = 1 and B = W or Mo. The structure consists of perovskite-like layers (MoO_4^{2-} or WO_4^{2-}) of corner-sharing distorted octahedra separated by bismuth-oxygen sheets $(Bi_2O_2)^{2+}$ [25, 26, 27] (cf. Chapter 1). Using polarized Raman spectroscopy on an oriented Bi_2WO_6 single crystal, the assignment of Raman active modes of Bi_2WO_6 structure was achieved. Both octahedral and tetrahedral characteristics were found for the coordination of tungstate, so the coordination of W atoms could be described as both octahedra and tetrahedra depending on the way it is viewed. For γ-Bi_2MoO_6 structure, the distorted octahedral environment of Mo cation is more significant.

The Raman spectrum of γ-Bi_2MoO_6 powder in Fig. 2.15 shows three main bands in the high wavenumber range: the strong band at 795 cm^{-1} and two other bands with medium intensity at 721 and 845 cm^{-1}. They are presumably attributable to stretching vibrations $\nu_1(A_{1g})$ and $\nu_2(E_g)$ of the distorted MoO_6 octahedron in the orthorhombic structure. The bands between 270 and 360 cm^{-1} including 285, 327 and 354 cm^{-1} are assigned to the different components corresponding to the bending modes of the octahedron [27, 28, 29].

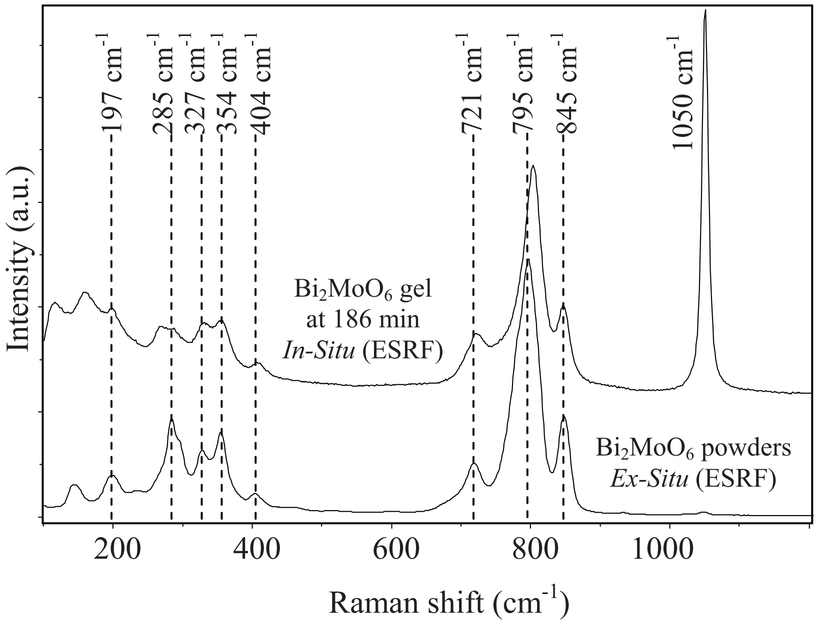

Fig. 2.15 Raman spectra of γ-Bi_2MoO_6 powder at room temperature in ESRF and γ-Bi_2MoO_6 gel at 186 min during the hydrothermal synthesis at 160°C.

However, such a distorted MoO_6 octahedron in γ-Bi_2MoO_6 structure can also be viewed as a distorted tetrahedron as shown in Fig. 2.16 because of the presence of two long bonds. The Mo-O vibration band distribution in Bi_2MoO_6 spectrum was evidenced by *I. Matsuura et al.* [30] by using G-F matrix method. This method, introduced by *E. B. Wilson*, relies on the fact that the frequency of the normal vibration is determined by the kinetic and potential energies of the system [31]. The matrix G^{-1} gives the kinetic energy in terms of arbitrary linear internal coordinates and the matrix F represents the potential energy in terms of these coordinates. The vibrational frequencies corresponding to the MoO_4 environment in Bi_2MoO_6 can be then calculated by using this method (Table 2.1) [30]. Most of the calculated wavenumbers are in good agreement with our experimental data.

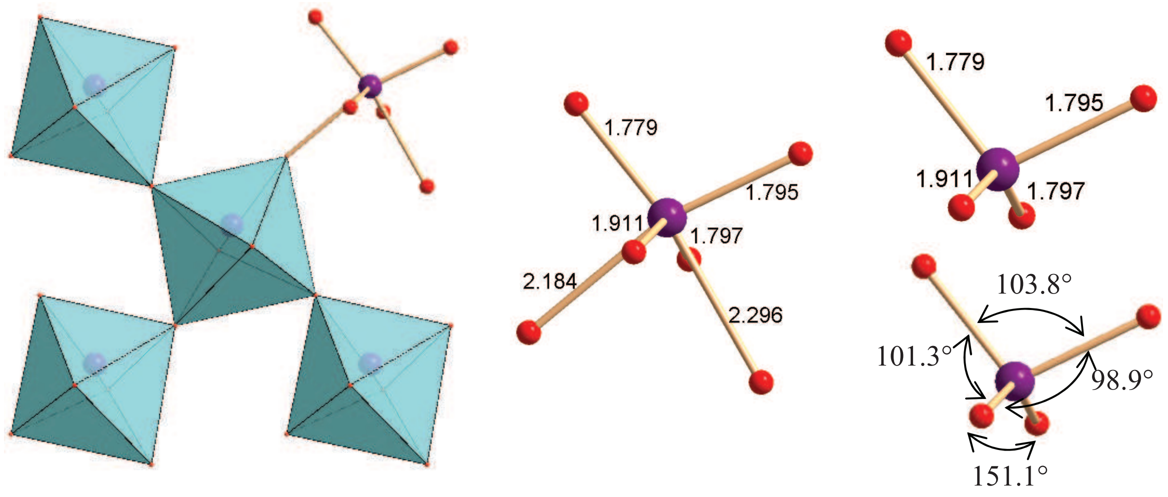

Fig. 2.16 a) Layer of corner-sharing Mo octahedra in γ-Bi_2MoO_6 structure according to Theobald [32] and b) Octahedral and tetrahedral description of the environment of Mo in γ-Bi_2MoO_6 structure.

Table 2.1 Band Positions for MoO_4 in Bi_2MoO_6. calculated by G-F matrix method [30].

	Ref [30].		Observed
Calculated (cm^{-1})	IR (cm^{-1})	Raman (cm^{-1})	Raman (cm^{-1})
865	842	848	845
780	798	799	795
693	735	717	721
613	600	-	-
376	375	399	404
355	354	354	354
337	304	326	327
287	287	293	285
196	-	194	197

4.2.2. *In-situ* Raman spectroscopy study

• *General aspects*

The last spectrum obtained at the end of experiment at 160°C (cf. Fig. 2.11) is compared to that of γ-Bi_2MoO_6 in Fig. 2.15. They show the same feature, except for the spectrum obtained from *in-situ* study where two extra bands are observed, a small band at 711 cm^{-1} and a strong line at 1050 cm^{-1}. They correspond to the angular deformation and the symmetric stretching mode of NO_3^- anion that are present in the solution [33]. The spectrum of the Bi_2MoO_6 powder also shows better defined Raman bands with a lower background because of the better crystallization of the Bi_2MoO_6 powder which is in solid state. From both Fig. 2.15 and 2.17, it is worth noting that the band at 140 cm^{-1} for the powder shifts to 160 cm^{-1} for that in the *in-situ* study. Some bands in the *in-situ* spectrum are more pronounced than in the powder spectrum, e.g., the 198 cm^{-1} band is better defined and the band at 266 cm^{-1} is more intense. These distinctive bands correspond to the vibrations of bismuth oxide which are assigned to internal modes above 200 cm^{-1} and external modes below 200 cm^{-1} [34]. The different features of these bands could be explained by the fact that during the hydrothermal synthesis of γ-Bi_2MoO_6, the high pressure in the cell probably enhances the preferential orientation of particles. The presence of nitrate could be also responsible for these differences.

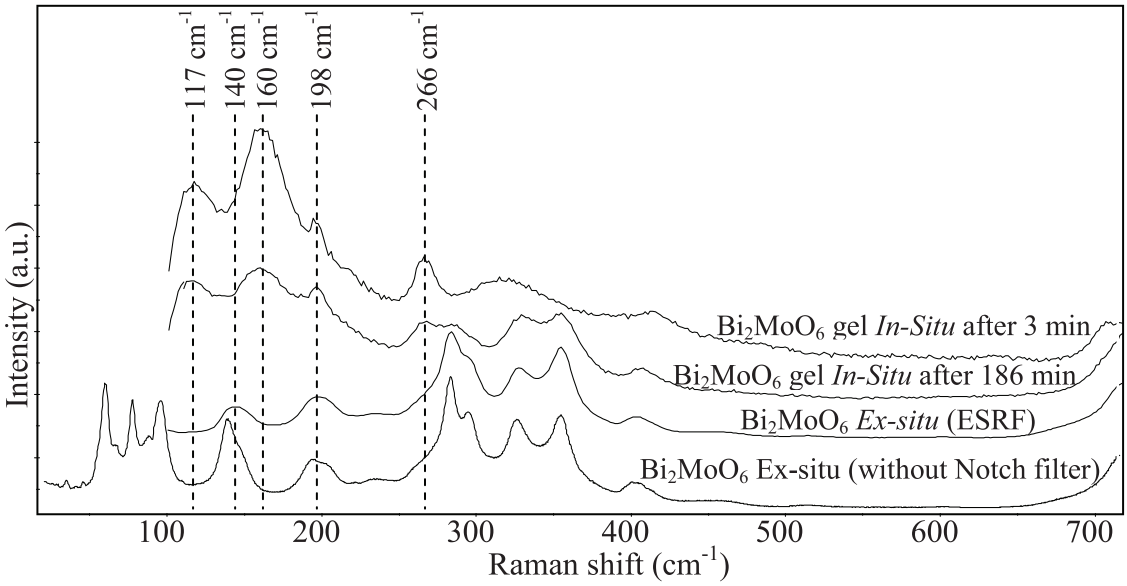

Fig. 2.17 The low wavenumber range of Raman spectra collected during the hydrothermal synthesis of γ-Bi_2MoO_6 at 160°C at 3 and 186 min and Raman spectra collected on γ-Bi_2MoO_6 powder at ESRF and UCCS (without notch filter).

Concerning the peak at 117 cm^{-1}, it is difficult to conclude if it is a Raman band. Indeed its intensity at the low wavenumber side is much lower than the baseline which should be usually high due to the approach to the exciting line. Hence, this peak could be a discrepancy related to the partially charged collection of CCD detector. In order to verify the possibility of extra peaks due to interferences caused by the Notch filter, the spectra collected at ESRF were compared to the spectrum of the γ-Bi_2MoO_6 powder collected on a krypton ion laser spectrometer at UCCS without a Notch filter. The experimental setup of the Raman spectrometer used at UCCS is described in Chapter 3: *Ex-situ* study. Usually, the Notch filter is used to reject the Rayleigh scattered light, but it does not allow detection below 100 cm^{-1} and it could also bring out some extra bands in the low wavenumber range. In our case, the two spectra are similar. The one collected at UCCS provides a larger range of wavenumbers, below 100 cm^{-1}, with a better spectral resolution, and it does not show any peak at 117 cm^{-1}. This experiment leads to the conclusion that the 117 cm^{-1} peak observed in the *in-situ* spectra is due to the partially charged collection of CCD detector.

• ***Local environment of molybdenum atoms during the reaction***

We shall first discuss the evolution of Mo coordination during the hydrothermal synthesis of γ-Bi_2MoO_6 observed by Raman spectroscopy. Since the bending modes are overlapped by the vibration of bismuth oxide groups, only the stretching modes between 650 and 975 cm^{-1} are worthwhile to examine (Fig. 2.18).

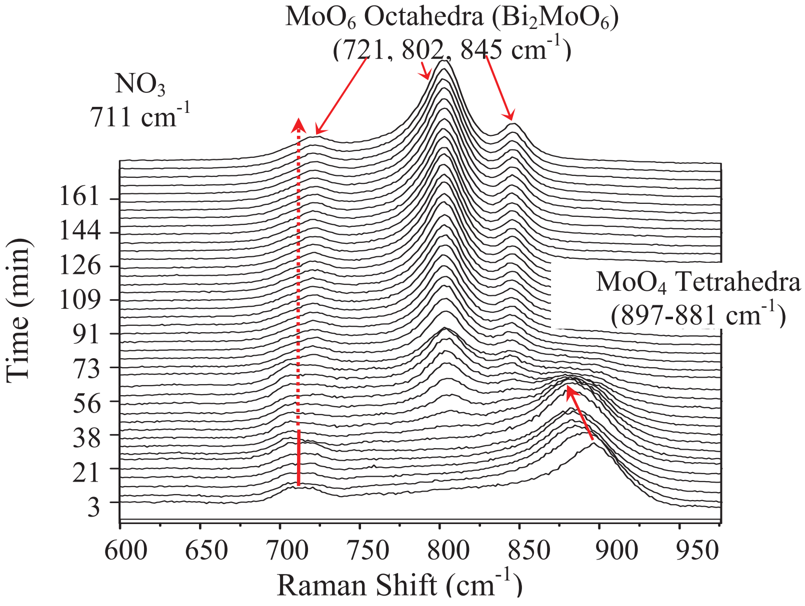

Fig. 2.18 Raman spectra collected during the hydrothermal synthesis of γ-Bi_2MoO_6 at 160°C (corresponding to Mo local environment).

In the Raman spectrum of the starting gel mixture shown in Fig. 2.18, the broad band at 897 cm^{-1} and weak band at 841 cm^{-1} correspond to symmetric $\nu_1(A_1)$ and anti-symmetric $\nu_3(F_2)$ Mo-O stretching modes of isolated MoO_4 tetrahedra, respectively [35, 36]. Other characteristic vibrations of tetrahedral species noticed around 318 cm^{-1} are assigned to angular deformations $\nu_2(E)$ and $\nu_3(F_3)$. These features confirm the presence of MoO_4 species in the initial stage of the reaction as observed by XANES.

As the reaction proceeds, the 897 cm^{-1} band shifts to 881 cm^{-1} during the first 20 min of reaction and then remains at this position. This remarkable shift is possibly due to the change in structural parameters of MoO_4 tetrahedra. The shifted wavenumber value is close to 880 cm^{-1}, the Mo-O stretching vibration of MoO_4 tetrahedra in the $CaMoO_4$ structure [28]. Interestingly, Beale *et al.* [11] claimed that the "β" phase, $Bi_2Mo_2O_9$ might be initially formed during the hydrothermal synthesis of γ-Bi_2MoO_6. The environment around Mo atoms in β-$Bi_2Mo_2O_9$ is also tetrahedral but its Raman band is located at 887 cm^{-1} [28]. After 30 minutes of reaction, the intensity of the 881 cm^{-1} band decreased while new bands appeared at 721, 845 cm^{-1} and at 802 cm^{-1} (strong, broad band) which are related to the Mo-O stretching modes of distorted MoO_6 octahedra in γ-Bi_2MoO_6 structure, as previously mentioned. Other bands found in the low wavenumber range are also assigned to γ-Bi_2MoO_6 structure.

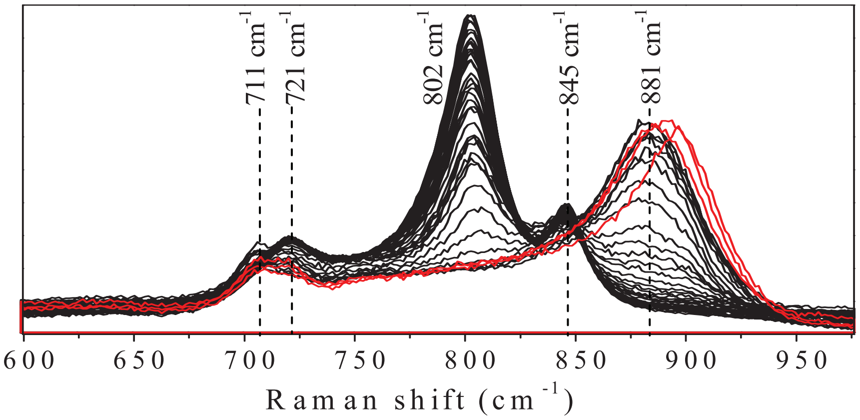

Fig. 2.19 Raman spectra collected during the hydrothermal synthesis of γ-Bi_2MoO_6 at 160°C (corresponding to Mo local environment) showing isosbestic points.

Consequently, the evolution of these Raman spectra revealed a change of the MoO_4 tetrahedral species, especially a perturbation or a change in structural parameters of MoO_4 tetrahedra that may be caused by the interaction between the positively charged $[Bi_2O_2]^{2+}$

layers and the negatively charged $[MoO_4]^{2-}$ molecules, before they transform to MoO_6 octahedra as in γ-Bi_2MoO_6 structure. This will be illustrated by the evolution of the MoO_4 stretching mode wavenumber plotted against the change in the relative abundance of MoO_4 and MoO_6 species during the reaction (Fig. 2.21). This behaviour is also confirmed by the isosbestic points (Fig. 2.19) that are found for the Raman spectra obtained after 20 min of heating, after the shift of the characteristic peak of MoO_4 from 897 cm^{-1} to 881 cm^{-1} which then remains at this wavenumber.

It is interesting to note that this change of tetrahedral species was not observed by XANES. This might be due to a higher sensitivity of Raman spectroscopy for observing the chemical environment of MoO_4 species, and may be also to a non optimised resolution of XANES spectra which is due to the limitation of acquisition time.

• ***Local environment of Bismuth atoms during the reaction***

Let us now discuss the evolution of the bismuth environment during the synthesis reaction. In general, Bi-O bands found at low wavenumber, below 200 cm^{-1}, are known to be external modes including translational and librational modes. While the internal modes of bismuth oxide molecules within the unit cell of a crystal occur in the medium and high wavenumber regions, usually between 200 and 700 cm^{-1}, the bands observed at *ca.* 455 and 620 cm^{-1} are assigned to the stretching modes of Bi-O or of Mo-O-Bi bonds [30, 34]. Regarding the evolution of bismuth oxide coordination during the hydrothermal synthesis reaction, the spectrum collected at the beginning of the reaction is generally similar to the one collected at the end of reaction, except for the bands in the 270-400 cm^{-1} range assigned to molybdate bending modes [30].

From the fact that the modification of Raman bands is not observed at the low wavenumber domain, especially below 270 cm^{-1}, we can conclude that there is *no significant modification of the local environment of bismuth* or crystalline structure during the synthesis. This remark is in agreement with the results of numerous Raman studies on the various substitutions of metal oxide compounds [37, 38]. It means that $Bi_2O_2^{2+}$ layers could have already been formed at the very beginning of the reaction (3 minutes after heating) and that these layers remain until the end of the reaction as a part of the γ-Bi_2MoO_6 framework.

4.3. Quantitative Analysis of XANES and Raman spectroscopy

XANES and Raman spectroscopy have proved to be promising tools to determine the contribution of each Mo component in mixed compounds [39, 40, 41, 42]. Therefore, it is possible to quantify the change of the relative abundance of MoO_4^{2-} and MoO_6 species during the synthesis.

According to our previous discussion, the Raman spectra evidenced a change of MoO_4 tetrahedral species during the initial stage of the reaction, this perturbation of MoO_4 is likely due to a change in their structural parameters that may be caused by the interaction between the negatively charged $[MoO_4]^{2-}$ species and the positively charged $[Bi_2O_2]^{2+}$ layers, before transforming to MoO_6 octahedra in γ-Bi_2MoO_6 structure. Consequently, we shall focus on the exchange of Mo species from the tetrahedral perturbed MoO_4 to MoO_6 octahedra in γ-Bi_2MoO_6. The quantification will be essentially performed for the spectra collected after the change of MoO_4. Three assumptions were made:

- No MoO_6 species are present in the gel before the perturbation of MoO_4 is complete.
- The first spectrum collected just after the perturbation of MoO_4 and the last spectrum collected at the end of each reaction (at 160, 170 and 180°C) are assumed to be that of a pure phase constituted fully of perturbed Mo tetrahedra (MoO_4) and Mo octahedra (MoO_6), respectively.
- Because of a direct transformation from perturbed MoO_4^{2-} tetrahedra to MoO_6 octahedra in γ-Bi_2MoO_6 structure, the gel sample observed during the reaction should be composed only of these two types of molybdenum coordination.

4.3.1. Quantitative analysis by Linear Combination Fit of XANES data

The XANES analysis of unknown samples by comparison of pre-peak, white line and absorption edge position to reference materials demonstrates that, from XANES alone, it is not possible to quantify each coordination type of Mo(VI). To overcome this limitation, a linear combination fit (LCF) was employed to analyze the spectral data afterwards [43, 44, 45]. The LCF analysis of XANES data was done using the Athena software package [18]. This quantitative analysis uses reference spectra of Mo(VI) species to allow the quantification of species in unknown, multiple-component mixtures. This method uses a least-squares fitting algorithm to refine the sum of reference spectra to an experimental spectrum.

By fitting the unknown spectrum with a linear combination of the standard spectra, the types of coordination environments of Mo(VI) and their relative contribution to the analyzed sample can be determined. The LCF analysis was carried out using the normalized XANES over the fit range: -40 eV < E_0 < 30 eV. Since the elongation of tetrahedral species is not observed by XANES, the data were fitted by using a combination of two standard XANES spectra: the first and the last spectrum collected of each reaction. All standards used the same E_0, all weights were set to be between 0 and 1, and the sum of weights was also set to 1.

The fitting results and fitting statistics (R-Factors) are given in Table 2.2. The changes in the relative abundance of MoO_4 and MoO_6 species during the reaction were plotted as a function of time for 160°C, 170°C and 180°C in Fig. 2.20. The position shift of MoO_4^{2-} Raman band during the reaction at 160°C was plotted against the change in the relative abundance of MoO_4^{2-} and MoO_6 species in Fig. 2.21. This plot shows that the MoO_4^{2-} tetrahedral species are modified to the perturbed MoO_4^{2-} before transforming to MoO_6 octahedra in γ-Bi_2MoO_6 structure.

Table 2.2 Composition of MoO_4 and MoO_6 with their R-factors obtained from LCF.

160°C				170°C				180°C			
Time (min)	Composition		R-Factor	Time (min)	Composition		R-Factor	Time (min)	Composition		R-Factor
	MoO_4	MoO_6			MoO_4	MoO_6			MoO_4	MoO_6	
3.0	100.0	0.0	-	8.0	100.0	0.0	0.00022	3.00	100.0	0.0	0.00020
16.3	100.0	0.0	0.00019	20.1	100.0	0.0	0.00026	14.87	100.0	0.0	0.00030
29.2	99.3	0.7	0.00034	33.4	70.2	29.8	0.00009	27.78	75.4	24.6	0.00012
41.2	86.9	13.1	0.00023	45.4	30.5	69.5	0.00015	39.63	22.6	77.4	0.00013
54.8	57.2	42.8	0.00011	58.3	14.1	85.9	0.00011	52.28	10.1	89.9	0.00009
66.7	35.5	64.5	0.00010	70.3	7.9	92.1	0.00015	64.18	1.7	98.3	0.00012
79.9	22.9	77.1	0.00010	83.4	3.0	97.0	0.00015	77.05	3.0	97.0	0.00015
91.8	14.6	85.4	0.00016	95.5	6.8	93.2	0.00017	88.90	1.2	98.8	0.00012
104.7	8.5	91.5	0.00011	108.9	1.1	98.9	0.00013	102.33	0.0	100.0	0.00021
116.5	3.6	96.4	0.00014	120.8	1.0	99.0	0.00017	118.82	0.0	100.0	0.00017
129.4	11.0	89.0	0.0002	134.0	0.0	100.0	0.00019				
141.4	5.4	94.6	0.00007	145.9	0.0	100.0	0.00025				
154.7	0.0	100.0	0.00014	158.9	3.5	96.5	0.00016				
166.6	0.0	100.0	-	170.8	0.0	100.0	0.00013				

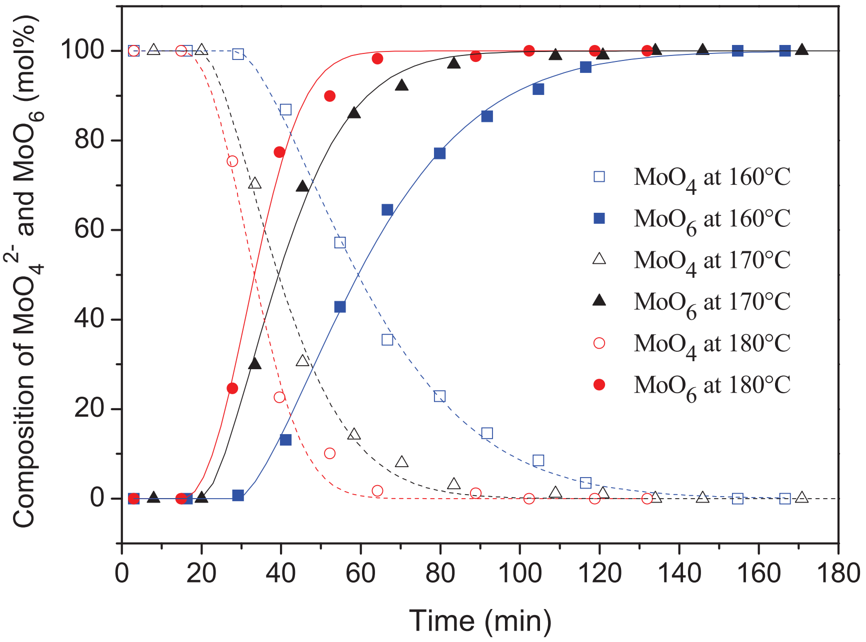

Fig. 2.20 The changes in the relative abundance of MoO_4^{2-} and MoO_6 species during the hydrothermal synthesis of γ-Bi_2MoO_6 at 160°C, 170°C and 180°C, deduced from LCF analysis of XANES spectra.

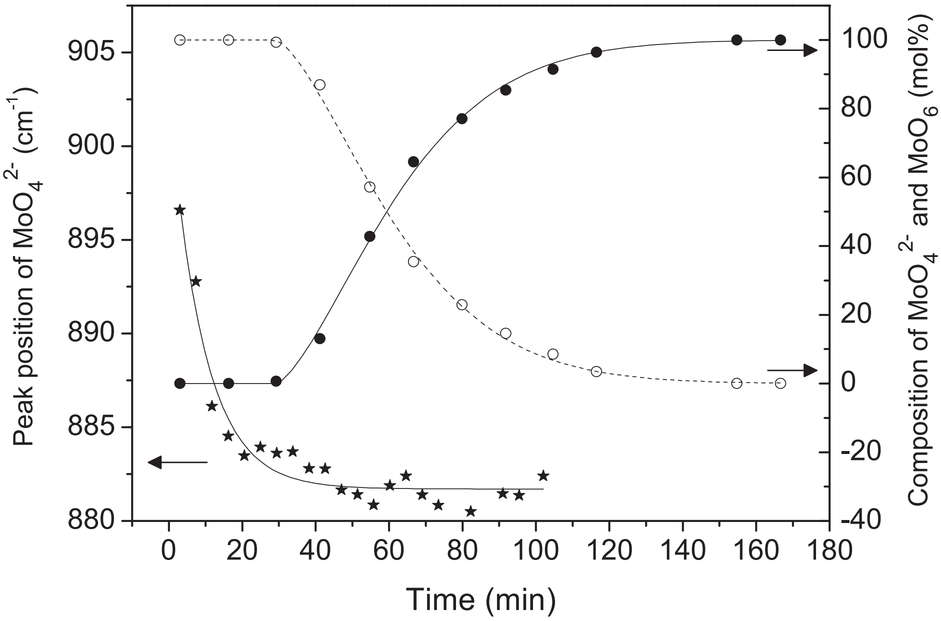

Fig. 2.21 Plots of the position shift of MoO_4^{2-} Raman band (★) and the composition of MoO_4^{2-} (○) and MoO_6 (●) species (from XANES spectra) during the hydrothermal synthesis of γ-Bi_2MoO_6 at 160°C.

4.3.2. Quantitative analysis of Raman bands

Raman spectroscopy has proved to be an excellent non-destructive tool, not only for qualitative purposes, but also for quantitative analysis and is widely applied in analysis of polymorphic forms of pharmaceutical compounds [46, 47] or mixed crystalline phase compounds [48]. The proportions of each compound in the mixed sample are generally determined by using the ratio of intensities or areas of two Raman bands characteristic of these two species. Moreover, Raman scattering is able to provide a spectral range from few cm^{-1} to 4000 cm^{-1} that can be collected with sub-seconds time resolution for materials with high cross-sections. Consequently this technique has been used over the last decades to follow the fast chemical exchange for time resolved experiments, as well as, during *in-situ* study of catalytic materials under working conditions. The catalytic activity and selectivity can be related to changes in the catalysts structure [49]. The kinetic and the equilibrium constant of reactions in glasses can be determined [50].

• ***Limitation***

In practice, the quantitative analysis of Raman spectra is a difficult task due to broad, overlapping bands and frequency shift. In addition, the ratios between peak areas are not always equal to ratios between the abundance of species [46, 48, 49, 51, 52, 53]. The area of a Raman line does not only depend on the concentration of each component but also depends on the incident laser power, the frequency of scattered radiation, the absorptivity of the materials involved in the scattering and the response of the detection system. Hence, the area under a Raman peak can be expressed [48, 54] as

$$\boldsymbol{A}(\nu) = \boldsymbol{I}_0\boldsymbol{K}(\nu)\boldsymbol{C} \tag{2.13}$$

where $\boldsymbol{I}_0$ is the intensity of the excitation laser line

ν is the frequency

$\boldsymbol{C}$ is the concentration of the Raman active species

$\boldsymbol{K}(\nu)$ is a factor which includes the frequency dependent terms: the overall spectrophotometer response, the self-absorption of the medium and the molecular scattering properties.

The ***K***(ν) factor is also proportional to the frequency (ν), Raman scattering cross-section ($\sigma(\nu)$) and Boltzmann factor ($exp(-E_j/kT)$), as described in Eq. 2.14.

$$K(\upsilon) \propto \upsilon^4 \bullet \sigma(\upsilon) \bullet \exp\left(\frac{-E_j}{kT}\right) \tag{2.14}$$

Subsequently, the ratio between peak areas of two species, MoO_4 and MoO_6 in our cases, can be expressed as:

$$\frac{A_{MoO_4}^{\upsilon_{MoO_4}}}{A_{MoO_6}^{\upsilon_{MoO_6}}} = \frac{K_{MoO_4}^{\upsilon_{MoO_4}}}{K_{MoO_6}^{\upsilon_{MoO_6}}} \times \frac{C_{MoO_4}}{C_{MoO_6}} \tag{2.15}$$

The quantification of Raman spectra by comparison of relative peak areas must therefore be considered with care because the absolute or relative Raman scattering factors are unknown.

To partly overcome this limitation, an external calibration is conventionally used to determine the relative Raman scattering factors. A calibration curve is generally obtained from Raman spectra of the standard samples of known concentrations. Quincy et *al.* [52] determined Raman scattering factor of MoO_3 on the TiO_2 support from the relative peak areas of molybdate bands and MoO_3 bands, the calibration was carried out by using a mass balance. An alternative approach was suggested by Baltrus et *al.* [53] who quantified the MoO_3 on an alumina support by using a mass balance and measurements with KNO_3 as an internal standard. The internal standardization technique was also applied with $K_2Mg_2(SO_4)_3$ to deduce the MoO_3 content in the MoO_3-TeO_3 glasses [55]. In the latter, the peaks area ratio calculation was achieved by using a symmetric Gaussian-type profile function to deconvolute the Raman spectra. It is worth noting that relative Raman scattering factors for MoO_3 differ between these different studies.

However this external calibration method seems to be very complicated to perform, especially for an *in-situ* study, because the Raman spectra of standard samples are extremely difficult to carry out under identical working conditions. Interestingly, recent works revealed the possibility of performing a quantitative Raman spectroscopy without external calibration. Ohler and Bell [41] could directly determine the exchange of ^{18}O for ^{16}O in Mo=O bond during reaction with H_2/O_2 by using Lorentzian deconvolution to determine the relative peak areas. Furthermore, Bergwerff et *al.* [42] suggested a multivariate curve resolution (MCR) with which the spectra can be deconvoluted into pure component spectra with their concentration. This analysis was conducted to determine the speciation of polyoxomolydate as a function of pH and the results showed a good correlation with the theoretical plots.

The purpose of this present study was to determine the evolution of MoO_4, MoO_6 composition during the hydrothermal synthesis of Bi_2MoO_6 by quantitative Raman spectroscopy technique without the necessity of external calibration. Although the quantification of Mo species was previously accomplished by XANES technique, it is expected that the transformation of Mo species could be better resolved with shorter acquisition time of the Raman spectra. Our quantification approach is based on the deconvolution of Raman bands by using a statistical fit of both Gaussian and Lorentzian functions to determine ratio between peak areas of the two species, MoO_4 and MoO_6. The reliability of this method will be verified by comparing with linear combination fit (LCF) analysis that uses a least-squares fitting algorithm to refine the sum of reference spectra or pure component spectra and the quantitative distribution of the reference spectra can be referred to their concentration. Subsequently, the quantification of Raman spectra will be validated by comparison with the quantitative information obtained previously from XANES.

• ***Deconvolution of Raman spectra***

According to our previous discussion, the Raman analysis showed the perturbation of MoO_4 tetrahedral species accompanied with an absence of isosbestic points for the Raman spectra obtained during the first 20 min of reaction when the peak position of MoO_4 shifts from 897 cm^{-1} to 881 cm^{-1} (Fig. 2.21). Because we are interested in the transformation of molybdate species from perturbed MoO_4 tetrahedra to MoO_6 octahedra in γ-Bi_2MoO_6, the quantification was performed only for the Raman spectra in which the characteristic peak position of MoO_4 remains constant at 881 cm^{-1}. The spectra with the peak position of MoO_4 located above 881 cm^{-1} are assumed to be composed by only MoO_4 tetrahedra because of the absence of the characteristic MoO_6 band (Fig. 2.19).

The Raman bands in the range of 600-975 cm^{-1} are assigned to molybdenum oxide stretching modes of both tetrahedral and octahedral coordinations. The integrated areas of these corresponding bands can be obtained as illustrated in Fig. 2.22. However, a small line at 711 cm^{-1} corresponding to the bending mode of NO_3 anion [33] can not be neglected and it has to be subtracted from the area calculation.

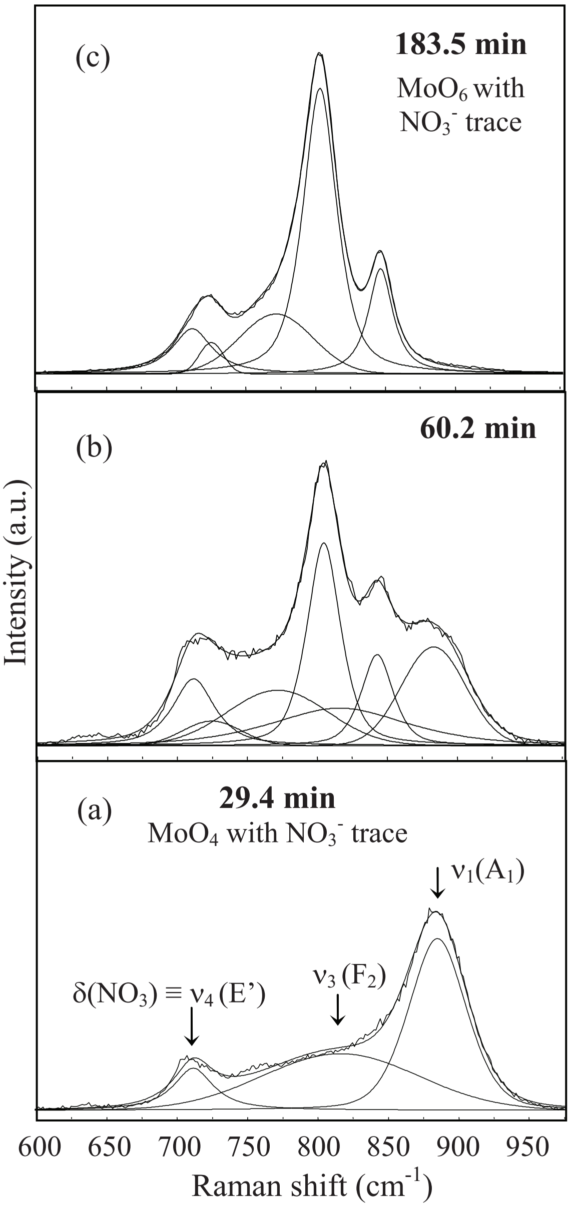

Fig. 2.22 The deconvolution of base-line substracted Raman spectra collected at 29.4 min (a), at 60.2 min (b) and at 183.5 min (c) during the hydrothermal synthesis of γ-Bi_2MoO_6 at 160°C.

All vibration bands of these three compounds: NO_3, MoO_4 and MoO_6 are therefore overlapped hence a deconvolution is indispensable to determine the peak areas of molybdate species. To do so, the Raman analysis Jobin Yvon's Labspec software was employed. All spectra were first background-subtracted by a linear baseline and then normalized. The Raman spectra were fitted by using a statistical fit of both Gaussian and Lorentzian function for deconvoluting all Raman bands.

The Raman bands of perturbed MoO_4^{2-} tetrahedral species in Fig. 2.22(a) were fitted for Mo=O symmetric stretching vibration ($\nu_1(A_1)$: 881 cm^{-1}) and Mo=O antisymmetric stretching vibration ($\nu_3(F_2)$: 815 cm^{-1}) [35, 36]. For the bands corresponding to the Mo octahedral species of γ-Bi_2MoO_6 in Fig. 2.22(c), they are presumably stretching modes $\nu_1(A_{1g})$ and $\nu_2(E_g)$ of the distorted MoO_6 octahedron in the orthorhombic distorted structure [27, 28, 29]; they were fitted for 724, 771, 803 and 845 cm^{-1}, in good agreement with the inter-molecular coupling.

It is worth noting that the deconvolution of an overlap of MoO_6 bands located at 710-850 cm^{-1} in this study only aims to determine the surface area. It does not refer to the distribution of each vibration modes.

During the reaction, the molybdenum oxide stretching bands of both MoO_4 and MoO_6 evolved smoothly; the two stretching bands of MoO_4 decreased while all stretching vibration bands of MoO_6 increased with the reaction time. The fraction of tetrahedral Mo oxide species was then calculated from the fraction of the total area under the MoO_6 bands: 724, 771, 803 and 845 cm^{-1} to the total area corresponding to the vibration of molybdates.

$$\frac{\sum A_{MoO_6}^{\upsilon_{MoO_6}}}{\sum A_{MoO_6}^{\upsilon_{MoO_6}} + \sum A_{MoO_4^{2-}}^{\upsilon_{MoO_4^{2-}}}} \qquad (2.16)$$

Due to the overlap of the nitrate bands and all molybdate bands of MoO_4 and MoO_6 species, the peak parameters cannot be determined by fitting the spectra independently from each other. According to Fig. 2.22(b), the bands of MoO_4 tetrahedron, $\nu_3(F_2)$ at 815 cm^{-1} and $\nu_1(A_1)$ at 881 cm^{-1} strongly overlapped with other molybdate bands. The positions of these bands were subsequently hold constant and the ratio of the $\nu_3(F_2)$ peak area to the $\nu_1(A_1)$ area was constrained. Moreover, since the nitrate feature overlapped with the MoO_6 bands and was small, its position, width and height previously obtained from the spectra of MoO_4, were simply held constant in order to fit the spectra of MoO_6.

With all precautions, the evolution of MoO_4 and MoO_6 composition during the hydrothermal synthesis of Bi_2MoO_6 was consequently deduced by deconvoluting Raman spectra and it will afterward be verified by linear combination fit (LCF) analysis

• ***Linear combination fit (LCF) analysis of Raman spectra***

Since the peak area determination by deconvoluting a Raman spectrum is not unique, i.e., there may be more than one solution; the reliability of this method has to be verified. The LCF analysis may offer different and complementary tools for the quantification of Mo species. This technique was previously employed for the quantitative analysis of XANES spectra.

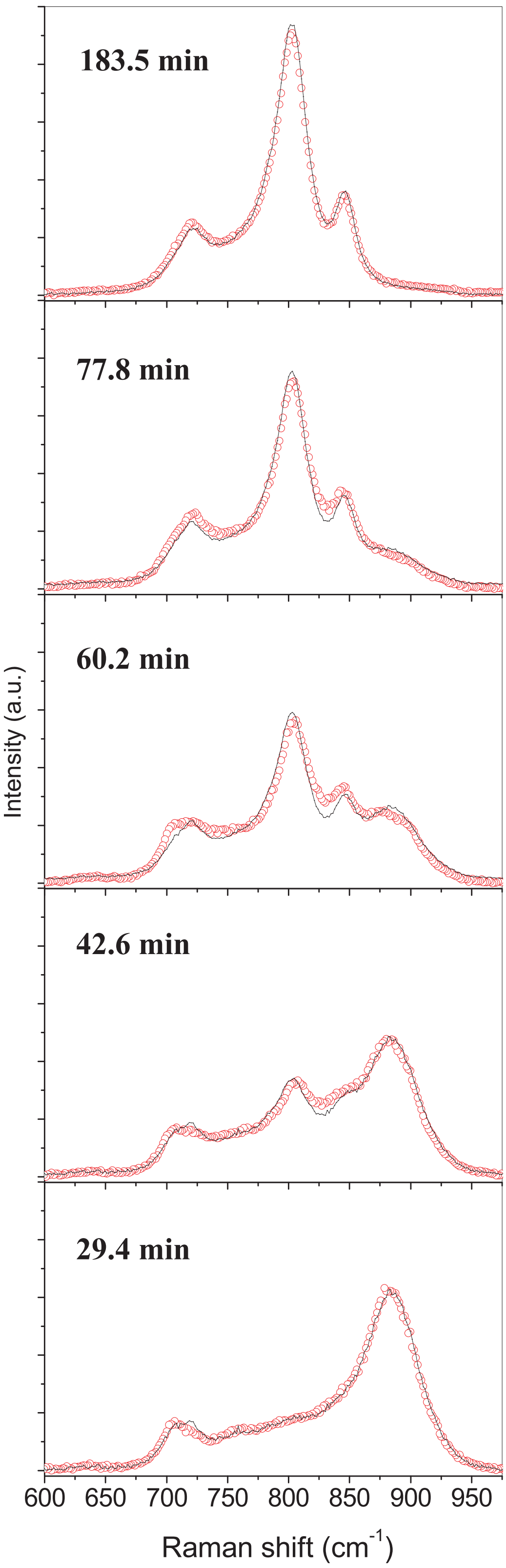

Fig. 2.23 Comparison between Raman spectra (red circles) and spectra obtained from LCF (black lines) after 29.4, 42.6, 60.2, 77.8 and 183.5 min of reaction at 160°C (bottom to top).

This analysis uses linear combinations of reference spectra or pure component spectra to construct a model spectrum; and their ratio will be refined by using least-squares fitting algorithm to minimise the difference between the model and the experimental spectra.

The LCF analysis of Raman spectra was done using the multiple regression function in Matlab program [56]. All spectra were first background-subtracted by a linear baseline and then normalized before LCF analysis over the fit range: 600 cm^{-1} < Raman shift < 975 cm^{-1}. The data were fitted by using a combination of two standard Raman spectra from a perturbed MoO_4 spectrum and a MoO_6 spectrum in order to obtain the relative contribution of both coordination types in each spectrum. For example, for the reaction at 160°C, a spectrum collected at 16.2 min was used as a standard spectrum for perturbed MoO_4 species since it was the first spectrum with a peak position remaining constant at 881 cm^{-1}. A spectrum collected at 139 min was used as a standard spectrum for MoO_6 octahedra in γ-Bi_2MoO_6 because it is one of the first spectra of the pure phase Bi_2MoO_6. The last spectrum of the reaction is unfavourable due to the influence of time of reaction on the crystallite size that would affect on the ratio of peak intensity.

A good fit between the calculated and experimental spectra was obtained, as demonstrated in Fig. 2.23.

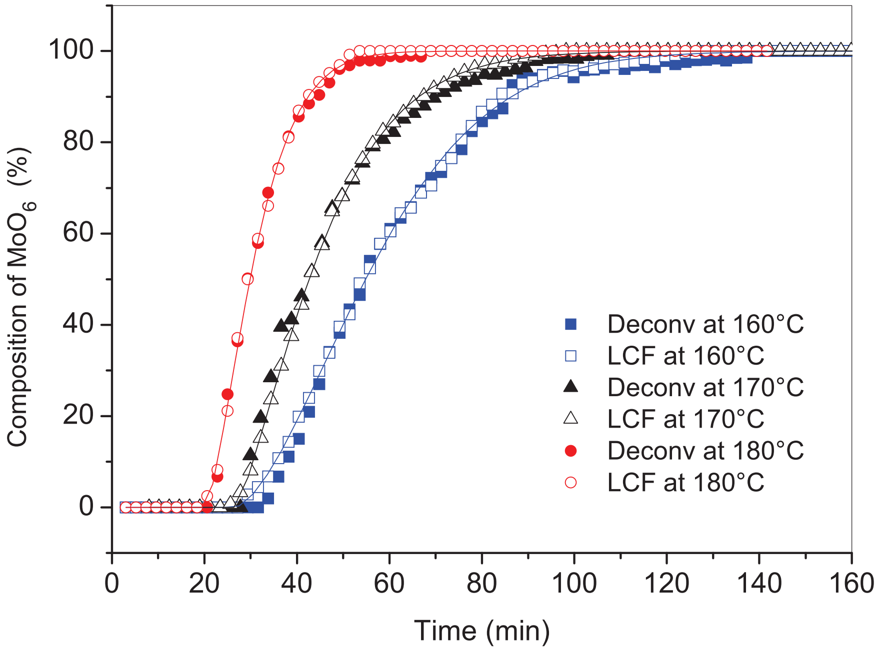

Fig. 2.24 The change in the relative abundance of MoO_6 species, deduced from deconvolution and LCF of Raman spectra, during the hydrothermal synthesis of γ-Bi_2MoO_6 at 160°C (■, □), 170°C (▲, △) and 180°C (●, ○).

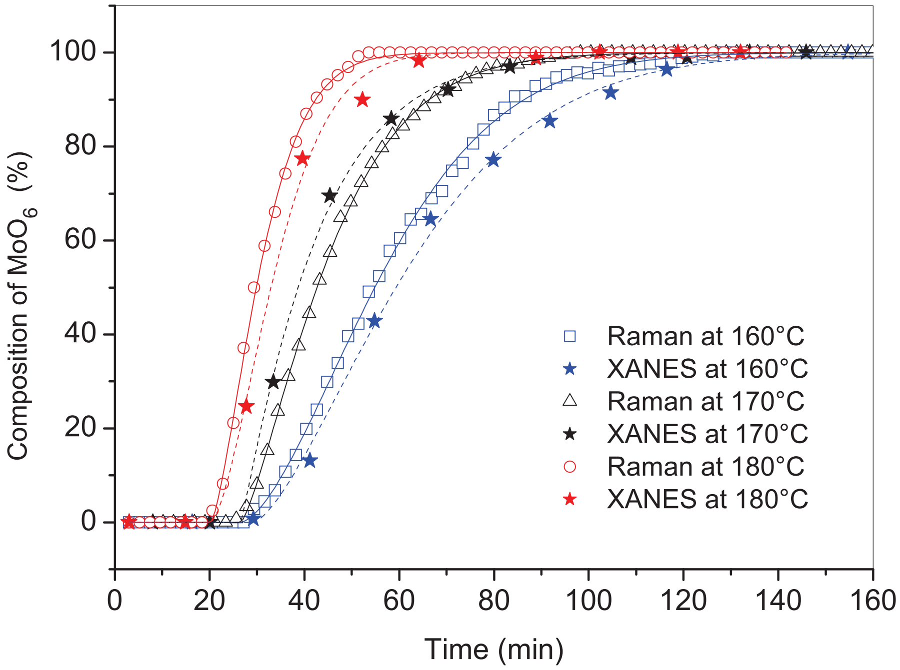

Fig. 2.25 The change in the relative abundance of MoO_6 species, deduced from LCF of Raman and XANES spectra, during the hydrothermal synthesis of γ-Bi_2MoO_6 at 160°C (□,★), 170°C (△,★) and 180°C (○,★).

The LCF analysis of change in abundance of MoO_4 and MoO_6 species during the reaction was achieved. The reliability of the deconvoluted Raman spectra was confirmed by the coincidence of the results of linear combination fit (LCF) analysis obtained for the similar values of MoO_4 and MoO_6 composition for all three temperatures: 160, 170 and 180°C. From Fig. 2.24, we can thus conclude that whatever the analysis methods, deconvolution or LCF of Raman spectra, they come up with the same results: *both can be used to quantify the molybdate species*.

The abundance of MoO_4 and MoO_6 species deduced by Raman and XANES Spectra are plotted as a function of time for the three temperatures: 160, 170 and 180°C, as shown in Fig. 2.25. Good correlation results between the two spectroscopic techniques were observed. The average deviation between the two techniques is within 3 min for the MoO_6 compositions below 80%. One must recall that XANES was recorded every 13 minutes whereas a Raman spectrum was recorded every 2 minutes. It is shown that the LCF analysis and the ratio of MoO_4 and MoO_6 integrated area obtained by deconvolution of Raman Spectra can really determine the composition of each species during the course of the reaction. It is interesting that, in our case, the quantitative results from this Raman spectroscopy technique is reliable compared to XANES techniques due to the higher time-resolution.

The evolution of MoO_6 species follows a sigmoid curve for all temperatures. As expected, a faster evolution is observed when the temperature increases due to faster reaction rates. In the following, these results will be used to study the kinetics of the reaction and to compare with X-ray diffraction results.

4.4. Extended-Range Environment (Crystalline Structure): HRPD

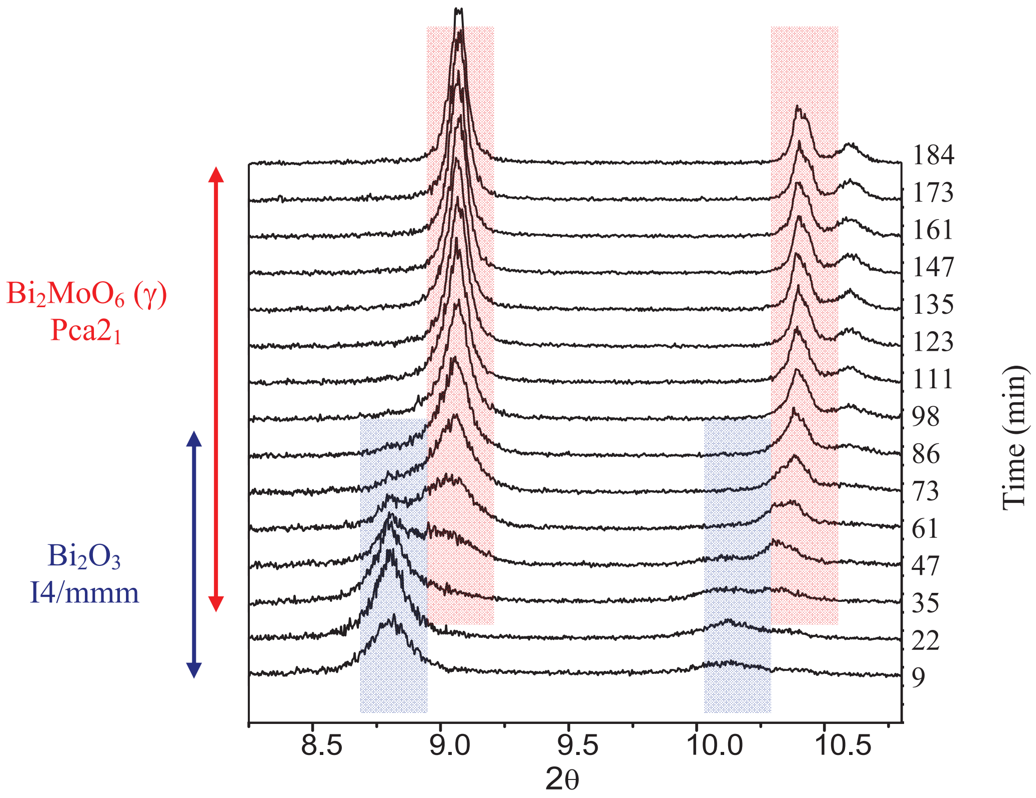

Fig. 2.26 *In-situ* XRD patterns collected during the hydrothermal synthesis of γ-Bi_2MoO_6 at 160°C (λ=0.5 Å).

By HRPD, a crystalline phase was observed from the first few minutes of the reaction. However, the γ-Bi_2MoO_6 started to grow only after 30 minutes of the reaction (Fig. 2.26). *Irrespective of the reaction temperature*, an intermediate phase was evidenced and two steps of phase formation appeared to take place. Unlike previous studies [8, 11] in which position sensitive detectors with poor angular resolution were used, the HRPD data obtained here are of very high quality. This high resolution enabled the use of XRD refinement by the *Rietveld method* to refine each pattern. However the complete structure refinement could not be achieved in these studies because of the short d-spacing range needed to obtain high spatial and time-resolution. Only the unit-cell parameters, the overall Debye-Waller parameter and the crystallite size were refined. The background of XRD refinement, including the *Rietveld* method and crystallite size calculation, was previously given in details (cf. Characterization techniques). The quantitative analysis was carried out as well, in order to study the kinetics of the crystal growth process.

4.4.1. Phase identification and XRD refinement by the Rietveld method

• *Fluorite structure of Bi_2O_3*

The Fluorite structure of Bi_2O_3 was used to refine the initial HRPD data but a good fit was only obtained when the structure was compressed along the [001] direction. Indeed the first pattern, recorded at the initial stages of the reaction, could be indexed in a tetragonal unit cell with the following parameters: a = 4.0237(4) Å ($a_F = a*\sqrt{2}$ = 5.6904(4) Å in the cubic fluorite lattice) and c = 5.558(1) Å. The relationship between the distorted fluorite unit cell and the tetragonal unit cell is illustrated in Fig. 2.27. The refinement was finally performed in I 4/mmm space group with Bi in 2a (0, 0, 0) and O in 4d (0, ½, ¼) with an occupancy of 75% for the O site. Only bismuth was introduced in the 2a site although the presence of molybdenum in this site cannot be excluded.

Concerning the peak shape, a uniform broadening of Bragg peaks was observed, which is due to small crystallite sizes. An isotropic size model (or the simple Scherrer formula) was used to refine the Bi_2O_3 crystallite size and revealed that particles about 10 nm in size were present in the system. A good fit between the observed and the calculated data was obtained, as indicated in Fig. 2.28. After 40 minutes of reaction, the Bi_2O_3 phase gradually disappeared while γ-Bi_2MoO_6 reflections began to appear in the HRPD patterns. During the transformation, the intensity of the peaks corresponding to the distorted fluorite form of Bi_2O_3 decreases without change in unit-cell parameters. The presence of the γ-Bi_2MoO_6 phase only was observed after 120 minutes.

• *Structure of γ-Bi_2MoO_6*

The γ-Bi_2MoO_6 structure was refined using the structural model proposed by Theobald *et al.* [32]. Similar to the case of the Bi_2O_3 phase, only the unit-cell parameters, the overall Debye Waller parameter and crystallite sizes were refined. In contrast to Bi_2O_3 case, the FWHM of Bragg peaks of several reflections of γ-Bi_2MoO_6 appeared to vary, which was due to the anisotropic shape of crystallites. To take into account this broadening, a linear combination of spherical harmonics of the 4th order [15] was used together with the Scherrer formula. In good agreement with the layered structure, the refinement revealed a platelet shape for the γ-Bi_2MoO_6 crystallites. The observed, calculated and difference profiles are presented with the shape of γ-Bi_2MoO_6 crystallites in Fig. 2.29.

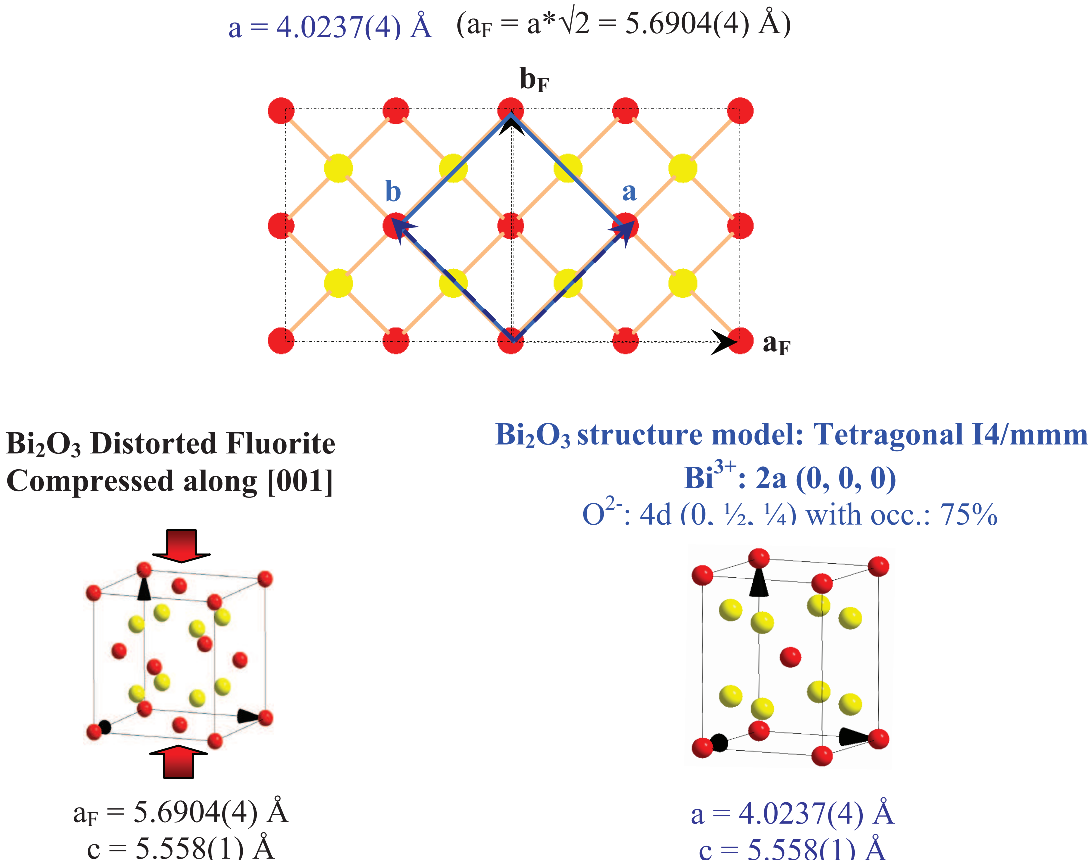

Fig. 2.27 Initial phase structure: Bi_2O_3 distorted fluorite structure

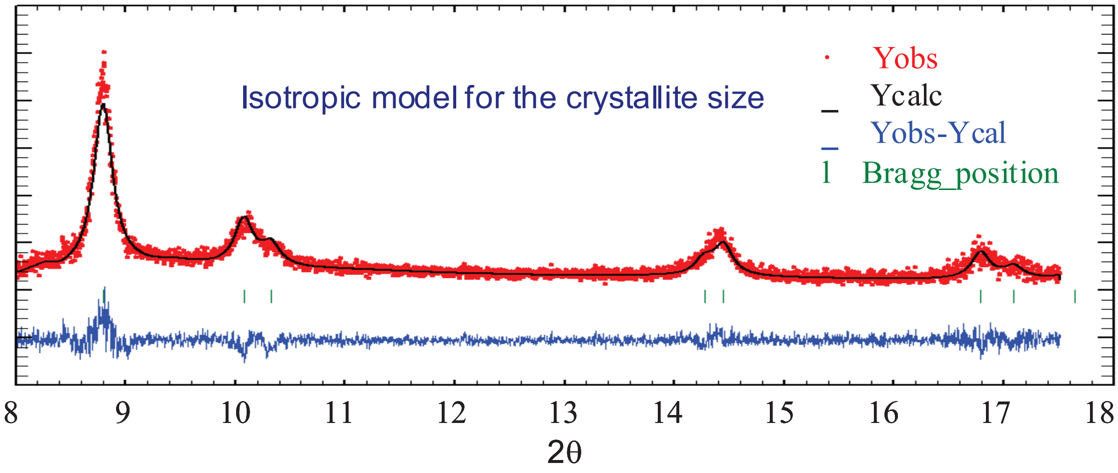

R_{Bragg}	R_F	R_p	R_{wp}	R_{exp}
5.61	3.79	30.5	35.1	40.13

Fig. 2.28 XRD refinement using isotropic model for crystallite size on XRD pattern collected at 160°C after 9 min of experiment, with background corrected agreement factors.

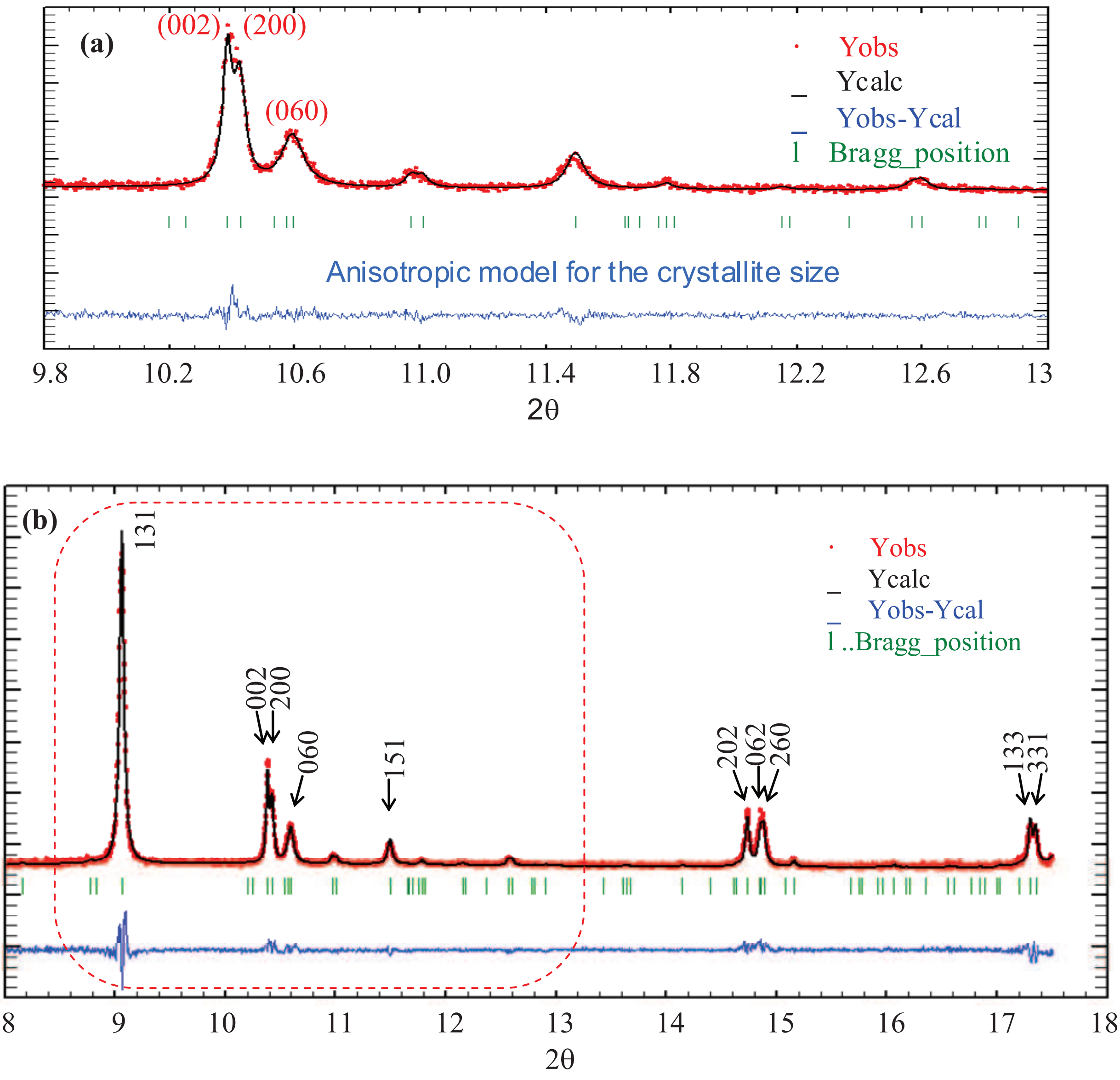

R_{Bragg}	R_F	R_p	R_{wp}	R_{exp}
5.40	6.18	22.0	31.7	28.78

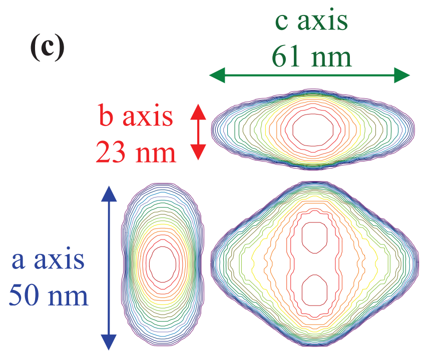

Fig. 2.29 XRD refinement using an anisotropic model for crystallite size from the XRD pattern collected at 160°C after 184 min of experiment, with background corrected agreement factors. a) A zoom of the XRD pattern in the range of 9.8-13°. b) XRD patterns in the angle range studied with the agreement factors. c) A model of crystallite morphology obtained.

Table 2.3 The *Rietveld* refinement results of XRD patterns collected 160°C

temps	Bi_2O_3				Bi_2MoO_6				
	Cell parameters (Å)			$B_{overall}$	Cell parameters (Å)				$B_{overall}$
	a	a_F	c		a	b	b_F	c	
9.00	4.0237(4)	5.6904(4)	5.558(1)	12.4(2)	-	-	-	-	-
22.30	4.0177(4)	5.6819(4)	5.5711(8)	12.6(3)	-	-	-	-	-
35.22	4.0185(4)	5.6830(4)	5.565(1)	13.6(4)	5.538(4)	16.268	5.423	5.592(4)	7(1)
47.18	4.0185	5.6830	5.565	11.6(6)	5.542(1)	16.268	5.423	5.577(1)	9.9(4)
60.78	4.0185	5.6830	5.565	19(2)	5.5269(6)	16.268(4)	5.423(1)	5.5692(7)	9.2(3)
72.67	4.0185	5.6830	5.565	19	5.5191(6)	16.259(4)	5.420(1)	5.5497(8)	9.3(3)
85.88	4.0185	5.6830	5.565	19	5.5139(4)	16.258(2)	5.4194(6)	5.5380(5)	8.6(2)
97.78	4.0185	5.6830	5.565	19	5.5094(4)	16.249(1)	5.4164(5)	5.5291(4)	8.3(2)
110.67	4.0185	5.6830	5.565	19	5.5083(3)	16.255(1)	5.4184(5)	5.5290(3)	8.1(2)
122.53	-		-	-	5.5050(3)	16.247(1)	5.4157(4)	5.5249(2)	8.3(2)
135.42	-		-	-	5.5057(2)	16.2551(9)	5.4184(3)	5.5261(2)	8.5(2)
147.37	-		-	-	5.5031(2)	16.2489(8)	5.4163(3)	5.5237(2)	8.7(2)
160.73	-		-	-	5.5047(2)	16.2543(9)	5.4181(3)	5.5246(2)	8.4(2)
172.62	-		-	-	5.5024(2)	16.2461(8)	5.4154(3)	5.5226(2)	8.6(2)
184.47	-		-	-	5.5036(2)	16.2496(6)	5.4165(3)	5.5246(1)	8.8(2)

Time (min)	Bi_2O_3		Bi_2MoO_6			
	Concentration (mol%)	Size (nm)	Concentration (mol%)	Size (nm)		
				(002)	(200)	(060)
9.00	100	9.1	0	-	-	-
22.30	100	12.9	0	-	-	-
35.22	89(3)	12	11(2)	16.4	16.0	4.4
47.18	37(1)	13.1	63(3)	16.4	16.0	4.4
60.78	25(2)	14.3	75(3)	18.0	22.3	5.7
72.67	10.0(8)	14.3	90(3)	18.5	25.3	6.6
85.88	7.0(6)	14.3	93(2)	24.6	26.5	9.0
97.78	4.1(5)	14.3	96(3)	32.5	28.9	11.8
110.67	1.7(5)	14.3	98(3)	39.2	32.9	14.3
122.53	0	-	100	44.8	34.5	16.8
135.42	0	-	100	50.0	36.7	18.7
147.37	0	-	100	50.9	39.8	20.2
160.73	0	-	100	50.5	39.7	19.9
172.62	0	-	100	53.2	41.8	22.5
184.47	0	-	100	61.3	49.8	23.1

Table 2.4 The *Rietveld* refinement results of XRD patterns collected 170°C

temps	Bi_2O_3				Bi_2MoO_6				
	Cell parameters (Å)			$B_{overall}$	Cell parameters (Å)				$B_{overall}$
	a	a_F	c		a	b	b_F	c	
14.00	4.0189(4)	5.6836(5)	5.5758(8)	12.4(3)	-	-	-	-	-
26.05	4.0152(4)	5.6783(6)	5.570(1)	13.1(3)	5.547(2)	16.276	5.425	5.580(3)	8.4
39.43	4.011(2)	5.672(2)	5.573(4)	17(1)	5.5298(9)	16.276(5)	5.425(2)	5.566(1)	8.4(3)
51.37	4.011	5.676	5.573	17	5.5175(6)	16.251(2)	5.4169(8)	5.5374(7)	9.4(2)
64.33	4.011	5.676	5.573	17	5.5093(4)	16.257(1)	5.4191(5)	5.5292(3)	9.1(2)
76.33	4.011	5.676	5.573	17	5.5050(3)	16.249(1)	5.4165(4)	5.5253(2)	9.0(2)
89.40	-	-	-	-	5.5050(3)	16.254(1)	5.4181(4)	5.5262(2)	8.6(3)
101.45	-	-	-	-	5.5034(2)	16.248(1)	5.4161(3)	5.5242(2)	8.3(2)
114.92	-	-	-	-	5.5042(2)	16.252(1)	5.4175(3)	5.5257(2)	8.8(2)
126.80	-	-	-	-	5.5026(2)	16.2462(9)	5.4154(3)	5.5228(2)	8.6(2)
139.98	-	-	-	-	5.5040(2)	16.2521(9)	5.4174(3)	5.5251(2)	8.4(2)
151.87	-	-	-	-	5.5018(2)	16.2443(9)	5.4148(3)	5.5228(2)	8.7(3)
164.85	-	-	-	-	5.5028(2)	16.2507(7)	5.4169(2)	5.5247(1)	8.9(2)
176.80	-	-	-	-	5.5011(2)	16.2426(7)	5.4142(2)	5.5228(1)	8.6(2)
189.63	-	-	-	-	5.5027(2)	16.2503(8)	5.4168(2)	5.5245(1)	9.2(2)

temps	Bi_2O_3		Bi_2MoO_6			
	Concentration (mol%)	Size (nm)	Concentration (mol%)	Size (nm)		
				(002)	(200)	(060)
14.00	100	12.8	0	-	-	-
26.05	84(2)	12.1	16.3(9)	18.6	19.4	5.2
39.43	32(2)	11.6	68(4)	18.6	19.4	5.2
51.37	8.5(6)	11.6	91(3)	21.6	26.5	8.6
64.33	4.4(5)	11.6	96(3)	38.5	28.4	14.1
76.33	0.9(5)	11.6	99(3)	51.9	36.0	16.9
89.40	0	-	100	51.9	36.9	19.4
101.45	0	-	100	51.0	41.7	21.7
114.92	0	-	100	60.9	44.4	22.2
126.80	0	-	100	60.0	43.9	23.8
139.98	0	-	100	60.4	48.9	24.1
151.87	0	-	100	68.6	49.4	24.8
164.85	0	-	100	63.3	51.5	27.3
176.80	0	-	100	65.5	52.2	26.5
189.63	0	-	100	71.5	54.1	27.6

Table 2.5 The *Rietveld* refinement results of XRD patterns collected 180°C

Time (min)	Bi_2O_3				Bi_2MoO_6				
	Cell parameters (Å)			$B_{overall}$	Cell parameters (Å)				$B_{overall}$
	a	a_F	c		a	b	b_F	c	
9.00	4.0206(4)	5.6860(6)	5.570(1)	11.8(2)	-	-	-	-	-
20.87	4.0164(4)	5.6801(6)	5.5708(9)	11.9(2)	5.524(6)	16.246	5.415	5.565(8)	8.9
33.78	4.016(2)	5.680(2)	5.554(5)	18(1)	5.5266(7)	16.246(4)	5.415(1)	5.5615(8)	8.9(3)
45.63	4.016	5.680	5.554	18	5.5099(4)	16.256(1)	5.4186(5)	5.5299(3)	9.4(2)
58.28	4.016	5.680	5.554	18	5.5069(2)	16.2536(8)	5.4179(3)	5.5281(1)	8.8(2)
70.18	-		-	-	5.5035(2)	16.2451(8)	5.4150(3)	5.5248(1)	8.7(2)
83.05	-		-	-	5.5047(2)	16.2517(7)	5.4172(2)	5.5261(1)	8.8(2)
94.90	-		-	-	5.5031(2)	16.2457(8)	5.4152(3)	5.5239(2)	9.0(2)
108.33	-		-	-	5.5040(2)	16.2511(7)	5.4171(2)	5.5259(1)	9.0(2)
124.82	-		-	-	5.5038(1)	16.2524(7)	5.4175(2)	5.5259(1)	8.7(2)
138.00	-		-	-	5.5019(2)	16.2450(7)	5.4150(2)	5.5237(1)	9.5(2)

Time (min)	Bi_2O_3		Bi_2MoO_6			
	Concentration (mol%)	Size (nm)	Concentration (mol%)	Size (nm)		
				(002)	(200)	(060)
9.00	100	9.7	0	-	-	-
20.87	95(2)	10.5	5.3(7)	18.1	19.1	6.3
33.78	29(2)	10.2	71(3)	18.1	19.1	6.3
45.63	4.1(6)	10.2	96(3)	39.6	29.3	12.8
58.28	0.4(5)	10.2	100(2)	56.6	40.4	19.3
70.18	0	-	100	60.9	44.8	24.1
83.05	0	-	100	67.6	48.1	25.6
94.90	0	-	100	68.7	50.4	26.3
108.33	0	-	100	69.0	53.5	27.7
124.82	0	-	100	69.0	55.7	29.5
138.00	0	-	100	81.1	59.1	32.9

The XRD refinements were carried out for all XRD patterns collected at 160, 170 and 180°C. The refined unit-cell parameters, overall Debye Waller parameter and crystallite size are given in Table 2.3, 2.4, 2.5, respectively. The evolution of crystallite size and morphology with time was derived from these *Rietveld* refinement results. Between *ca.* 120 and 180 minutes of reaction, the aspect-ratio remains the same although growth in all the directions appears to take place, which suggests that the morphology is not altered during the growth process.

4.4.2. Kinetics of the crystallization process of γ-Bi_2MoO_6

According to the previous discussion, an intermediate phase is formed during the reaction and γ-Bi_2MoO_6 exhibits a highly anisotropic morphology. It is therefore important to perform a kinetic analysis that would, afterwards, help to optimize the condition of production of γ-Bi_2MoO_6 catalyst and to control the crystal growth: its size, shape and morphology.

In previous studies followed by *in-situ* EDXRD measurements at 110-150°C [8, 10, 11], it was claimed that at 120°C there was no favoured direction of crystallization by noticing the simultaneous growth of all main reflections of γ-Bi_2MoO_6. In contrast to other temperatures, a two-dimensional growth crystallization mechanism was later found which is diffusion-controlled and has a decreasing rate of nucleation. It is worth noting that these reactions follow an isokinetic process by which the reaction mechanism does not change within the temperature range study. However, these experiments revealed neither the existence of the intermediate phase nor the occurrence of a phase transformation during the reaction.

As we found that an intermediate phase crystallized at 160-180°C; it is obvious that the reaction exhibits a different reaction mechanism which has to be studied. However, the information obtained from HRPD with a time resolution of 7 min, would not give enough detailed and accurate kinetic analysis compared to EDXRD technique. To overcome this limitation, the quantitative results obtained previously from LCF analysis of Raman spectra with an acquisition time of 2 minutes will be employed. According to our knowledge, Raman technique is rarely used for studying the isothermal crystallization kinetics. However, Feth *et* *al*. [57] have recently demonstrated that the recrystallization process of amorphous Ciclesonide can be detected and quantified by the hot-stage Raman microscopy.

Since the Raman bands account not only for the crystalline phase but also those of the amorphous phase, the use of quantitative Raman spectroscopy for the investigation of such phenomena should be therefore considered with care. In our case, the use of Raman technique will be fulfilled only if:

- The crystallization of Bi_2MoO_6 is a direct transformation from Bi_2O_3 to Bi_2MoO_6.
- The change in the Mo environment is a direct transformation from perturbed MoO_4^{2-} tetrahedral species to MoO_6 octahedra in γ-Bi_2MoO_6.
- The consumption rates of perturbed MoO_4^{2-} tetrahedral species are equivalent to those of Bi_2O_3.

To justify these assumptions, the evolution of MoO_6 species obtained from XANES and Raman scattering was compared with the evolution of γ-Bi_2MoO_6 obtained from XRD at all temperatures: 160°C, 170°C and 180°C.

• ***Quantitative Analysis of XRD data***

The quantification of Bi_2O_3 and Bi_2MoO_6 compositions was achieved through XRD refinement by using Fullprof program. The composition obtained from Fullprof program is usually given in weight fraction. The Bi_2O_3 and Bi_2MoO_6 compositions has to be changed from weight fraction to molar fraction, in order to compare these results to those obtained from XANES and Raman scattering techniques. The molar fraction values of Bi_2O_3 and Bi_2MoO_6 for the reaction at 160, 170 and 180°C are given in Table 2.3, 2.4 and 2.5, respectively and plotted in Fig. 2.30 a) against time.

The curves in Fig. 2.30 a) confirmed a direct transformation of Bi_2O_3 (intermediate phase) to γ-Bi_2MoO_6 via a solid-solid transformation.

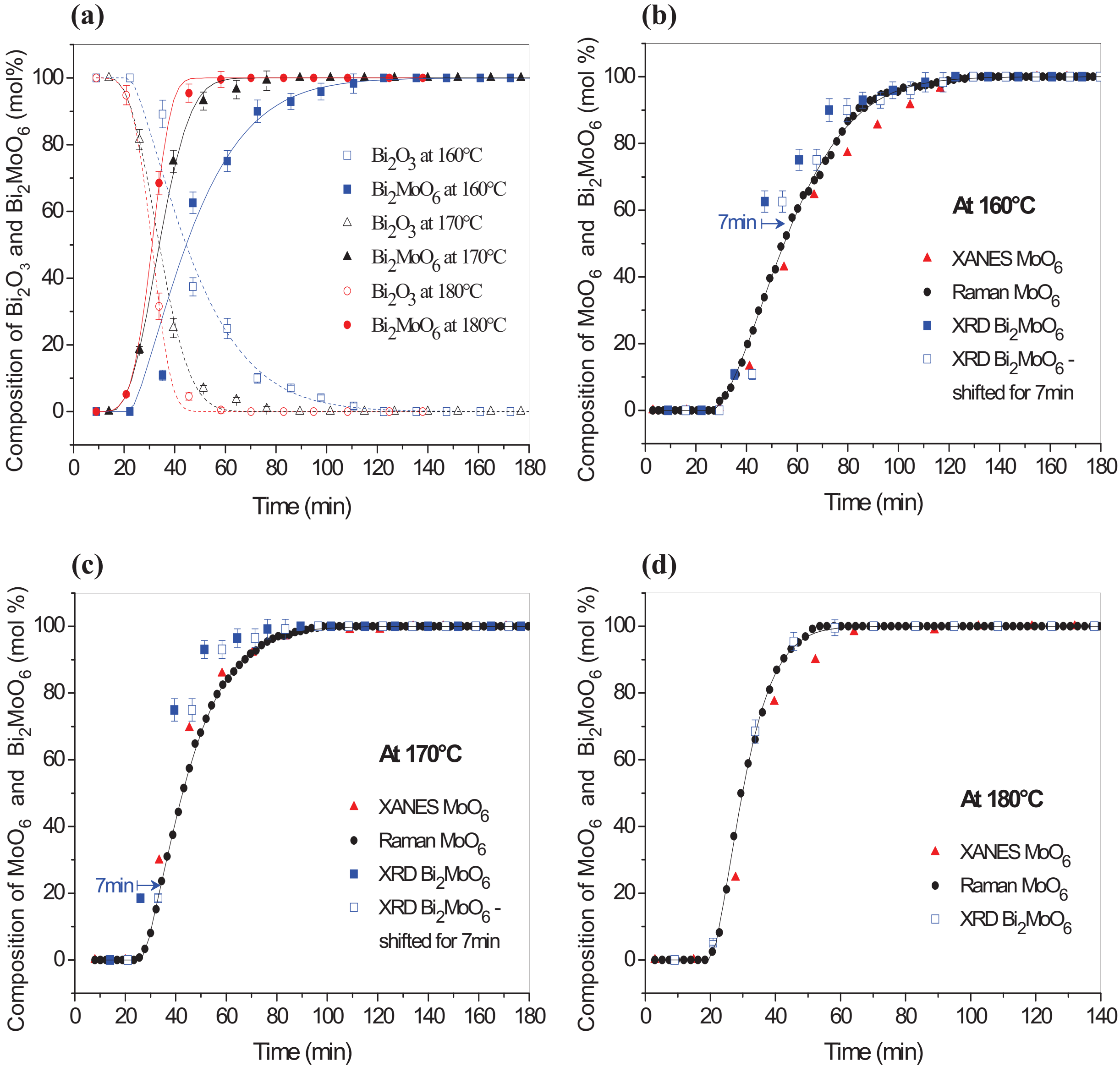

Fig. 2.30 a) XRD monitoring the evolution of Bi_2O_3 and Bi_2MoO_6 contents during the reaction at 160°C (□,■), 170°C (△,▲) and 180°C (○,●). Evolution of MoO_6 obtained from XANES (▲) and Raman scattering (●) and Bi_2MoO_6 obtained from XRD (□,■) at 160°C (b), 170°C (c) and 180°C (d).

The sigmoidal curves of Bi_2MoO_6 contents are typical of a crystallization process consisting of (i) an initial induction time (t_{ind}) followed by (ii) a slow growth of initial nuclei before (iii) a rapid transformation into Bi_2MoO_6 particles until all of the reactant is consumed. The growth of Bi_2MoO_6 at 160, 170 and 180°C takes about 100, 75 and 60 min, respectively to reach completion (Fig. 2.30 a). It is clear that the rate of crystallization increases with temperature. However, it is difficult to determine the induction time from these HRPD data because the collection time is too long (about 7 min and every 13 min) which would lead to a significant error.

In order to have better statistical data, the evolution of Bi_2MoO_6 contents obtained from XRD was compared with the MoO_6 composition obtained from XANES and Raman scattering for the reaction at 160, 170 and 180°C in Fig 2.30 b), c) and d), respectively. Interestingly, a good correlation of transformation kinetics was observed at 180°C. At 160 and 170°C, it appears that the rate of MoO_6 transformations is the same as that of γ-Bi_2MoO_6 but with a delay time of about 7 min. This might be due to the long collection time of HRPD. Despite of this uncertain induction time, and since the formation rate of MoO_6 obtained from Raman scattering is comparable to that of γ-Bi_2MoO_6 obtained from XRD, the former results can consequently be used to determine the mechanisms of crystallization process of γ-Bi_2MoO_6.

• ***Kinetic evaluation of the formation of γ-Bi_2MoO_6***

The Johnson-Mehl-Avrami kinetic model was employed to obtain information about the isothermal crystallization kinetics of γ-Bi_2MoO_6 at different temperatures. This nucleation and growth approximation was simultaneously proposed by Johnson and Mehl [58], and by Avrami [59, 60, 61], and later by Erofe'ev [62]. They assumed that the germ nuclei necessary for the transformation to a new phase are already present in the initial phase. Generally these nuclei are generated at certain heterogeneities in the initial phase and their number can be altered by temperature and duration of reaction. When the internal free energy of the new phase is lower than in the initial phase, a cluster of the new phase, called germ nuclei, is created. These may consist of foreign particles with an adsorbed layer of the newly forming phase or tiny crystals of the new phase. It is proposed that (i) some of these nuclei become active growth nuclei for grains of the new phase, or (ii) others are ingested by these growing nuclei, or (iii) they dissolve back into the old phase. These growth nuclei continue to grow until all the old phase is consumed.

The Johnson-Melh-Avrami equation is represented in Eq. 2.17. This model has been used for analyzing a variety of solid-state process such as phase transitions [63, 64, 65], phase transformations of Aurivillius phases [66, 67] as well as crystallization under hydrothermal conditions of bismuth molybdate catalysts [10, 11], zeolites [68, 69, 70] and nano materials [71, 72].

$$\alpha = 1 - \exp[-(kt)^n] \qquad (2.17)$$

The extent of reaction (α) is the extensive quantity describing the progress of a chemical reaction corresponding to the number of chemical transformations. The extent of reaction (α) in time (t) is related to the rate constant (*k*) and the Avrami exponent (*n*). It is worth noting that time (t) in these equations refers to the time after a period of induction (t_{ind}). In our case, the extent of reaction (α) for each temperature was achieved through the normalization of the γ-Bi_2MoO_6 contents monitored by *in-situ* Raman spectroscopy. Their values were then plotted against the reaction time in Fig. 2.31.

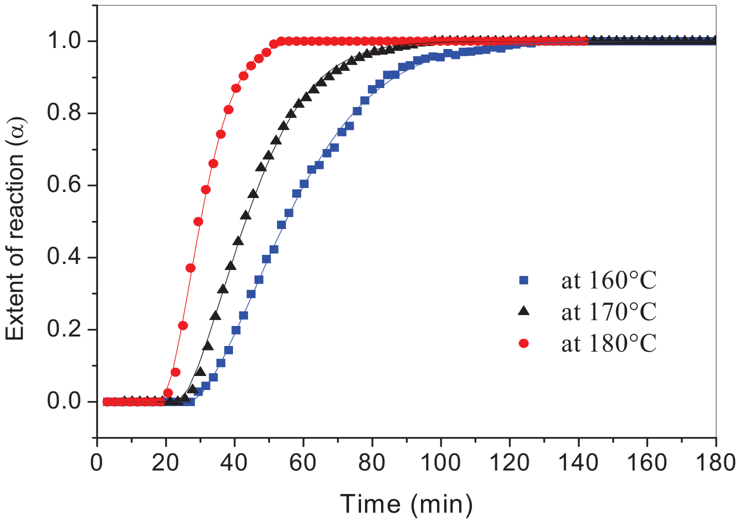

Fig. 2.31 Crystallization curves of γ-Bi_2MoO_6 monitored by *in-situ* Raman spectroscopy at 160, 170 and 180°C.

Once the Avrami exponent value is known, it is possible to establish the mechanism of crystallization process of these reactions. However, the determination and interpretation of the Avrami exponent are delicate in several situations, e.g., when the reaction mechanism changes during the course of the reaction, when it is different according to different experimental conditions, when the zero time is difficult to establish or when the reaction is controlled by heat transfer phenomena, etc.

To partly overcome these difficulties, a mathematical approach proposed by Sharp *et al.* [73] was employed for kinetic analysis as well. This method assumes that the Johnson-Melh-Avrami equation (Eq. 2.17) can be expressed in Eq. 2.18.

$$\ln[-\ln(1-\alpha)] = n\ln k + n\ln t \tag{2.18}$$

Using a reduced-time scale, the Sharp-Hancock plots give rise to approximately linear plots of ln [- ln (1 - α)] against ln *t*, giving slopes corresponding to the exponent (n) values. The Sharp-Hancock analysis was performed for α values from 0.15 to 0.80, because the results obtained from the three different techniques (XRD, XANES and Raman spectroscopy), are the most convincing and coherent in this range of α. Moreover, deviations in the initial and the final periods of reaction can affect the results.

The resulting Sharp-Hancock plots for γ-Bi_2MoO_6 at various temperatures are presented in Fig. 2.32. Three linear Sharp-Hancock plots confirm that these reactions can be represented by a nuclei growth model. It appears that the reaction mechanism did not change in the α range study, as shown by a straight line obtained for reaction at each temperature. The derived rate constants (*k*) and Avrami exponents (*n*) are given in Table 2.6. These values are in the same range than those obtained by Beale *et al.* [8, 10, 11] for the same system but at lower temperatures, from 110 to 150°C. However, the Avrami exponent values obtained in the present work are between 1.5 and 1.8, are slightly higher than 0.97-1.19 obtained in the previous study.

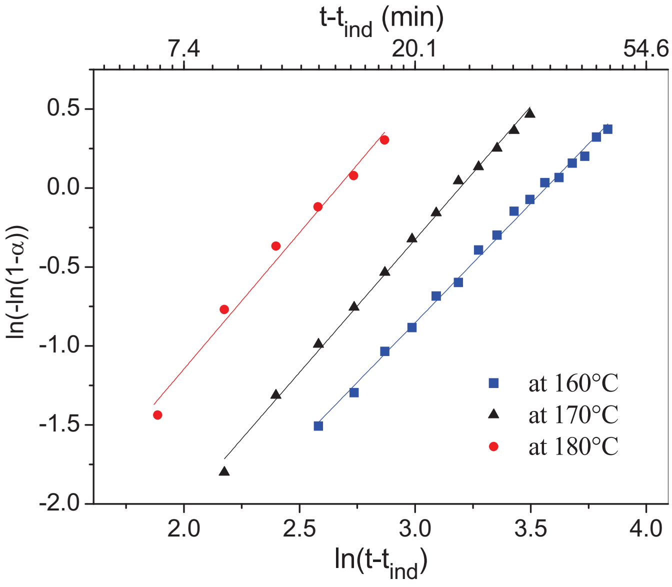

Fig. 2.32 Sharp-Hancock plots for the data recoded at various temperatures: 160, 170 and 180°C over the data range of $0.15 < \alpha < 0.80$.

Table 2.6 Avrami exponents (n) and rates of crystallization (k) as derived from Sharp-Hancock analysis in Fig. 2.32.

Temperature (°C)	n	k (min^{-1})	R^2 factors
160	1.51	0.0283	0.9966
170	1.68	0.0410	0.9969
180	1.73	0.0697	0.9859

According to the analysis of Hulbert [74], the difference in the exponent values corresponds to different growth mechanisms. He proposed the mathematical models derived from the Johnson-Melh-Avrami equation which can be all expressed in Eq. 2.18 for nuclei growth models with various boundary conditions (phase-boundary controlled or diffusion controlled). Table 2.7 summarizes the values of *n*, which can be obtained for different growth mechanisms.

Table 2.7 Summary of nuclei growth models with the corresponding *n* values [74].

	Phase-boundary controlled	Diffusion controlled
Three-dimensional growth		
- Constant nucleation rate	4	2.5
- Zero nucleation rate	3	1.5
- Decreasing nucleation rate	3-4	1.5-2.5
Two-dimensional growth		
- Constant nucleation rate	3	2
- Zero nucleation rate	2	1
- Decreasing nucleation rate	2-3	1-2
One-dimensional growth		
- Constant nucleation rate	2	1.5
- Zero nucleation rate	1	0.5
- Decreasing nucleation rate	1-2	0.5-1.5

It is worth noting that only three cases of nucleation rate are considered here. The nucleation rate is either zero, or constant, or it is a maximum at the beginning of the transformation and decreases during the course of the reaction.

With the Avrami exponent values *n* obtained between 1.5 and 1.8 (Table 2.6), various crystallization mechanisms with a decreasing nucleation rate are all possible: 1D-growth with a phase-boundary control, 2D- or 3D- growths with a diffusion control are all possible. It is clear that considering only the Avrami exponent value is not enough to determine the growth mechanism in this case. Thereby, other information should be considered.

According to the previous results from XRD refinement, it is revealed that the γ-Bi_2MoO_6 crystallites grow anisotropically, forming the platelet-shaped crystallites during the course of the reaction. So we are convinced that the growth mechanism of γ-Bi_2MoO_6 at 160-180°C should be a 2D-growth process which is diffusion-controlled and has a decreasing rate of nucleation. This mechanism is similar to the one proposed for lower temperatures reported by Beale *et al* [8, 10, 11], but with a higher rate of nucleation. The increase of the nucleation rate with temperature is commonly observed for ceramics [65] and glasses in certain range of temperatures [75].

The 2D-growth process of γ-Bi_2MoO_6 is believed to be strongly related to its layered Aurivillius-type structure consisting of $[Bi_2O_2]^{2+}$ layers alternated with layers of corner-sharing MoO_6 octahedra. This could be explained by Gibbs-Curie-Wulf theorem [76], stating that the shape of a crystal is determined by the relative specific surface energy of each facet of the crystal. It is suggested that, under equilibrium condition, the crystallographic plane with the highest density of atoms (along the *a* and *c* axes), has the lowest interfacial energy, and that the minimum growth rate is in the direction normal to the plane.

However, the growth process of a crystal can be influenced by other factors as well, such as the method of preparation or the chemical potential environment in the solution [77], etc. It is thus possible to obtain the particles of Aurivillius phase in other forms such as elongated grains [78] or rod-like form [66] for other conditions of reaction.

4.4.3. Hypothesis on the formation of γ-Bi_2MoO_6

In the previous section, the crystallization mechanism of γ-Bi_2MoO_6 under hydrothermal synthesis was shown to be strongly influenced by its structure. In this section we attempt to explain how this growth process occurs at the atomic scale with the help of the XRD refinement results.

The evolution of the cell parameters of Bi_2O_3 and Bi_2MoO_6 obtained previously from XRD refinement was plotted as a function of time at 160, 170 and 180°C in Fig. 2.33.

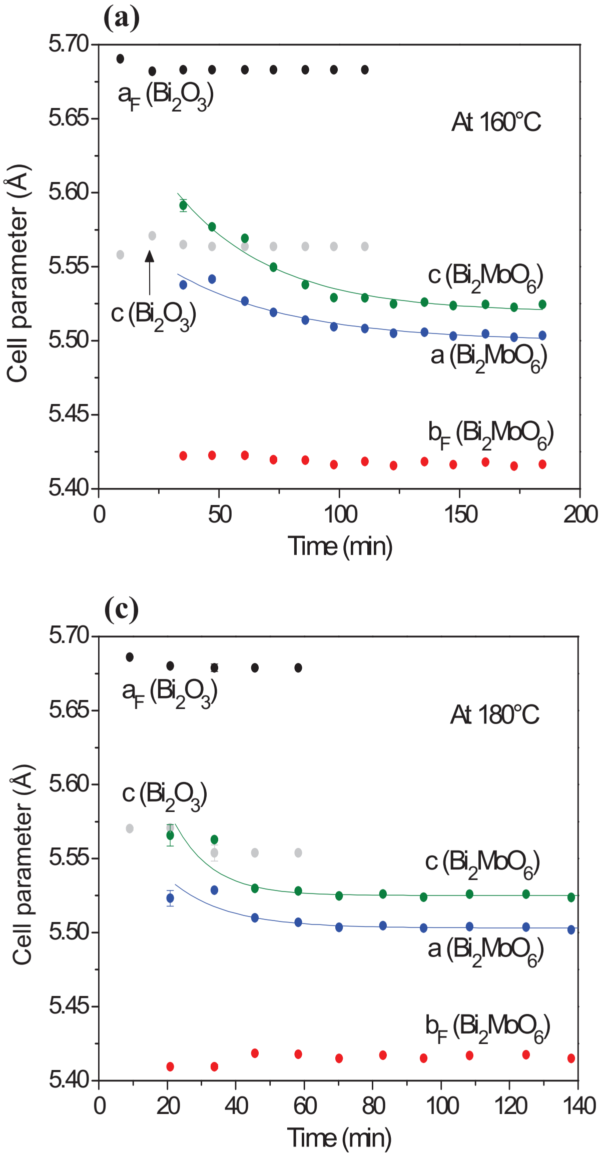

Fig. 2.33 Evolution of cell parameters of Bi_2MoO_6 and Bi_2O_3 during the hydrothermal synthesis of γ-Bi_2MoO_6 at 160°C (a), 170°C (b) and 180°C (c).

To allow a better comparison, the cell parameters of Bi_2O_3 and Bi_2MoO_6 were transformed to the fluorite unit cell parameters. As previously mentioned, the *a* cell parameter of Bi_2O_3 can be described as $a_F = a*\sqrt{2}$ in fluorite unit cell whereas the *b* cell parameter remains the same. Approximately, the γ-Bi_2MoO_6 structure can also be viewed as a stack of three fluorite-like unit cells along [010] direction. The *b* cell parameter of γ-Bi_2MoO_6 can thus be described as $b_F = b/3$ in fluorite unit cell while *a* and *c* cell parameters remain the same.

According to the evolution of cell parameters during the reaction, in the intermediate domain in which the two phases coexist, the refined *a* and *c* parameters of the Bi_2MoO_6 phase strongly decrease during the crystallization process as shown by the shift of the main Bragg peaks towards higher 2θ angles in Fig. 2.34.

It is worth noting that if we extrapolate these *a* and *c* unit cell parameters, they converge to those of the distorted fluorite Bi_2O_3. Moreover these two parameters correspond to the *bismuth oxide layers* of the Bi_2MoO_6 structure which suggests the possible growth of γ-Bi_2MoO_6 crystallites from the initial Bi_2O_3 particles. In addition, the accuracy in the b parameter was very poor at the first moment of the formation of Bi_2MoO_6. The lack of intensity in the 0k0 reflections could be due to a very small platelet thickness along [010] or to the disorder in the stacking of layers along [010] direction. This idea is also supported by a remarkable correlation between the reflection planes of Bi_2O_3 and those of γ-Bi_2MoO_6 presented in Fig. 2.34.

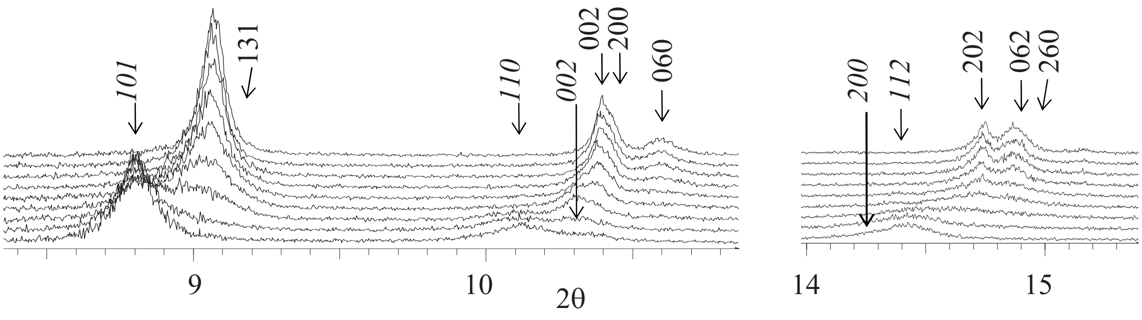

Fig. 2.34 XRD patterns collected during the hydrothermal synthesis of γ-Bi_2MoO_6 at 160°C (λ=0.5 Å). Peaks are indexed in a *tetragonal unit cell* (a = 4.0 Å. c = 5.55 Å) and an orthorhombic unit cell (a = 5.50 Å. b= 16.24 Å. c= 5.52 Å) for the *initial* Bi_2O_3 and the final γ-Bi_2MoO_6 forms, respectively.

Since Bi_2O_3 and γ-Bi_2MoO_6 structures can be described as a distorted fluorite and a stack of three fluorite-like structures, it was thus possible to relate the reflection planes of these two structures to those of fluorite unit cell. The relation between the reflection planes of Bi_2O_3 and γ-Bi_2MoO_6 is demonstrated in Fig. 2.35 and in Table 2.8. It seems justified, therefore, to assume that γ-Bi_2MoO_6 forms from the initial Bi_2O_3 crystallites while tetrahedral Mo(VI) undergoes modification.

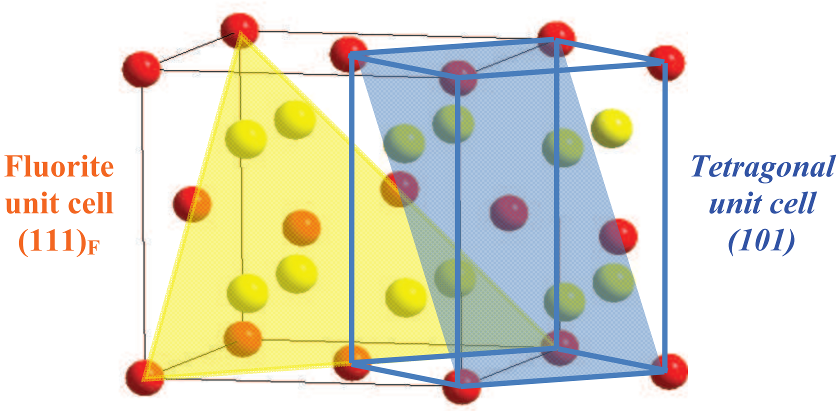

Fig. 2.35 An example of correlation between the tetragonal *(101)* plane of Bi_2O_3 and the cubic $(111)_F$ plane of a fluorite unit cell.

Table 2.8 The correlation between reflection planes of Bi_2O_3 and γ-Bi_2MoO_6.

Bi_2O_3 *Tetragonal (I4/mmm)*	Fluorite unit cell Cubic (Fm3m)	γ-Bi_2MoO_6 Orthorhombic ($Pca2_1$)
(101)	$(111)_F$	(131)
(110) / (002)	$(200)_F$ / $(020)_F$ / $(002)_F$	(002) / (200) / (060)
(200) / (112)	$(220)_F$ / $(022)_F$ / $(202)_F$	(202) / (062) / (260)

5. CONCLUSIONS

In summary, from XANES and Raman scattering, isolated tetrahedral molybdenum species, MoO_4, were evidenced in the initial stage of the synthesis. In this first step, Raman scattering revealed the perturbation of MoO_4 species before converting to a distorted octahedron, an evolution which was not shown by XANES. Simultaneously to the appearance of octahedral species, the γ-Bi_2MoO_6 structure started to grow. Although it was not possible with the current data to accurately define the atomic architecture of the initial and intermediate phases, it was possible to propose that a distorted fluorite structure acts as a skeleton for the conversion to the two-dimensional γ-Bi_2MoO_6 Aurivillius type structure. From XRD data, at the temperature range studied here (160-180°C), the crystal growth of γ-Bi_2MoO_6 occurs in two steps: spherical Bi_2O_3 particles, 10 nm in diameter first form before the growth of highly anisotropic γ-Bi_2MoO_6 platelets from these particles.

The ratio of MoO_4 and MoO_6 species during the reaction was quantified by XANES, its evolution was similar to the ratio of Bi_2O_3 and γ-Bi_2MoO_6 phases during the reaction. Moreover, a better resolution in time was obtained with Raman data of which the quantification was performed by a linear combination of reference spectra. From these data, it is shown that a diffusion-controlled 2D growth process occurs from the Bi_2O_3 particles. Therefore, the reaction occurs in two steps through the formation of Bi_2O_3 particles in the initial stages, and the growth of highly anisotropic platelets in a second step. It is inferred that Bi_2O_3 particles are involved in the crystal growth process and this result could be of first importance for its catalytic activity. However, one can not exclude the possible presence of molybdenum in the initial Bi_2O_3 form, in which case it would be in a tetrahedral coordination. In order to fully understand the formation of catalyst particles, *ex-situ* characterizations were performed and will be detailed in the next chapter.

Therefore, this study has shown that the combination of XRD, XANES and Raman scattering *in-situ* techniques is a powerful tool for understanding the structural formations and transformations, which will further enable us to control the crystal growth of a crystalline catalytic material like γ-Bi_2MoO_6.

References

[1] J. F. Brazdil, D. D. Suresh, and R. K. Grasselli, *J. Catal.*, 1980, **66**, 347–367.

[2] Y. Moro-oka, *Appl. Catal. A*, 1999, **181**, 323–329.

[3] W. J. M. van Well, N. C. S. M. T. Le, S. Hoste, and P. Stoltze, *J. Mol. Catal. A: Chem.*, 2006, **256**, 1–8.

[4] R. P. Rastogi and A. K. Singh, *J. Solid State Chem.*, 1982, **42**, 136–148.

[5] P. A. Batist, J. F. H. Bouwens, and G. C. A. Schuit, *J. Catal.*, 1972, **25**, 1–11.

[6] M. T. Le, W. J. M. V. Well, I. V. Driessche, and S. Hoste, *Appl. Catal. A: Gen.*, 2004, **267**, 227–234.

[7] M. Yoshimura and S. Somiya, *Mat. Chem. and Phys.*, 1999, **61**, 1–8.

[8] A. Beale and G. Sankar, *Nucl. Instr. and Meth. Phys. Res. B*, 2003, **199**, 504–508.

[9] H. Li, K. Li, and H. Wang, *Mat. Chem. and Phys.*, 2009, **116**, 134–142.

[10] A. M. Beale and G. Sankar, *Chem. Matter*, 2003, **15**, 146–153.

[11] A. M. Beale, L. M. Reuilly, and G. Sankar, *Appl. Catal. A: Gen.*, 2007, **325**, 290–295.

[12] H. Li, C. Liu, and K. Li, *J. Mater. Sci.*, 2008, **43**, 7026–7034.

[13] A. A. Eliseev, V. A. Efremmov, G. M. Kuzmicheva, E. S. Konovalova, V. I. Lazorenko, Y. B. Paderno, and S. Y. Khlyustova, *Kristallografiya*, 1986, **31**, 803–805.

[14] G. Caglioti, A. Paoletti, and F. Ricci, *Nucl. Instrum.*, 1958, **3**, 223–228.

[15] M. Järvinen, *J. Appl. Cryst.*, 1993, **26**, 525–531.

[16] W. Smith and G. Dent, *Modern Raman Spectroscopy - A Practical Approach*, Wiley, 2005.

[17] E. Boccaleri, F. Carniato, G. Croce, D. Viterbo, W. van Beek, H. Emerich, and M. Milanesio, *J .Appl.Cryst.*, 2007, **40**, 684–693.

[18] B. Ravel and M. Newville, *J. Synchrotron Rad.*, 2005, **12**, 537–541.

[19] M. Newville, *J. Synchrotron Rad.*, 2001, **8**, 322–324.

[20] J. Rodriguez-Carvajal, *Commission Powder Diff. Int. Union Cryst., Newsletter*, 2001, **26**, 12–19.

[21] P. Thompson, D. E. Cox, and J. B. Hastings, *J. Appl. Cryst.*, 1987, **20**, 79–83.

[22] G. A. Waychunas, *Am. Mineral.*, 1987, **72**, 89–101.

[23] J. Wong, F. W. Lytle, R. P. Messmer, and D. H. Mayotte, *Phys. Rev. B*, 1984, **30**, 5596–5610.

[24] M. Antonio, R. Teller, D. Sandstrom, M. Mehicic, and J. Brazdil, *J. Phys. Chem.*, 1988, **92**, 2939–2944.

[25] J. H. G. Bode, H. R. Kuijt, M. A. J. T. Lahey, and G. Blasse, *J. Solid State Chem.*, 1973, **8**, 114–119.

[26] J. . G. Thompson, S. Schmid, and R. L. Withers, *J. Solid State Chem.*, 1992, **101**, 309–321.

[27] P. R. Graves, G. Hua, S. Myhra, and J. G. Thompson, *J. Solid State Chem.*, 1995, **114**, 112–122.

[28] F. Hardcastle and I. Wachs, *J. Raman Spectrosc.*, 1990, **21**, 683–691.

[29] R. Murugan, R. Gangadharan, J. Kalaiselvi, S. Sukumar, B. Palanivel, and S. Mohan, *J. Phys.: Condens. Matter*, 2002, **14**, 4001–4010.

[30] I. Matsuura, R. Schut, and K. Hirakawa, *J. Catal.*, 1980, **63**, 152–166.

[31] K. Nakamoto, *Infrared and Raman spectra of Inorganic and Coordination compounds Part A*, Wiley, 2009.

[32] F. Theobald, A. Laarif, and A. W. Hewat, *Ferroelectrics*, 1984, **56**, 219–237.

[33] I. Nakagawa and J. Walter, *J. Chem. Phys.*, 1969, **51**, 1389–1397.

[34] F. Hardcastle and I. Wachs, *J. Solid State Chem.*, 1992, **97**, 319–331.

[35] N. Weinstock, H. Schulze, and A. Müller, *J. Chem. Phys.*, 1973, **59**, 5063–5067.

[36] T. T. Basiev, A. A. Sobol, Y. K. Voronko, and P. G. Zverev, *Opt. Mat.*, 2000, **15**, 205–216.

[37] M. K. Jeon, Y.-I. Kim, S.-H. Nahm, and S. Woo, *J. Phys. D: Appl. Phys.*, 2006, **39**, 5080–5085.

[38] J. P. Smit, H.-S. Kim, J. D. Pless, P. C. Stair, and K. R. Poeppelmeier, *Inorg. Chem.*, 2006, **45**, 521–528.

[39] T. Ressler, J. Wienold, R. Jentoft, and T. Neisius, *J. Catal.*, 2002, **210**, 67.

[40] A. M. Beale, M. T. Le, S. Hoste, and G. Sankar, *Solid State Sci.*, 2005, **7**, 1141–1148.

[41] N. Ohler and A. T. Bell, *J. Phys. Chem. B*, 2005, **109**, 23419–23429.

[42] J. A. Bergwerff, T. Visser, and B. M. Weckhuysen, *Catal. Today*, 2008, **130**, 117–125.

[43] K. A. Pokrovski and A. T. Bell, *J. Catal.*, 2006, **241**, 276–286.

[44] I. T. Vargas, M. A. Alsina, P. A. Pasten, and G. E. Pizarro, *Corrosion Sci.*, 2009, **51**, 1030–1037.

[45] D. G. Beak and R. T. Wilkin, *J. Contam. Hydrol.*, 2009, **106**, 15–28.

[46] C. G. Kontoyannis, *J. Pharm. Biomed. Anal.*, 1995, **13**, 73–76.

[47] P. Niemelä, M. Päällysaho, P. Harjunen, M. Koivisto, V.-P. Lehto, J. Suhonen, and K. Järvinen, *J. Pharm. Biomed. Anal.*, 2005, **37**, 907–911.

[48] N. V. Vagenas and C. G. Kontoyannis, *Vibr. Spectrosc.*, 2003, **32**, 261–264.

[49] G. Mestl, *J. Mol. Catal. A: Chem.*, 2000, **158**, 45–65.

[50] V. P. Zakaznova-Herzog, W. J. Malfait, F. Herzog, and W. E. Halter, *J. Non-Cryst Solids*, 2007, **353**, 4015–4028.

[51] M. Dieterle, G. Mestl, J. Jäger, Y. Uchida, H. Hibst, and R. Schlögl, *J. Mol. Catal. A: Chem.*, 2001, **174**, 169–185.

[52] R. B. Quincy, M. Houalla, and D. M. Hercules, *J. Catal.*, 1987, **106**, 85–92.

[53] J. P. Baltrus, L. E. Makovsky, J. M. Stencel, and D. M. Hercules, *Anal. Chem.*, 1985, **57**, 2500–2503.

[54] D. Strommen and K. Nakamoto, *Laboratory Raman Spectroscopy*, J. Wiley & Sons, New York, 1984.

[55] T. Sekiya, N. Mochida, and S. Ogawa, *J. Non-Cryst. Solids*, 1995, **185**, 135–144.

[56] I. The MathWorks.

[57] M. P. Feth, J. Volz, U. Hess, E. Sturm, and R.-P. Hummel, *J. Pharm. Sci.*, 2008, **97**, 3765–3780.

[58] W. A. Johnson and R. F. Mehl, *J. Trans. Am. Inst. Metall. Pet. Eng.*, 1939, **135**, 416–442.

[59] M. Avrami, *Kinetics of Phase Change. III. Granulation, Phase Change, and Microstructure*, 1941, **9**, 177–184.

[60] M. Avrami, *J. Chem. Phys.*, 1940, **8**, 212–224.

[61] M. Avrami, *J. Chem. Phys.*, 1939, **7**, 1103–1112.

[62] B. V. Erofe'ev, *C. R. (Dokl.) Acad. Sci. l'URSS*, 1946, **52**, 511–514.

[63] S. Ito, N. Umehara, H. Takata, and T. Fujii, *Solid State Ionics*, 2004, **172**, 403–406.

[64] C. Tomasi, M. Scavini, A. Cavicchioli, A. Speghini, and M. Bettinelli, *Thermochimica Acta*, 2005, **432**, 2–9.

[65] X. P. Wang, G. Corbel, S. Kodjikian, Q. F. Fang, and P. Lacorre, *J. Solid State Chem.*, 2006, **179**, 3338–3346.

[66] S.-Y. Jung, S.-J. Hwang, and Y.-M. Sung, *J. Cryst. Growth*, 2003, **254**, 92–99.

[67] H. Giefers, F. Porsch, and G. Wortmann, *Solid State Ionics*, 2005, **176**, 199–207.

[68] A. T. Davies, G. Sankar, C. R. A. Catlow, and S. M. Clark, *J. Phys. Chem. B*, 1997, **101**, 10115–10120.

[69] R. I. Walton, F. Milange, D. O'Hare, A. T. Davies, G. Sankar, and C. R. A. Catrow, *J. Phys. Chem. B*, 2001, **105**, 83–90.

[70] M. O'Brien, M. Sanchez-Sanchez, A. M. Beale, D. W. Lewis, G. Sankar, and C. Catlow, *J. Phys. Chem. C.*, 2007, **111**, 16951 – 16961.

[71] R. I. Walton, F. Millange, R. I. Smith, T. C. Hansen, and D. O'Hare, *J. Am. Chem. Soc.*, 2001, **123**, 12547–12555.

[72] R. Kiebach, N. Pienack, W. Bensch, J.-D. Grunwaldt, A. Michailovski, A. Baiker, T. Fox, Y. Zhou, and G. R. Patzke, *Chem. Mater.*, 2008, **20**, 3022–3033.

[73] J. D. Hancock and J. H. Sharp, *J. Am. Cer. Soc.*, 1972, **55**, 74–77.

[74] S. F. Hulbert, *J. Brit. Ceram. Soc.*, 1969, **6**, 11–20.

[75] K. Matusita, T. Komatsu, and R. Yokota, *J. Mater. Sci.*, 1984, **19**, 291–296.

[76] ed. I. Sunagawa, *Morphology of crystals Part A*, Terra Scientific and D. Reidel, 1987.

[77] Z. A. Peng and X. Peng, *J. Am. Chem. Soc.*, 2002, **124**, 3343–3353.

[78] P. Duran, F. Capel, C. Moure, M. Villegas, J. F. Fernandez, J. Tartaj, and A. C. Caballero, *J. Europ. Ceram. Soc.*, 2001, **21**, 1–8.

CHAPTER 3

Ex-Situ Study of γ-Bi_2MoO_6 Hydrothermal Synthesis

SUMMARY OF CHAPTER 3

Chapter 3

Ex-Situ Study of γ-Bi_2MoO_6 Hydrothermal Synthesis

1. INTRODUCTION

In the preceding chapter dealing with the *in-situ* study of the hydrothermal conditions of γ-Bi_2MoO_6, it has been clearly shown that crystals of γ-Bi_2MoO_6 are nucleated from an intermediate distorted fluorite structure related to Bi_2O_3. However, at this stage, some points remain uncertain. What is the exact composition of the intermediate form? Does it contain any molybdenum in the structure? In addition, one wonders how the pH of the initial mixture affects the Mo local environment, as well as how the grain morphology is in accordance or not with the X-ray study. Aiming to fully understand the crystal growth of the γ-Bi_2MoO_6 catalyst, this study was completed by a study of pH effect upon the hydrothermal synthesis of γ-Bi_2MoO_6 and an *ex-situ* study of the solid formation at 180°C. The solid formed at different times of reaction was characterized by XRD, Scanning electron microscopy (SEM), Energy dispersive X-ray spectroscopy (EDS), Transmission electron microscopy (TEM) and Raman scattering.

2. COMMON CHARACTERIZATION TECHNIQUES

2.1. Powder X-ray diffraction (XRD)

Room temperature XRD powder diffraction patterns were collected with a Bruker AXS D8 advance diffractometer equipped with a SolX energy dispersive detector in the 5° – 80° range with a step of 0.02° and a counting time of 2 sec per step, using CuKα radiation ($\lambda_{K\alpha 1}$ = 1.5406 Å).

High temperature X-ray diffraction patterns were performed on a Siemens Bruker D8 diffractometer equipped with an Anton Paar HTK 1200N high temperature chamber and a one dimensional detector (Vantec-1). The sample was placed on a Pt foil. The experiments were performed from room temperature to 800°C with a heating rate of 0.05°C/s and a diffractogram was recorded every 25°C, in the 10° – 70° range in 2θ, with a step of 0.015° and a counting time of 0.2 sec per step.

2.2. Raman Scattering

Room temperature Raman spectra were recorded with the 647.1 nm excitation line from a Spectra Physics krypton ion laser. All spectra were collected at a very low laser power (3 mW at the sample). The beam was focused on the samples using the macroscopic configuration. The scattered light was analyzed with an XY Raman Dilor spectrometer equipped with an optical multichannel detector (liquid nitrogen-cooled charge coupled device). In the investigated 15-1200 cm^{-1} range, the spectral resolution was approximately 0.5 cm^{-1}.

High temperature Raman spectroscopy was performed on the same spectrometer equipped with a CCR1000 catalyst cell reactor distributed by Linkam Scientific Instruments Ltd, using the microscopic configuration. The sample was introduced in an alumina crucible, and deposited on an alumina/silica fabric filter for heating up to 800°C.

2.3. Scanning Electron Microscopy – Energy Dispersive X-Ray Spectroscopy Analyses (SEM - EDS)

In general, Scanning Electron Microscopy and Energy dispersive X-Ray Spectroscopy are based on the irradiation of a focalized electron beam on the surface of the sample. When the electron beam interacts with the material, several physical processes occur: secondary electrons, backscattered electrons and X-ray emissions, giving different informations:

- The secondary electrons are ejected from the specimen atoms by inelastic scattering interactions with the primary electron beam. Due to their low energy (~100eV), these secondary electrons are only emitted from a few nanometers from the sample surface. Since these electrons are sensitive to the variation on the surface, they give information on the surface topography.

- Backscattered electrons are high-energy electrons originated from the primary electrons that are backscattered from the sample by elastic scattering process. In contrast to the secondary electrons, the backscattered electrons are emitted from a few micrometers form the sample surface and are sensitive to the atomic number of element. As the heavy elements backscatter electrons more strongly than light elements, the contrast between areas in the backscattered electron images can be used to discriminate between different chemical compositions.

- Characteristic X-rays are emitted when the impact of the incident electron removes an inner shell electron from the sample, causing a higher energy electron to fill the shell and to release the energy. These emitted X-rays are usually detected by means of an energy dispersive detection. The technique is called Energy Dispersive Spectroscopy (EDS). The energy and intensity of the emitted X-rays are used to determine the composition and the abundance of elements in the sample.

In the present work, SEM-EDS were used to examine microstructural features (grains, grain boundaries) and chemical compositions of the samples. The analysis was performed on a Hitachi S4700 electron microscope.

2.4. Transmission Electron Microscopy (TEM)

Transmission Electron Microscopy (TEM) was carried out on a Philips CM30 microscope. The microstructural features were studied at the nanoscale.

2.5. Thermogravimetric (TG)/ Differential Thermal (DT) combined analysis

TG/DT combined analysis was carried out using a SETARAM 92-1600 instrument. The sample was placed in a platinum crucible which was heated at a heating/cooling rate of 5°C/mn under air flow.

3. INFLUENCE OF PH DURING HYDROTHERMAL SYNTHESIS

It is known that the pH, the concentration or the metallate type precursor in solution may affect the spatial element distribution in the solid catalyst precursor by way of the formation of various polyoxometallates.

3.1. Literature reviews

3.1.1. Influence of pH

The synthesis of bismuth molybdenum oxide was reported to be extremely dependent on the pH value [1]. Beale [2] studied the hydrothermal synthesis of three bismuth molybdate phases: α-$Bi_2Mo_3O_{12}$, β-$Bi_2Mo_2O_9$ and γ-Bi_2MoO_6 at 140°C for 20 hours for $1 \leq pH \leq 9$. The results are summarized in Table 3.1.

Table 3.1 The effects of pH and reactant stoichiometry on the final crystal structure. All samples were hydrothermally treated at 140°C for 20 hours [2].

pH	α-gel (Bi/Mo=2/3)	β-gel (Bi/Mo=1)	γ-gel(Bi/Mo=2)
1.0	α	Unknown + α	Amorphous + γ
2.0	Poorly crystalline + α	Unknown + α	Amorphous + γ
3.0	Amorphous + α	Amorphous + α	Amorphous + γ
4.0	Amorphous + γ	Amorphous + γ	Amorphous + γ
6.0	Amorphous + γ	Amorphous + γ	Poorly crystalline + γ
7.0	γ	γ	γ
9.0	γ	γ	γ

Interestingly, γ-Bi_2MoO_6 itself can be prepared from a gel in which Bi/Mo atomic ratio is equal to that in α (Bi/Mo = 2/3) or β (Bi/Mo = 1) at pH ≥ 7.0. The γ-phase is also predominant in the gels at pH ≥ 4.0 and it is also present in every synthesis carried out using the γ−gel over the entire pH range used in this study. However, as the pH decreases from 7.0 to 1.0, the crystallinity of the γ-phase decreases. On the contrary, for the synthesis of α-$Bi_2Mo_3O_{12}$, a combination of both correct reactant stoichiometry and pH is necessary, while the β-$Bi_2Mo_2O_9$ cannot be obtained by hydrothermal synthesis even with careful control of stoichiometry and pH.

3.1.2. Influence of the metallate precursor and Raman spectra

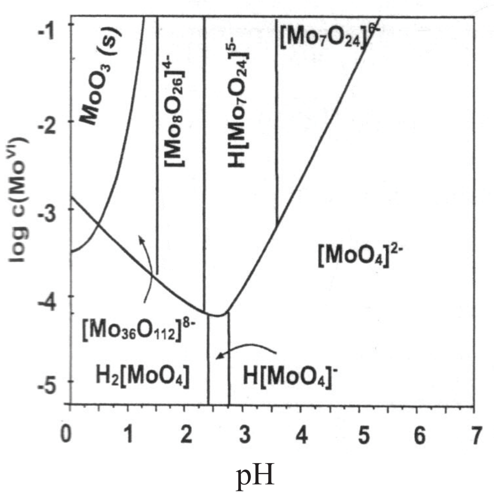

Fig. 3.1 Predominance diagram of various polyoxomolydates in aqueous solutions at different pH [8].

It appears that the polyoxomolybdate species play an important role in bismuth molybdate hydrothermal synthesis.

The polyoxomolydates in aqueous solutions have been widely studied by several authors using Raman scattering [3, 4, 5, 6, 7]. Himeno *et al*. [3] identified six different forms of polyoxomolydates in aqueous solutions. They are summarized in Table 3.2 and illustrated in the predominance diagram in Fig. 3.1 [8]. Fig. 3.2 shows examples of molecular structure of three of them. Other polyoxomolydates such as $[Mo_2O_5]^{2+}$ appear at pH below 0.4 with Raman bands at 953 and 920 cm^{-1} [9]. The condensation to $MoO_3.xH_2O$, "molybdenum acid", occurs at pH below 1 [10].

Table 3.2 Raman band positions for various polyoxomolydates in aqueous solutions [3].

Polyoxomolybdate	pH range	Characteristic Raman bands
$[MoO_4]^{2-}$	14-6.5	897, 841, 318
$[Mo_7O_{24}]^{6-}$	5.8-3.5	943, 903, 840, 790, 560, 422, 362, 219, 170
$[Mo_3O_{10}]^{2-}$	4.4-2.9	950
α-$[Mo_8O_{26}]^{4-}$	2.8-1.9	959
β-$[Mo_8O_{26}]^{4-}$	2.8-1.9	971
$[Mo_{36}O_{112}]^{8-}$	1.6-0.6	982, 955, 901

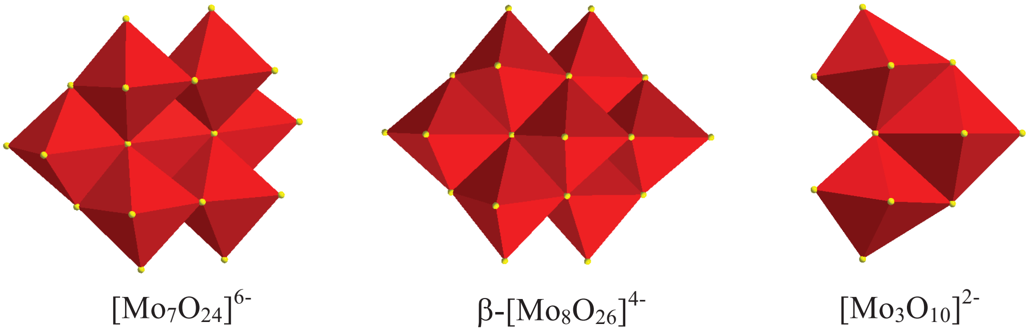
$[Mo_7O_{24}]^{6-}$ β-$[Mo_8O_{26}]^{4-}$ $[Mo_3O_{10}]^{2-}$

Fig. 3.2 Polyhedral representations of $[Mo_7O_{24}]^{6-}$, β-$[Mo_8O_{26}]^{4-}$ and $[Mo_3O_{10}]^{2-}$ molecular anions.

3.2. Experiments: Preparation of titrated ammonium molybdate solutions

Several solutions containing ammonium molybdate were prepared at different pH to obtain different oxo-precursors to see their influence on the preparation of γ-Bi_2MoO_6. The nature of polyoxomolydates was later studied by Raman spectroscopy. Ammonium molybdate solutions were prepared by dissolving 1.7655 g of $(NH_4)_6Mo_7O_{24}\bullet 4H_2O$ in 11.25 ml of ammonia which is about 0.127 M. They were then titrated with different volumes of 65 wt% nitric acid solution to get the final solutions with desired pH values: 1, 4, 6, 7 and 10. The titrated solutions were then introduced into the glass tubes which were sealed for analysis by Raman scattering (macroscopic configuration).

3.3. Results and discussion

The Raman spectra of ammonium molybdate solutions are illustrated in Fig. 3.3, together with spectra of $(NH_4)_6Mo_7O_{24}•4H_2O$ powder and of *in-situ* experiment. The line at 1050 cm^{-1} corresponds to the vibrations of NO_3^- anion in nitric acid solution. As expected, the Raman bands revealed the type of oxo-precursor. At pH > 6, bands at 319, 842 and 898 cm^{-1} indicate the presence of $[MoO_4]^{2-}$ in the solution. At pH 6, the bands corresponding to $[Mo_7O_{24}]^{6-}$ appear at 215, 362 and 940 cm^{-1} in addition to those of the $[MoO_4]^{2-}$. Upon further acidification at pH 4, the band at 940 cm^{-1} (terminal M=O) shifts to higher frequency and is then located at 946 cm^{-1}. According to Dieterle [8] and Bergwerff *et al.* [11], this shift is due to the protonation of the $[Mo_7O_{24}]^{6-}$ anion to $[HMo_7O_{24}]^{5-}$. At pH = 1, Raman bands are located at 898, 956 and 984 cm^{-1}. These new bands are assigned to the formation of the $[Mo_{36}O_{112}]^{8-}$ anion.

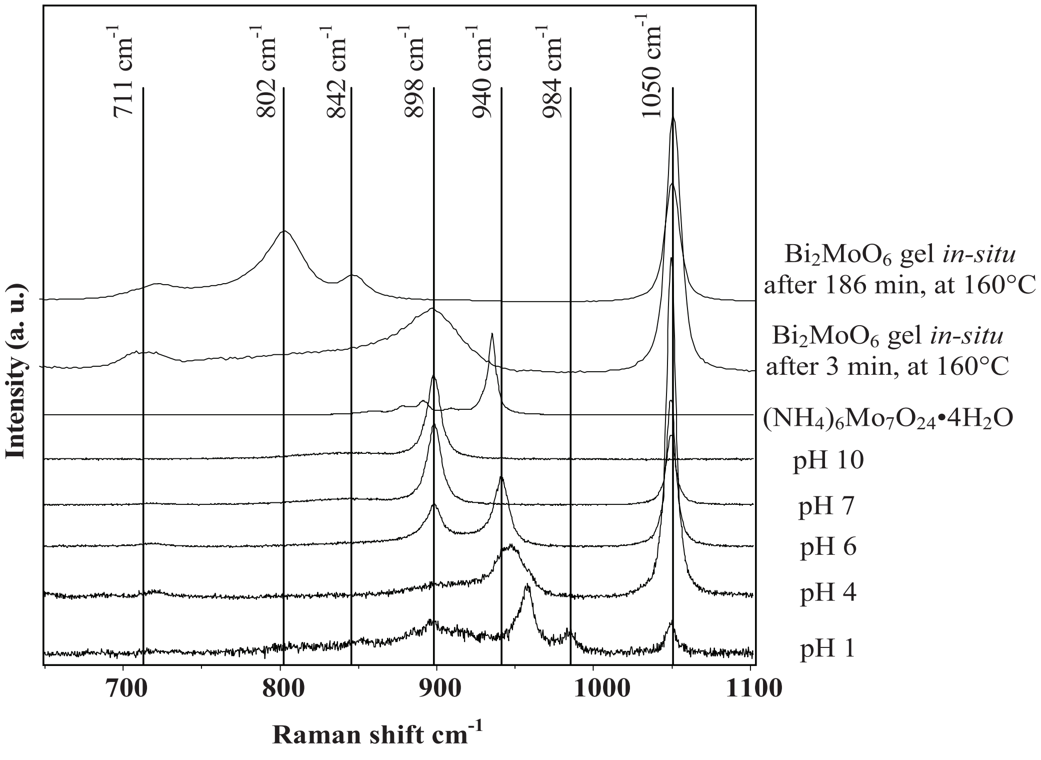

Fig. 3.3 Raman spectra of the titrated ammonium molybdate solutions at different pH values compared to $(NH_4)_6Mo_7O_{24}•4H_2O$ powder and spectra from *in-situ* experiment.

The pH dependence of the observed species is in good agreement with literature. Consequently, the formation of the pure crystallized γ-Bi_2MoO_6 from a gel at pH ≥ 7.0 is obviously related to the necessity of the monomeric molydates, $[MoO_4]^{2-}$, in the reaction.

4. *EX-SITU* STUDY: SYNTHESIS AND FORMATION OF Bi_2MoO_6

4.1. Preparation of γ-Bi_2MoO_6

The γ-Bi_2MoO_6 was prepared by using the same procedure of hydrothermal method described for *in-situ* study. The main difference is that the gel for *ex-situ* study was prepared from a greater amount of the two solutions: A (2.3298 g of Bi_2O_3 dissolved in 5.8 ml concentrated HNO_3) and B (0.8829 g of $(NH_4)_6Mo_7O_{24}•4H_2O$ dissolved in 5.6 ml ammonia). The pH of this mixture was always adjusted to be higher than 6 before loading it into a 20-mL Teflon-lined autoclave which was then introduced in a preheated oven at 180°C. The experiments were stopped at different times (30 min, 1h, 1h10, 1h20, 1h30, 2h and 20h), and the autoclave was let to cool down for 2h to room temperature. The precipitate was then filtered and washed with warm deionised water and further dried in air at room temperature. In one experiment, the precursor was filtered before the reaction in order to identify the sample in the initial stage.

4.2. Characterization of samples after different times of reaction

The XRD patterns and the Raman spectra of the precursor and of samples after different times of reaction in a conventional autoclave under hydrothermal conditions are presented in Fig. 3.4 and Fig. 3.5 respectively. A similar two-step evolution as found for the *in-situ* study was observed, an intermediate phase being first formed before it transforms to γ-Bi_2MoO_6.

However, the kinetics of the *in-situ* and *ex-situ* reactions is clearly different. *Ex-situ* experiments showed that the transformation from the intermediate phase to γ-Bi_2MoO_6 lasted for 20 min and that γ-Bi_2MoO_6 starts to form after 1h10, *vs*. 40 min and 20 min for *in-situ* experiments, respectively. These time shifts are possibly due to the high thermal inertia of the conventional autoclave during heating and cooling. The equilibrium may not be reached for small time of reaction and the slow cooling rate may favour the progress of reaction. The difficulty to control the reaction time during *ex-situ* experiments emphasizes the ability of *in-situ* technique to get information on the kinetics and mechanisms of the γ-Bi_2MoO_6 formation. However, the aim of the *ex-situ* study in the present chapter is to identify the composition and to clarify the structure of the intermediate form.

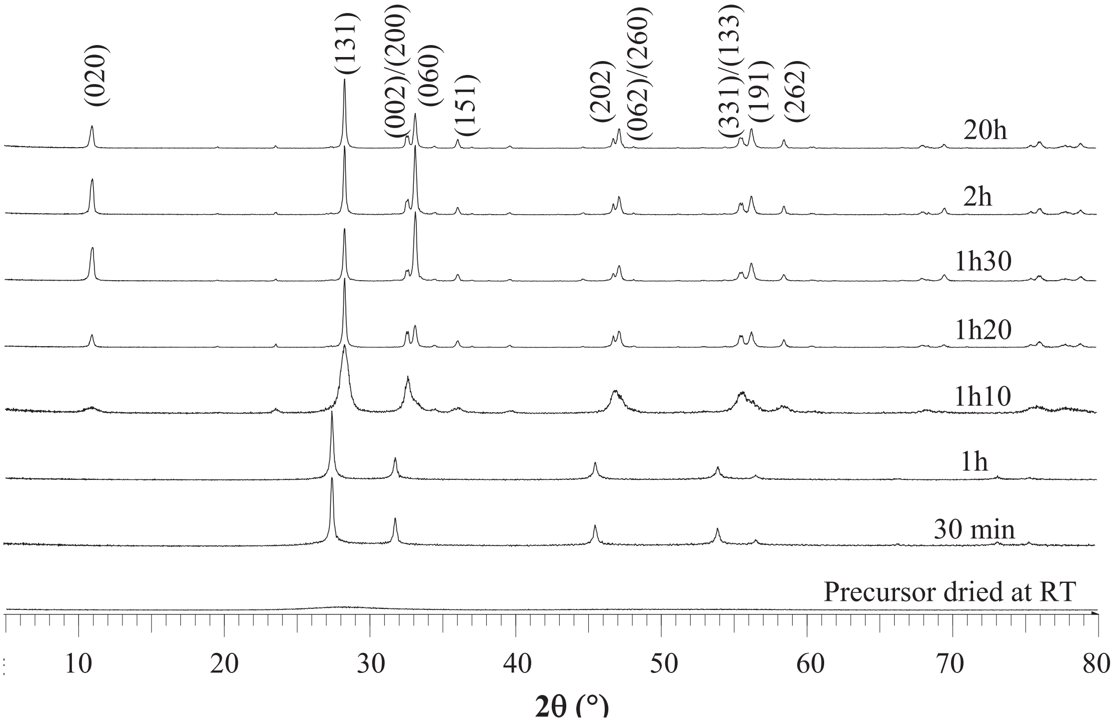

Fig. 3.4 XRD powder diffraction patterns of samples prepared by hydrothermal method at 180°C for different reaction times.

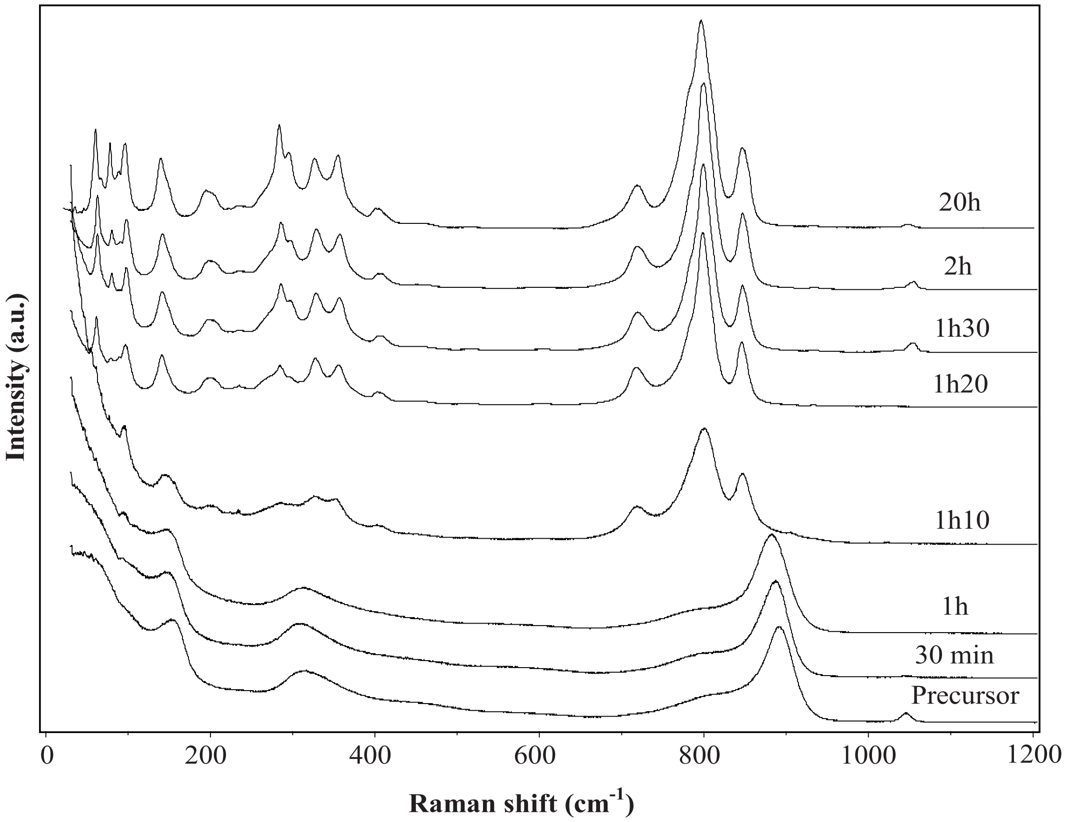

Fig. 3.5 Raman spectra of samples prepared by hydrothermal method at 180°C for different reaction times.

• *Light on the intermediate compound*

From the stacked of XRD patterns presented in Fig. 3.4, it is seen that a poorly crystalline phase exists for the precursor dried at 25°C. After 30 minutes of hydrothermal treatment, the intermediate crystalline phase first formed. According to the XRD patterns shown in Fig. 3.6, the precursor phase was still present after 30 minutes, while it disappeared after 1h of reaction.

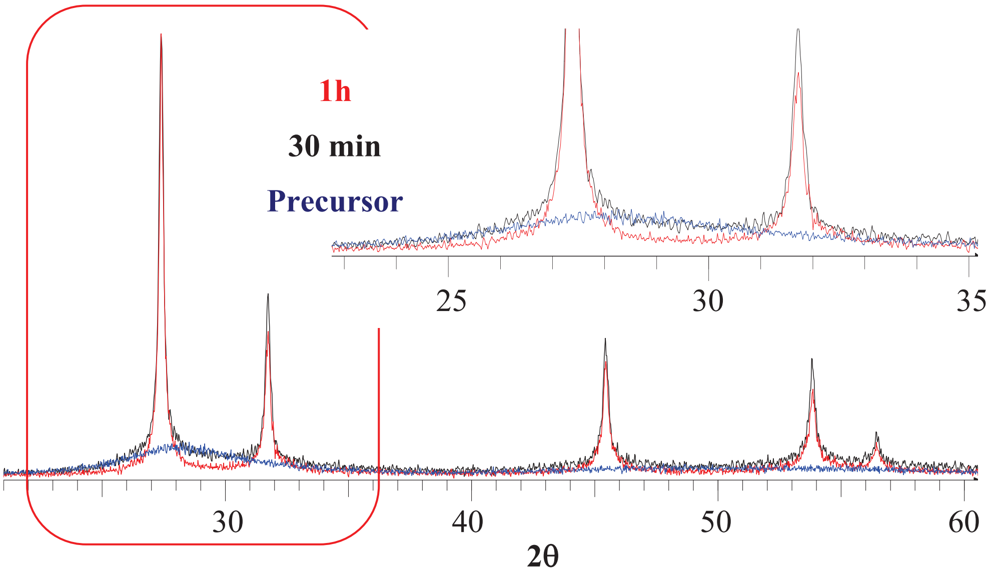

Fig. 3.6 Illustration of the different backgrounds at 23° < 2θ < 35° for the XRD patterns of the precursor and of the sample prepared by hydrothermal method at 180°C, after 30 minutes and 1h of reaction.

The same crystalline phase was found in the sample synthesized for 30 minutes and 1h, however, it is better crystallized with increasing time. Since no shift of the Bragg peak positions was observed, one can conclude that the composition of the crystalline phase formed after 30 minutes is the same as the phase observed after 1h. The unit cell parameters of this phase were refined in a fluorite unit cell. Unlike *in-situ* results in which a tetragonal form, which could be viewed as a distorted fluorite was evidenced, here, a good fit was obtained only when a cubic cell with a=5.638(4) Å was considered. The difference in the symmetry of structure could be the result of the autogenous pressure generated during the *in-situ* reaction. Again the advantage of an *in-situ* study for an accurate characterization of a reaction process is emphasized.

Therefore, it is interesting to verify if the crystallite size of the intermediate phase obtained from *ex-situ* study is identical to that obtained from *in-situ* studies. The XRD profile analysis of the intermediate phase, in the 1h-sample, was examined using Fullprof program [12]. The instrumental resolution was deduced from a LaB_6 [13] XRD diagram. To model the XRD profile, a pseudo-Voigt function pV(x) which is formally defined as a linear combination of a Lorentzian(L) and a Gaussian(G) with a constant ratio (η) [14], was tentatively used.

$$pV(x) = \eta L(x) + (1-\eta)G(x) \qquad 0 \le \eta \le 1 \tag{3.1}$$

However, attempts to refine the XRD profile led to a $\eta > 1$ (*ca.* 1.25). This super-Lorentzian profile is characterized by a strong peak broadening especially at the foot of peaks, as shown in Fig. 3.7 a) and c).

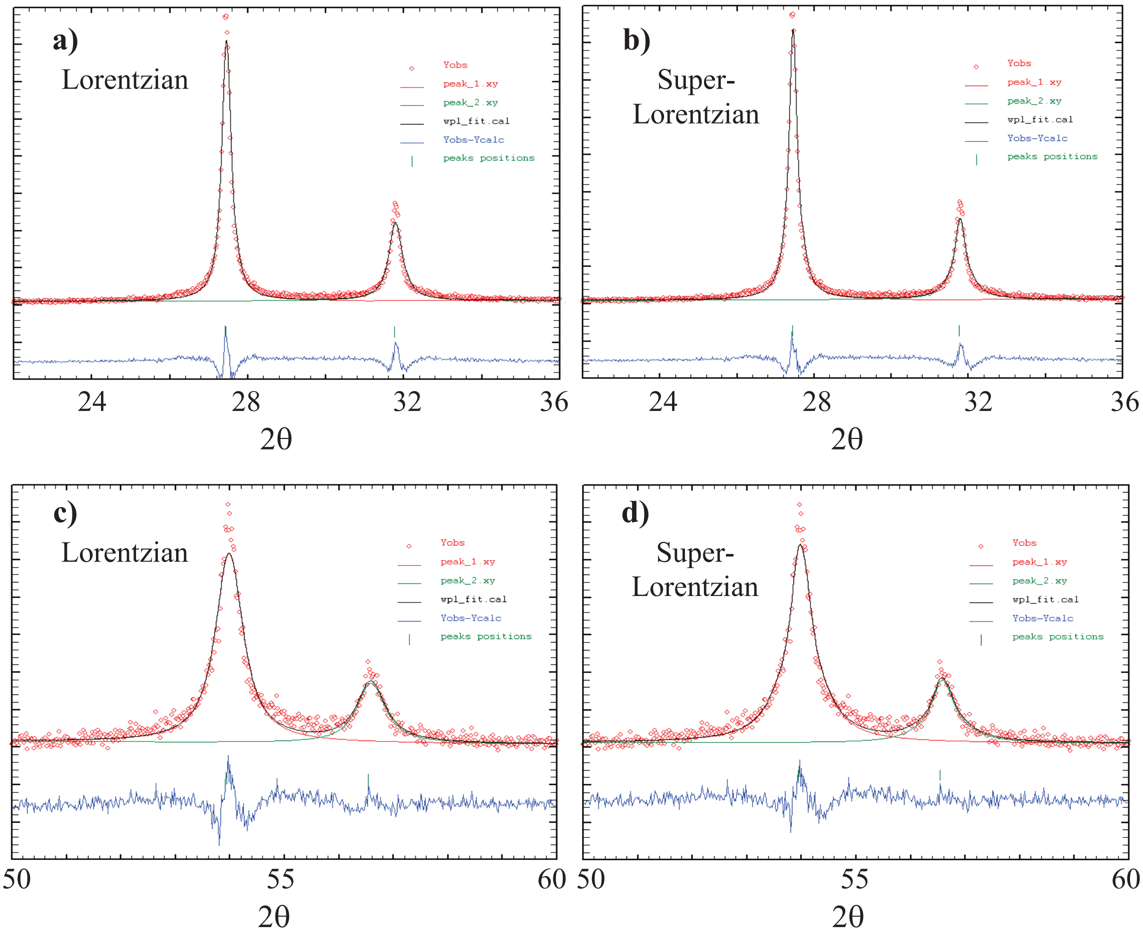

Fig. 3.7 Peak shape of XRD Bragg peaks of the sample after 1 hour of reaction, fitted using a Lorentzian function a), c), and using a super-Lorentzian function b), d).

Such a particular XRD profile could possibly be explained by the existence of at least two populations of particles of different crystallite sizes: strong peaks would characterize the bigger particles, and the broadening at the foot of the peaks would refer to the smaller ones. TEM was therefore carried out on theses particles. Micrographs presented in Fig. 3.8 confirmed that particle sizes may be very different, and that very small particles are present.

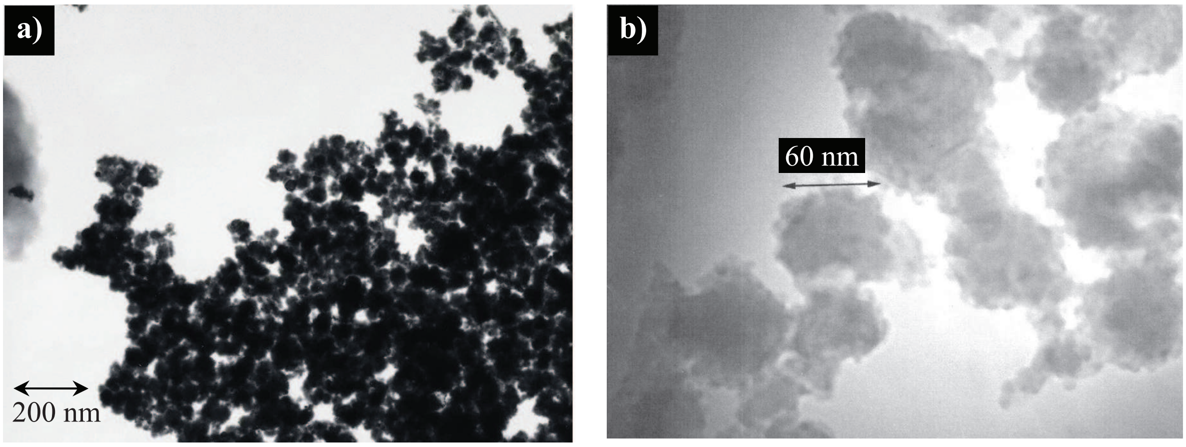

Fig. 3.8 TEM images of the samples prepared by hydrothermal method at 180°C for 1h at two different magnifications.

Although, it might be erroneous because of the presence of particles with different sizes, an analysis of the evolution of the Full Width at Half Maximum of Bragg peaks was carried out for the samples after 30 minutes and 1 hour of reaction. The Williamson and Hall plots [15] corresponding to both samples are given in Fig. 3.9.

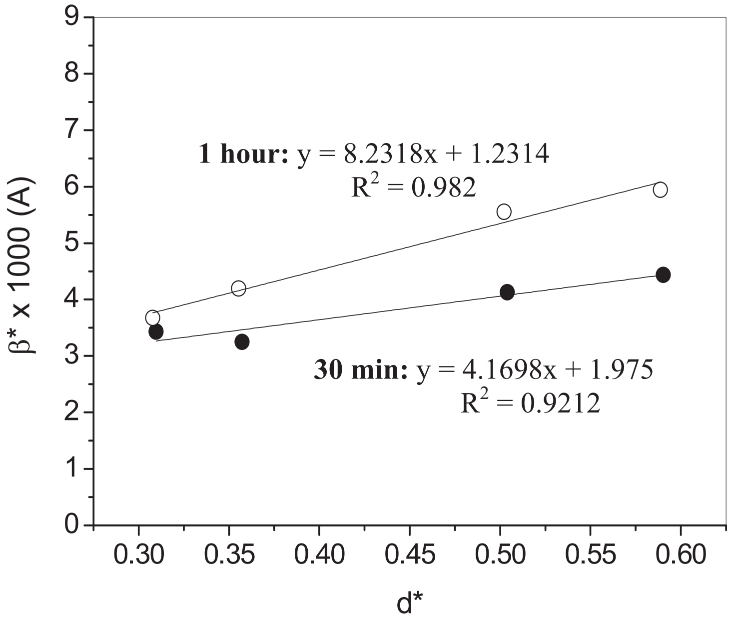

Fig. 3.9 Plot of *β** as a function of *d**

Reciprocal coordinates, where $\beta^* = \frac{\beta \cos\theta}{\lambda}$, $d^* = \frac{2\sin\theta}{\lambda}$ and β being the integral breadth of each peak, were used. Only the four main peaks of the fluorite structure were investigated. To be able to use the fit function of the Winplotr interface, a pseudo-Voigt with a η constraint forced at 0.98 was used. The diffractometer resolution was derived from a LaB_6 pattern. According to Williamson and Hall, a linear evolution is expected.

$$\beta^* = \frac{1}{D} + 2\varepsilon d^* \tag{3.2}$$

where D is the average apparent size of crystallites and ε is the root-mean-square (rms) strain [16, 17] or the so-called maximum strain. A horizontal line would account for a size effect, only whereas a straight line through the origin would account for a strain effect. Interestingly, here a slope and a y-intercept were noticed for both contributions. The maximum strain calculated from the slope values was 2% after 30 minutes of reaction, and two times higher (4%) after 1h of reaction. The mean crystallite size being obtained from the y-intercept values would be 50 nm and 80 nm after 30 minutes and 1 hour of reaction.

According to Fig. 3.5, there are similarities between Raman spectra obtained by *in-situ* and *ex-situ* characterizations. It is worth noting that Mo species in tetrahedral environment were already present in the dried precursor, as indicated by the Raman bands located at 833 and 891 cm^{-1}. After 30 min and 1h, the strong band shifts from 891 cm^{-1} to 886 cm^{-1} and to 881 cm^{-1}, respectively. Meanwhile the local environment of molybdenum does not change and remains tetrahedral. However, this frequency decrease is probably due to a perturbation or a change in structural parameters of MoO_4 tetrahedra that may be caused by the interaction between the negatively charged $[MoO_4]^{2-}$ molecules and the intermediate phase fluorite structure which can be viewed as the positively charged $[Bi_2O_2]^{2+}$ layers from the bismuth oxide fluorite structure (cf. Chapter 2).

Interestingly, in the 30 min sample spectrum, the Raman band position at 886 cm^{-1} indicates a particular local environment of Mo between a nearly regular isolated MoO_4^{2-} and a perturbed MoO_4 species. The presence of the isolated Mo tetrahedra and the shift in frequency were also observed during the *in-situ* study. However, at that time, it was uncertain whether Mo atoms were incorporated in the intermediate structure or remained in the solution because the experiments were performed in liquid state. Here, with dried samples, it is certain that the molybdate species characterized by Raman spectroscopy are all in solid state. In addition, the very low background of the XRD pattern of the 1h-sample is an indication that there is no amorphous phase in this powder. Consequently, it means that molybdate species are present in the fluorite structure. Thereby, one can conclude that the intermediate phase of fluorite-like structure, which formed as an intermediate compound during *in-situ* experiments, is actually a Bi/Mo solid solution written $(Bi_{1-x}Mo_x)_2O_{3+\delta}$. The results of these complementary *ex-situ* experiments clarify one of the ambiguities that arose in Chapter 2.

After 1h10 of experiment γ-Bi_2MoO_6 starts to crystallize and becomes the main compound, but its crystalline state is poor. The presence of $(Bi_{1-x}Mo_x)_2O_{3+\delta}$ in this sample is hardly noticeable in XRD pattern but it is more visible in the Raman spectra in which the characteristic bands of MoO_4 species, though weak, are clearly observed beside those of MoO_6 species. In contrast, a single γ-Bi_2MoO_6 phase was obtained after 1h20 of heating. This conclusion is consistent with XRD patterns and Raman spectra in which the characteristic bands of MoO_6 species in Bi_2MoO_6 structure, including three main Raman bands at 721, 802 and 845 cm^{-1}, are found.

In order to evidence the Mo contents in the samples prepared for different times of reaction, Energy dispersive X-Ray Spectroscopy (EDS) analyses were performed. The EDS results are reported in Table 3.3. As expected, the Mo stoichiometry is close to the theoretical value of Bi_2MoO_6 (*ca*. 2 % of error). Good homogeneity is noticed in the samples after 1h10 in accordance with XRD patterns that indicate the presence γ-Bi_2MoO_6 only. For shorter times of reaction, the presence of Mo in the intermediate phase is ascertained but its content seems to be smaller than in γ-Bi_2MoO_6 (Bi/Mo = 2). The existence of the $(Bi_{1-x}Mo_x)_2O_{3+\delta}$ solid solution is confirmed, but x is smaller than 0.5.

Table 3.3 Bi and Mo contents in the samples after hydrothermal synthesis at 180°C for different times, obtained from Energy dispersive X-ray spectroscopy (EDS) analyses.

Sample	Zone 1		Zone 2	
	Bi (wt%)	Mo (wt%)	Bi (wt%)	Mo (wt%)
Precursor	79.1	20.9	81.4	18.6
30 min	85.7	14.4	83.4	16.6
1h	83.9	16.1	85.1	14.9
1h10	78.1	21.9	79.4	20.6
1h20	78.9	21.1	78.4	21.6
1h30	79.7	20.3	84.0	16.0
2h	77.8	22.2	81.6	18.4
20h	80.0	20.0	81.1	18.9
Bi_2MoO_6 (theoretical values)	81.33	18.67		

SEM was carried out on the precursor and the precipitates after hydrothermal reaction for various times in order to study the microstructural features of these samples. The resulting images are shown in Fig. 3.10.

The grains of the precursor are nearly spherical, about 50 nm in diameter. After 30 min and 1h of heating, grains are slightly bigger. This is in good agreement with the crystallite size deduced from XRD analysis which would indicate single crystal grain. They exhibit spherical shape and correspond to the intermediate crystalline phase of fluorite structure (cf. Fig. 3.4). The size of the first particles of γ-Bi_2MoO_6 which appear after 1h10 of reaction is variable. The particles display irregular disc shapes, in good agreement with the morphology of crystallites which was deduced from the *in-situ* XRD characterization. It is also worth noting that the thickness of theses particles is very small and smaller than the size of the precursor particles. Ten minutes later, they transform rapidly into irregular plates which are about 3 times larger. Then, these platelets grow slowly with the reaction time. This behaviour was also observed by XRD analysis. The XRD peak profile of Bi_2MoO_6 is highly broadened after 1h10 of reaction. Only 10 minutes later, it becomes narrow and shows a similar shape for the rest of the reaction (Fig. 3.11).

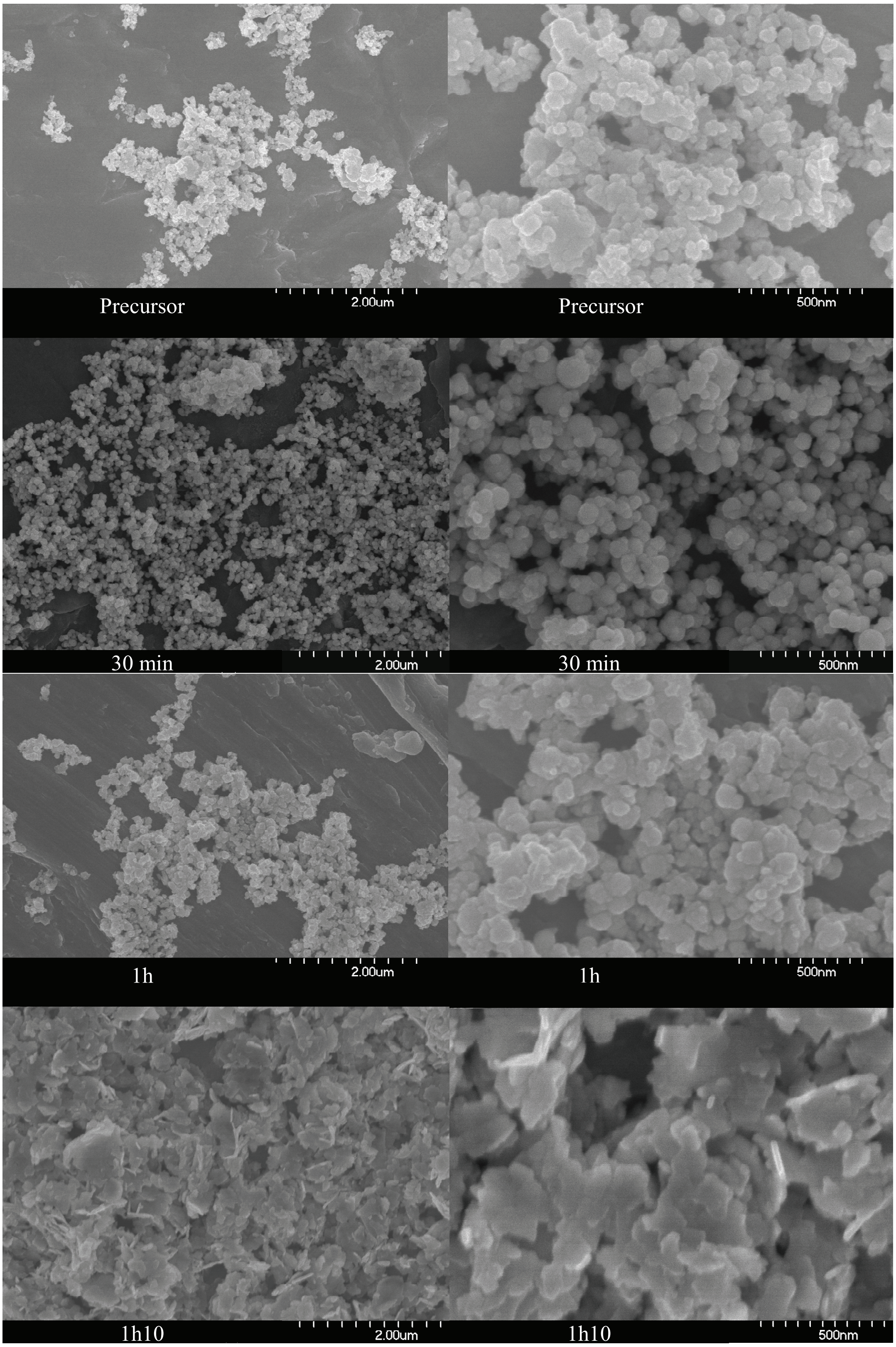

Fig. 3.10 SEM micrographs of the precursor and of the samples prepared by hydrothermal method at 180°C for 30 min (top), 1h and 1h10 (bottom) at two magnitudes.

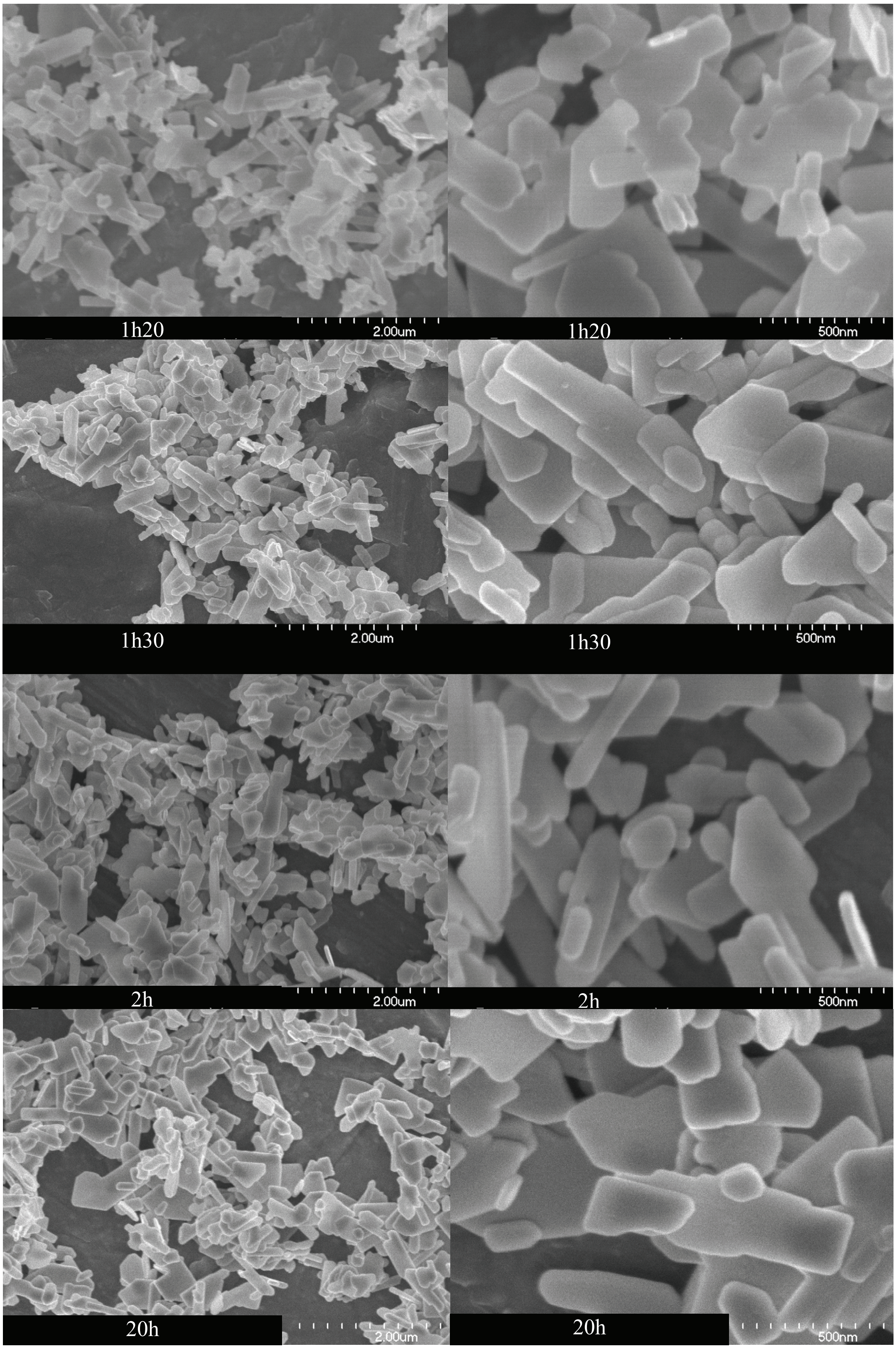

Fig. 3.10 (foll.) SEM micrographs of the samples prepared by hydrothermal method at 180°C for 1h20, 1h30, 2h and 20h (from top to bottom) at two magnitudes.

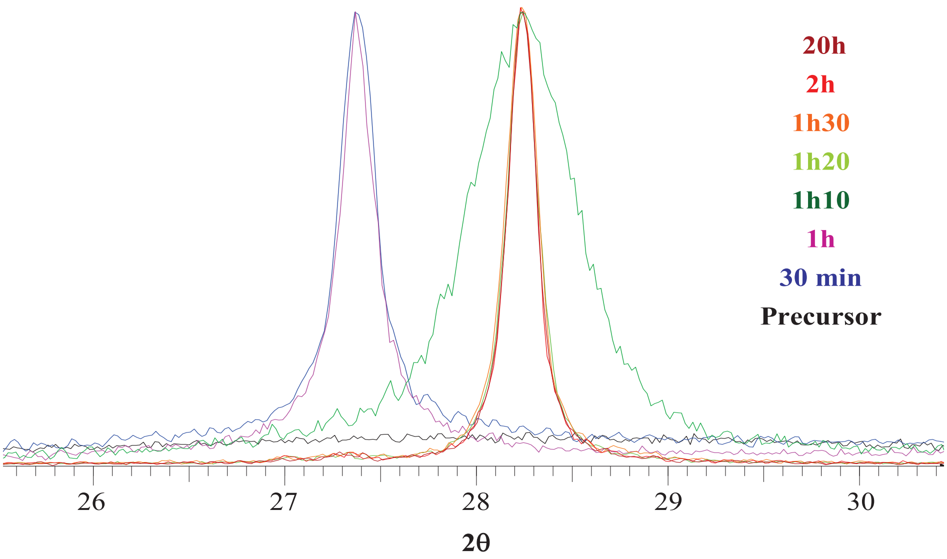

Fig. 3.11 Evolution of main peak of the intermediate phase (at 27.4°) and of γ-Bi_2MoO_6 (at 28.3°) in the samples prepared by hydrothermal method at 180°C for different reaction times (on the normalized XRD patterns).

This observation confirm the two-step mechanism that was evidenced from the *in-situ* study (chapter 2): Isotropic 'Bi_2O_3' particles first grow in the initial stage followed by highly anisotropic platelets of γ-Bi_2MoO_6 in a second step.

According to the previous discussion in the Chapter 2: *In-situ* study, the two dimensional growth of γ-Bi_2MoO_6 is strongly related to its structure. The γ-Bi_2MoO_6 structure belongs to the Aurivillius family that is built up by the intergrowth of $Bi_2O_2^{2+}$ and pseudo-perovskite layers. The anisotropy of this crystal structure generally results in a characteristic lamellar-like growth habit, where the shortest direction corresponds to the stacking direction, giving rise to γ-Bi_2MoO_6 platelets with a very small thickness along [010].

This platelet morphology can also enhance an inhomogeneous distribution of crystal orientation which is referred to the so-called preferential orientation effect. With the platelet shape, the γ-Bi_2MoO_6 particles will naturally lay along the (010) plane, perpendicular to the layer-stacking *b* axis. The intensity of the (010) reflection plane will be drastically influenced by the preferred orientation. This effect is clearly observed in the XRD patterns which were collected in Bragg Brentano geometry.

The preferential orientation effect is more pronounced in the XRD patterns of precipitates after 2h30 of hydrothermal treatment presented in Fig. 3.4. The intensity of the

(020) plane at 10.9° and (060) plane at 33.1°C change from one XRD pattern to another but the intensity of these two peaks evolved in the same way.

To conclude, this SEM analysis confirmed the calculated crystallite shapes obtained from XRD refinement in the *in-situ* study. The intermediate phase first formed in nearly spherical particles before transforming into the γ-Bi_2MoO_6 platelets. An increase of strain seems to occur in the intermediate form before it splits into thin γ-Bi_2MoO_6 particles.

5. STRUCTURE OF THE INTERMEDIATE PHASE

According to the XRD and Raman scattering results in Fig. 3.4 and Fig. 3.5, as well as to EDS experiments that were discussed previously, the Mo tetrahedral species appear to be incorporated in the intermediate phase structure as $(Bi_{1-x}Mo_x)_2O_{3+\delta}$ solid solution. To verify this hypothesis, the structure of the precipitate obtained after 1 hour of reaction was carefully analyzed by XRD and Raman scattering at high temperature.

5.1. Studies at high temperature

Another way to show the existence of Mo inside the intermediate fluorite structure is to heat this powder until it transforms to the high temperature phase which will be easier to identify. TGA/DTA (Thermogravimetric Analysis/Differential Thermal Analysis) and separate XRD and Raman scattering studies were performed during the phase transformation, from room temperature to 800°C. The sample after 1h of hydrothermal synthesis will be more particularly studied.

5.1.1. Thermogravimetric Analysis (TGA) and Differential Thermal Analysis (DTA)

During the heating process of the sample after 1h of hydrothermal synthesis from room temperature to 800°C, two weight losses are shown by TGA (Fig. 3.12): ~1.09% from room temperature to 209°C and ~0.28% between 209 and 460°C. Some small fluctuations of the TGA curve at temperatures above 460°C may be due to the instrumental errors. No variation is observed above 460°C during heating to 800°C. During the cooling process (from 800°C), no variation was observed all the way down to room temperature.

The second mass loss is related to an exothermic process at 240°C. Gases released during the heating process were identified by mass spectrometry. The first and second mass losses appear to correspond to the elimination of water and nitrate/ammonium compounds, respectively. However, there are some other peaks in DTA curve which are not correlated with mass losses: a large broad exothermic peak at 427°C, two small endothermic peaks located at 670, 690°C during heating process and a small exothermic peak found at 348°C on cooling, respectively. These signatures might indicate the phase transformations that will be studied more precisely by high temperature X-ray diffraction techniques.

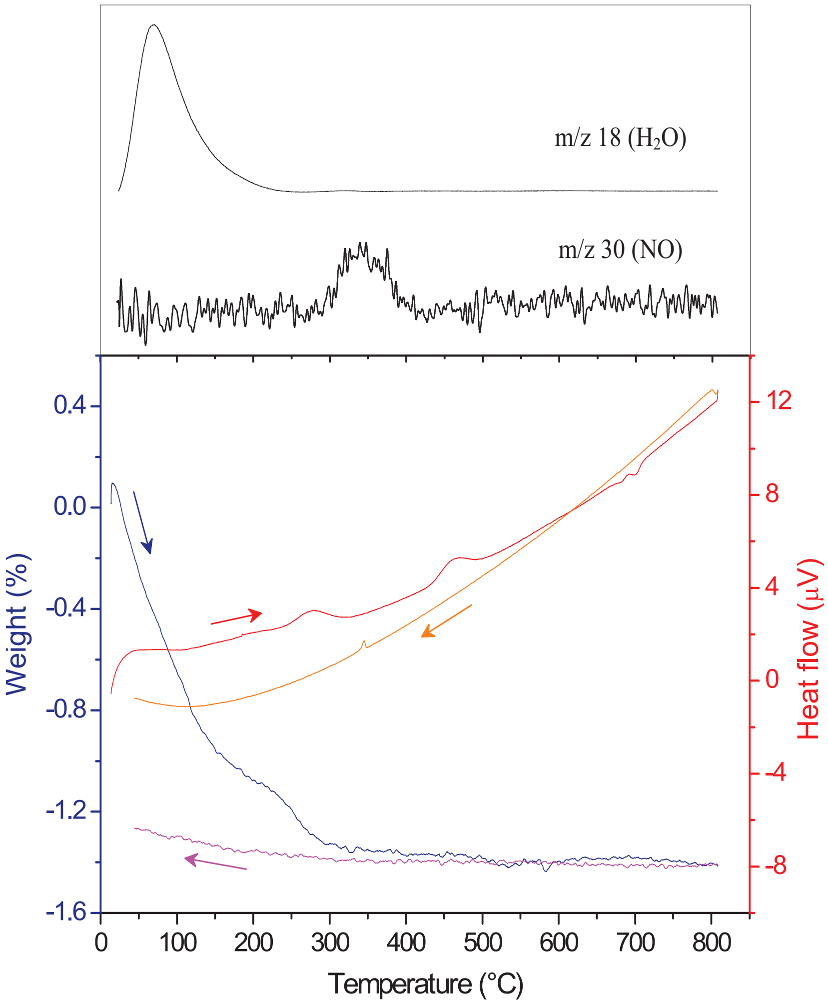

Fig. 3.12 Simultaneous TGA/DTA of the sample after 1 h of reaction at 180°C and mass spectra corresponding to the evolved gases H_2O and NO during heating.

5.1.2. High temperature X-ray diffraction

The XRD patterns collected at various temperatures are given in Fig. 3.13. The fluorite structure which was observed at room temperature appeared to be stable up to 400°C, then it suddenly transformed at 420°C and a second transformation was observed at 680°C.

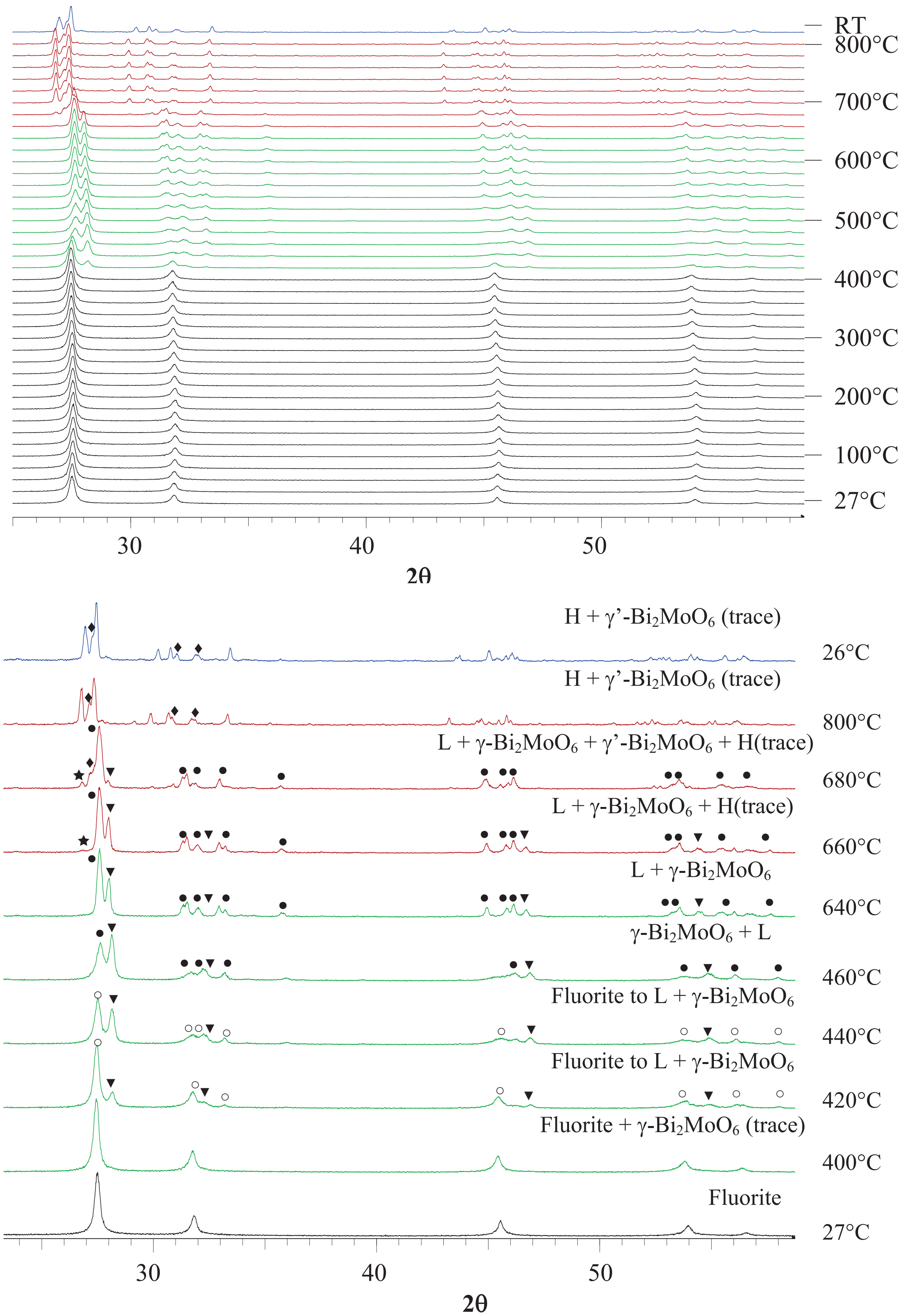

Fig. 3.13 Stack of XRD patterns of the 1h hydrothermal sample heated from room temperature to 800°C in air. ○: Fluorite to L-$Bi_{2n+4}Mo_nO_{6(n+1)}$, ●: L-$Bi_{2n+4}Mo_nO_{6(n+1)}$, ▼: γ-Bi_2MoO_6, ★: H-$Bi_{2n+4}Mo_nO_{6(n+1)}$ (ε solid solution), ♦: γ'-Bi_2MoO_6.

The final XRD pattern of the sample after the experiment at 800°C (Fig. 3.14) reveals the presence of two phases: A member of ε solid solution (for $27.75 \leq Bi/Mo \leq 25.75$) [18, 19] and γ'-$Bi_2MoO_6$, the high temperature form of γ-Bi_2MoO_6). This is an indirect proof of the initial composition of the sample which is $Bi/Mo > 2$. If the composition of the precipitate had corresponded exactly to Bi_2MoO_6, only γ'-Bi_2MoO_6 would have been expected. This result confirms the data previously obtained by EDS analyses which showed that the bismuth content in the intermediate phase was slightly higher than in Bi_2MoO_6. A careful examination of the XRD patterns collected between 400°C and 600°C, revealed that besides γ-Bi_2MoO_6 a compound of the $Bi_{2n+4}Mo_nO_{6(n+1)}$ series, recently evidenced by Vila *et al.* [20, 21, 22, 23, 24], is presented.

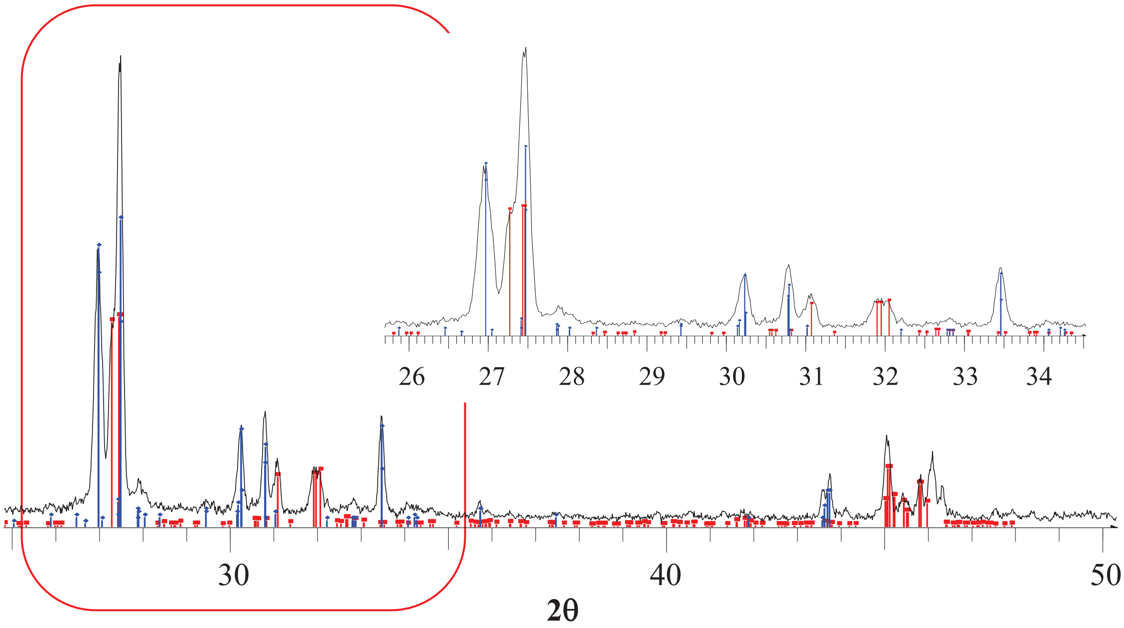

Fig. 3.14 XRD pattern of the 1h hydrothermally treated sample after heating at 800°C is identified as $Bi_{26}Mo_{10}O_{69}$ and γ'-Bi_2MoO_6 (PDF number: 01-089-0563 88-16 (blue) and 01-089-0563 88-16 (red), respectively).

For a better understanding of this phase transformation, a background knowledge of the structure of $Bi_{2n+4}Mo_nO_{6(n+1)}$ series is necessary. The $Bi_{12}Mo_4O_{30}$ (with $n = 4$) powder was first obtained by Vila *et al*. [20], in 2004. A wet-chemistry procedure was employed to obtain first a precipitated reactive precursor that was then annealed at different temperatures for different times leading to isolated polycrystalline polymorphs. From the same preparation method, the $Bi_{10}Mo_3O_{24}$ with $n = 3$, was obtained a year later [21] followed by the discovery of two other compositions: $Bi_{14}Mo_5O_{36}$ with $n = 5$ and $Bi_{16}Mo_6O_{42}$ $n = 6$ in 2007 [22].

However, an accurate structural determination was achieved only in 2009 by HREM, neutron diffraction and X-ray diffraction [23, 24]. The crystal data of the $Bi_{2n+4}Mo_nO_{6(n+1)}$ series compounds (n = 3, 4, 5 and 6) are given in Table 3.4. The structures of the $Bi_{2n+4}Mo_nO_{6(n+1)}$ series (with n = 3, 4, 5 and 6) are illustrated in Fig. 3.15. The structures can be viewed as a stack of $[Bi_{2n+4}O_{2n+6}]^{2n+}$ layers which run parallel to the (001) plane surrounded by groups of n isolated MoO_4 tetrahedra. The groups of $nMoO_4$ are inserted into channels along [010] and bordered by Bi lone pairs.

Table 3.4 Crystal data of the low temperature forms of $Bi_{2n+4}Mo_nO_{6(n+1)}$ series compounds [23].

Data	Bi/Mo=3.33 $Bi_{10}Mo_3O_{24}$ LT n=3	Bi/Mo=3 $Bi_{12}Mo_4O_{30}$ LT n=4	Bi/Mo=2.8 $Bi_{14}Mo_5O_{36}$ LT n=5	Bi/Mo=2.66 $Bi_{16}Mo_6O_{42}$ LT n=6
System	Monoclinic	Monoclinic	Monoclinic	Monoclinic
Space Group	$C2$	$P2_1/a$	$C2$	$P2_1/a$
a (Å)	23.7282(2)	29.0674(4)	34.476(2)	39.97(2)
b (Å)	5.64906(6)	5.64795(7)	5.6414(3)	5.632(4)
c (Å)	8.68173(9)	8.6620(1)	8.6433(4)	8.634(4)
β (°)	95.8668(7)	97.98(1)	99.69(1)	101.02(2)
V (Å^3)	1157.62(1)	1408.3(2)	1657.1(1)	1907.6(2)
Z	2	2	2	2

A polymorphism study was carried out for $Bi_{12}Mo_4O_{30}$, one of the $Bi_{2n+4}Mo_nO_{6(n+1)}$ series [20]. The TGA/DTA analysis revealed two high-temperature polymorphous: H-$Bi_{12}Mo_4O_{30}$ and H'-$Bi_{12}Mo_4O_{30}$. The L⇔ H-$Bi_{12}Mo_4O_{30}$ (at 700°C) is partially reversible but the transition H⇔ H'-$Bi_{12}Mo_4O_{30}$ (at 860°C) is not reversible. H-$Bi_{12}Mo_4O_{30}$ corresponds to the bismuth rich limit of the ε solid solution as proposed by Galy [25]. This phase transforms into H' phase just before the melting point. More interestingly, the TGA/DTA and high temperature XRD analyses revealed several phase transformations of the precipitated reactive precursor during the heat treatment, from room temperature to 850°C. This study evidenced a remarkable transformation from the precursor to γ-Bi_2MoO_6 at 400°C before the formation of $Bi_{12}Mo_4O_{30}$ at 500°C. The phase transition L⇔ H-$Bi_{12}Mo_4O_{30}$ later occurred at 700°C.

$Bi_{10}Mo_3O_{24}$: n=3, space group $C2$
$[Bi_{10}O_{12}](MoO_4)_3$ crystal network

$Bi_{14}Mo_5O_{36}$: n=5, space group $C2$
$[Bi_{14}O_{16}](MoO_4)_5$ crystal network

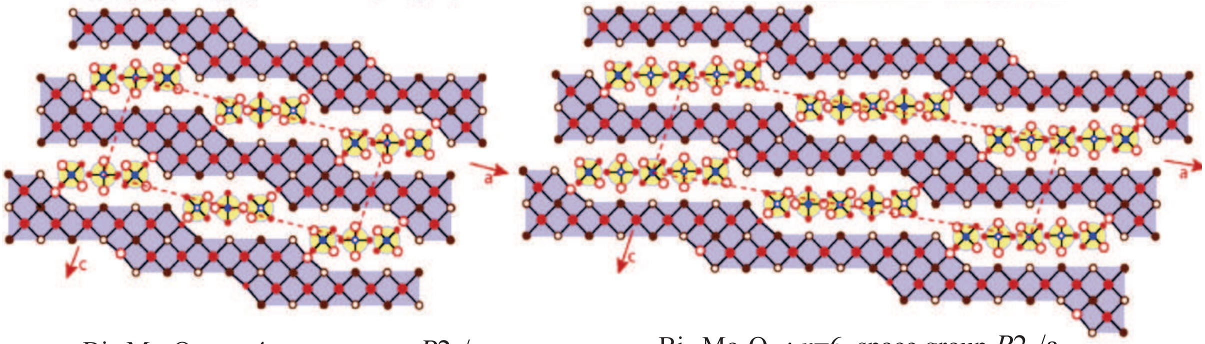

$Bi_{12}Mo_4O_{30}$: n=4, space group $P2_1/a$
$[Bi_{12}O_{14}](MoO_4)_4$ crystal network

$Bi_{16}Mo_6O_{42}$: n=6, space group $P2_1/a$
$[Bi_{16}O_{18}](MoO_4)_6$ crystal network

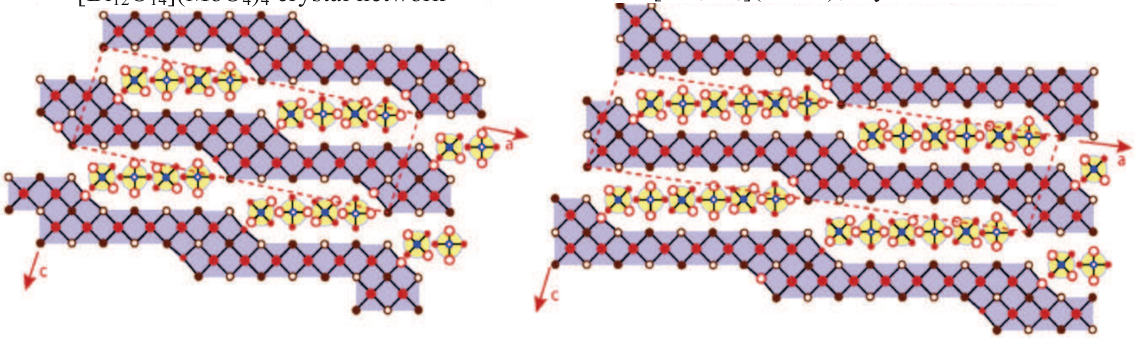

Fig. 3.15 Structure of $Bi_{2n+4}Mo_nO_{6(n+1)}$ serie [23].

The H-$Bi_{12}Mo_4O_{30}$ phase belongs to the well-known $[Bi_{12}O_{14}]^{8+}$ columnar structural-type which corresponds to the ε solid solution [18, 19]. The phase transitions between precursor ⇔ γ-Bi_2MoO_6 ⇔ L- ⇔ H-$Bi_{2n+4}Mo_nO_{6(n+1)}$ were also found for other compositions *i.e.* $Bi_{14}Mo_5O_{36}$ and $Bi_{16}Mo_6O_{42}$ in the recent study [22] with slightly different transition temperatures, except for $Bi_{10}Mo_3O_{24}$ [21], the Bi rich composition, which decomposes into a mixture of ε phase and $Bi_{38}Mo_7O_{78}$ [26].

In our high temperature X-ray diffraction experiment, the thermal evolution of the γ-Bi_2MoO_6 and the $Bi_{2n+4}Mo_nO_{6(n+1)}$ series compound above 420°C correlates well with the polymorphism study of $Bi_{12}Mo_4O_{30}$. The γ-Bi_2MoO_6 starts to form at 420°C, resulting in a large broad exothermic peak observed at 427°C in DTA curve. After an increase of 40°C, it is well crystallized while the fluorite phase gradually transforms to a $Bi_{2n+4}Mo_nO_{6(n+1)}$ phase. In good agreement with the literature [20, 22], from 460°C to 640°C, the intensity of peaks related to γ-Bi_2MoO_6 decreases with temperature while $Bi_{2n+4}Mo_nO_{6(n+1)}$ becomes well crystallized. However, at 640°C the γ-Bi_2MoO_6 does not totally transform into $Bi_{2n+4}Mo_nO_{6(n+1)}$. This is likely due to the higher amount of Mo in our sample compared to

$Bi_{2n+4}Mo_nO_{6(n+1)}$. At high temperatures, above 660°C, the phase transition from γ-Bi_2MoO_6 into γ'-Bi_2MoO_6 (the high temperature form of Bi_2MoO_6) occurs just before that of $Bi_{2n+4}Mo_nO_{6(n+1)}$ into a ε-type structure. It is worth noting that these phase transitions correlate well with the two small endothermic peaks, located at 670 and 690°C, observed in DTA curve. Moreover, the formation of a phase belonging to the ε solid solution is also in good agreement with the endothermic peaks observed in DTA on cooling at 345°C which likely corresponds to the monoclinic ⇔ triclinic transformation observed for molybdenum rich compositions of the ε solid solution [18].

5.1.3. High temperature Raman scattering

The phase transitions observed by HTXRD were confirmed by Raman spectroscopy. A stack of Raman spectra recorded from room temperature to 800°C is shown in Fig. 3.16.

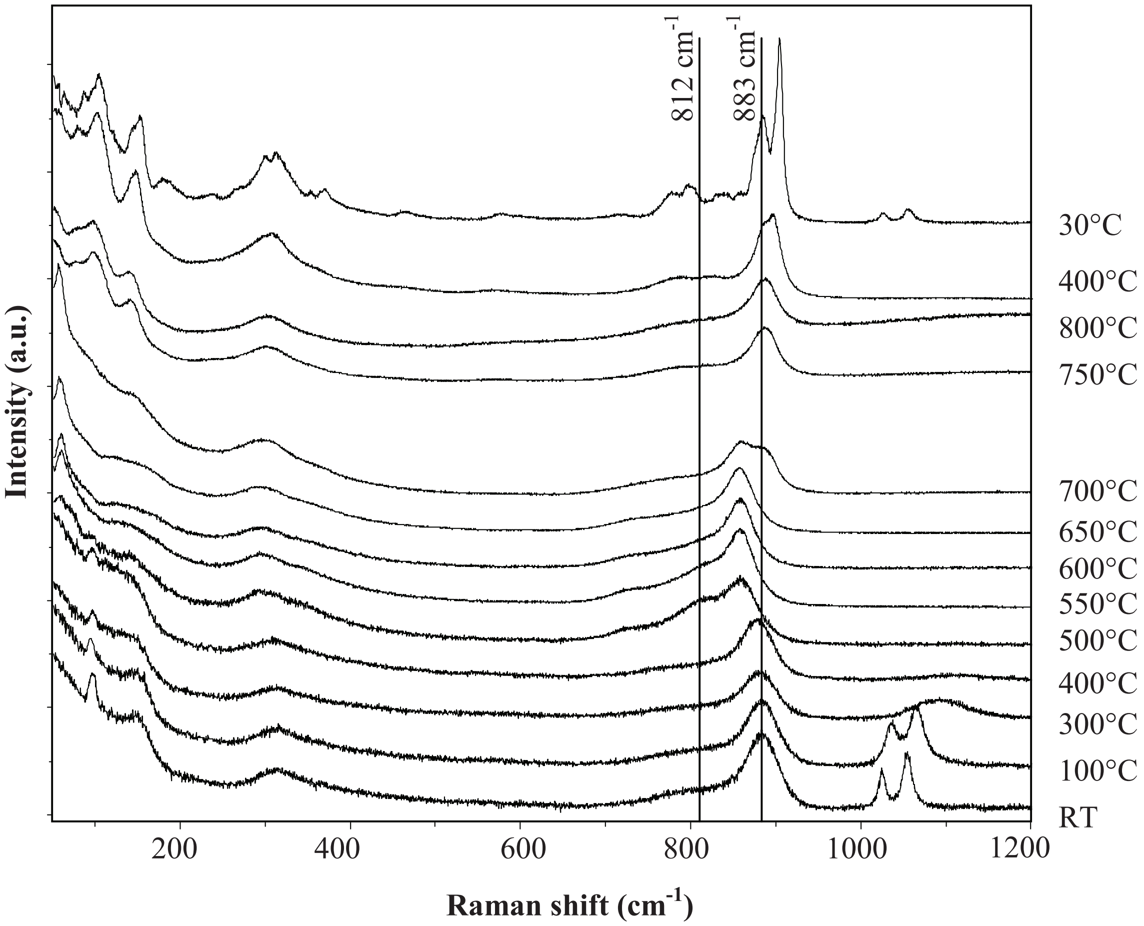

Fig. 3.16 Stack of Raman spectra of the 1h hydrothermally treated sample heated from room temperature to 800°C.

As mentioned previously (cf. Chapter 2), Raman bands observed below 400 cm^{-1} are generally assigned to bending, wagging and translational and librational motions of the different species in the crystal while bands observed above 600 cm^{-1} are assigned to stretching motions of Mo-O bond [27, 28]. Since the bending mode range is probably overlapped by the vibration of bismuth oxide group, only the stretching modes observed in the range of 700-950 cm^{-1} are useful to us. Interestingly, the general aspects of the evolution of Raman spectra show two significant changes in the local environment of Mo atoms at about 400 and 700°C which are coincidently related to the two phase transition temperatures observed by XRD: from the fluorite intermediate phase to γ-Bi_2MoO_6 and L-$Bi_{2n+4}Mo_nO_{6(n+1)}$ first and then from γ-Bi_2MoO_6 and L-$Bi_{2n+4}Mo_nO_{6(n+1)}$ to γ'-Bi_2MoO_6 and ε solid solution.

The Raman spectrum of the 1h-sample collected at room temperature in Fig. 3.16, shows the medium band at 883 cm^{-1} and weak band at around 812 cm^{-1} which correspond to symmetric $\nu_1(A_1)$ and anti-symmetric $\nu_3(F_2)$ Mo-O stretching modes of MoO_4 tetrahedra, respectively. Other characteristic vibrations of tetrahedral species noticed around 318 cm^{-1} are assigned to angular deformations $\nu_2(E)$ and $\nu_3(F_3)$. The absence of significant spectral variation in the thermo-Raman spectra collected in the temperature interval from 25 to 400°C revealed that the intermediate phase structure was not dramatically disturbed in this range of temperature. The two small extra bands at 1024 and 1054 cm^{-1}, corresponding to the vibrations of NO_3^- anion in bismuth nitrate or/and ammonium nitrate, shift to 1035 and 1064 cm^{-1}, respectively and disappear at about 500°C. This behaviour correlates well with the mass losses observed in the TGA curve and the evolution of NO observed by mass spectrometry from 209°C to 460°C, indicating the elimination of these compounds.

The first spectral variation, observed in the temperature range 400-500°C, is shown for the transformation from the fluorite intermediate phase to L-$Bi_{2n+4}Mo_nO_{6(n+1)}$ and γ-Bi_2MoO_6. The main characteristic peak of MoO_4 tetrahedra shifts from 883 to 877 cm^{-1} at 400°C and later to 858 cm^{-1} at 500°C. This frequency shift indicates the change in the structural parameters of the molybdates, which could be influenced by the different environment of MoO_4 tetrahedra, probably due to the different type of bismuth oxide network on going from the intermediate phase to the L-$Bi_{2n+4}Mo_nO_{6(n+1)}$. Furthermore, the spectrum at 500°C also shows some characteristic Raman bands of γ-Bi_2MoO_6, such as a small band at 720 cm^{-1} and a shoulder at 812 cm^{-1}, which could be an envelope of two other characteristic peaks at 799 and

848 cm^{-1} [27]. No significant modification was observed from 500°C to 650°C. The decrease in intensity of the characteristic Raman bands of γ-Bi_2MoO_6 was only noticed, in good agreement with XRD results which showed that a fraction of γ-Bi_2MoO_6 transforms to L-$Bi_{2n+4}Mo_nO_{6(n+1)}$ in this temperature range.

The second spectral variation occurring at about 700°C would indicate the transformation from γ-Bi_2MoO_6 and L-$Bi_{2n+4}Mo_nO_{6(n+1)}$ to γ'-Bi_2MoO_6 and ε solid solution, respectively. At 700°C, the appearance of a new band at 886 cm^{-1} was observed, followed by the extinction of the characteristic Raman bands of L-$Bi_{2n+4}Mo_nO_{6(n+1)}$, located at 858 cm^{-1}, at 800°C. The two principal medium bands at 858 and 886 cm^{-1} in the Raman spectrum collected at 700°C could refer to at least two types of MoO_4 tetrahedra surrounded by different arrangements of bismuth oxide system. The first one is assigned to MoO_4 tetrahedra intercalated between the $[Bi_{2n+4}O_{2n+6}]^{2n+}$ layers in L-$Bi_{2n+4}Mo_nO_{6(n+1)}$ structure. The second one would be assigned to MoO_4 tetrahedra filling in the space between the $[Bi_{12}O_{14}]^{8+}$ columns in γ'-Bi_2MoO_6 and ε-type structure. Due to the similarity of the latter two structures and the thermal effect for the high temperature measurement, it is difficult to discriminate each component spectrum. The characteristic Raman bands of γ-Bi_2MoO_6 are not found, as shown by XRD results, at 700°C, meaning that γ-Bi_2MoO_6 is fully transformed at this stage of reaction.

The Raman spectra collected back from 800 to 25°C, revealed no major changes in the spectral profile. A thorough observation of the room temperature spectrum reveals a better defined peak profile: the intensity of all bands increases while their width decreases and the highest Mo-O stretching frequency shifts from 886 to 903 cm^{-1}. This observation could be explained by the thermal effect at high temperature. Back to the room temperature, the Raman bands characteristic of nitrates, at 1026 and 1055 cm^{-1}, appear again below 400°C. This is likely due to the condensation of nitrates on the powder during the cooling process because no gas flow was used for this experiment.

5.2. Structural study of the 1h sample after heating at 800°C by Raman scattering

The room-temperature Raman spectrum of the 1h-sample after heating at 800°C is compared with spectra of $Bi_{25.75}Mo_{10}O_{68.625}$ (the molybdenum rich limit of the ε solid solution) and γ'-Bi_2MoO_6 in Fig. 3.17.

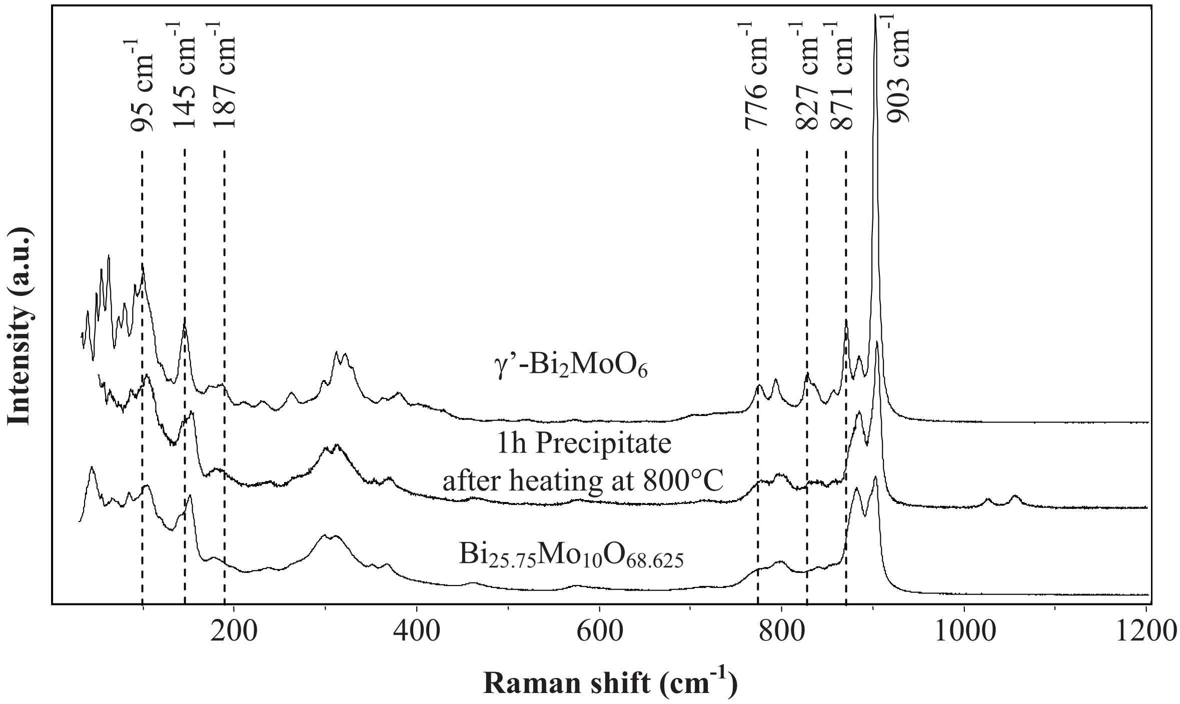

Fig. 3.17 The room temperature Raman spectra of the 1h hydrothermally treated sample after heating at 800°C compared to those of $Bi_{25.75}Mo_{10}O_{68.625}$ and γ'-Bi_2MoO_6.

In good agreement with the high-temperature XRD, the Raman spectrum of the sample is very similar to that of $Bi_{25.75}Mo_{10}O_{68.625}$ (the upper limit of the ε solid solution) and it also contains some Raman bands of γ'-Bi_2MoO_6, (shown by dashed lines) indicating the presence of $Bi_{25.75}Mo_{10}O_{68.625}$ as a major phase and γ'-Bi_2MoO_6 as a minor phase. The two small extra bands at 1026 and 1055 cm^{-1} correspond to the vibrations of NO_3^- anion in bismuth nitrate or/and ammonium nitrate.

To understand the Raman spectrum of this mixture, a good understanding of each component spectrum and their corresponding structure is necessary. Unfortunately, the Raman bands of the ε solid solution and the assignment of vibration modes of the γ' form of Bi_2MoO_6 structure have never been studied in the past. Only a few short Raman analyses of γ'-Bi_2MoO_6 have been carried out. The Raman spectra of γ'-Bi_2MoO_6 shows a strong Raman line at 903

cm^{-1} with other several weaker lines in the 776-903 cm^{-1} range. They correspond to symmetric $\nu_1(A_1)$ and anti-symmetric $\nu_3(F_2)$ Mo-O stretching modes of MoO_4 tetrahedra and their values are compared with those published by Matsuuura *et al.* [29] and Hardcastle and Wachs [27] in Table 3.5. The absence of Mo-O stretching bands in the 540-730 cm^{-1} region argues against the presence of MoO_6 octahedra as well as of bridged MoO_4 and MoO_5 species [29]. Since the wavenumber value of the strongest Mo-O stretching band is close to 897 cm^{-1}, which is the stretching vibration of distorted MoO_4 in $Na_2MoO_4.2H_2O$ and $Bi(FeO_4)(MoO_4)_2$, the Mo coordination in this structure is thought to be isolated distorted MoO_4 [29]. This hypothesis was later confirmed by Buttrey *et al*. [30].

Indeed the complete structure model of γ'-Bi_2MoO_6 was resolved by Buttrey *et al.* [30] using single X-ray diffraction and powder neutron diffraction data (Fig. 3.18a) (cf. Chapter 1). Four types of Mo atoms were found. The tetrahedra of Mo(1), Mo(3) and Mo(4) form square tunnels enclosing a single column of Bi^{3+} sites and these square tunnels are arranged in pairs and are further surrounded by other MoO_4 tetrahedra of Mo(2). These four molybdates form isolated distorted tetrahedra with 16 different Mo-O distances (1.718(12)-1.871(12) Å) and a variation of O-Mo-O bond angles (102.33(59)° - 124.75(51)°). On the contrary, the tetrahedron found in $BaMoO_4$ is a regular, with Mo-O bond length of 1.7658(24) Å and a O-Mo-O bond angle of about 109° (108.325(118) and 111.789(107)°) [31]. The three Raman lines characteristic of Mo-O stretching modes in such a regular tetrahedron are assigned to the symmetric mode (A_g) at 888 cm^{-1} and anti-symmetric modes (B_g and E_g) at 835 and 789 cm^{-1}, respectively [32].

Table 3.5 Summary of the Bi_2O_3-MoO_3 Raman band positions

γ'-Bi_2MoO_6				$Bi_{25.75}Mo_{10}O_{68.625}$
ir [27]	Raman [27]	Raman [29]	Raman	Raman
890_{sh}	892_{100}	897_{vs}	902_{100}	903_{100}
880_{sh}	883_{30}		884_{16}	881_{89}
868_{vs}	864_{41}	865_{m}	870_{25}	
	851_{23}		856_{8}	854_{26}
				840_{25}
		$829_{w, sh}$	828_{13}	
825_{m}	822_{37}	822_{m}		
810_{vs}				
780_{w}	787_{25}	788_{m}	793_{10}	797_{29}
	770_{29}	771_{m}	774_{9}	776_{22}
740_{m}				
710_{s}	695_{25}			715_{7}
645_{m}				
562_{m}				574_{9}
527_{w}				
467_{w}				461_{11}
391_{w}	399_{9}		401_{5}	
380_{w}	375_{13}		380_{7}	
	359_{10}		362_{6}	367_{27}
				351_{26}
335_{w}			320_{17}	
300_{w}	315_{25}	316_{m}	311_{18}	310_{51}
290_{vw}	303_{27}	$294_{w, sh}$	297_{11}	298_{51}
	258_{16}		262_{8}	262_{9}
	226_{9}		231_{5}	236_{24}
		208_{w}	210_{5}	
			186_{10}	177_{32}
			145_{24}	150_{85}

* vw=very weak; w=weak; m=medium; s=strong; vs=very strong; sh=shoulder

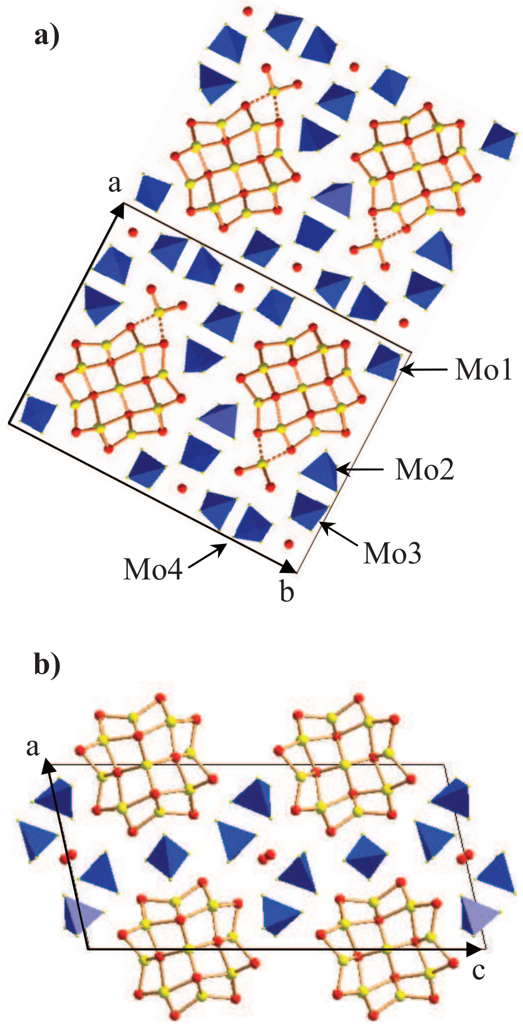

Fig. 3.18 a) γ'-Bi_2MoO_6 structure projected along the c axis [30] compared with b) $Bi_{26}Mo_{10}O_{69}$ structure (the parent compound of ε solid solution) projected along the b axis [18].

Matsuuura *et al.* [29] and Hardcastle and Wachs [27] noted that the multiple Mo-O bond lengths and MoO_4 tetrahedron types in γ'-Bi_2MoO_6 would explain the split of the stretching vibration bands of a regular tetrahedron into several stretching bands at 776, 794, 828, 856, 871, 885 and 903 cm^{-1}. Subsequently, the shortest Mo-O bond distance of about 1.718 Å would be responsible for the highest stretching wavenumber occurring above 856 cm^{-1}. Interestingly, several Raman bands of $Bi_{25.75}Mo_{10}O_{68.625}$ appear at the same frequency as those of γ'-Bi_2MoO_6. This is explained by the similarity of these two structures, as illustrated in Fig. 3.18, which both exhibit a fluorite-cation arrangement. The structure of $Bi_{26}Mo_{10}O_{69}$: the parent compound of $Bi_{25.75}Mo_{10}O_{68.625}$ was determined by single X-ray diffraction and powder neutron diffraction [18, 19, 33]. The description of this structure was also given in detail in the first chapter.

From Fig. 3.18, the rose-shaped $[Bi_{12}O_{14}]^{8+}$ column in $Bi_{26}Mo_{10}O_{69}$ was found to be a predominant part of the bismuth oxide latin cross-shaped channels in γ'-Bi_2MoO_6. The $[Bi_{12}O_{14}]^{8+}$ column displays the same geometry, dimensions and thickness in both cases. The latin cross-shaped channels in γ'-Bi_2MoO_6 are obtained by linking the rose-shaped $[Bi_{12}O_{14}]^{8+}$ columns with Bi_2O_2 chains. The isolated MoO_4 tetrahedra fill in the space between these channels of bismuth oxide [18].

However, only three types of Mo atoms were found in the $Bi_{26}Mo_{10}O_{69}$ structure. Two of them, Mo(1) and Mo(2), surround the isolated Bi(7) atom coordinated with 8 O atoms. The Mo(3) type MoO_4 tetrahedra are not involved in the Bi(7) coordination, they are only shared between the two rose-shaped $[Bi_{12}O_{14}]^{8+}$ columns. These three molybdates are also isolated distorted tetrahedra with 9 different Mo-O bond lengths: two shortest bond distances, 1.65(2) and 1.69(3), and others (1.71(3)-1.85(3) Å) which are also found in γ'-Bi_2MoO_6 structure [19]. These similar Mo-O bond lengths could explain why all the Mo-O stretching bands of $Bi_{25.75}Mo_{10}O_{68.625}$ spectrum are found in the γ'-Bi_2MoO_6 spectrum but with different intensity. For the two shortest bond distances: 1.65(2) and 1.69(3) in $Bi_{25.75}Mo_{10}O_{68.625}$, it is possible that the presence of these bonds could be one of the factors that influence the large peak shape of the highest vibration frequency at 903 cm^{-1}. The wider Raman bands observed for $Bi_{25.75}Mo_{10}O_{68.625}$ could also be caused by the oxygen defects found in this structure which is strongly related to its good ionic conductivity property [34].

5.3. Correlation between polymorphs of Bi_2MoO_6 and $Bi_{2n+4}Mo_nO_{6(n+1)}$ series

The phase transitions of γ-Bi_2MoO_6 and L-$Bi_{2n+4}Mo_nO_{6(n+1)}$ ⇔ γ'-Bi_2MoO_6 and the high-temperature $[Bi_{12}O_{14}]^{8+}$ provide a new insight into structural relationship between these phases. The similarity between the high-temperature forms, γ'-Bi_2MoO_6 and the ε solid solution, has been previously demonstrated. The structure of the low-temperature forms, γ-Bi_2MoO_6 and L-$Bi_{2n+4}Mo_nO_{6(n+1)}$, are strongly related as well.

The structure of $Bi_{2n+4}Mo_nO_{6(n+1)}$ series can also be described as a crystallographic shear derived from Aurivillius-type phase such as γ-Bi_2MoO_6 (with n=∞), consisting of $[Bi_2O_2]^{2+}$ layers alternated with layers of corner-sharing MoO_6 octahedra [24], as shown in Fig. 3.19. However, the local environments of Mo surrounded by O in these two structures are different, a tetrahedral coordination in the former and an octahedral coordination in the latter. The Mo surrounding in γ-Bi_2MoO_6 is highly distorted and characterized by two longer Mo-O bond lengths. This is likely due to the $6s^2$ lone pair of Bi that perturbs tetrahedral coordination of Mo atom. This assumption is also consistent with the presence of the perfect MoO_4 tetrahedra in the La_2MoO_6 structure [35], a similar structure to that of γ-Bi_2MoO_6.

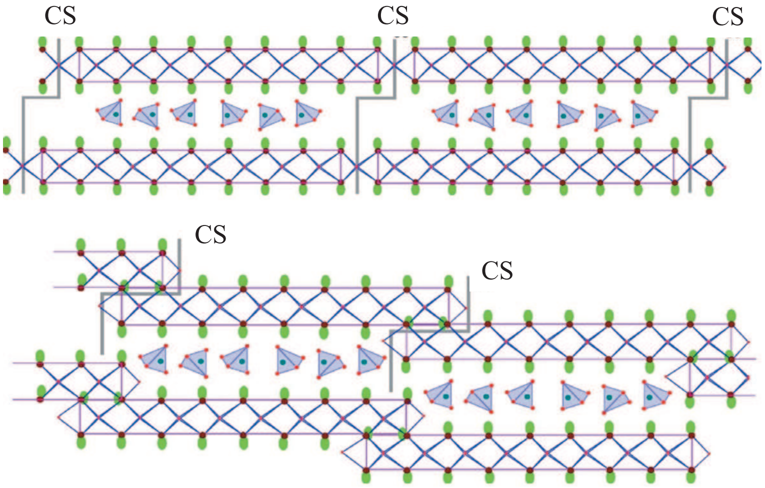

Fig. 3.19 Crystallographic shear (CS) operation applied to γ-Bi_2MoO_6 every six $[MoO_4]$ tetrahedral gives rise to the $Bi_{16}Mo_6O_{42}$ structure. Gray lines indicate the CS operation [24].

Coming back to the structure of the $Bi_{2n+4}Mo_nO_{6(n+1)}$ series, it is built upon $[Bi_{2n+4}O_{2n+6}]^{2n+}$ layers surrounded by groups of isolated MoO_4 tetrahedra (Fig. 3.15 and Fig. 3.19). As these layers can also be viewed as blocks of fluorite structure, a model based on this consideration of the formation of γ-Bi_2MoO_6 can be proposed.

6. TENTATIVE SCENARIO TO EXPLAIN THE γ-Bi_2MoO_6 FORMATION

From the *in-situ* study, it was clear that under hydrothermal conditions, γ-Bi_2MoO_6 forms from a distorted fluorite structure. The *ex-situ* experiments give us new insights:

1) At pH > 6, MoO_4^{2-} species are present in the solution at the beginning of the reaction. This seems to be a requisite for the formation of γ-Bi_2MoO_6.
2) The intermediate form is $(Bi_{1-x}Mo_x)_2O_{3+\delta}$ solid solution with fluorite structure, in which Mo content is slightly lower than in γ-Bi_2MoO_6.
3) The Mo (VI) atoms are present as isolated tetrahedral MoO_4^{2-} species in the fluorite structure.
4) When the hydrothermal reaction time increases, the composition of the intermediate fluorite structure remains the same but a slight increase of the particle size is observed and an increase of strain is likely to occur.
5) The first particles of Bi_2MoO_6 are characterized as thin platelets.
6) By heating in air, the intermediate form transforms to a mixture of γ-Bi_2MoO_6 and a member of the L-$Bi_{2n+4}Mo_nO_{6(n+1)}$ series. The structure of the latter can be viewed as Bi-O blocks of fluorite structure spaced with MoO_4 species ordered along [010].

Therefore, according to the *in-situ* and *ex-situ* studies during hydrothermal synthesis of γ-Bi_2MoO_6, it appears that this phase forms from a distorted fluorite structure in which MoO_4 species are randomly distributed. As the reaction time increases, these species would self-organize, leading to an increase of strain and to the division of starting structure into thin strips of Bi_2MoO_6. Then, these thin platelets further grow into well crystallized γ-Bi_2MoO_6. These assumptions are supported by XRD and SEM, as shown in Fig. 3.20.

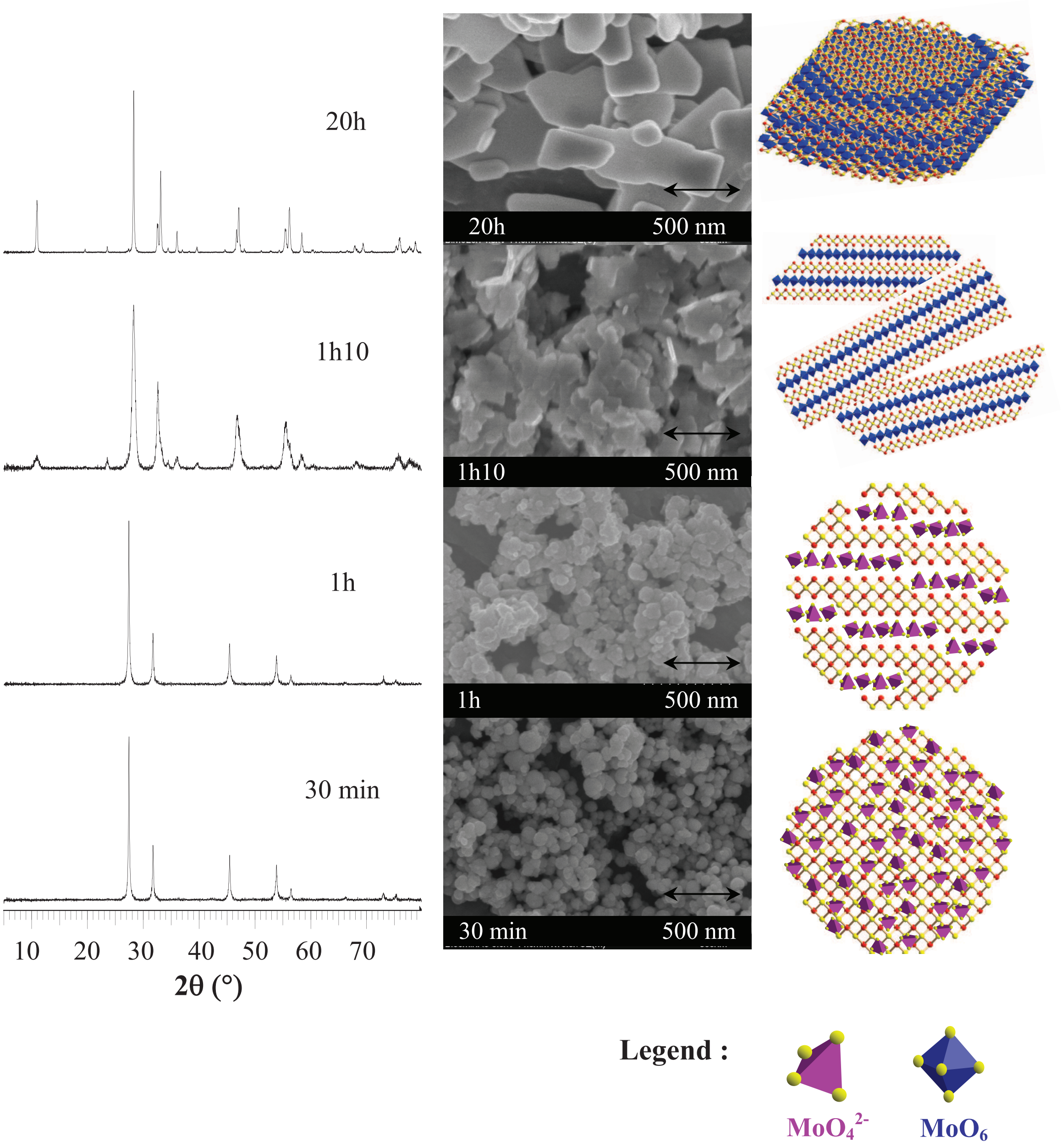

Fig. 3.20 XRD patterns, SEM pictures and proposed atomic-level schemas of the sample prepared by hydrothermal synthesis at 180°C for 30 min, 1 h, 1h30 and 20h.

7. CONCLUSION

The *in-situ* characterization by combination of high resolution X-ray diffraction, XANES and Raman Scattering has proven to be a powerful technique to study the formation of a solid, as shown in Chapter 2. It allows the accurate characterization of compounds in real conditions. Moreover, kinetic information on crystal growth is obtained, whereas in *ex-situ* experiment, reaction times may be erroneous because of thermal inertia during the heating and cooling process.

However, the analysis of the sample morphology by *ex-situ* characterization gives new insights in the crystal growth process and by combining *in-situ* and *ex-situ* characterization; a mechanism of γ-Bi_2MoO_6 formation can be proposed. γ-Bi_2MoO_6 grows from $(Bi_{1-x}Mo_x)_2O_{3+\delta}$ solid solution with fluorite structure in which the arrangement of MoO_4 species leads to the division of particles into thin strips of γ-Bi_2MoO_6, the first particles of γ-Bi_2MoO_6. It is interesting to note the structural similarities between both high-temperature and low-temperature forms of the ε solid solution (around the parent compound $Bi_{26}MoO_{69}$) and Bi_2MoO_6, which are both derived from the fluorite structure. However, the former, being oxygen deficient, is a good oxide ion conductor whereas the latter is a good catalyst. With the aim to combine the oxide ionic conductivity of the ε solution and the catalytic properties of γ-Bi_2MoO_6, the development of a Catalytic Dense Membrane Reactor (CDMR) is possible. The catalytic applications of these materials are the aim of Chapter 4 of this thesis.

References

[1] F. Trifiro, H. Hoster, and R. D. Scale, *J. Catal.*, 1972, **25**, 12–24.

[2] A. M. Beale *Novel Low Temperature Methods for mixed complex oxide catalysts and their characterization using in situ SR techniques* PhD thesis, University College London and Davy-Faraday Reseach Laboratory of The Royal Institution of Great Britain, 2003.

[3] S. Himeno, H. Niiya, and T. Ueda, *Bull. Chem. Soc. Japan*, 1997, **70**, 631–637.

[4] W. Griffith, *J. Chem. Soc. A*, 1970, pp. 286–291.

[5] W. Griffith and P. Lesniak, *J. Chem. Soc. A*, 1969, **1066-1071**.

[6] F. Gonzalez-Vilchez and W. P. Griffith, *J. Chem. Soc., Dalton Trans.*, 1972, pp. 1416 – 1421.

[7] K.-H. Tytko and O. Glemser, *Adv. Inorg. Chem.*, 1976, **19**, 239–315.

[8] M. Dieterle *In Situ Resonance Raman Studies of molybdenum Oxide Based Selective Oxidation Catalysts* PhD thesis, Fachbereich Chemie der Technischen Universität Berlin, 2001.

[9] G. Johansson, L. Pettersson, and N. Ingri, *acta.chem.scand.*, 1979, **33a**, 305–312.

[10] S. Saleem and G. Aruldhas, *Pramana*, 1983, pp. 283–291.

[11] J. A. Bergwerff, T. Visser, and B. M. Weckhuysen, *Catal. Today*, 2008, **130**, 117–125.

[12] J. Rodriguez-Carvajal, *Commission Powder Diff. Int. Union Cryst., Newsletter*, 2001, **26**, 12–19.

[13] A. A. Eliseev, V. A. Efremmov, G. M. Kuzmicheva, E. S. Konovalova, V. I. Lazorenko, Y. B. Paderno, and S. Y. Khlyustova, *Kristallografiya*, 1986, **31**, 803–805.

[14] P. Thompson, D. E. Cox, and J. B. Hastings, *J. Appl. Cryst.*, 1987, **20**, 79–83.

[15] G. K. Williamson and W. H. Hall, *Acta Metal.*, 1953, **1**, 22–31.

[16] A. R. Stokes and A. J. C. Wilson, *Proc. Phys. Soc. London*, 1944, **56**, 174–181.

[17] ed. R. L. Snyder, H. J. Bunge, and J. Fiala, *Microstructure Analysis from Diffraction*, International Union of Crystallography, 1999.

[18] R. N. Vannier, G. Mairesse, F. Abraham, and G. Nowogrocki, *J. Solid State Chem.*, 1996, **122**, 394–406.

[19] R. N. Vannier, F. Abraham, G. Nowogrocki, and G. Mairesse, *J. Solid State Chem.*, 1999, **142**, 294–304.

[20] E. Vila, J. M. Rojo, J. E. Iglesias, and A. Castro, *Chem. Mater.*, 2004, **16**, 1732–1739.

[21] E. Vila, J. E. Iglesias, J. Galy, and A. Castro, *Solid State Sci.*, 2005, **7**, 1369–1376.

[22] E. Vila, A. R. Landa-Canovas, J. Galy, J. E. Iglesias, and A. Castro, *J. Solid State Chem.*, 2007, **180**, 661–669.

[23] J. Galy, J. Hernandez-Velasco, A. R. Landa-Canovas, E. Vila, and A. Castro, *J. Solid State Chem.*, 2009, **182**, 1177–1187.

[24] A. R. Landa-Canovas, E. Vila, J. Hernandez-Velasco, J. Galy, and A. Castro, *Acta Cryst. B*, 2009, **65**, 458–466.

[25] J. Galy, R. Enjalbert, P. Rozier, and P. Millet, *Solid State Sci.*, 2003, **5**, 165–174.

[26] N. Sharma, R. B. Macquart, M. Christensen, M. Avdeev, Y.-S. Chen, and C. D. Ling, *J. Solid State Chem.*, 2009, **182**, 1312–1318.

[27] I. Matsuura, R. Schut, and K. Hirakawa, *J. Catal.*, 1980, **63**, 152–166.

[28] F. Hardcastle and I. Wachs, *J. Raman Spectrosc.*, 1990, **21**, 683–691.

[29] F. D. Hardcastle and I. E. Wachs, *J. Phys. Chem.*, 1991, **95**, 10763–10772.

[30] D. J. Buttrey, T. Vogt, U. Wildgruber, and W. R. Robinson, *J. Solid State Chem.*, 1994, **111**, 118–127.

[31] V. Nassif, R. E. Carbonio, and J. A. Alonso, *J. Solid State Chem.*, 1999, **146**, 266–270.

[32] J. C. Sczancoski, L. S. Cavalcante, N. L. Marana, R. O. da Silva, R. L. Tranquilin, M. R. Joya, P. S. Pizani, J. A. Varela, J. R. Sambrano, M. S. Lid, E. Longoc, and J. Andrése, *Current Applied Physics*, 2010, **10**, 614–624.

[33] D. J. Buttrey, T. Vogt, G. P. A. Yap, and A. L. Rheingold, *Mater. Res. Bull.*, 1997, **32**, 947–962.

[34] L. Holmes, L. Peng, I. Heinmaa, L. A. O'Dell, M. E. Smith, R.-N. Vannier, and C. P. Grey, *Chem. Mater.*, 2008, **20**, 3638–3648.

[35] J. S. Xue, M. R. Antonio, and L. Soderholm, *Chem. Mater.*, 1995, **7**, 333–340.

CHAPTER 4

Experiments in Catalytic Dense Membrane Reactor

SUMMARY OF CHAPTER 4

Chapter 4
Experiments in Catalytic Dense Membrane Reactor

1. INTRODUCTION

Nowadays, selective oxidation of light hydrocarbons by heterogeneous catalysis is the basis for the synthesis of a large part of the monomers or modifiers used for the production of fibers and plastic, which represents a large segment of the modern chemical industry. The selective oxidation of light hydrocarbons has been intensively studied over the last decades [1, 2, 3, 4, 5, 6, 7, 8]. It is one of the most attractive and challenging process due to the high potential as feedstock for providing more useful chemical products. However, the major problem of this process is the low selectivity of the desired products because the products are usually more active than the reactants, resulting partly in complete oxidation to CO_2. One of the effective methods to increase the selectivity to the target products can be accomplished by optimizing the process design.

As already written in Chapter 1: Aim, Background and Key Concepts, the selective oxidation of hydrocarbons follows the redox mechanism determined by Mars and Van Krevelen [9]. This mechanism relies on the direct participation of oxygen ions O^{2-} of oxide catalyst (oxygen lattice) in the reaction products. However, it is known that the direct formation of CO_2 can be promoted when the gaseous oxygen present in the reactor interacts directly with hydrocarbon which is usually the case in conventional reactors. It was found possible to achieve higher selectivity to the desired products by "isolating" the gaseous oxygen while the catalyst reacts with the hydrocarbon. The result is the decoupling of the two steps of the redox mechanism that may be performed either along time (pulse and periodic feed reactors) or along space (circulating fluid bed reactor, catalytic membrane reactor) [10, 11].

The Catalytic Dense Membrane Reactor is one of the most interesting devices which can combine reaction and separation in a single unit [11]. The potential of membrane has been demonstrated at the laboratory scale for the direct and oxidative dehydrogenation hydrocarbons [2, 12]. Despite some tries, this concept is not applied at the industrial scale

[13]. The principal limitation of the development of membrane reactors is the membrane itself. The optimization of the existing membranes and the development of new membrane materials that would be more appropriate, are still necessary and deserve studies for a future use of membranes in industrial applications.

One of the most important characteristics of the membrane is its high oxide ion conductivity. In this context, the ε solid solution based on the parent compound $Bi_{26}Mo_{10}O_{69}$ could be a good candidate as a membrane material. It was demonstrated to exhibit a high conductivity at low temperature and its physico-chemical properties have been well characterized [14, 15, 16, 17, 18, 19]. Although the catalytic properties of these compounds have not yet been well established, it is expected that the two principal elements of this solid solution, bismuth associated with molybdenum, would favor the partial oxidation of propylene, possibly to acrolein. In case the catalytic properties would not be correct, a solution would be to deposit γ-Bi_2MoO_6, well known as an efficient catalyst for the reaction, on the membrane surface to enhance the catalytic activity of the system. The use of $Bi_{25.75}Mo_{10}O_{68.625}$ as a membrane whose composition is close to γ-Bi_2MoO_6 in the Bi_2O_3-MoO_3 binary diagram should avoid any chemical incompatibility with γ-Bi_2MoO_6 catalyst and any evolution of chemical composition during the catalytic process.

Therefore, the aim of the final part in this manuscript is to examine the feasibility of such membranes and to study their properties in the oxidation of propylene. To do so, the physicochemical and electric properties of $Bi_{25.75}Mo_{10}O_{68.625}$ have to be investigated. More particularly, the sintering process to obtain a dense membrane (relative density > 90%) will have to be optimized, in order to avoid leaks or direct path of oxygen gas to interact with hydrocarbon. The experimental procedures, the membrane and the reactor will have also to be adjusted for improving the oxygen permeation.

2. TECHNIQUES

2.1. Physicochemical Characterization Techniques

Several techniques were used to characterize the powder and membranes before and after the catalytic reaction. Some of them were already desscribed in former chapters (XRD, SEM-EDS, TGA/DTA). X-Ray Photoelectron Spectroscopy (XPS) to study the upper nm-depth of samples and BET to obtain the specific surface area will be described here, together with conductivity measurements and catalytic bench scale experiments, including the catalytic dense membrane reactor (CDMR).

2.1.1. X-Ray Photoelectron Spectroscopy (XPS)

X-Ray Photoelectron Spectroscopy (XPS) is a surface chemical analysis technique that can be used to characterize the surface chemistry of a material within 10 nm from the surface. In general, when X-rays or electromagnetic radiation interacts with the material, the radiation is scattered, transmitted or absorbed. The dominant process in the X-Ray Photoelectron Spectroscopy is the photoelectric effect, whereby the photon is absorbed, transferring its energy to the ejected photoelectron. The kinetic energy of these photoelectrons is equal to the incident-photon energy minus the binding energy of the electron. The number of photoelectrons and the binding energy are used to quantify and identify the element or chemical species, respectively.

From XPS spectra, it is possible:

- To identify all elements (except H and He) and to determine their atomic concentration (0.1% detection limit and 10% error),
- To determine the nature of the chemical bond, the local environment and oxidation number of the elements,
- To verify the uniformity of elemental composition on the top of the surface or in the depth by ion beam etching.

XPS analysis was carried out with a VG ESCALAB 220 spectrometer under ultra high vacuum condition (10^{-7} Pa). The powder and the membrane were analyzed before and after the reaction in order to check any modification in the surface composition and to know the oxidation/reduction state of different elements that would occur during the catalytic reaction.

2.1.2. BET Surface Area Measurement

The Brunauer-Emmett-Teller (B.E.T.) method is widely used for the calculation of surface area of solids by physical adsorption of gas molecules (N_2). It is assumed that the nitrogen molecules physically adsorb on a solid in layers, there is no interaction between each adsorption layer and the Langmuir theory can be applied to each layer. The BET equation can be expressed by:

$$\frac{1}{v[(P_0/P)]-1} = \frac{1}{v_m C} + \frac{(C-1)}{v_m C}\frac{P}{P_0} \tag{4.1}$$

where P and P_0 are the equilibrium and the saturation pressure of absorbates at the adsorption temperature, respectively; v is the volume of nitrogen adsorbed; v_m is the volume of nitrogen monolayer adsorbed and C is a constant that is related to the heat adsorption. In general, the linear relationship between $1/v[(P_0/P)-1]$ and P_0/P is maintained in the range of about $0.05 < P/P_0 < 0.30$. The slope and y-intercept of the plot $1/v[(P_0/P)-1]$ vs. P_0/P are used to determine the quantity of nitrogen adsorbed and therefore to calculate the BET surface area.

The analysis of the surface area of powder was carried out using Micromeritics ASAP 2010. Prior to measurement, powder samples were degassed at 150°C.

The surface area of the γ-Bi_2MoO_6 catalyst was determined by BET method, as given in Table 4.1.

Table 4.1 Surface area measurements for γ-Bi_2MoO_6 hydrothermally synthesized before and after calcination.

Sample	BET surface area m^2/g
γ-Bi_2MoO_6 non calcined	8.2 ± 0.5
γ-Bi_2MoO_6 calcined at 550°C	4.0 ± 0.5

2.1.3. Conductivity Measurement

• *Principle*

Impedance Spectroscopy is a technique that measures the impedance of a system by applying an alternating current (AC) potential and measuring the current over a range of frequency. There are several electrical circuit models for a charge transport mechanism in a ceramic, however, the simplest one is a resistor *R* and a capacitor *C*, as shown in Fig. 4.1.

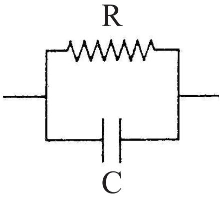

Fig. 4.1 Circuit model of a resistor and a capacitor in parallel.

The impedance of this equivalent circuit is expressed in terms of the resistance *R*, the capacity *C* and the frequency ω in Eq. (4.2)

$$Z = \frac{1}{\frac{1}{R} + i\omega C} \tag{4.2}$$

The impedance can be separated into its real, *Z'*, and imaginary, *Z"*, parts:

$$Z = \frac{\frac{1}{R}}{\left(\frac{1}{R}\right)^2 + (\omega C)^2} - i\frac{\omega C}{\left(\frac{1}{R}\right)^2 + (\omega C)^2} = Z' - iZ'' \tag{4.3}$$

A plot of *Z'* vs -*Z"* (as dependent parameters of ω) known as the Nyquist plot, will result in a semicircle of radius *R*/2 in Fig. 4.2. The time constant of this simple circuit is defined as:

$$\tau_0 = RC = \frac{1}{\omega_0} \tag{4.4}$$

It corresponds to the characteristic relaxation time of the sample. Substituting ω_0 from Eq. (4.3) into Eq. (4.4) gives *Z'* = *R*/2, *Z"* = *R*/2, so that the characteristic frequency lies at the peak of the semicircle.

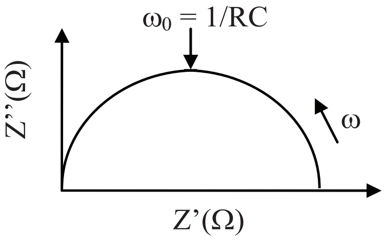

Fig. 4.2 Nyquist plot for a circuit of a resistor and a capacitor in parallel.

However, the Nyquist plot of a polycrystalline sample appears more complex. It exhibits an arc at high frequency, a second arc at intermediate frequencies, and a third arc at the lowest frequencies, as shown in Fig. 4.3 a). The corresponding circuit model is shown in Fig. 4.3 b). Three parallel RC circuits are connected together. The first circuit (R_b and C_b) is assigned to the *grain interior* behavior, the second one (R_{gb} and C_{gb}) is the *grain boundary* behavior and the third one (R_{el} and C_{el}) is the *electrode behavior*.

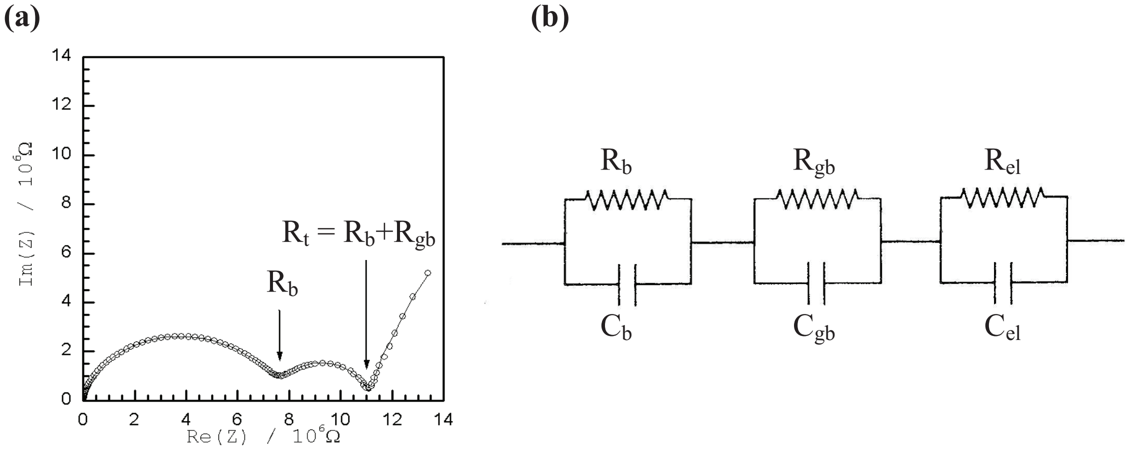

Fig. 4.3 a) Nyquist plot and b) Circuit model of a polycrystalline sample in which components in parallel have been connected together.

In our study, the conductivity of the material was deduced from the total resistant (R_t) which corresponds to the sum of the bulk resistance (R_b) and the grain boundary resistance (R_{gb}). For a cylindrical sample with parallel surfaces of the same surface area, the conductivity σ is calculated from Eq. (4.5) and is expressed in S.cm^{-1}.

$$\sigma = \frac{1}{R_t} \times \frac{e}{S} \qquad (4.5)$$

where e is the thickness and S is the cross-section area or the surface of the sample.

Moreover, the ionic conductivity is strongly dependent with the temperature and it can be expressed as:

$$\sigma = \frac{A}{T}\exp\left(-\frac{\Delta E_a}{RT}\right) \tag{4.6}$$

where A, E_a, R and T are the pre-exponential term, the activation energy, the gas constant (8,314 J.K^{-1}.mol^{-1}) and the temperature (in Kelvins), respectively.

• ***Experiments***

Electrical measurements were performed on a pellet (4.36 mm in diameter, 7.43 mm height, 97% relative density) sintered at 850°C for 1 h. The surface was first sputtered with a thin layer of gold (Emscope SC 500 sputter coater) and it was then painted with a gold past (6440 DMC^2 France) and treated at 650°C for 1h with a 5°C/min heating-cooling rate. Both methods are used to assure a good adhesion and durability of gold electrode on the two sufaces of the sample.

To measure the total conductivity, under static air, as a function of temperature, a Solartron 1255 frequency response analyser was used in the 1 Hz to 1 MHz range with a 400 mV amplitude signal, between 200°C and 800°C. The measurements were perfomed with a 20°C step and a 1 h holding time between each measurement.

To measure the conductivity under varying oxygen partial pressure (from 1 to $4\cdot10^{-5}$ atm) as a function of temperature, a Solartron 1260 frequency response analyser was used in the 0.1 Hz to 1 MHz range with a 20 mV amplitude signal between 600°C and 750°C. The measurements were performed with a 50°C step and about 12h holding time for the conductivity to be stabilized at a given temperature before each measurement. It is interesting to note that the conductivity measurements were carried in a one-atmosphere chamber (Fig. 4.4), unlike membrane reactor.

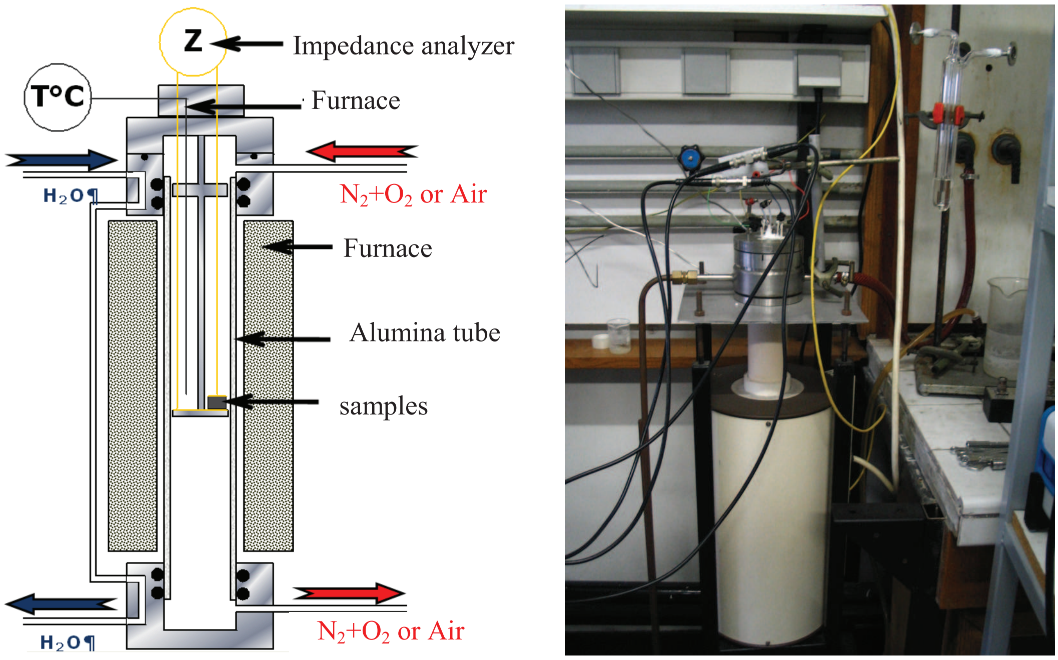

Fig. 4.4 Conductivity measurement chamber.

2.2. Catalytic Techniques

All catalytic experiments, electrochemical characterization and oxygen permeation measurements on the membrane were carried out using an experimental setup which is composed of three parts:

- The reactor system.
- The CDMR reactor.
- The Analysis System: reactants and products were analyzed by mass spectrometer.

2.2.1. Reactor System

The membrane reactor was placed in a tubular furnace equipped with a temperature controller (connected with a furnace thermocouple and a reactor thermocouple which is placed close to the membrane). The reactor was divided into three parts which are connected to three gas flow distributions, as illustrated in Fig. 4.5.

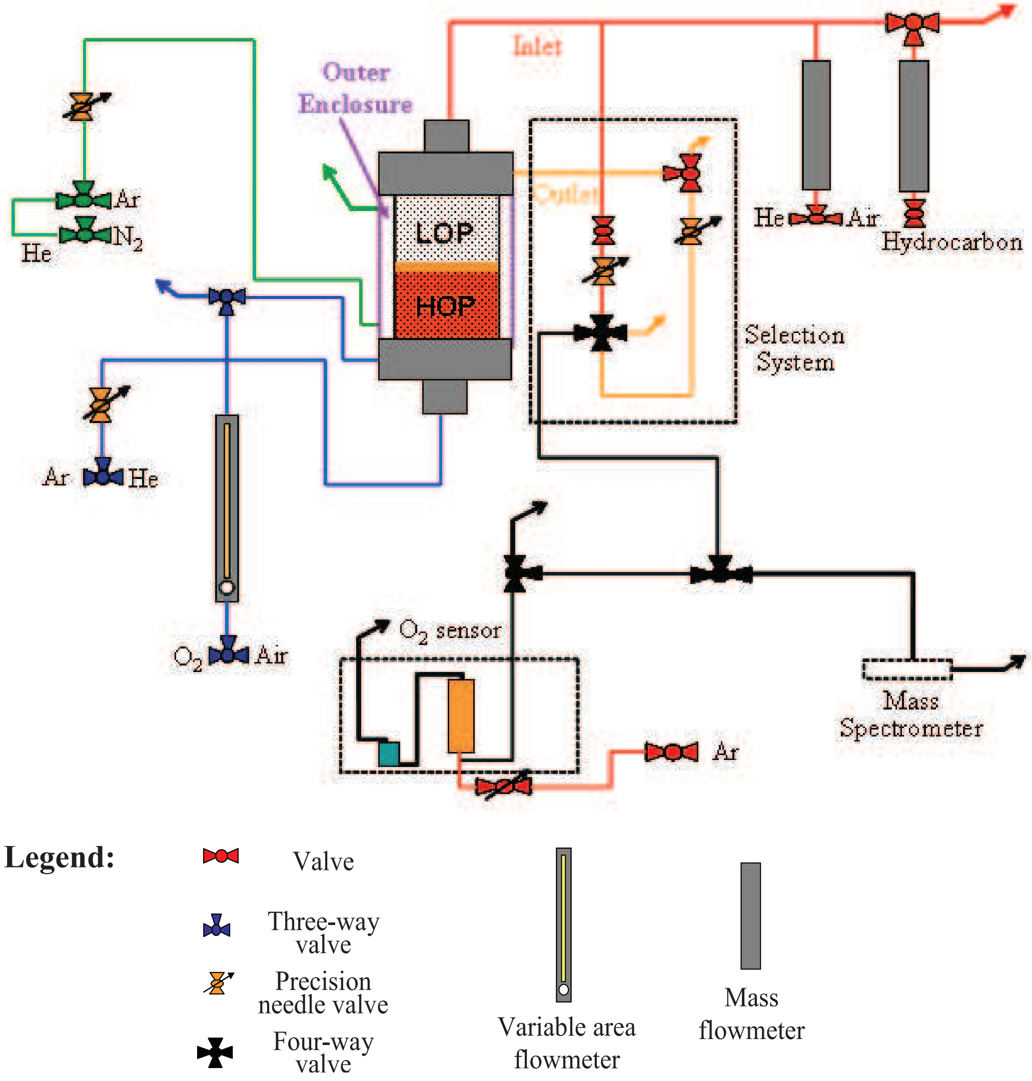

Fig. 4.5 Schematic of the reactor system

- The High Oxygen Partial Pressure side (HOP) was fed with air or oxygen with a flow rate controlled by flowmeter. The oxygen concentration in this part can be varied by dilution with helium or argon. With a three-way valve, the inlet and outlet flow rate can be verified by a bubble flowmeter.

- The Low Oxygen Partial Pressure side (LOP) was fed with helium in which the hydrocarbon can be diluted. All flow rates were controlled by mass flowmeters.

- The outer enclosure was fed with non reactive gas, i.e. nitrogen, helium or argon, to control and to reduce possible leakages at constant flow rate controlled by flowmeter. The purity of nitrogen and argon was 99.9% and of helium was 99.9999%.

The selection system allows the analysis of either the gas inlet or the gas outlet. It is possible to choose, either passing only the gas inlet (or outlet) of the reactor to be analyzed or dividing the flux into two parts so that the flow rate of one can be measured while the other is being analyzed. Two precision needle valves are added to adjust the flow rate of the divided fluxes (usually in the same proportion) or to modify the contact time in the reactor. A four-way valve is used to choose either inlet or outlet gas to be analyzed. The gas can be analyzed by either a mass spectrometer or an oxygen sensor depending on the position of a four-way valve. Argon feed is required for the use of the oxygen sensor.

2.2.2. Catalytic Dense Membrane Reactor

The reactor consists of the dense membrane which is sealed between two mullite (aluminosilicate) or alumina tubes by using a pyrex ring (or a ceramic glass powder as sealing agent) to allow the gas-tightness between the HOP (High Oxygen Partial Pressure side) and the LOP (Low Oxygen Partial Pressure side), as illustrated in Fig. 4.6 and Fig. 4.7.

An alumina ring covers the membrane sidewall to protect the membrane and to allow the tightness. The outer enclosure part of the reactor is used to check possible leaks between the LOP and HOP parts. Moreover, the inert gas fed in this part of reactor would help to isolate the membrane reactor and the external environment and to limit the oxygen diffusion from the side of the membrane into the LOP part.

Fig. 4.6 Picture of a membrane sealed with pyrex glass.

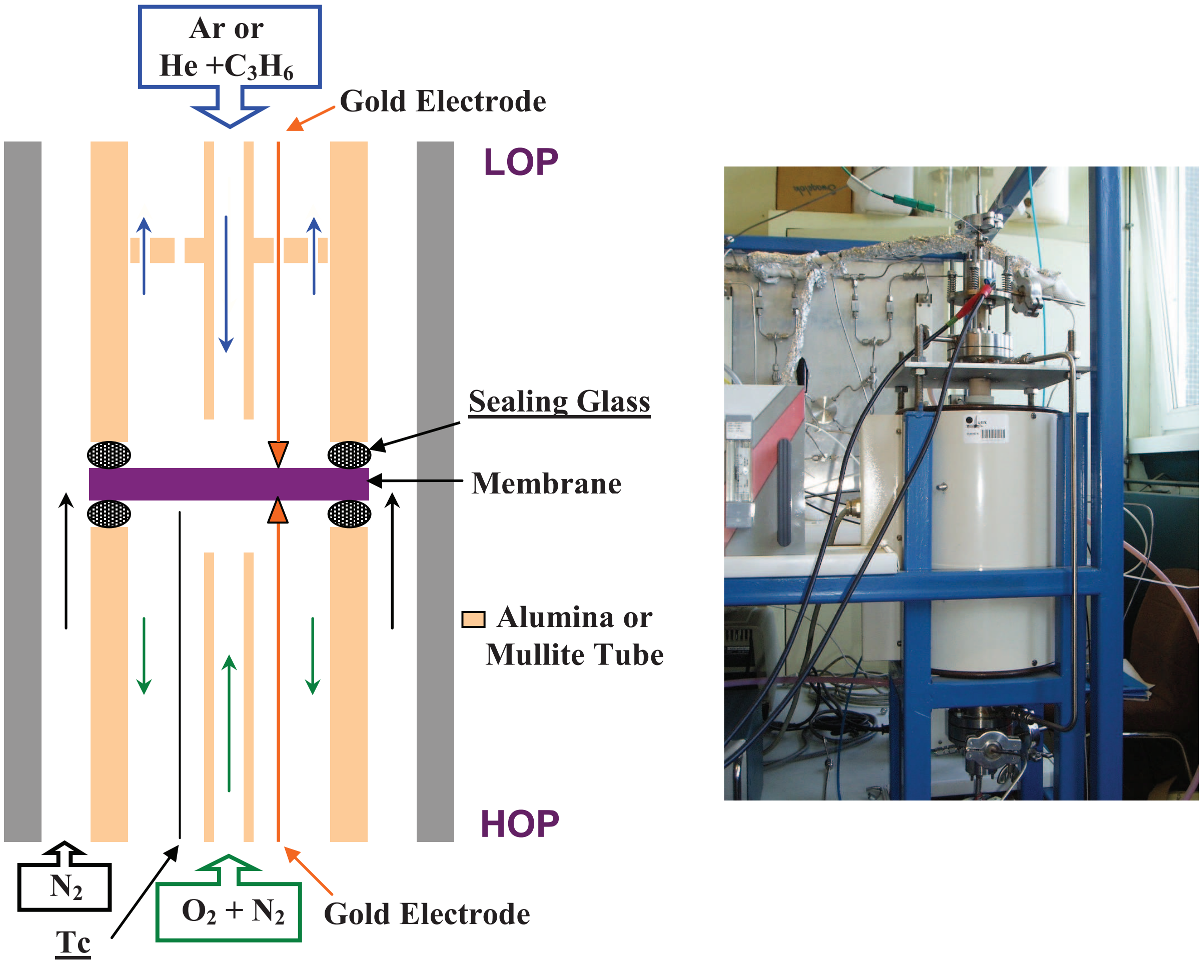

Fig. 4.7 Schematic of the CDMR reactor

2.2.3. System of Analysis

With a four-way valve, the gas inlet and outlet can be directed:

- To an oxygen sensor (Setnag) in order to measure the oxygen concentration in the gas at HOP and LOP parts, to determine the oxygen permeation of the membrane.

- Or to a quadrupole mass spectrometer (Pfeiffer Omnistar) to follow the catalytic reactions.

The quadrupole mass spectrometer was used to analyze continuously several preselected mass-to-charge ratios: m/z (Table 4.2) and to follow the evolution of the reactants and the formed products. In order to discriminate the signal of a product from the background noise, the gas outlet was measured periodically to compare with the gas inlet of the reactor. By this operation the hydrocarbon pressures as well as the total pressure were known.

Table 4.2 Masses measured by the quadrupole mass spectrometer and their corresponding products.

m/z Product	2	4	15	16	18	26	28	29	32	40	41	44	56	67	72	78
H_2	100															
He		100														
H_2O				1.8	100											
Ar										100						
N_2							100	0.7								
CO				2.8			100	1.2								
O_2				18					100							
CO_2				16			13					100				
Methane			85	100												
Ethane			4.7			22.2	100	20								
Propane			7.2			9.8	61	100		2.6	15	24				
Ethylene				1.8		53	100	1.8								
Propene				5.5		13.8	1.8			29.5	100					
Benzene						3.2	2									100
Hexadiene							2.7	4.6		5.5	100			100		
Acrolein						72.8	53	56.2		2			100			
Acrylic Acid						52.5	17.5	6.2				15.6	1.5		64.5	

From Table 4.2, it is worth noting that a mass-to-charge ratio can correspond to several fractions of different products. The values in gray color correspond to the measured mass of each product. The different contributions, calculated from the background noise, are required to determine the signal corresponding to each measured product. These signals are later converted to the partial pressure of the corresponding products in the reactor.

Especially for the case of N_2 and CO, they both correspond to the 28 mass-to-charge ratio. In order to avoid any confusion, nitrogen should not be used to sweep neither in the outer enclosure nor in the LOP and HOP parts. Ethane and ethylene belong to this mass-to-charge ratio as well. Consequently, the partial pressure of all these gases is taken into account in the quantification of CO.

2.3. Electrochemical Analysis Techniques for CDMR

2.3.1. Galvanodynamic and Galvanostatic mode

The galvanostatic and galvanodynamic polarization measurements are referred to the current imposition on the membrane which results in the voltage difference between two electrodes, offering opportunities to drive the O^{2-} through the membrane into the desired direction and to modify the catalytic reactivity of the membrane. It is worth noticing that the polarization can be performed only on a ***pure ionic conductor*** membrane while a short circuit may occur on a ***mixed ionic and electronic conductor*** membrane.

In order to achieve these measurements, electrodes have to be deposited on the surface of the membrane and they are contacted to two gold wires (Fig. 4.8) which are connected to the external electrical accessories, i.e. Solartron 1260, current generator or voltmeter.

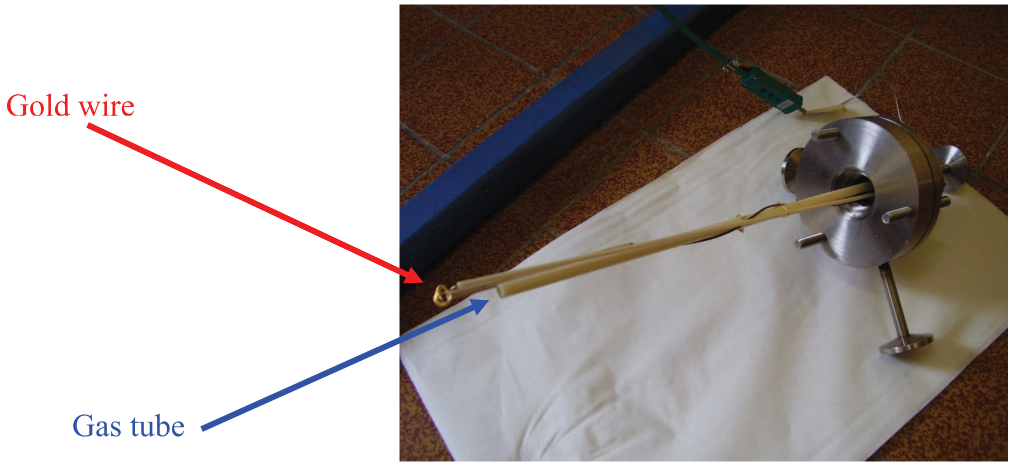

Fig. 4.8 Gold electrode in the HOP part of the reactor.

The first galvanostatic and galvanodynamic polarization measurements were performed under air flow in both LOP and HOP sides of the membrane reactor, with the aim of determining the range of applied current amplitude in which the membrane will operate properly without degradation. Usually, a linear relationship between voltage and current according to Ohm's law should be observed for the working range of current amplitude.

The galvanostatic and galvanodynamic measurements were carried out using a Solartron 1260 impedance analyzer. In the galvanostatic method, the current was applied from 0.1 mA up to 120 mA with about 3 minutes holding time for the stabilization of voltage at each measurement. In the galvanodynamic method, the current density was increased by step of 0.001 mA from 0.1 to 120 mA with a 0.1 mA/s sweeping rate.

In this work, the galvanostatic polarization has also been used in the CDMR to force the diffusion of oxygen through the membrane from HOP (air) to react with the hydrocarbon in LOP side,. This process is sometimes called ***anodic polarization***. The current was generated from a DC power supply (FX1730), and the potential difference was measured by a PHM220 Lab pH meter (Radiometer analytical SAS.). The current was increased by step of 10 mA from 10 mA to 50 mA.

2.3.2. Oxygen Permeation Measurement

The oxygen permeation flux through the membrane can be measured by an electrochemical oxygen sensor (Setnag) [20]. In order to determine this permeation flux, the partial pressure contained in the helium feed gas $Po_{2\ (initial)}$ has to be controlled while the oxygen partial pressure after passing through the membrane reactor $Po_{2\ (finale)}$ is being measured.

Knowing the experimental conditions, the oxygen fluxes J_{O2} (mol.cm².s^{-1}) diffusing through the membrane can be deduced from:

$$J_{O_2} = \frac{\Delta X \cdot D \cdot P_t}{R \cdot S \cdot T} \qquad (4.7)$$

where ΔX is the difference of oxygen molar fraction calculated from the final and initial oxygen pressure.

P_t is the total pressure of the feed gas (Pa)

D is the inlet gas flow rate of the reactor (cm^3.min^{-1})

R is the gas constant which is equal to 8.314 J.k^{-1}.mol^{-1}

S is the surface area of the sample (cm²)

T is the temperature (K)

2.4. Experimental Procedures for Catalytic Experiments

• *Set up*

The membrane was carefully displayed between the two ceramic tubes which were sealed to the membrane with a sealing glass at high temperature. Depending on temperature range at which the reaction proceeds, two reactors differing by the nature of tube and the sealant were used, mullite (aluminosilicate) tubes and pyrex ring as a sealant at 600-700°C, and two alumina tubes and a ceramic glass powder as a sealant at 500-600°C. To seal the membrane, the reactor was placed inside the furnace and heated slowly (5°C /min) to the sealing temperature (700°C for pyrex and 680°C for ceramic glass). The gas-tightness between HOP and LOP and the outer enclosure part were further controlled. The electrical contacts were verified. If there is any bad electrical contact or a short circuit from gold electrode, it is possible to take off carefully the head of the reactor and put it back properly. It is no need to take apart the whole reactor which would damage the membrane. The cooling down of the reactor to room temperature is avoided in order to prevent the cracking of the membrane due to the different thermal expansion of ceramic and sealing.

• *Procedure*

After setting up the flow rate of air in the HOP and helium in LOP (100 cm^3/min), the electrical properties or the oxygen permeation of the membrane were studied in the temperature range 500-700°C. Before starting any catalytic experiments, several operating parameters, such as flow rates, temperature, oxygen partial pressure in HOP and the flow rate of hydrocarbon before feeding into LOP (Table 4.3), were adjusted and controlled.

Table 4.3 Controlled parameters during the catalytic tests.

Temperature	500-600 (°C)
Hydrocarbon	Propene
PO_2 in HOP	0.21 atm (air)
He Total flow rate in LOP	100 cm^3/min
Inlet flow rate of LOP	50 cm^3/min
Outlet flow rate of LOP	50 cm^3/min
Contact time τ	2,3 s
Hydrocarbon flow rate	1 cm^3/min

Once the reactor was stabilized, the hydrocarbon was flowed in LOP and the evolution of reactants and products during the reaction was followed by means of the quadrupole mass spectrometer.

The conversion of hydrocarbon was calculated from the measured partial pressure, using the following equations.

$$Conversion\ \ (\%) = \frac{(P_{hydrocarbo\ n})_0 - (P_{hydrocarbo\ n})}{(P_{hydrocarbo\ n})_0} \times 100 \qquad (4.8)$$

Unfortunately, the selectivity of products and the carbon mass balance cannot be calculated in our present study due to difficulties to determine accurately the sensitivity factors for products such as water, acrolein, benzene and hexadiene.

For reactants and other products, precise gas mixtures allowed correct calibration and results are expressed in absolute pressure unit (Pa). For the other products, arbitrary sensitivity factors were attributed allowing comparative analysis and discussion of results obtained on different materials and reaction conditions.

3. PHYSICOCHEMICAL PROPERTIES OF $Bi_{25.75}Mo_{10}O_{68.625}$

Prior to the study of catalytic reaction in the CDMR, it was necessary to determine the physicochemical and electrical properties of $Bi_{25.75}Mo_{10}O_{68.625}$, as well as to optimize the elaboration of the dense membrane.

3.1. Synthesis

$$12.875\ Bi_2O_3 + 10\ MoO_3 \rightarrow Bi_{25.75}Mo_{10}O_{68.625}$$

The $Bi_{25.75}Mo_{10}O_{68.625}$ powder was prepared by solid state reaction in air, using stoichiometric amounts of pure oxides, MoO_3 (Acros, 99%) and Bi_2O_3 (Riedel-de Haën, 99.5%) which was first decarbonated by calcination at 600°C. The oxides were mixed and ground in an agate mortar and the mixture was preheated at 600°C for 12h. The preheated mixture was then ground and calcined at least 3 times, at 800°C for 12h with 5°C/min heating and cooling rates. The purity of the obtained solid was checked by X-ray diffraction (XRD) until a pure $Bi_{25.75}Mo_{10}O_{68.625}$ phase was formed.

3.2. Analysis of the polymorphism

Since the CDMR is operated at high temperature, a good understanding of the behaviour of the high-temperature polymorphs of $Bi_{25.75}Mo_{10}O_{68.625}$ is necessary. TGA/DTA and XRD analyses were performed to show the phase transformation between room temperature and 800°C.

3.2.1 Thermogravimetric/Differential Thermal Analysis (TGA/DTA)

The TGA curve of $Bi_{25.75}Mo_{10}O_{68.625}$ from room temperature to 1300°C displays a significant mass loss, about ~3.63 %, from 1015 to 1300°C (Fig. 4.9 a). This loss is related to the melting point of $Bi_{25.75}Mo_{10}O_{68.625}$ at about 976°C where a sharp endothermic peak was observed in the DTA curve and is likely due to the sublimation of molybdenum oxide. According to the polymorphism study of $Bi_{26}Mo_{10}O_{69}$ (the parent compound of the ε solid solution) reported by Vannier et *al*., the reversible phase transition triclinic ⇔ monoclinic occurred at ca. 310°C [14]. It is obvious that this phase transition should occur in $Bi_{25.75}Mo_{10}O_{68.625}$ as well. In order to verify the phase transition of the $Bi_{25.75}Mo_{10}O_{68.625}$ composition, a second TGA/DTA was carried out during heating and cooling between room temperature and 800°C (Fig. 4.9 b). No significant modification observed for the TG curves whereas the DT curves exhibit a thermal effect at 325°C. An endothermic and exothermic peak was observed during the heating and cooling process, respectively, that confirms the reversible phase transition triclinic ⇔ monoclinic of $Bi_{25.75}Mo_{10}O_{68.625}$.

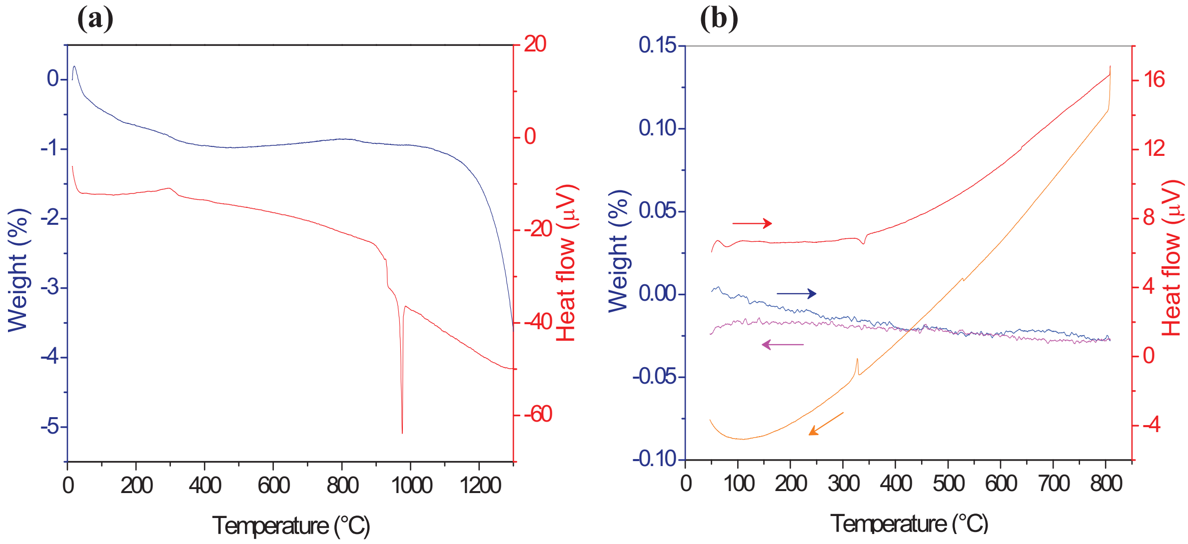

Fig. 4.9 TGA/DTA combined analyses of $Bi_{25.75}Mo_{10}O_{68.625}$ a) heated from room temperature to 1300°C and b) heating and cooling between room temperature and 800°C.

3.2.2. High Temperature X-ray Diffraction

To confirm the phase transition, X-ray diffraction was carried out from room temperature to 800°C, for heating and cooling processes (Fig. 4.10). The evolution of XRD patterns clearly revealed a reversible phase transition at ca. 350°C which correlates well with the temperature observed by DTA. This phase transition correlates well with the study of $Bi_{26}Mo_{10}O_{69}$, the parent compound of $Bi_{25.75}Mo_{10}O_{68.625}$, in which the phase transition occurs at about 310°C. Vannier *et al.* [14] also found that the transition temperature decreased when the bismuth content increased. This is in good agreement with a slightly higher transformation temperature of $Bi_{25.75}Mo_{10}O_{68.625}$.

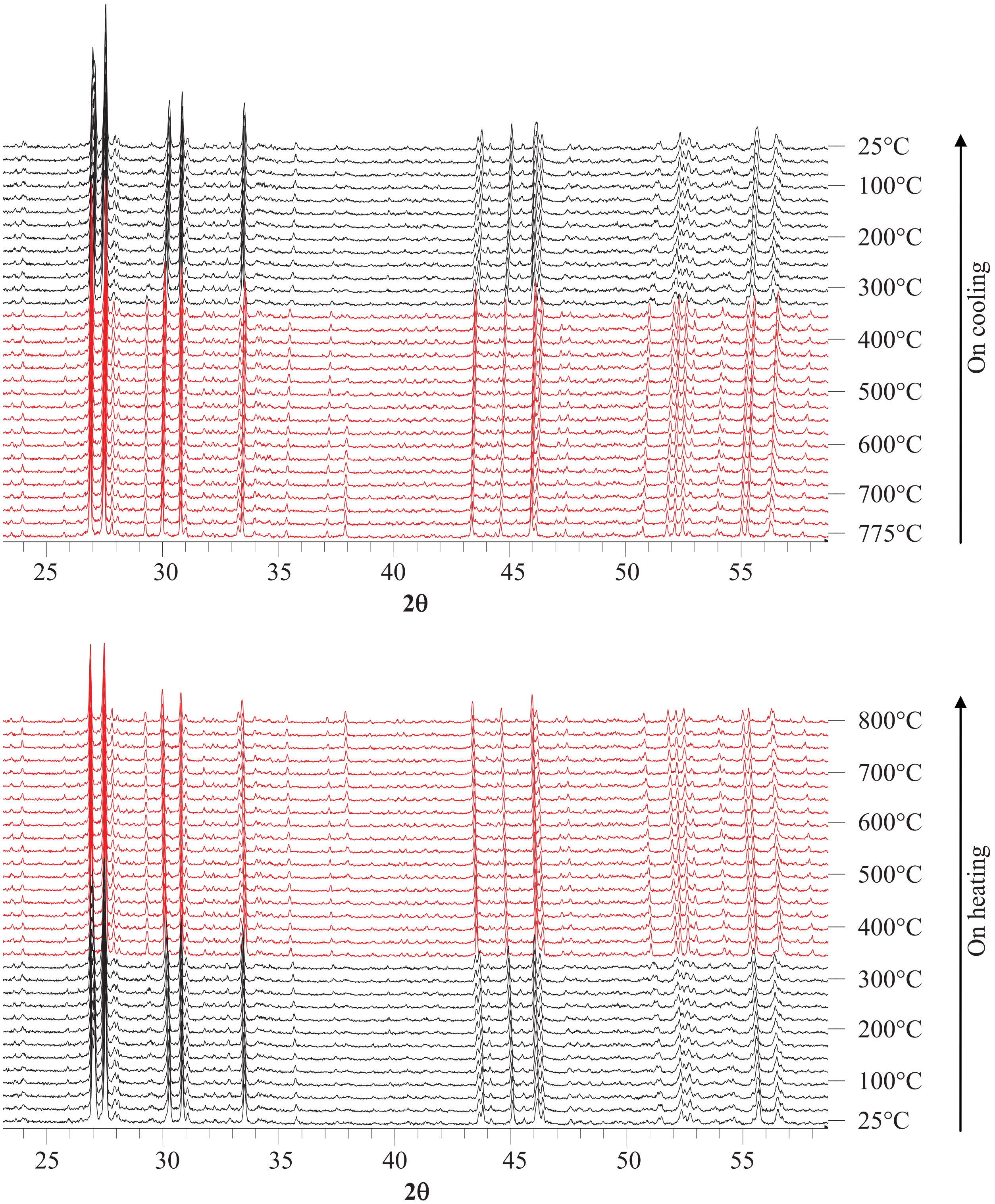

Fig. 4.10 Stack of XRD patterns of $Bi_{25.75}Mo_{10}O_{68.625}$ heated from room temperature to 800°C (below) and cooled to room temperature (above).

3.3. Preparation of Dense $Bi_{25.75}Mo_{10}O_{68.625}$ Ceramic

3.3.1. Powder Preparation

A SEM microscograph image of the $Bi_{25.75}Mo_{10}O_{68.625}$ powder synthesized at 800°C by solid state reaction is shown in Fig. 4.11 a. The grain size appears highly inhomogeneous and too big to elaborate dense ceramics. Therefore this powder was milled with a Netzsch R41-25/4/FDA batch agitator mill. About 55 g of powder was milled in ethanol with 2-mm-diameter yttrium stabilized zirconia (94.8 wt% of ZrO_2 and 5.2 wt% of Y_2O_3) balls. The milling was completed by using a Nylon grinding disc in a 570 cm^3 Teflon jar. The rotating speed was fixed to be about 1000 round/min. The efficiency of milling was followed by Scanning Electron Microscopy on the obtained particles (Fig. 4.11 b, c and d). After 4 hours of attrition milling, the particle size decreased to less than 1 μm.

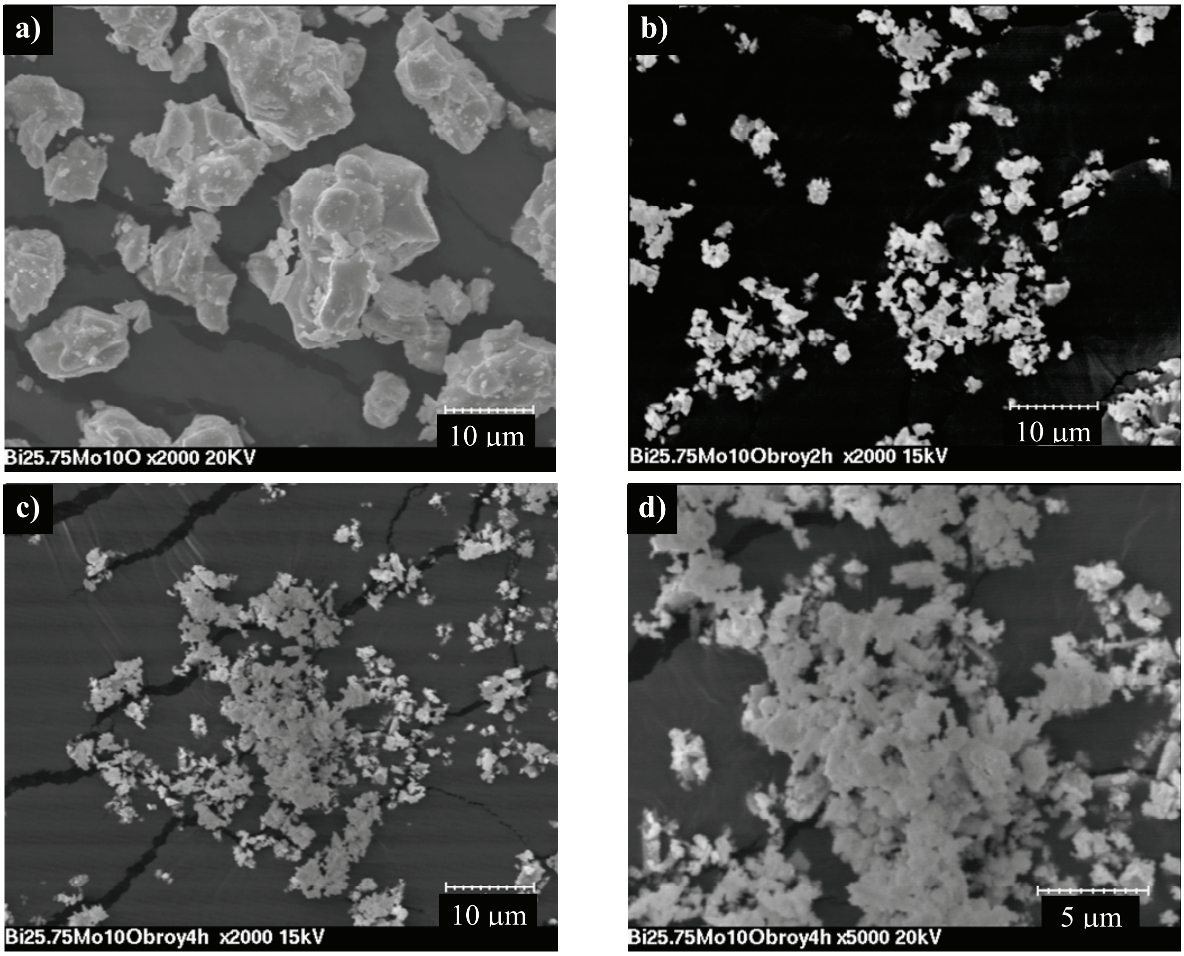

Fig. 4.11 Scanning electron micrographs of $Bi_{25.75}Mo_{10}O_{68.625}$ powder synthesized at 800°C (a), after milling for 2 hours (b) and after milling for 4 hours (c. and d. with different magnifications).

3.3.2. Optimization of the Sintering

Sintering is a method for manufacturing objects from ceramic powder. This technique offers at least two advantages: improving the mecanical consolidation by increasing the adhesion between particles and increasing the density by reducing the pores (the powder is heated just below the melting point) of a ceramic.

In order to optimise the sintering conditions, a non-isothermal sintering study was carried out by a Linseis L75 dilatometer. A green cylindrical pellet (4.54 mm in diameter, 3.97 mm height, 63% relative density) was prepared from the attrition milled powder by uniaxial prepressing followed by 180 MPa isostatic pressing. The relative density is the ratio of the experimental density deduced by measuring the mass and pellet dimension to the theoretical density calculated from crystallographic parameters (mass of a unit volume in a crystal lattice). The thermal cycle with 5°C/min heating and cooling rates with a maximum temperature at 900°C was used to investigate the linear shrinkage of $Bi_{25.75}Mo_{10}O_{68.625}$ pellet. The maximum temperature should be situated below the melting point observed previously in the TGA/DTA curves (Fig. 4.9 a), at about 976°C. The linear shrinkage curve and linear shrinkage rate of $Bi_{25.75}Mo_{10}O_{68.625}$ as a function of temperature are shown in Fig. 4.12.

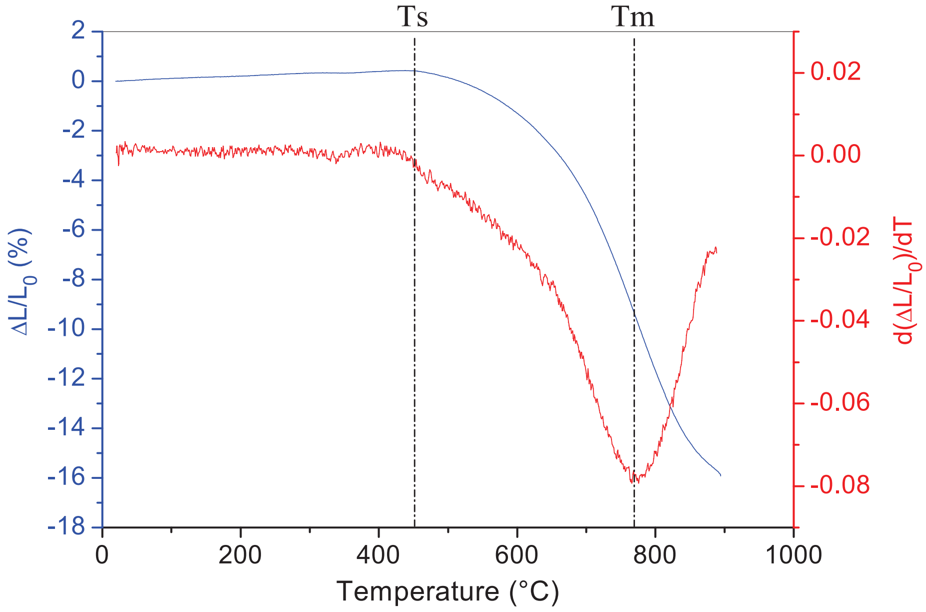

Fig. 4.12 Linear shrinkage and linear shrinkage rate as a function of temperature for attrition milled $Bi_{25.75}Mo_{10}O_{68.625}$ powder with a 5°C/min heating rate.

Two characteristic temperatures are deduced: the starting shrinkage temperature (Ts) and the temperature of the maximum shrinkage rate (Tm). The shrinkage of $Bi_{25.75}Mo_{10}O_{68.625}$ starts at approximately 450°C (Ts) and the maximum shrinkage rate is found at 770°C (Tm). The sintering process ends at about 900°C with a final shrinkage of about 16%. After the dilatometric study, the relative density of this $Bi_{25.75}Mo_{10}O_{68.625}$ pellet reached 98%. Above this temperature, the shrinkage was expected to be negligible, the grain growth would become more significant and cracks would occur.

In order to determine the optimal sintering temperature, $Bi_{25.75}Mo_{10}O_{68.625}$ pellets were sintered for one hour at temperatures between Tm=770°C and the melting point (976°C). To do so, pellets (10 mm in diameter and approximately 4 mm height) were prepared by uniaxial prepressing followed by 180 MPa isostatic pressing. The average relative density of the green pellets was about 63%. Then, the green samples were placed on the top of a $Bi_{25.75}Mo_{10}O_{68.625}$ powder layer in an alumina trail and sintered at 825 and 850°C with 5°C/min heating and cooling rates. A higher sintering temperature was not investigated as it will likely lead to grain growth and to crack formation in the ceramic. After sintering, the relative density of the pellet sintered at 850°C was 98% which is slightly higher than the 96% relative density obtained for the pellet sintered at 825°C.

The difference of density values between these two sintered pellets can possibly be explained by their different microstructure which was studied by SEM. To examine the surface of sintered pellets, a thorough preparation is necessary. The samples were polished using SiC paper of 1000, 1200 and 2400 and 3-μm-diameter diamond powder and they were later etched at a temperature at least 50°C below the sintering temperature (775 and 800°C) for 30 min, to enhance the grain boundaries. The surface was sputtered with a thin layer of gold using Emscope SC500 sputter coater before the SEM characterization.

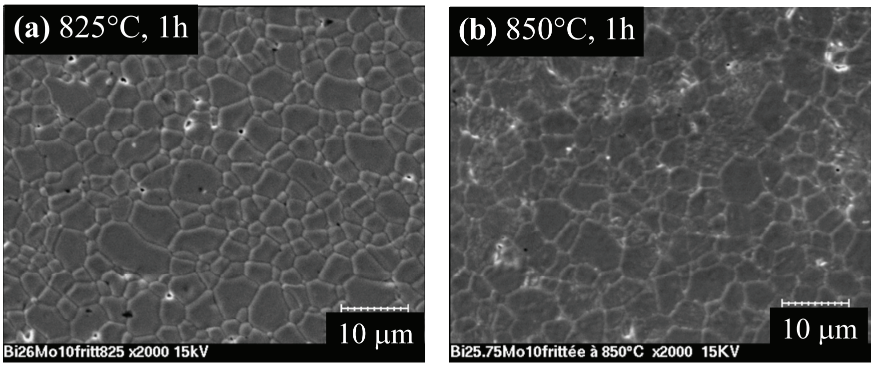

Fig. 4.13 Scanning electron micrographs of $Bi_{25.75}Mo_{10}O_{68.625}$ sintered at:
a) 825°C for 1 hour
b) 850°C for 1 hour

The micrographs (Fig. 4.13) revealed the microstructure of the $Bi_{25.75}Mo_{10}O_{68.625}$ pellets at the final stage of sintering process at 825 and 850°C. They both had a similar grain size but the only difference was the presence of pores for the lower sintering temperature at 825°C which explains its lower relative density. *Consequently*, sintering at 850°C for 1 hour was chosen as the optimized sintering conditions for $Bi_{25.75}Mo_{10}O_{68.625}$.

3.4. Electrical Properties of $Bi_{25.75}Mo_{10}O_{68.625}$

3.4.1. Conductivity of $Bi_{25.75}Mo_{10}O_{68.625}$ under Air

The total electrical conductivity of $Bi_{25.75}Mo_{10}O_{68.625}$ was measured by impedance spectroscopy from 200 to 800°C on an optimised dense ceramic. Two heating-cooling cycles were performed. The plots of $Bi_{25.75}Mo_{10}O_{68.625}$ conductivity are compared to the conductivity data of YSZ (Yttria-Stabilized Zirconia, ZrO_2-8 mol% Y_2O_3) [21] in Fig. 4.14. The remarkable change in the slope of the Arrhenius plots, around 340°C, is due to the phase transition of $Bi_{25.75}Mo_{10}O_{68.625}$ from monoclinic to triclinic symmetry.

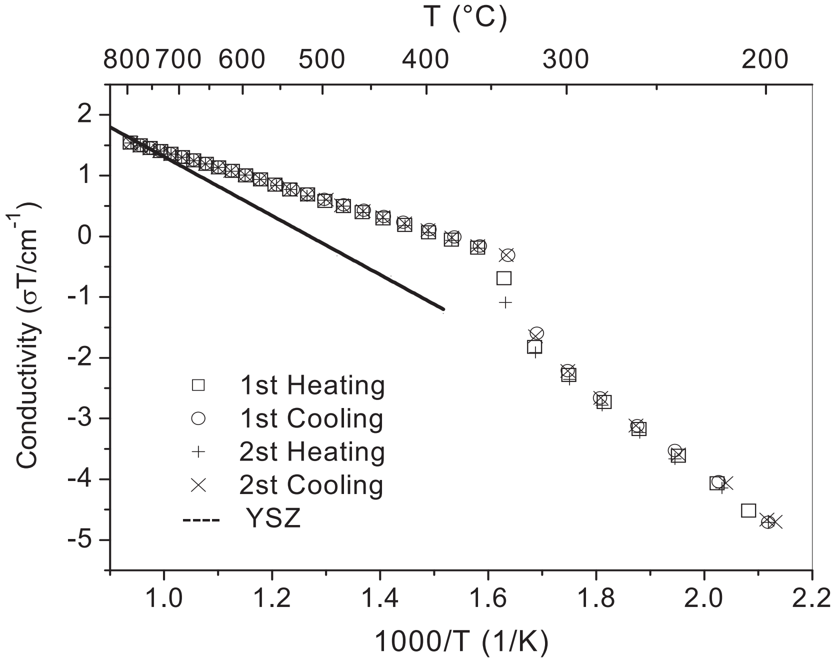

Fig. 4.14 Arrhenius plot of conductivity of $Bi_{25.75}Mo_{10}O_{68.625}$ together with the conductivity data of YZS.

From the conductivity obtained in the second cooling process, the average activation energy values calculated for the triclinic (below 320°C) and monoclinic (above 360°C) were 1.28 ± 0.03 eV and 0.525 ± 0.002 eV, respectively. Besides, there was no evolution of conductivity between heating and cooling process, except a slight difference around the transition temperature, which would indicate the good stability of the material in general. It is worth noting that the conductivity of $Bi_{25.75}Mo_{10}O_{68.625}$ is clearly higher than that of YSZ (Yittria-stabilized Zirconia) for temperatures below 650°C, with rather low activation energy for oxide ion conduction which is characteristic of bismuth based conductors. This makes $Bi_{25.75}Mo_{10}O_{68.625}$ an appropriate membrane for CDMR applications, operating at temperatures higher than 360°C to avoid the phase transition.

3.4.2. Conductivity of $Bi_{25.75}Mo_{10}O_{68.625}$ under Partial pO_2

We have just seen that $Bi_{25.75}Mo_{10}O_{68.625}$ has a good conductivity at low temperature. However it was still uncertain whether the material is a pure ionic conductor or a mixed ionic electronic conductor. Therefore, the conductivity measurements as a function of oxygen partial pressure were performed at different temperatures in order to determine the nature of charge carriers. It is known that the features of ionically or electronically conducting materials can be differenciated by the way in which their defect concentration varies with the external factors such as temperature, oxygen partial pressure and other imposed thermodynamic parameters. Moreover, it has been seen that some ionically conducting materials can become electronically conducting (p or n-type) depending on the atmosphere.

Usually the Brouwer approximation is used to describe the effect of oxygen partial pressure on the defect equilibria. Three regions are present:

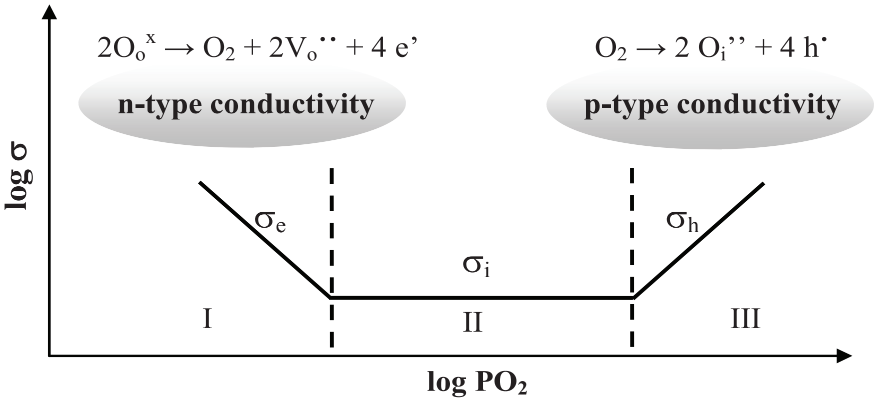

Fig. 4.15 Brouwer diagram: Defect equilibrium diagram

- **Region I** at low oxygen partial pressure: Predominant defects are the electron (e'), '***n-type conductivity σ_e***', even though oxygen vacancies ($V_o^{\bullet\bullet}$) are also present. The defect equilibrium at low oxygen partial pressure is given by

$$2O_o^x \rightarrow O_2 + 2V_o^{\bullet\bullet} + 4e' \qquad (4.9)$$

According to the Brouwer diagram, upon decrease of the oxygen partial pressure, the lattice oxygen is oxidized to oxygen gas and the ceramic is consequently reduced.

- Region II at intermediate oxygen partial pressure: The conductivity of the material is independent of oxygen partial pressure and, thus, the majority of charge carriers is oxygen ions. *Consequently* the predominent conductivity is '***ionic conductivity σ_i***'.

- **Region III** at high oxygen partial pressure: Predominant defects are electron holes ($h^{\bullet}$), '***p-type conductivity σ_h***', although interstitial anions (O_i'') are also present. The defect equilibrium at high oxygen partial pressure can be given by

$$O_2 \rightarrow 2O_i'' + 4h^{\bullet} \qquad (4.10)$$

Therefore, as the oxygen partial pressure increases, the oxygen diffuses in the structure and the electron hole concentration increases to preserved electroneutrality. The ceramic is consequently oxidized.

The conductivity of $Bi_{25.75}Mo_{10}O_{68.625}$ was measured as a function of oxygen partial pressure: 1, 0.21, $9.08\cdot10^{-4}$, $1.18\cdot10^{-4}$ and $3.86\cdot10^{-5}$ atm in the temperature range of 600-750°C in order to determine the nature of charge carriers.

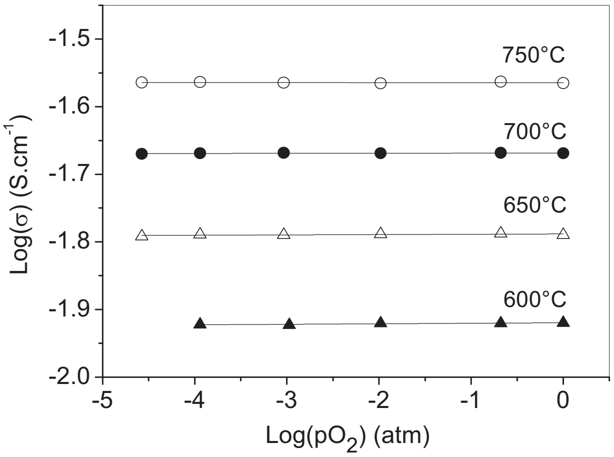

Fig. 4.16 A plot of total conductivity of $Bi_{25.75}Mo_{10}O_{68.625}$ as a function of oxygen partial pressure at 600 , 650, 700 and 750°C.

From the plot of total conductivity of $Bi_{25.75}Mo_{10}O_{68.625}$ vs. oxygen partial pressure in Fig. 4.16, it is clear that the conductivity of $Bi_{25.75}Mo_{10}O_{68.625}$ is effectively independent of oxygen partial pressure between 600°C and 750°C, and for oxygen partial pressures from 10^{-5} to 1 atm. Consequently, it is concluded that **$Bi_{25.75}Mo_{10}O_{68.625}$ is a pure ionic conductor in this range of oxygen partial pressure and temperature**.

As previously mentioned in Chapter 1, the CDMR applications require a good oxygen permeation which is strongly dependent to the ionic conductivity, for oxide ion diffusion, and also to the electronic conductivity, for electronic diffusion. Moreover, the oxygen surface exchange can limit the oxygen permeation as well. However, the surface exchange kinetics in $Bi_{25.75}Mo_{10}O_{68.625}$ are still unknown. Although $Bi_{25.75}Mo_{10}O_{68.625}$ has a high ionic conductivity but a negligible electronic conductivity, it is clear that this material cannot provide any oxygen permeation. The same difficulty was encountered in the study of BIMEVOX membranes in the frame of Hervé Bodet PhD thesis [22]. To improve the oxygen permeation rate, a BIMEVOX/Au *cermet* was first tested, but, as shown by E. Capoen et *al*. in a previous study [23, 24], the oxygen transport in the ceramic was limited by the oxygen surface exchange kinetics. Therefore, an electrical bias was applied in order to force the oxygen transfer through the ceramic, [25].

The same methodology was applied to the $Bi_{25.75}Mo_{10}O_{68.625}$ membrane. At first, a *cermet* membrane was built to increase the electronic conductivity. A current supply was further used to control the oxygen diffusion. In the latter case, γ-Bi_2MoO_6 was deposited onto the surface in order to modify the catalytic activity of the membrane.

4. $Bi_{25.75}Mo_{10}O_{68.625}$-Ag *CERMET* FOR CDMR APPLICATIONS

Making a *cermet* membrane to improve the oxygen flux by increasing the electronic conductivity of the membrane seems to be a promising means. The *cermet* designation corresponds to a mixed CERamic-METal compound and we choose to work on a $Bi_{25.75}Mo_{10}O_{68.625}$-Ag *cermet* with 60 vol% of $Bi_{25.75}Mo_{10}O_{68.625}$ and 40 vol% of silver. Silver was chosen because its cost is lower compared with gold and its chemical compatibility with $Bi_{25.75}Mo_{10}O_{68.625}$ is good. 40 vol% of silver was chosen to ensure a good percolation of the oxide ion conducting ($Bi_{25.75}Mo_{10}O_{68.625}$) and the electronically conducting (Ag) phases.

Indeed, Wu and Liu found that the percolation treshold should be 1/3 volume fraction, and that the ambipolar conductivity (c.f. Chapter 1, CDMR applications) would be relatively high when the volume fraction of each phase is within the range 1/3 to 2/3 [26]. This was verified in the case of YSZ-Pd *cermet* for which the YSZ-Pd (30 vol%), which displayed discontinuous Pd phase, provided a much lower oxygen permeability than YSZ-Pd (40 vol%) continuous Pd phase in Fig. 4.19 [27].

4.1. Synthesis and Sintering Optimization

The *cermet* powder was prepared by mixing $Bi_{25.75}Mo_{10}O_{68.625}$ powder and silver powder (Aldrich, 99.9%, 2-3.5 µm grain size) in ethanol. A homogeneous mixture was obtained by supersonic bath and the ethanol was then evaporated slowly by using a rotative evaporator. To obtain the wanted volume concentration, the mass of each component was calculated using the following equation:

$$m_{\mathrm{Bi}_{25.75}\mathrm{Mo}_{10}\mathrm{O}_{68.62}} = \frac{m_{total}}{\left[1 + \frac{(1-x)}{x} \times \frac{d_{Ag}}{d_{\mathrm{Bi}_{25.75}\mathrm{Mo}_{10}\mathrm{O}_{68.62}}}\right]} \tag{4.11}$$

$m_{\mathrm{Ag}} = m_{\mathrm{tot}} - m_{\mathrm{Bi25.75Mo10O68.625}}$

x is the volume concentration of $Bi_{25.75}Mo_{10}O_{68.625}$ in the *cermet*

$d_{\mathrm{Ag}} = 10.55$ g/cm^3

$d_{\mathrm{Bi25.75Mo10O68.625}} = 7.51$ g/cm^3

The sintering optimization was proceeded by using the same preparation methods than described for sintering the pure $Bi_{25.75}Mo_{10}O_{68.625}$. A non-isothermal sintering study was carried out on a green *cermet* pellet after uniaxial pressing and iso-static pressing at 180 MPa (3.97 mm in diameter, 4.42 mm height, 69% relative density). A thermal cycle: heating and cooling rates of 5°C/min with a maximum temperature at 900°C, the same temperature as that of the pure ceramic, was used to investigate the linear shinkage of $Bi_{25.75}Mo_{10}O_{68.625}$-Ag *cermet* pellet.

The shrinkage curves of the $Bi_{25.75}Mo_{10}O_{68.625}$-Ag *cermet* in Fig. 4.17 are completely different from that of the ceramic alone. They show two shrinkages and the moltening of the *cermet* after the critical temperature (Tc) at 750°C where the final shinkage is about 52.57%. This could be explained by the moltening of silver when the temperature gets close to its melting point at about 961.8°C. The first shrinkage was found between 385 and 570°C, with the starting shrinkage temperature (Ts_1) and the temperature of the maximum shrinkage rate (Tm_1) at 385 and 455°C, respectively. The second shrinkage was located between 570 and 750°C which is characteristic by Ts_2 at 570 and Tm_2 at 665°C. It appears that the optimal sintering temperature of $Bi_{25.75}Mo_{10}O_{68.625}$-Ag *cermet* should be between Tm_2 at 665 and the critical temperature (Tc) at 750°C because above this temperature, the silver would molten and the distribution of silver particles would be inhomogeneous.

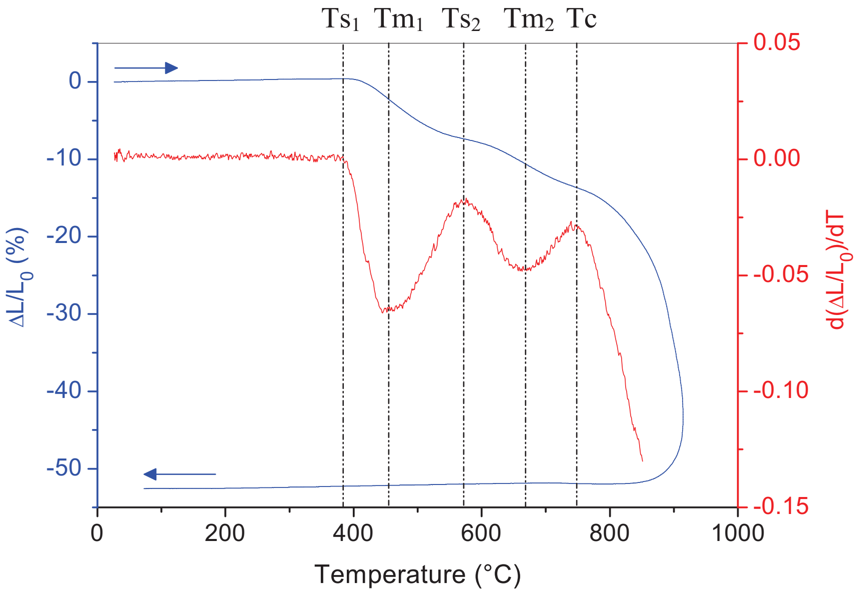

Fig. 4.17 Linear shrinkage (heating-cooling) and linear shrinkage rate (heating) as a function of temperature for $Bi_{25.75}Mo_{10}O_{68.625}$ powder with a 5°C/min heating-cooling rate.

The sintering conditions of $Bi_{25.75}Mo_{10}O_{68.625}$-Ag *cermet* were first investigated on a small pellet (10 mm in diameter and approximately 4 mm height) at 750°C for one hour with a 5°C/min heating-cooling rate. After sintering, the pellet had a 95.57% relative density which is reasonably good enough for the CDMR applications. The microstructure and the distribution of silver in this pellet were studied by SEM with backscattered electrons. Prior to SEM analysis, the sample was prepared by polishing the surface, etched at 700°C for 30 min to enhance the grain boundaries and sputtering the surface with gold.

The SEM micrographs collected by secondary and backscattered electrons (Fig. 4.18 c and d, respectively) reveal the microstructure of the $Bi_{25.75}Mo_{10}O_{68.625}$-Ag *cermet* pellet at the final stage of sintering process at 750°C. The image collected by secondary electrons in Fig. 4.18 c shows only the texture, the roughness and few small holes on the surface of the membrane. While the image collected by backscattered electrons in Fig. 4.18 d shows extra information about the distribution of silver in the pellet, the ceramic and silver are discriminated by a contrast in color: the black parts correspond to silver and the white parts correspond to ceramic. In general the silver distribution appears homogeneous.

Afterward, a membrane to be used for the CDMR applications was prepared by the same method used previously for other pellet, but with a larger dimension (about 20 mm in diameter). The green $Bi_{25.75}Mo_{10}O_{68.625}$-Ag *cermet* membrane was then sintered at 750°C for one hour. The two surfaces of the membrane were polished first with a SiC paper of 1000 and then another SiC paper of 220 to increase the surface area to improve the catalytic activity [28]. A SEM image of the membrane with a rough surface for CDMR applications is shown in Fig. 4.18 b.

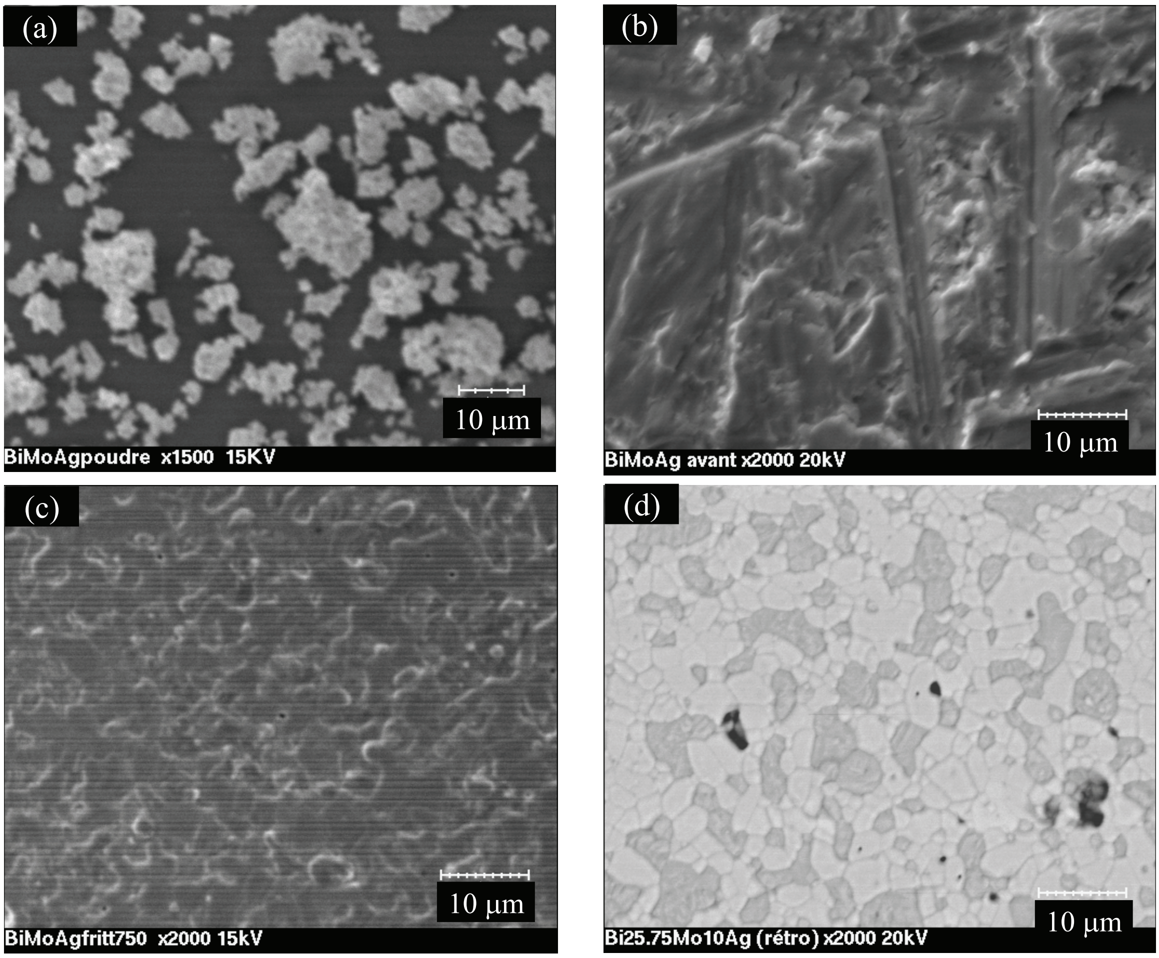

Fig. 4.18 Scanning electron micrographs of $Bi_{25.75}Mo_{10}O_{68.625}$–Ag *cermet* powder a), membrane with a rough surface for CDMR applications b), dense pellet sintered at 750°C for 1 hour viewed with secondary electrons c) and backscattered electrons d).

4.2. CDMR Applications

4.2.1. Oxygen Permeation

The oxygen permeation flux through the dense *cermet* membrane was measured under oxygen partial pressure of air (21% of O_2) (HOP) and He (~10^{-6} P_{O2} atm) (LOP), in the temperature range of 600-700°C. A pyrex ring was used as a sealing agent to assure the gas-tightness between the LOP and HOP parts. The oxygen fluxes J_{O2} (mol.cm².s^{-1}) diffusing through the membrane were deduced from equation $J_{O_2} = \frac{\Delta X.D.Pt}{R.S.T}$ (cf. 2.3.2 Oxygen Permeation Measurement). They are given in Table 4.4 and plotted in Fig. 4.19.

Table 4.4 The oxygen permeation fluxes through a $Bi_{25.75}Mo_{10}O_{68.625}$-Ag *cermet* dense membrane.

Temperature (°C)	O_2 conc. (outlet) (ppm)	Jo_2 (ppm.ml/min.cm^2)	log(Jo_2) (ml/min.cm^2)	Jo_2 (μmol/s.cm^2)	log(Jo_2) (μmol/s.cm^2)
602	2.8	103	-3.99	7.0×10^{-5}	-4.16
625	3.3	124	-3.91	8.4×10^{-5}	-4.07
649	3.7	159	-3.80	1.1×10^{-4}	-3.97
676	5.2	231	-3.64	1.6×10^{-4}	-3.80
700	7.1	301	-3.52	2.0×10^{-4}	-3.69

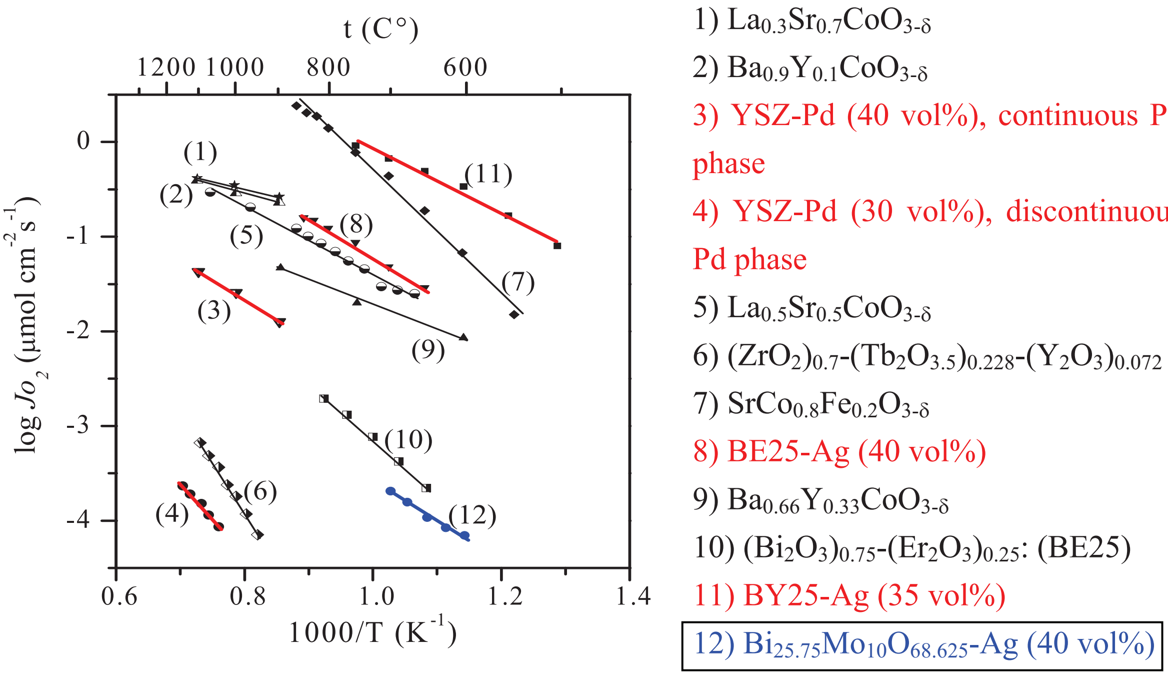

Fig. 4.19 The oxygen permeation fluxes through a $Bi_{25.75}Mo_{10}O_{68.625}$-Ag *cermet* dense membrane compared with other references [27].

According to the oxygen permeation flux results, it is clear that the oxygen permeation of the $Bi_{25.75}Mo_{10}O_{68.625}$-Ag *cermet* dense membrane was very modest despite an addition of metal (i.e. Ag). Their values are even lower than that of $(Bi_2O_3)_{0.75}$-$(Er_2O_3)_{0.25}$ (referred to as BE25). This oxide is generally considered as a pure ionic conductor even though it has a minor p-type electronic conductivity, with an ionic transference number close to unity (t_i is 0.992 at 700°C and 0.987 at 800°C) [29]. However, the oxygen permeation flux of BE25 increases by about two orders of magnitude after an addition of 40 vol% Ag [27]. Thereby, it is possible to assume that the oxygen permeation trough the $Bi_{25.75}Mo_{10}O_{68.625}$-Ag dense membrane is not limited by the electronic conductivity, but rather by the slow kinetics of oxygen exchange at the surface of the ceramic. Sometimes called electrode reactions, they correspond to the dissociation of gaseous oxygen (HOP side) and the recombination of O^{2-} (LOP side).

$$O_2 + 4e^- \rightarrow 2O^{2-} \qquad \text{HOP side}$$

$$2O^{2-} \rightarrow O_2 + 4e^- \qquad \text{LOP side}$$

Although the $Bi_{25.75}Mo_{10}O_{68.625}$-Ag membrane has a low oxygen permeation flux, it is still interesting to identify its catalytic activity in the membrane reactor. $Bi_2V_{0.8}Ta_{0.2}O_{5.5}$ (BITAVOX) is an example of membranes which provides low permeating oxygen ($pO_2^{LOP} <$ 100 Pa) and which was active in the oxidation of light alcanes [28]. For this material, it was shown that the oxygen permeation was limited by the recombination of O^{2-} at LOP. However, the reaction with hydrocarbon provided an alternative way for the extraction of oxygen from the membrane.

4.2.2. Catalytic Activity

The catalytic results obtained with $Bi_{25.75}Mo_{10}O_{68.625}$-Ag *cermet* dense membrane for the oxidation of ethane and propane are reported in Table 4.5. A stationary regime was observed for all reactions, as shown in Fig. 4.20 - Fig. 4.23. The conversion was very low (< 1%) in all cases. Because of the absence of oxygen permeation, CO and CO_2 were not measured in these studies. Surprisingly, some water was generated in all reactions but unfortunately it could not be quantified. In general, the $Bi_{25.75}Mo_{10}O_{68.625}$-Ag *cermet* seemed inactive for the oxidation of light alcane. Only some small amounts of hydrogen and hydrocarbons such as CH_4, C_2H_4 and C_3H_6 were obtained.

Table 4.5 The distribution of product pressures at different temperatures.

Temperature (°C)	H_2 (Pa)	C_2H_4 (Pa)	CH_4 (Pa)	C_3H_6 (Pa)	O_2 (Pa)
C_2H_6					
675	5.0	3.6	0.0	0.0	0.0
700	7.3	4.5	0.0	0.0	0.0
C_3H_8					
650	2.2	1.3	2.3	2.0	0.0
700	4.1	3.7	5.8	3.1	0.0

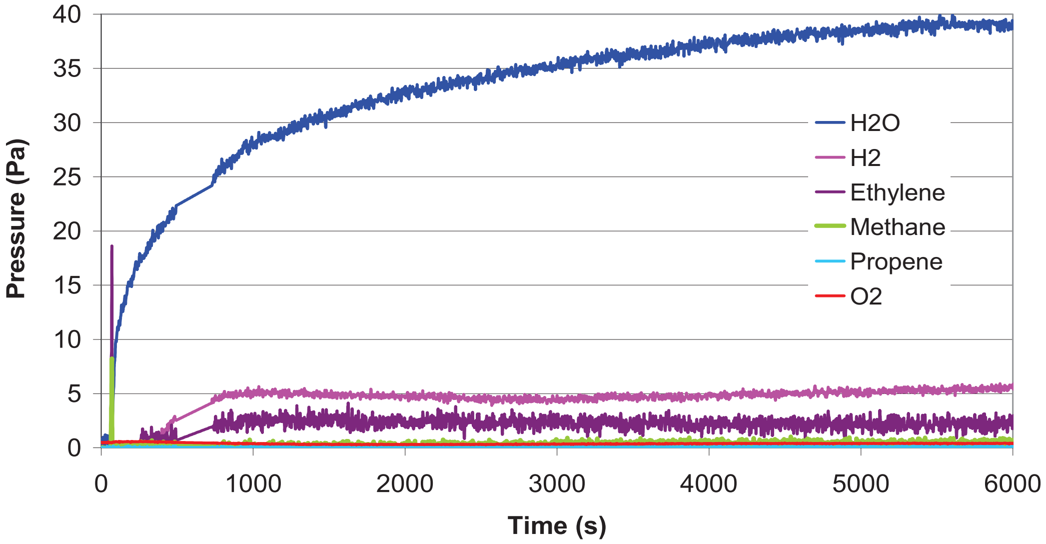

Fig. 4.20 Distribution of product pressures vs. time using a $Bi_{25.75}Mo_{10}O_{68.625}$-Ag *cermet* membrane (675°C, 1% C_2H_6/He in LOP, air in HOP).

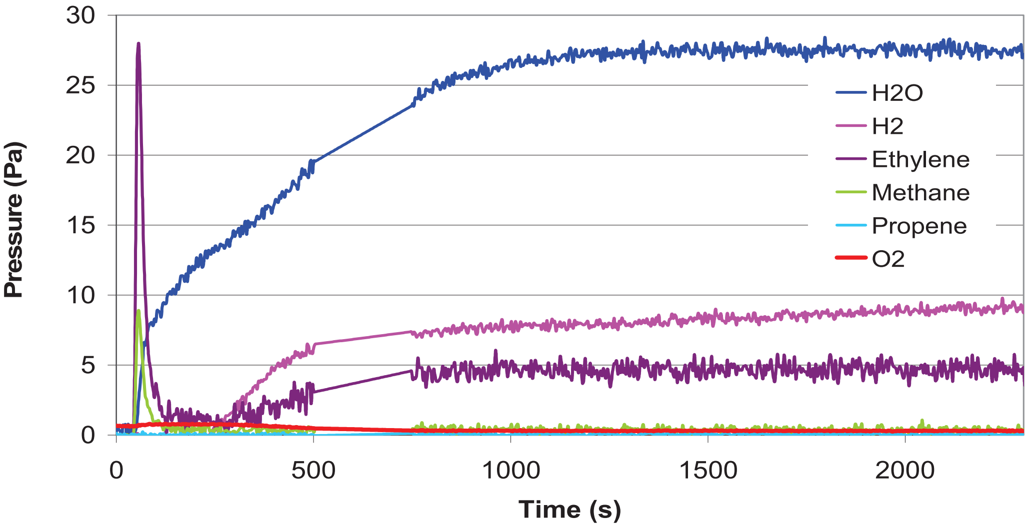

Fig. 4.21 Distribution of products pressures vs. time using a $Bi_{25.75}Mo_{10}O_{68.625}$-Ag *cermet* membrane (700°C, 1% C_2H_6/He in LOP, air in HOP).

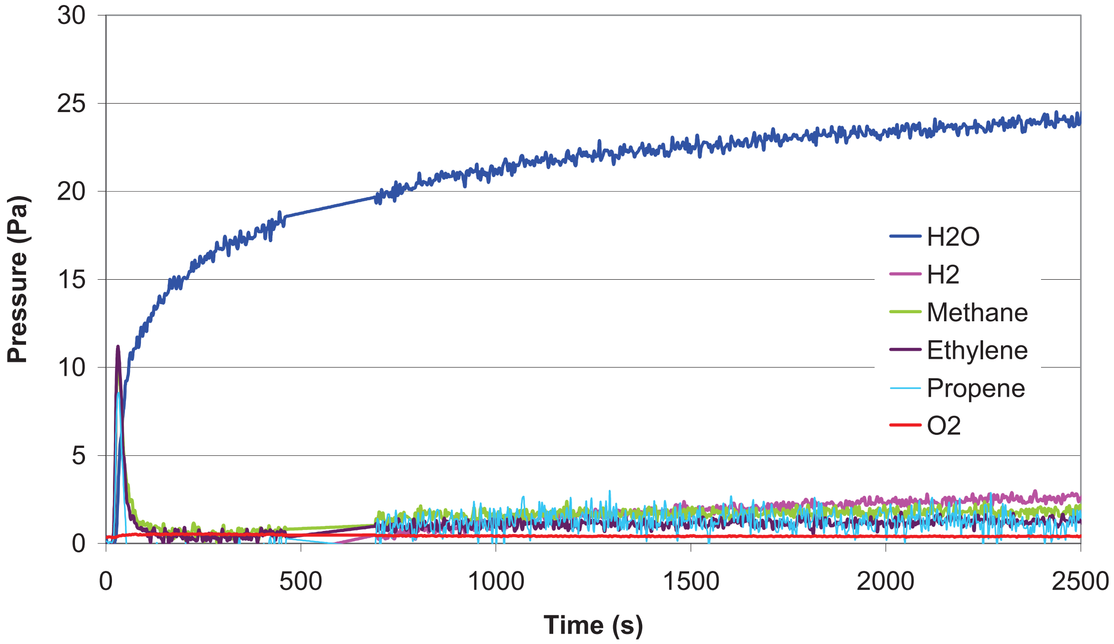

Fig. 4.22 Distribution of products pressures vs. time using a $Bi_{25.75}Mo_{10}O_{68.625}$-Ag *cermet* membrane (650°C, 1% C_3H_8/He in LOP, air in HOP).

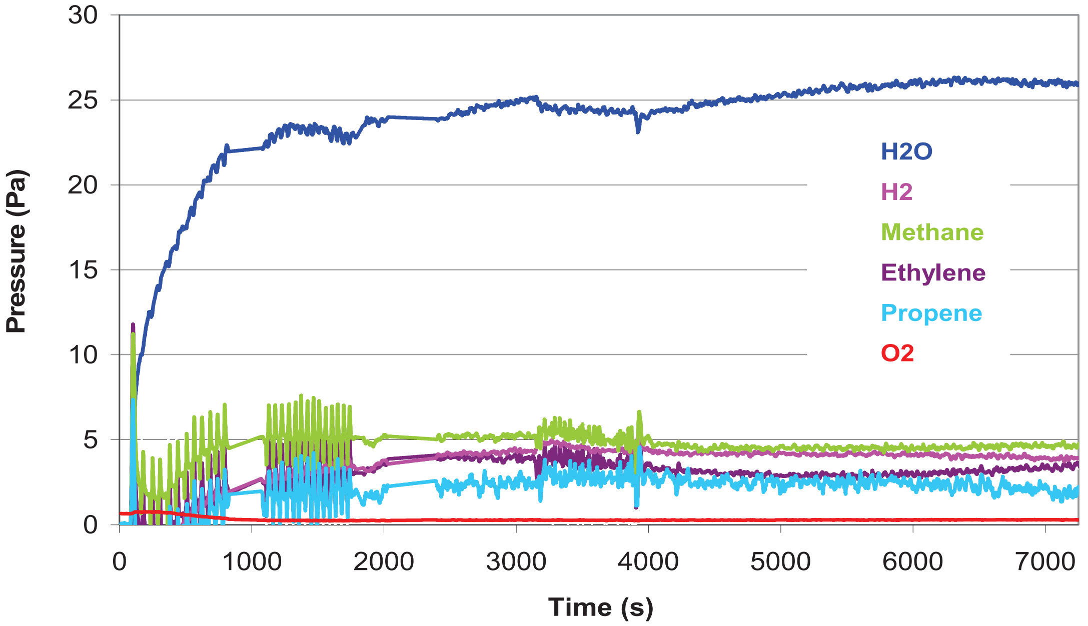

Fig. 4.23 Distribution of product pressures vs. time using a $Bi_{25.75}Mo_{10}O_{68.625}$-Ag *cermet* membrane (700°C, 1% C_3H_8/He in LOP, air in HOP).

* The oscillation of product pressures observed in this experiment is due to an unidentified electrical interference affecting the mass flowmeter and/or the mass spectrometer.

4.2.3. Characterization of membrane after catalytic experiments

In Fig. 4.24 a, a SEM-EDX analysis of membrane shows that the texture of the $Bi_{25.75}Mo_{10}O_{68.625}$-Ag *cermet* membrane at the LOP side was modified after the catalytic reaction. The grains became bigger and more crystallized but, unexpectedly, the membrane appeared more porous. From the image collected by backscattered electrons in Fig. 4.24 b, the distribution of ceramic and silver is shown by a contrast in color. According to EDS (Fig. 4.24 c), it is possible to deduce that the black and white colors correspond to silver and ceramic, respectively. The inhomogeneous distribution of ceramic and silver probably resulted from the softening of silver while the membrane was working at high temperature for a long time. Therefore, the discontinuous silver phase could be one of the important factors which caused the low permeation of the membrane. As in the case of BIMEVOX membrane, the low kinetics of oxygen surface exchange may also be the reason for low permeation. Moreover, because the oxygen dissociation and recombination process would occur basically at the triple point ceramic/Ag/gas phase, the number of catalytic active sites is considerably limited.

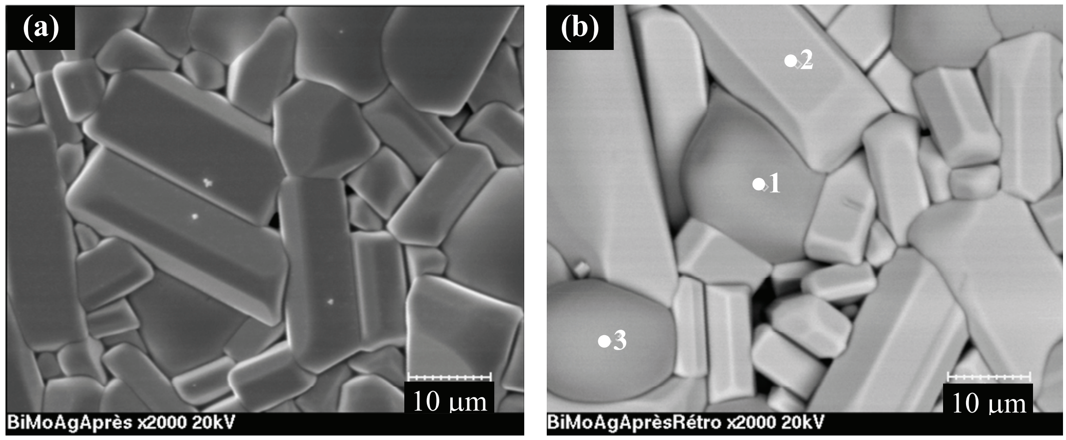

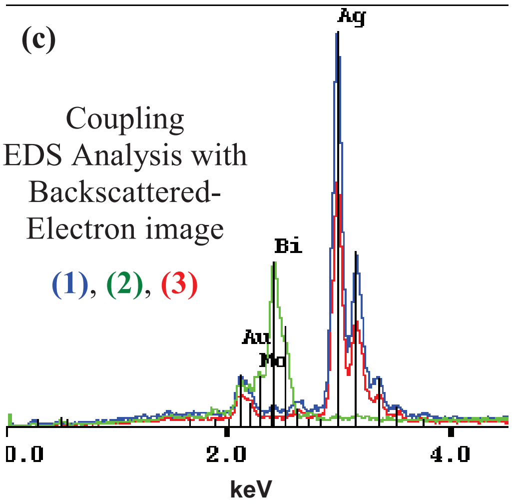

Fig. 4.24 Scanning electron micrographs of $Bi_{25.75}Mo_{10}O_{68.625}$–Ag *cermet* membrane at the LOP side after catalytic tests viewed with secondary electrons a) and backscattered electrons b) and EDS analysis c).

5. $Bi_{25.75}Mo_{10}O_{68.625}$ FOR CDMR APPLICATIONS

The previous study has demonstrated that the addition of metal (i.e. Ag) in the $Bi_{25.75}Mo_{10}O_{68.625}$ membrane is not only ineffective, but also brings out some difficulties in utilization of this membrane for CDMR applications. Indeed, the oxygen permeation of $Bi_{25.75}Mo_{10}O_{68.625}$ membrane could not be improved, and the silver phase was discontinuous as a result of the low softening point of silver.

Another option to increase the oxygen permeation flux is to impose an electric current to control the oxygen diffusion through the membrane. This type of membrane reactor is called ***electrochemical membrane reactor*** or ***Solid-Electrolyte Membrane Reactor*** (SEMR). As written before, such a reactor was already tested with BIMEVOX as membrane [22, 25]. Both surfaces of a BICOVOX (ME = Co) ceramic were recovered by a BICOVOX/Au *cermet* to allow the application of an electrical bias. The reactor was operated in the partial oxidation of propane at 700°C. It was shown that the propane conversion was steady and amounted to X_{C3} = 10-12 mol% whatever the applied polarization, H_2 being the main product with selectivity S_{H2} around 55-60 mol%. However at this temperature, one could not exclude thermal cracking which would account for the high selectivity to hydrogen. At open voltage circuit (OCV), no product of oxidation was observed except water which could not be quantified. Under anodic polarization, traces of CO and a small increase of propylene content were noticed but with a decrease of the H_2 production due to its oxidation into water. Therefore the effects were modest but they showed the possibility of such a SEMR system to modify the catalytic properties of membrane.

Under an electrical bias, the oxygen permeation flux can be provided at lower temperature. Therefore, to limit the possibility of thermal cracking but also to allow the possibility to use γ-Bi_2MoO_6 as a catalyst at the membrane surface at LOP, it was decided to build a reactor similar to the reactor studied by H. Bodet [22, 25] but with a $Bi_{25.75}Mo_{10}O_{68.625}$ membrane which can operate at temperatures below 600°C.

5.1. Preparation of $Bi_{25.75}Mo_{10}O_{68.625}$ -Au *Cermet* Electrode

An external circuit and a current generator will be added to the membrane reactor in order to control and increase the oxygen permeation flux through the $Bi_{25.75}Mo_{10}O_{68.625}$ membrane. For our study, the use of a *cermet* composite electrode seemed more attractive than a pure metal because of the higher specific surface area of a *cermet* electrode that can accelerate the electrode reaction process [30]. A porous *cermet* electrode is composed of metal particles, pores and electrolyte particles. The metal component, i.e. gold in our case, is considered as a basic building block indispensable for the electrode. It supplies and transmits electrons for the electrode reaction and allows electronic current to pass through the system. The pores account for about 50% of the total electrode volume. This porous structure facilitates the gas to freely reach the active sites, i.e. tripe phase boundary (TPB), where the mass and the charge transfers occur. As a consequence, $Bi_{25.75}Mo_{10}O_{68.625}$-Au *cermet* electrodes were deposited on the $Bi_{25.75}Mo_{10}O_{68.625}$ membrane to ensure good adhesion and the electrode reaction.

The *cermet* powder of $Bi_{25.75}Mo_{10}O_{68.625}$-Au was prepared by using the same method previously described (in cf. 4.1) but in this case a gold paste (Ferro couleurs France S.A., 85-90 wt% Au, d50% ≤ 1µm) was used instead of silver powder. Two compositions of *cermet* were prepared according to the protocol used by H. Bodet [22, 25]: the first one contained 35 vol% Au and the second one contained 70 vol% Au. A controlled thickness layer of *cermet* was placed on the membrane by an adapted screen printing technique. The screen printing paste was prepared from the mixed 75 wt% *cermet* powder and 25 wt% polymer resin (EC3 resin is consisted of terpineol and ethylcellulose-terpineol). It should have an appropriate viscosity for the screen printing in an ink-blocking: perforated sticker (70 µm thickness and 12 mm in diameter) which was placed on the top of the membrane. A schematic of the $Bi_{25.75}Mo_{10}O_{68.625}$ membrane with two layers of *cermet* is shown in Fig. 4.25.

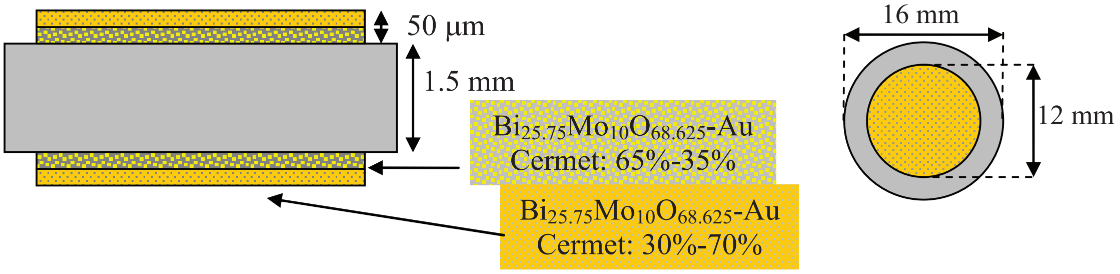

Fig. 4.25 A schematic of the $Bi_{25.75}Mo_{10}O_{68.625}$ membrane with two layers of *cermet* on both faces.

The first layer of *cermet* paste, corresponding to the 35 vol% Au composition, was deposited on the pretreated $Bi_{25.75}Mo_{10}O_{68.625}$ membrane described as follows: the green membrane pellet, prepared according to cf. 3.3.2, (1.8 mm in diameter) was first preheated at 700°C for 30 min, with a heating-cooling rate of 4°C/min. It was later polished with a SiC paper of 1000 to assure the parallelism of the membrane and then with another SiC paper of 220 to roughen the membrane surface for a better adhesion.

After the screen printing of the first layer of *cermet*, it should be pre-dried at 60°C in an oven before sintering at 850°C for 1 hour. The membrane with deposited *cermet* was heated in air slowly to eliminate the resin and achieve a layer of porous *cermet* with the thermal treatment, as described in Fig. 4.26. Later, the second layer of *cermet*, the 70 vol% Au composition, was put on the top of the first layer of *cermet* in the same conditions but with the different sintering temperature, at 750°C for 1 hour as shown in Fig. 4.27.

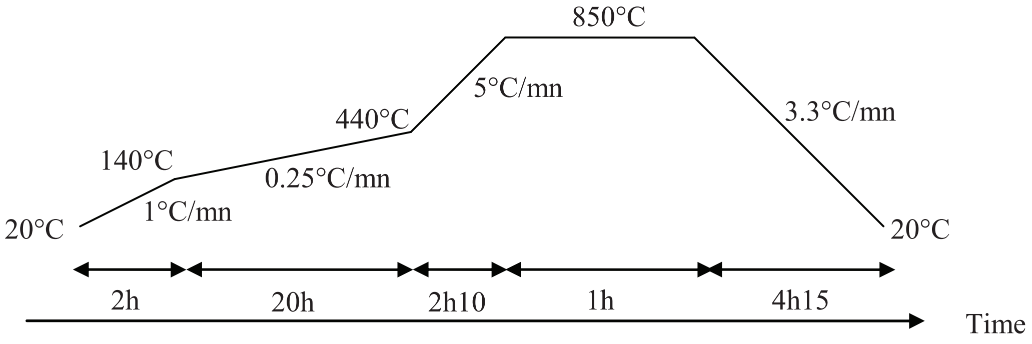

Fig. 4.26 Thermal treatment used for sintering the membrane with the first layer of *cermet*: the 35 vol% Au composition.

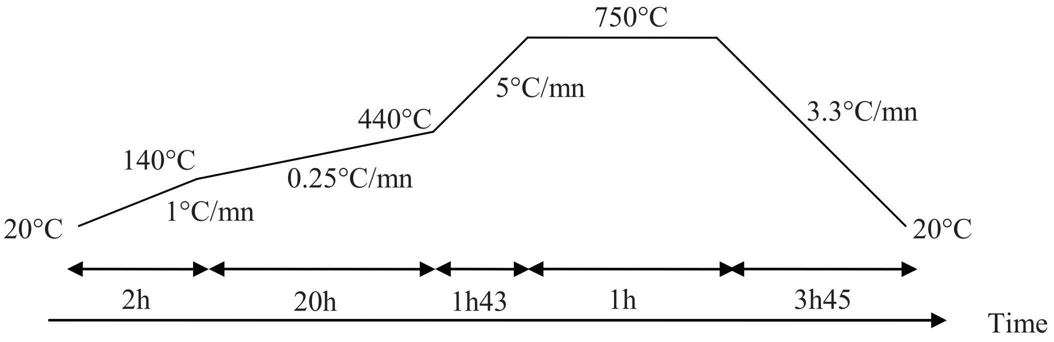

Fig. 4.27 Thermal treatment used for sintering the membrane with the second layer of *cermet*: the 70 vol% Au composition.

SEM-EDX analyses were carried out to examine the porous texture and chemical composition distribution of the $Bi_{25.75}Mo_{10}O_{68.625}$-Au *cermet* electrodes (Fig. 4.28). An observation of the electrode surface, in Fig. 4.28 a, illustrates the porosity obtained after the elimination of resin. The image collected by backscattered electrons in Fig. 4.28 b shows the distribution of ceramic and gold by a contrast in color. EDS analyses in Fig. 4.28 c confirm that the gray color corresponds to ceramic and the white one is assigned to gold. A homogeneous distribution of the ceramic and gold was observed. A cross-section SEM image of $Bi_{25.75}Mo_{10}O_{68.625}$ membrane with *cermet* electrodes in Fig. 4.28 d reveals two porous *cermet* layers of about 30 and 40 µm in thickness for the first and the second electrode layers, respectively.

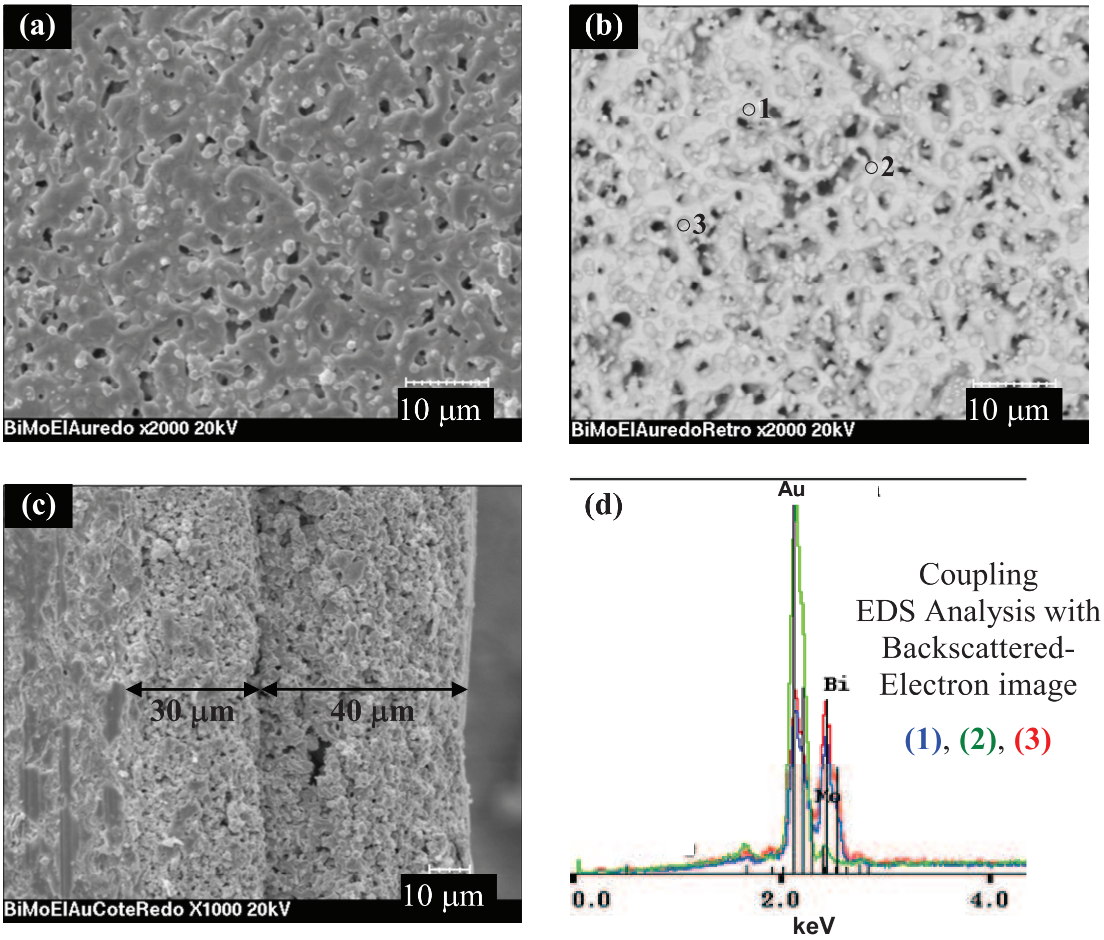

Fig. 4.28 Scanning electron micrographs of $Bi_{25.75}Mo_{10}O_{68.625}$-Au *cermet* electrode with secondary electrons a) and backscattered electrons b). Cross-section SEM images of $Bi_{25.75}Mo_{10}O_{68.625}$ membrane with *cermet* electrodes after sintering c) and EDS analysis d).

5.2. Electrical Properties of $Bi_{25.75}Mo_{10}O_{68.625}$ with *Cermet* Electrodes

The electrochemical properties of $Bi_{25.75}Mo_{10}O_{68.625}$ membrane with $Bi_{25.75}Mo_{10}O_{68.625}$ -Au *cermet* electrodes were investigated by the galvanostatic and galvanodynamic polarization methods. The oxygen production rate and current efficiency were also established.

5.2.1. Current Measurement

The voltage response of the membrane was measured under air atmosphere as a function of imposed current, by galvanostatic and galvanodynamic polarization methods (Fig. 4.29), in order to determine the working range of the applied current in which the membrane can operate properly.

In galvanostatic mode, a linear relationship between voltage and current according to Ohm's law was maintained in the range of 0.01 and 0.07A (Fig. 4.29). The slope of this linear region corresponds to the resistance of the membrane of about 37.4 Ω, in good agreement with the expected value of conductivity. A different behaviour was observed above 0.07A/cm^2 which might be due to the reduction of the $Bi_{25.75}Mo_{10}O_{68.625}$ membrane to Bi that exhibits a higher conductivity, leading to a decrease of resistance and voltage values which are clearly observed by the galvanostatic measurement. Consequently, the current will be applied in the range of 0.01-0.05A to avoid any membrane degradation.

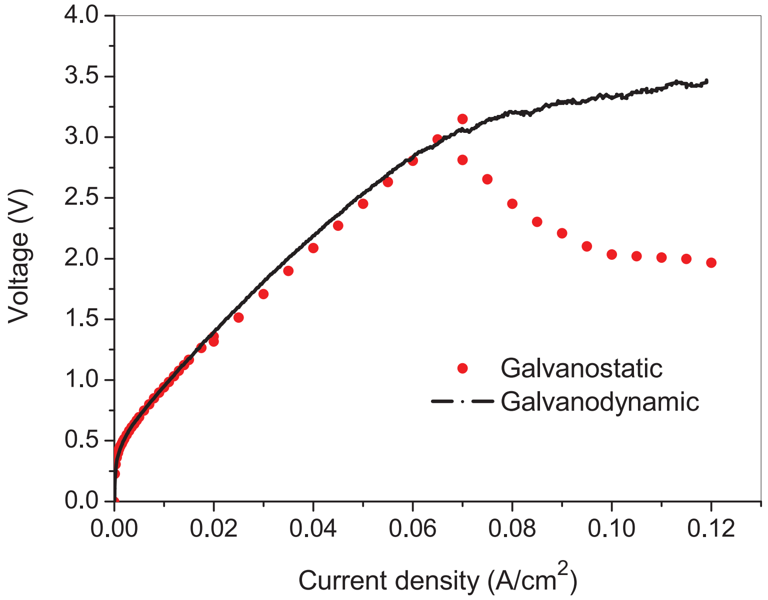

Fig. 4.29 Galvanostatic and galvanodynamic polarizations on the $Bi_{25.75}Mo_{10}O_{68.625}$ membrane with $Bi_{25.75}Mo_{10}O_{68.625}$-Au *cermet* electrodes at 500°C under air flow.

5.2.2. Oxygen Permeation Measurement

The current imposition (Fig. 4.30), which results in a constant potential difference between two electrodes, offers opportunities to drive the O^{2-} through the membrane into the desired direction (i.e. LOP) and to modify the catalytic reactivity of the membrane. The current, in the range of 10-50 mA, was in general applied to increase the oxygen permeation flux for the catalytic reaction at the LOP side. This process is sometimes called ***anodic polarization***. This current application is similar to the oxygen generator operations. The oxygen production rates were always measured in Air (HOP)/ He (LOP) before each catalytic reaction in order to verify the current efficiency and to estimate the amount of oxygen permeation flux electrically supplied during the reaction. The measured oxygen permeation flux values are given in Table 4.6.

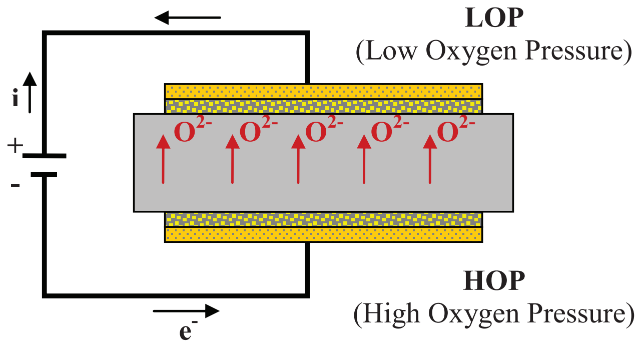

Fig. 4.30 Current application on the $Bi_{25.75}Mo_{10}O_{68.625}$ membrane to increase the oxygen permeation flux at the LOP (Low Oxygen Pressure).

Table 4.6 The oxygen permeation flux*, through the membrane with $Bi_{25.75}Mo_{10}O_{68.625}$-Au *cermet* electrodes (under He in LOP and air in HOP), provided by the current.

Experiment order	Current (mA)	Voltage (mV)	Jo_2 (ppm.ml/min.cm2)	Jo_2 (exp) (ml/min)	Jo_2 (th) (ml/min)	Current Efficiency (%)
500°C	0	-102	< 100	-	-	-
3rd	10	855	28031	0.028	0.037	76
	30	1593	88500	0.089	0.112	79
525°C	0	-107	< 100	-	-	-
4th	10	738	29351	0.029	0.037	78
	30	1381	89388	0.089	0.112	79
550°C	0	-124	< 100	-	-	-
1st	10	600	36167	0.036	0.037	97
	30	1115	100413	0.100	0.112	89
565°C	0	-149	< 100	-	-	-
2nd	10	552	31477	0.031	0.037	84
	30	1042	100139	0.100	0.112	89

*The incertitude on these values was of about 1%.

It is interesting to note that the measured oxygen permeation flux values are in general close to the theoretical values. In other words, the $Bi_{25.75}Mo_{10}O_{68.625}$ membrane operates with a current efficiency of more than 76% in this temperature range. Moreover, the potential differences ΔE_{exp} measured at open circuit voltage (OCV) are ΔE_{exp} = -102, -107, -124 and -149 mV at 500, 525, 550 and 565 °C, respectively. With air in HOP ($pO_2 = 0.21x10^5$ Pa), and assuming that the equivalent oxygen content in LOP was less than 10 ppm, from Nenst equation ΔE_{th} = -166, -171, -176 and -180 mV were expected from the two surfaces of the membrane at 500, 525, 550 and 565 °C, respectively. The experimental values show that the system is not at equilibrium and that the LOP face of the membrane is polarized. This polarization would suggest that the rate of exchange of oxygen molecules at the surface of the membrane is low, as if some oxide ions were blocked closed to the membrane surface. They may thus act as an oxygen reservoir available for oxidation of hydrocarbon. The same behavior was observed for BIMEVOX membrane, it was even more important since the potential at OCV was only a few mV [22, 25, 28]. This factor appeared to be a key parameter in the membrane stability.

5.3. CDMR Applications

5.3.1. $Bi_{25.75}Mo_{10}O_{68.625}$ Membrane with Cermet Electrode

The CDMR applications were performed by using the propylene as a reactant hydrocarbon for the temperatures in the following chronological order: 550, 565, 500 and 525°C. The anodic polarization was applied on the *cermet* covered membrane. The distributions of product pressures vs. time are reported in Fig. 4.31-Fig. 4.36.

At the beginning of the reaction at 550°C (Fig. 4.31), under open circuit voltage (OCV), only the formation of water was observed. Interestingly, the hydrogen production appeared later and it slightly increased with time. For reaction under anodic polarization, about 1700 seconds later, the distribution of products was in general affected by the applied current amplitude.

The current was increased by step of 10 mA from 10 mA up to 50 mA. An increase of the oxygen content in the gas phase with the current density was observed; this oxygen is not completely consumed during the reaction. From the distribution of products during the reaction at 500-565°C, only hydrogen production decreased while CO_2, acrolein and water formations increased as the current bias increases. A small increase of ethylene and CO production was also noticed. The formation of CO_2, acrolein and water can be accounted for by the selective oxidation ($C_3H_6 + O_2 \rightarrow C_3H_4O + H_2O$) and the total oxidation of propylene ($C_3H_6 + 4.5O_2 \rightarrow 3CO_2 + 3H_2O$), respectively. The small increase of ethylene and CO amount could result from the thermal cracking and incomplete oxidation, respectively. Therefore, even at these temperatures, one can not exclude the possibility of water formation from the reaction between H_2 (from cracking reactions) and oxygen diffusing through the membrane, which may explain the decrease of H_2.

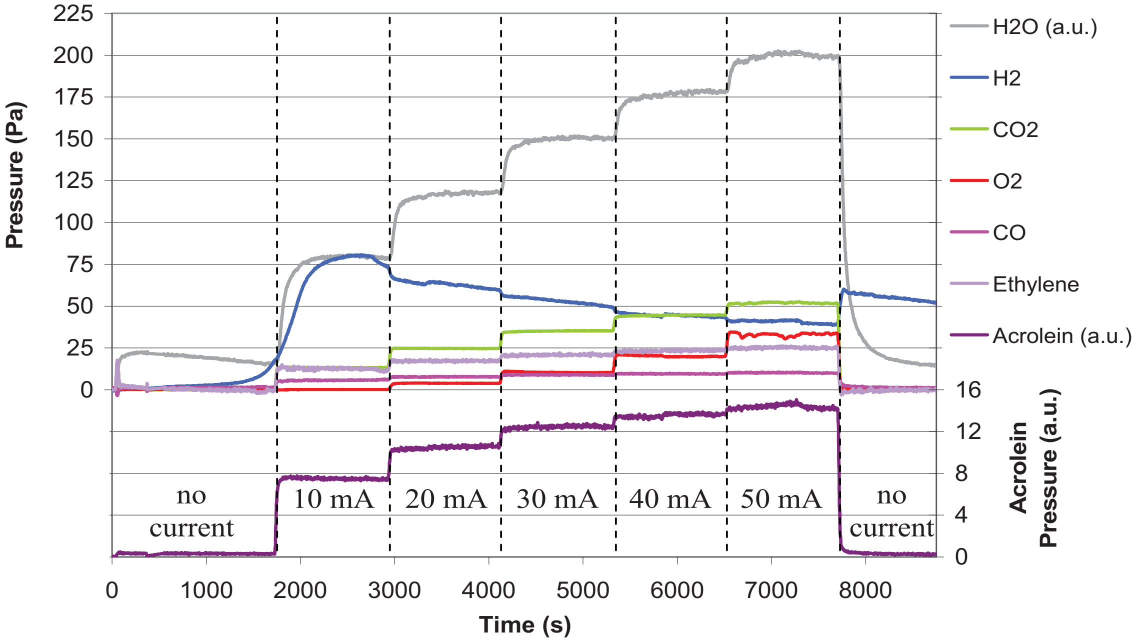

Fig. 4.31 Distribution of product pressures vs. time using a $Bi_{25.75}Mo_{10}O_{68.625}$ membrane with $Bi_{25.75}Mo_{10}O_{68.625}$-Au *cermet* electrodes (550°C, 1% C_3H_6/He in LOP, air in HOP).

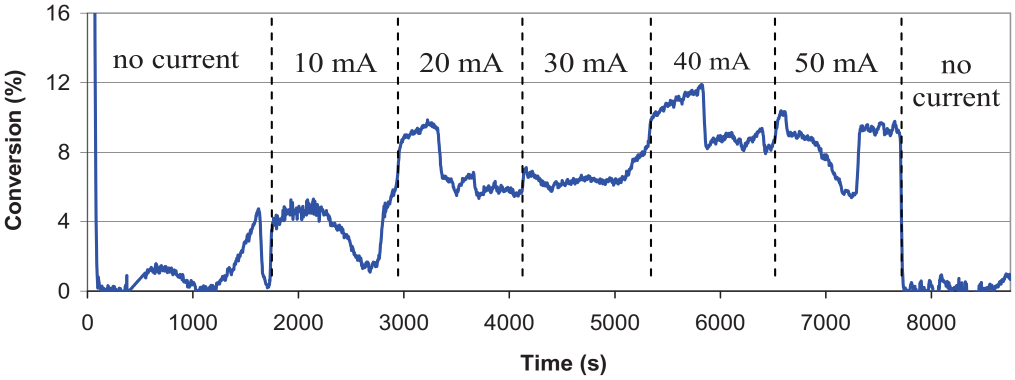

Fig. 4.32 Conversion of propylene vs. time using a $Bi_{25.75}Mo_{10}O_{68.625}$ membrane with $Bi_{25.75}Mo_{10}O_{68.625}$-Au *cermet* electrodes (550°C, 1% C_3H_6/He in LOP, air in HOP).

The increase of CO_2 is in line with the increased amount of oxgygen available for reaction due to the imposed current. What is more interesting is the increase of the selective oxidation products, acrolein in this case, in these conditions. This is clearly an effect of the CDMR concept, even though with increasing oxygen supply the indicative acrolein/CO_2 ratio tends to decrease; these values decrease 0.55 > 0.43 > 0.35 > 0.31 > 0.28 along increasing 10 < 20 < 30 < 40 < 50mA current, respectively. Unfortunately a precise measure of conversion was not possible probably due to electric interferences affecting the mass flow controllers. Nevertheless, according to Fig. 4.32, it is also interesting to note that the conversion of propylene increases slightly during the reaction. The behavior is however erratic and thus difficult to interpret.

The similar catalytic behavior of the membrane under anodic polarization was also observed at other temperatures, as shown in Fig. 4.33-Fig. 4.35. However, it is worth noting that hydrogen is obtained in large amounts during the catalytic reaction under open circuit voltage (OCV) at 500, 525 and 565°C. The production of hydrogen is probably due to cracking reaction, although some water is observed. H_2 was not observed only for the first catalytic reaction on the membrane under OCV at 550°C (Fig. 4.31). It appears that the activation of the membrane or the formation of some specific compounds formed on the membrane surface may favor cracking reaction. This transformation may occur after the first catalytic reaction.

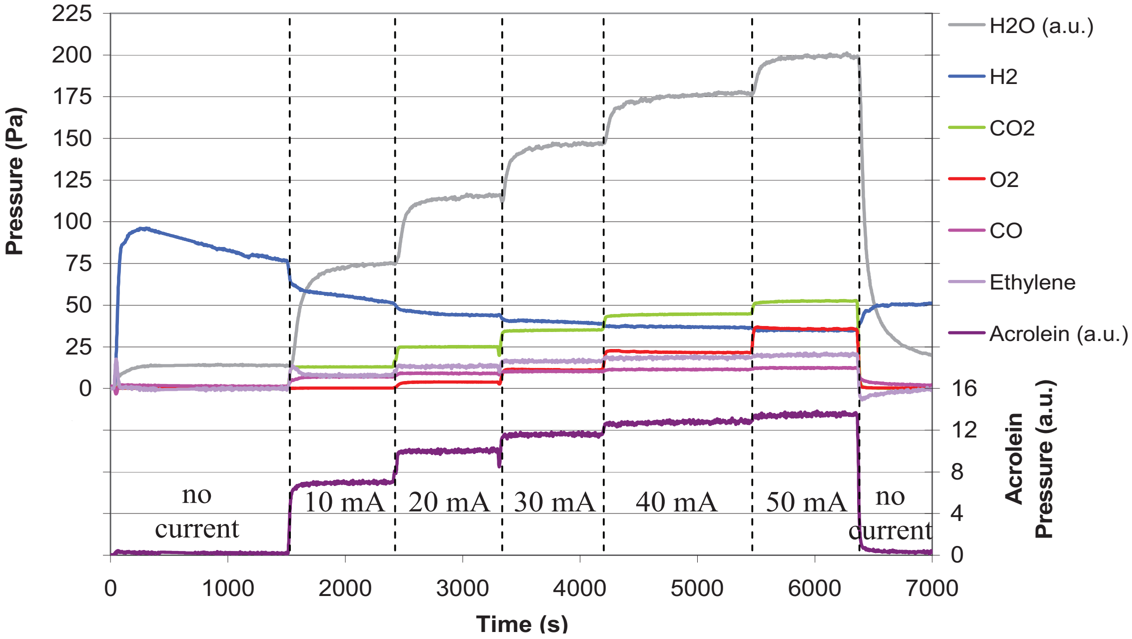

Fig. 4.33 Distribution of product pressures vs. time using a $Bi_{25.75}Mo_{10}O_{68.625}$ membrane with $Bi_{25.75}Mo_{10}O_{68.625}$-Au *cermet* electrodes (565°C, 1% C_3H_6/He in LOP, air in HOP).

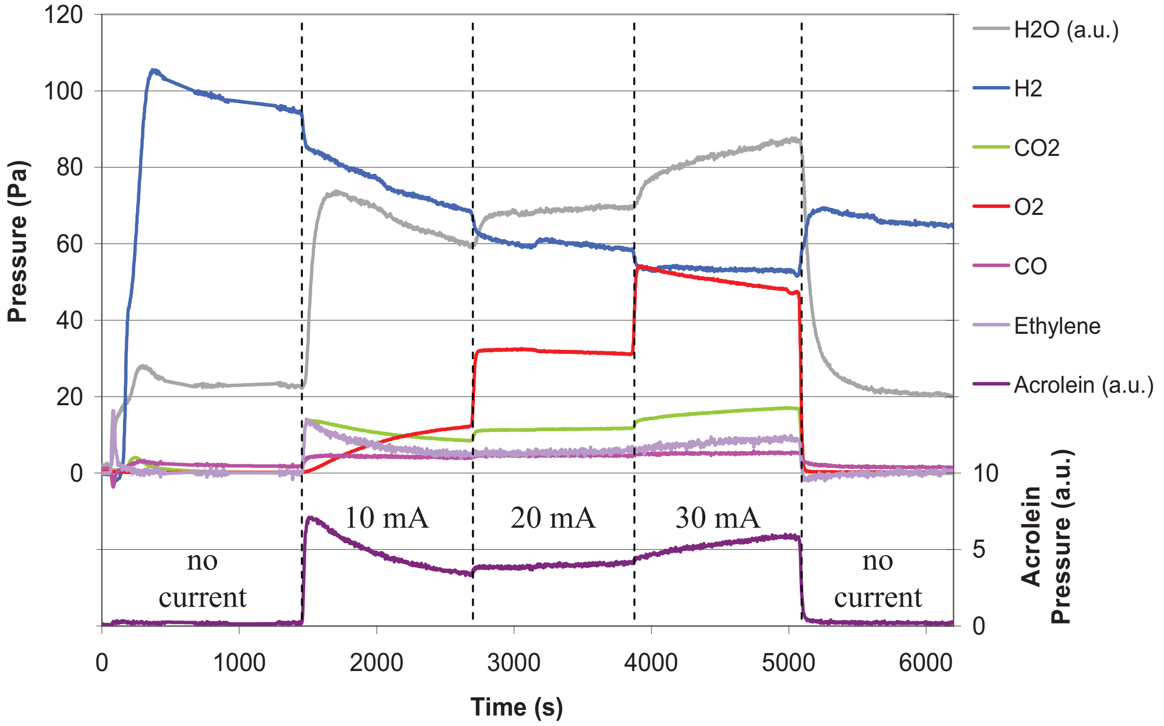

Fig. 4.34 Distribution of product pressures vs. time using a $Bi_{25.75}Mo_{10}O_{68.625}$ membrane with $Bi_{25.75}Mo_{10}O_{68.625}$-Au *cermet* electrodes (500°C, 1% C_3H_6/He in LOP, air in HOP).

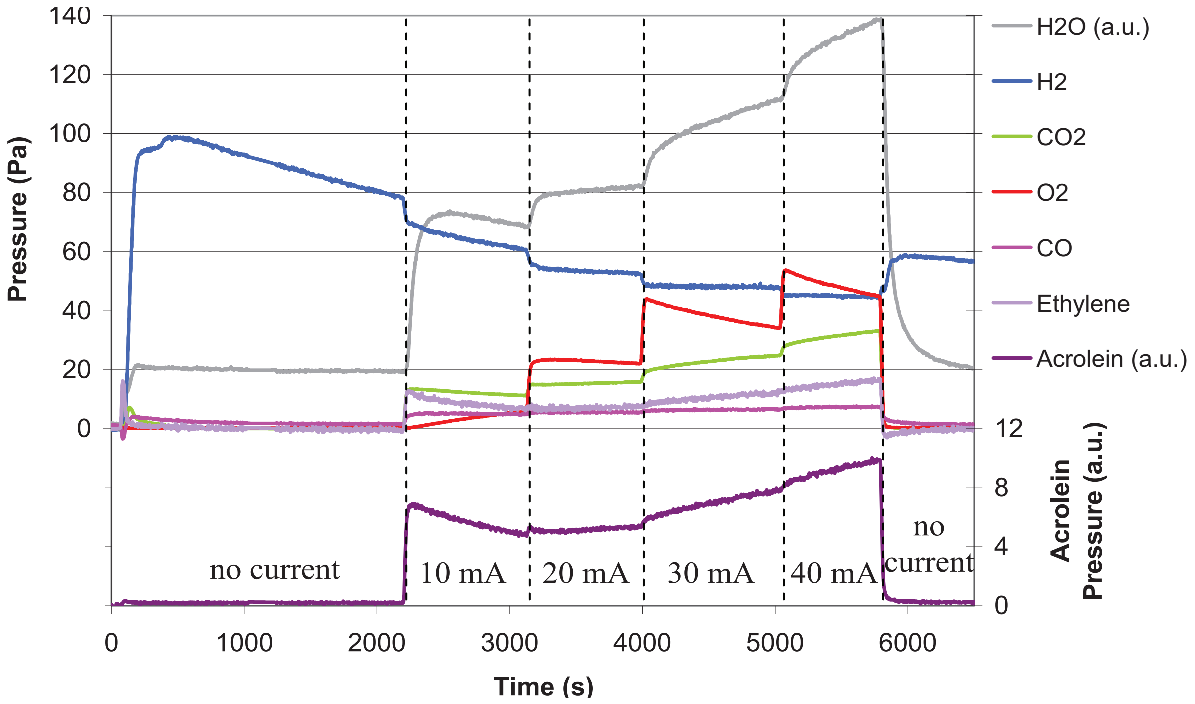

Fig. 4.35 Distribution of product pressures vs. time using a $Bi_{25.75}Mo_{10}O_{68.625}$ membrane with $Bi_{25.75}Mo_{10}O_{68.625}$-Au *cermet* electrodes (525°C, 1% C_3H_6/He in LOP, air in HOP).

Moreover, a complex **transient behavior** of the membrane under OCV at 500 and 525°C was observed at the beginning of the reaction. The evolution of the main products obtained during transient regime at 500°C is illustrated in Fig. 4.36. Initially, the formation of ethylene and CO_2 decreased to zero while the water amount increased and stabilized. Later, CO_2 was formed and disappeared again while the formation of hydrogen and CO increased and stabilized. A stationary regime was later observed with hydrogen as the main product.

It is also worth noting that at the lowest temperatures (500 and 525°C), the stabilization of the activity was slow, or in some cases it did not reach the steady state in the time scale of the experiments. At low current imposition (10mA) the products, in particular acrolein, reacted rapidly to the imposed current and then it decreased slowly while O_2 appeared progressively in the gas phase. At higher currents (30-40mA), oxygen appeared immediately in the gas phase and was slowly consumed for both total and selective oxidation reactions. At 20 mA current, both reactivity and oxygen permeation stabilized rapidly.

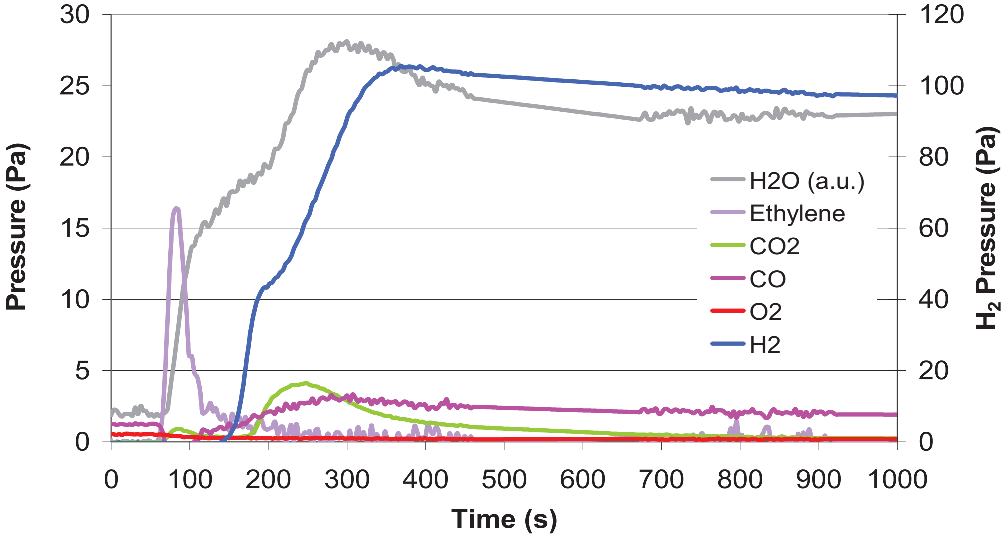

Fig. 4.36 Distribution of product pressures vs. time using a $Bi_{25.75}Mo_{10}O_{68.625}$ membrane with $Bi_{25.75}Mo_{10}O_{68.625}$-Au *cermet* electrodes (500°C, 1% C_3H_6/He in LOP, air in HOP).

On the contrary, at 550 and 565°C the active surface equilibrated rapidly in response to all the changes of imposed current. This behavior suggests that modifications occurred at the surface of the membrane affecting both reactivity and permeation. The rates of these phenomena are rather slow at the lowest temperatures explored (500 and 525°C) making the balance between permeation and reactivity very delicate and dependent on the amount of oxygen delivered to the LOP surface through the imposed current.

5.3.2. $Bi_{25.75}Mo_{10}O_{68.625}$ Membrane with Cermet Electrode and Bi_2MoO_6 Catalyst

To improve the catalytic activity of the membrane, γ-Bi_2MoO_6 catalyst was added to the membrane system. 200 mg of γ-Bi_2MoO_6 powder was loaded on the surface of the membrane at the LOP side. The distribution of products and conversion of propylene under open circuit voltage (OCV) at 500°C are shown in Fig. 4.37-Fig. 4.38.

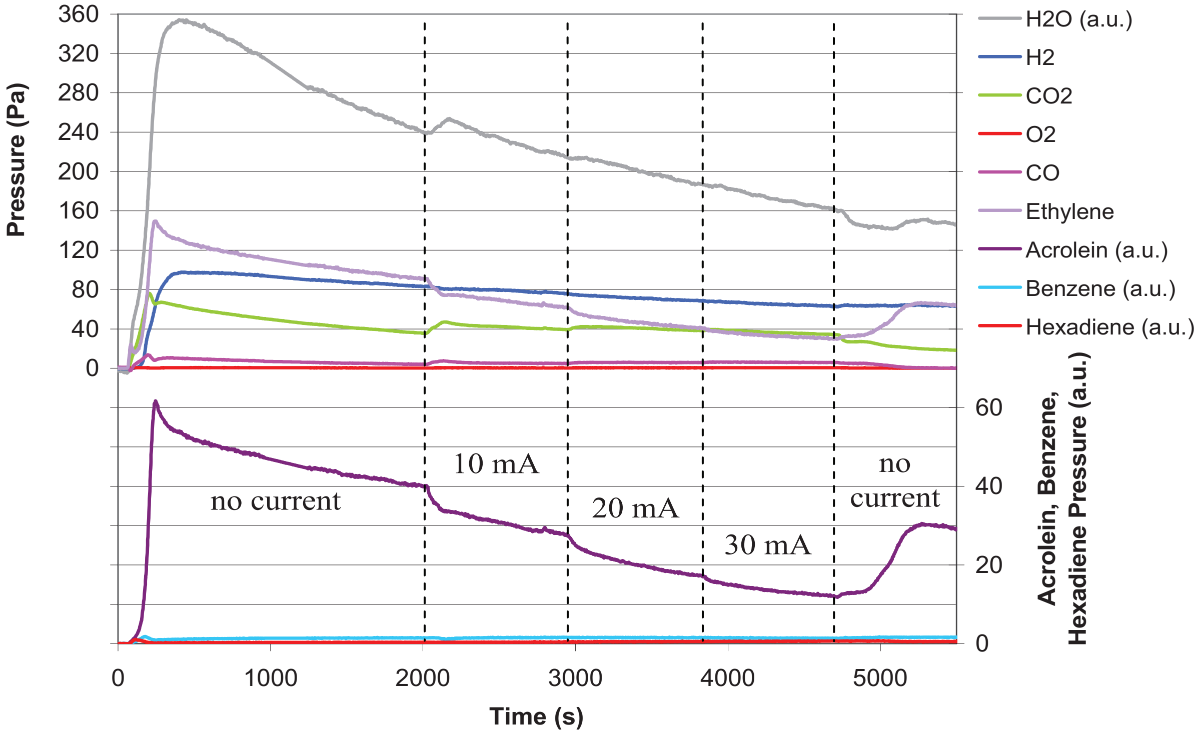

Fig. 4.37 Distribution of product pressures vs. time using the $Bi_{25.75}Mo_{10}O_{68.625}$ membrane with $Bi_{25.75}Mo_{10}O_{68.625}$-Au *cermet* electrodes and Bi_2MoO_6 as a catalyst powder (500°C, 1% C_3H_6/He in LOP, air in HOP).

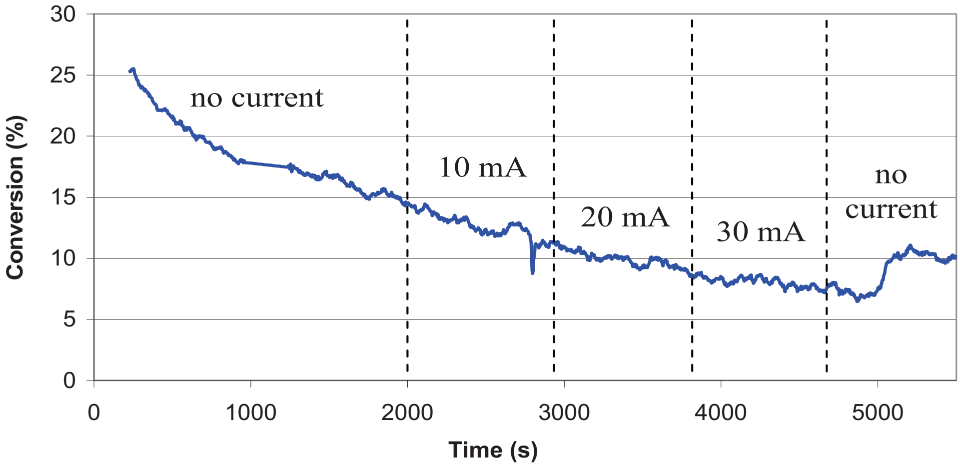

Fig. 4.38 Conversion of propylene vs. time using the $Bi_{25.75}Mo_{10}O_{68.625}$ membrane with $Bi_{25.75}Mo_{10}O_{68.625}$-Au *cermet* electrodes and Bi_2MoO_6 as a catalyst powder (500°C, 1% C_3H_6/He in LOP, air in HOP).

A higher and more stabilized conversion rate of propylene was observed. However, the decrease of propylene conversion and of product pressures with time, when compared with the reaction under OCV at the beginning and at the end of catalytic experiments, indicates that γ-Bi_2MoO_6 catalyst deactivated.

At the beginning of the reaction under OCV (Fig. 4.37), the formation of water, hydrogen, CO_2, ethylene, acrolein and small quantities of CO and benzene was observed. This is in contrast to the previous catalytic reaction with the sole membrane, in which only the formation of hydrogen and water was observed. It is clear that the formation of several products in this experiment should be promoted by γ-Bi_2MoO_6 catalyst. Interestingly, a short-time transient regime, accompanied with an optimum formation of hydrocarbons and oxidation products, was observed at the beginning of the reaction. A stationary regime was later observed with ethylene and hydrogen as main products.

Under anodic polarization, about 2000 seconds later, the distribution of products was in general affected by the applied current amplitude. The current was increased by step of 10 mA from 10 mA up to 30 mA. In contrast to experiments with γ-Bi_2MoO_6 catalyst, the production of dioxygen was not observed, which means that it might be completely consumed during the reaction. In general, the production of water, hydrogen and hydrocarbons decreased while CO and CO_2 formation increased as the current bias increased.

The catalytic behavior of the membrane in the presence of deposited γ-Bi_2MoO_6 catalyst under anodic polarization was clearly different as compared to the membrane without additional catalyst. The selective oxidation products of propylene like acrolein decreased while the total oxidation products of propylene like CO_2 increased with current amplitude. Consequently, the acrolein selectivity decreased as the current bias increased.

It should also be noted that cracking reactions producing mainly ethylene occur all along the process. Furthermore ethylene and acrolein curves run parallel, suggesting that both products are governed by the same rate limiting step of reaction path.

Interestingly, part of the initial activity and selectivity is recovered when the current is stopped. The phenomenon is not immediate and indicates that a transformation (restructuring) of the active surface occurs. The increase of activity is accompanied by cracking product (ethylene) and it does not affect the CO_2 pressure.

These results suggest that, without current, the reaction proceeds through the activation of propylene and that such activated species undergo cracking to produce ethylene, but also significant amounts of CO_2 and acrolein (indicative acrolein/CO_2 ratio of 1). When the current is imposed, the overall activity diminishes suggesting that the increase of oxygen supply would deactivate the sites responsible for activating propylene. The resulting activated species react more preferentially towards total oxidation, as the acrolein/CO_2 ratio decreases significantly ($0.68 > 0.44 > 0.37$) as the current increases ($10 < 20 < 30$mA).

The recovery of the initial behavior when the current is stopped is probably due to the renewed formation of the reduced species responsible for the activation of propylene. It also shows that the catalytic behavior observed is not due to a "one-shot" reduction and exhaustion of the oxygen contained in the Bi_2MoO_6 catalyst deposited at the surface of the membrane.

In order to better understand and compare the behavior of these materials for propylene oxidation, temperature programmed reactions have been performed on powder materials in a separate setup. Experiments were made in reductive conditions (1% propylene in inert gas) similar to those of the LOP compartment of CDMR or in more classical co-feed conditions (1% propylene +1% oxygen). The evolution of partial pressures and conversion versus time/temperature are shown in Fig. 4.39 for the reaction under reductive conditions (TPR). Experimental details and other figures (e.g. for Bi_2MoO_6 in cofeed and $Bi_{25.75}Mo_{10}O_{68.625}$ in both conditions) are assembled in appendix.

It is interesting to note that the indicative acrolein/CO_2 ratio of about 1, obtained from the reaction (Fig. 4.37) in the CDMR under open circuit voltage (OCV) at the beginning and the end of the reaction correlates well with the value obtained from the Temperature-Program Reduction (TPR) of Bi_2MoO_6 catalyst in propylene at the same temperature (Fig. 4.39 and Table 4.7). Moreover, this acrolein/CO_2 ratio value is largely higher than that obtained from cofeed reaction (of about 0.16) in gas mixture of oxygen and propylene also reported in Table 4.7 and illustrated in Appendix. Similar observations can be made for $Bi_{25.75}Mo_{10}O_{68.625}$ although the indicative acrolein/CO_2 ratios are globally lower than for Bi_2MoO_6.

These results, although still exploratory, suggest that it is indeed possible to create in a CDMR the necessary conditions for obtaining a more selective catalyst by working in the absence or at very low oxygen concentration in the gas phase. However, contrary to TP reactions were the lattice oxygen is consumed in a “one-shot” operation and would need a discontinuous regeneration step, the CDMR allows to provide the sufficient oxygen through diffusion through the membrane and thus to operate in a continuous way. They are very promising in respect to the development of such application but still need to be deepened. In particular, it is clear that such system depends on a delicate balance between several properties (oxygen diffusion, catalytic activity of surface species, gaseous oxygen concentrations, etc.) all intimately interconnected to each other.

Table 4.7 Comparison of catalytic results obtained from different catalytic reactions at 500°C

Operations	Current (mA)	500°C			550°C		
		Conv. (%)	pO_2 (Pa)	Acrolein/CO_2 ratio	Conv. (%)	pO_2 (Pa)	Acrolein/CO_2 ratio
CDMR **$Bi_{25.75}Mo_{10}O_{68.625}$**	0	<5%	<1	-	<5%	<1	-
	10	<5%	12	0.38	6%	<1	0.55
	20	<5%	31	0.35	6%	4	0.43
	30	<5%	47	0.35	8%	10	0.35
	40	-	-	-	9%	20	0.31
	50	-	-	-	10%	33	0.28
	0	<5%	<1	-	<5%	<1	-
CDMR **$Bi_{25.75}Mo_{10}O_{68.625}$** **+ Bi_2MoO_6**	0	24 to 14	<0.5	1.13	-	-	-
	10	14 to 11	<0.5	0.68	-	-	-
	20	11 to 8	<0.5	0.44	-	-	-
	30	8	<0.5	0.37	-	-	-
	0	8 to 10	<0.5	1.73	-	-	-
$Bi_{25.75}Mo_{10}O_{68.625}$							
TPR	-	<5%	0	0.20	5%	0	0.49
Co-Feed TP	-	<5%	1000	0.19	<5%	1000	0.21
Bi_2MoO_6							
TPR	-	11%	0	0.95	14%	0	1.47
Co-Feed TP	-	<5%	1000	0.16	6%	1000	0.14

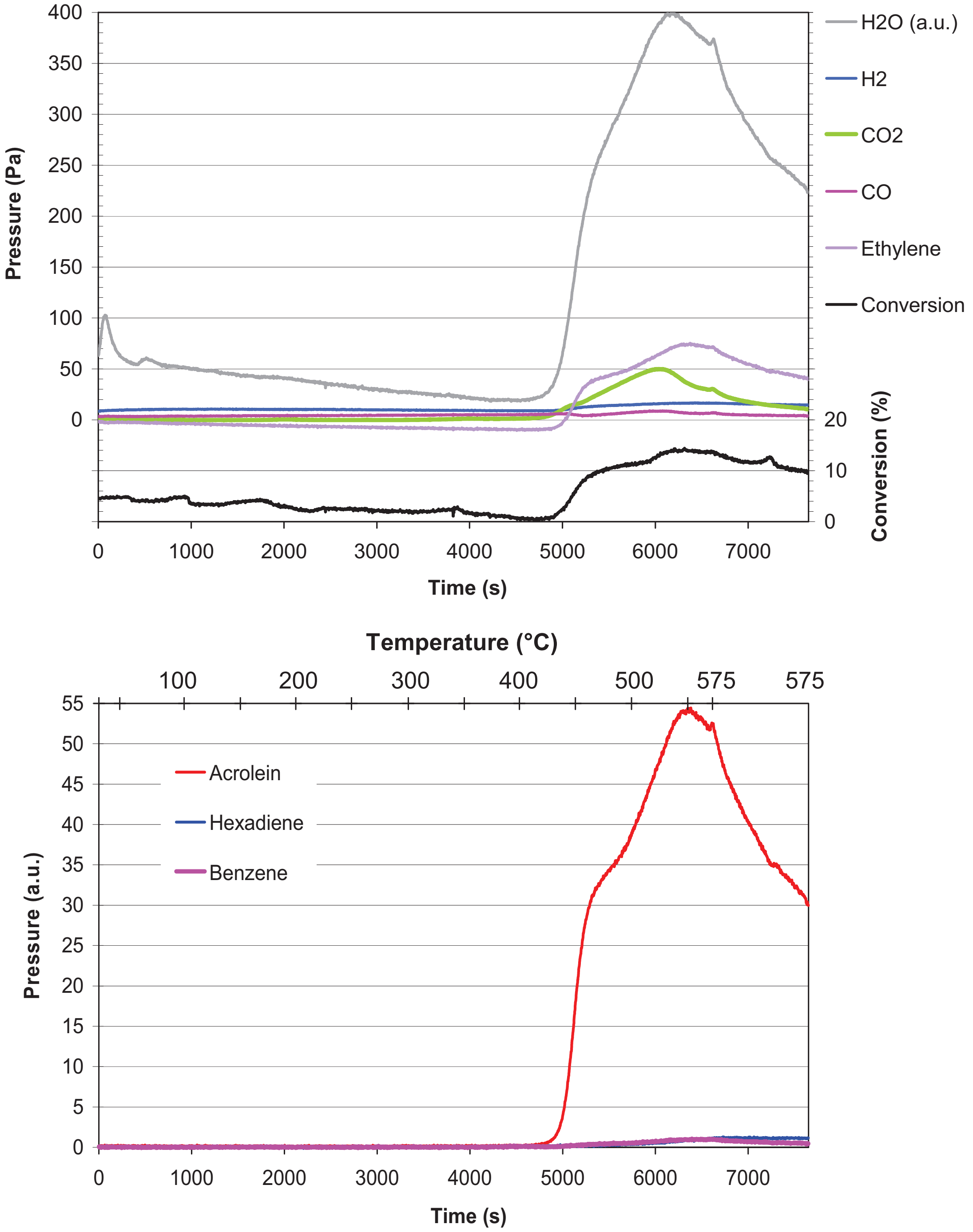

Fig. 4.39 Distribution of product pressures vs. time and temperature for the Temperature-Program Reduction (TPR) of Bi_2MoO_6 catalyst with 75 ml/min Ar, 24 ml/min He and 1 ml/min C_3H_6 in a conventional reactor.

5.4. Characterizations after catalytic experiments

The membrane and catalyst on the LOP side was characterized after the catalytic tests. The XRD pattern of $Bi_{25.75}Mo_{10}O_{68.625}$-Au *cermet* electrode after the CDMR applications confirms the presence of $Bi_{25.75}Mo_{10}O_{68.625}$, Bi_2MoO_6 and gold, as shown in Fig. 4.40. However, some small Bragg peaks of $Bi_2Mo_2O_9$ were found, that might be related to the degradation of the membrane.

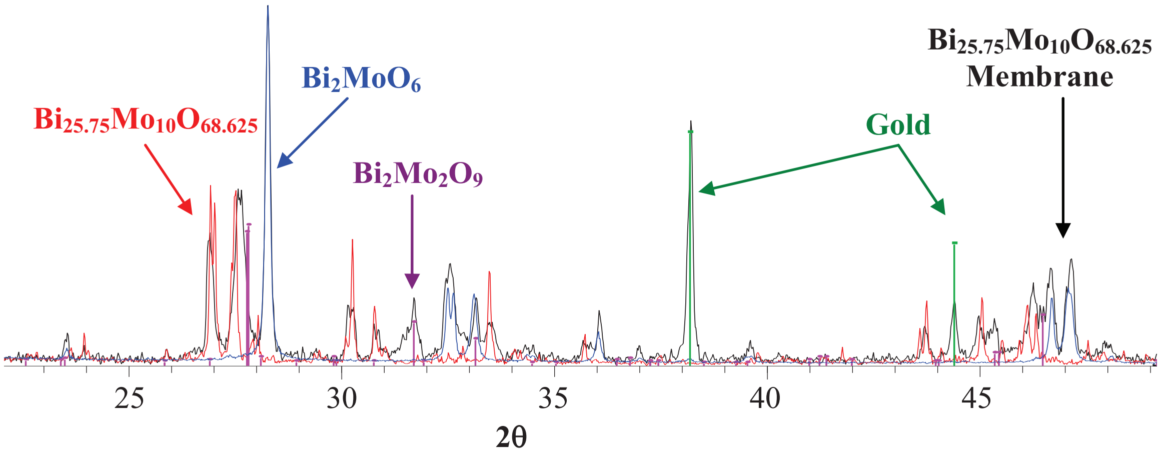

Fig. 4.40 XRD pattern of $Bi_{25.75}Mo_{10}O_{68.625}$-Au *cermet* electrode after the CDMR applications compared with that of $Bi_{25.75}Mo_{10}O_{68.625}$ and Bi_2MoO_6 powder before the test.

In addition, SEM images using secondary electrons and backscattered electrons in Fig. 4.41 show a homogeneous distribution of ceramic and gold on the membrane surface, which remains similar to the membrane before the reaction.

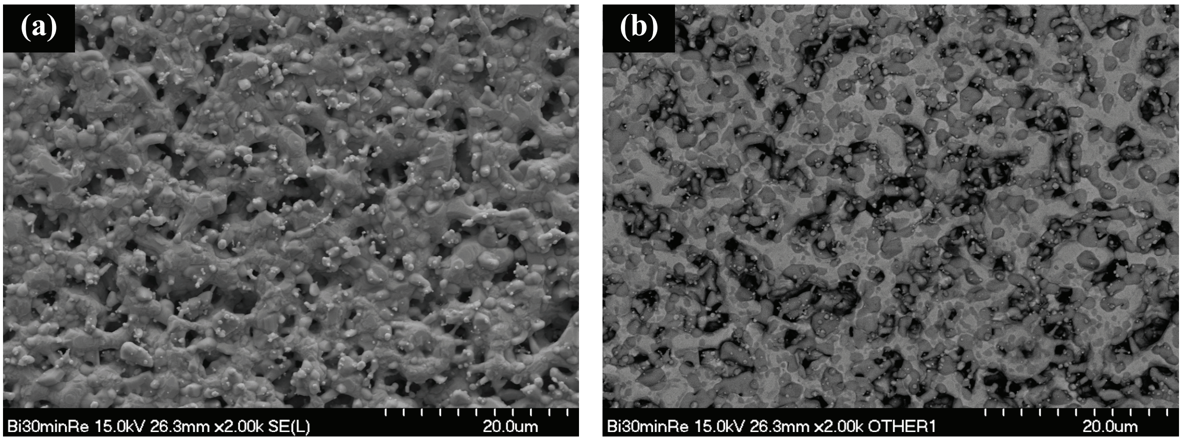

Fig. 4.41 Scanning electron micrographs of $Bi_{25.75}Mo_{10}O_{68.625}$-Au *cermet* electrode after the CDMR applications with secondary electrons a) and backscattered electrons b).

The 10 nm-depth of membrane and catalyst before and after the catalytic experiments on the LOP side were also characterized by X-ray Photoelectron Spectroscopy (XPS). The principal elements detected were Bi, Mo, O and Au, with the following binding energies: Bi^{3+} (4f7/2: 159 eV and 4f5/2: 165 eV), Mo^{6+} (3d5/2: 232 eV and 3d3/2: 236 eV), O^{2-} (1s: 530 eV) and Au (4f7/2: 84 eV and 4f5/2: 88 eV). About 28 atom% C was found in all materials, before and after reaction (BE 1s = 285 eV). The XPS spectra of the principal elements are illustrated in Fig. 4.42 and Fig. 4.43.

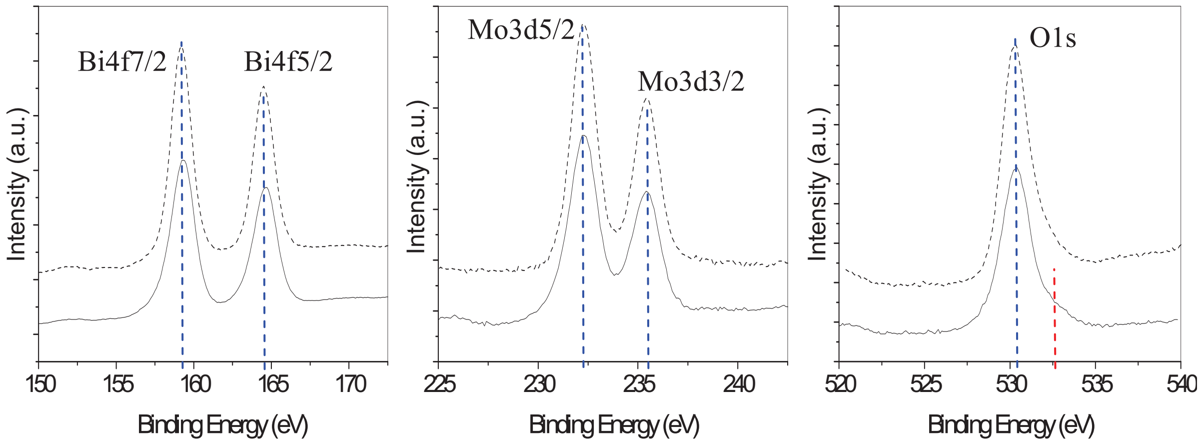

Fig. 4.42 XPS spectra of different elements (Bi, Mo, and O) on the LOP side of $Bi_{25.75}Mo_{10}O_{68.625}$ membrane surface (dashed line and solid line represent materials before and after the reaction, respectively).

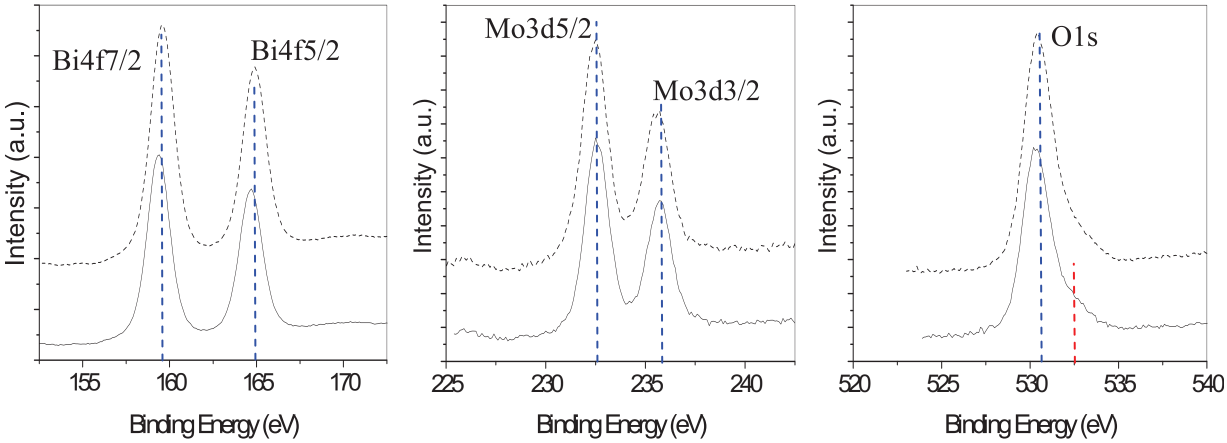

Fig. 4.43 XPS spectra of different elements (Bi, Mo, and O) of Bi_2MoO_6 catalyst deposited on the membrane surface (dashed line and solid line represent materials before and after the reaction, respectively).

The atomic percentages of elements found on the surface of materials were calculated from the peak areas (Table 4.8). The Bi/Mo ratios of membrane and catalyst before and after the reaction are higher than the theoretical values. This is quite common in bismuth-containing mixed oxides and is due to the ability of bismuth to segregate as bismuth oxide which is prone to sublimation [31]. Shaping the $Bi_{25.75}Mo_{10}O_{68.625}$ powder as a membrane leads to an increase by *ca*. 10% that may not be significant. It is worth noting that the membrane after the reaction is covered by some Bi_2MoO_6 catalyst powder which could explain its lower Bi/Mo ratio as compared with the membrane before reaction, as well as account for the absence of Au characteristic photopeaks.

Table 4.8 XPS Analysis of membrane and catalyst materials before and after catalytic reactions

Materials	Bi4f atom%	Mo3d atom%	O1s atom%	Au4f atom%	Experimental Bi/Mo ratio	Theoretical Bi/Mo ratio
Bi_2MoO_6 calcinated at 550°C	29.46	10.01	60.53	-	2.94	2
Bi_2MoO_6 after the reaction	28.90	10.56	60.54	-	2.74	2
$Bi_{25.75}Mo_{10}O_{68.625}$ membrane before the reaction	19.91	5.65	37.32	37.12	3.53	2.58
$Bi_{25.75}Mo_{10}O_{68.625}$ membrane after the reaction	31.44	10.16	58.40	-	3.10	2.58
$Bi_{25.75}Mo_{10}O_{68.625}$ powder	31.15	9.74	59.11	-	3.20	2.58

By comparison with XPS spectra of the membrane before and after the reaction, no shift of Mo binding energy was observed, indicating an absence of reduced species on the membrane surface after the reaction. The absence of reduced Mo specie like Mo^{5+} is common, even after catalytic reaction, in bismuth molybdate catalyst powders. Although it is known that such reduced specie occur on the surface during the reaction, they are quickly reoxidized as soon as the solid is put in air. Compared with Bi_2MoO_6 catalyst, a very slight shift in binding energy of Bi^{3+} toward low binding energies, by 0.02 eV and a larger FWHM (full-width at height medium) could be assigned to a partial reduction of Bi in Bi_2MoO_6 catalyst. Finally the shoulder observed in O1s photopeak at *ca*. 533 eV is probably due to silica that comes from the sealing glass.

6. CONCLUSION

By optimization of the powder preparation and of the sintering conditions to get a membrane, as well as the reactor assembly and operating conditions, we have studied the feasibility of a Catalytic Dense Membrane Reactor using bismuth molybdenum oxides. Since low catalytic activity and low oxygen permeation were observed with the *cermet* $Bi_{25.75}Mo_{10}O_{68.625}$-Ag membrane, an electrochemical membrane reactor was later built to take advantage of applying a current. It was based on a dense $Bi_{25.75}Mo_{10}O_{68.625}$ membrane onto which $Bi_{25.75}Mo_{10}O_{68.625}$-Au *cermet* electrodes were deposited.

Interestingly, a very low catalytic activity was observed at open circuit voltage, whereas the production of acrolein was noticed only when an electrical bias was applied. The membrane activity comes back to its initial stage when the current was turned off. After the deposition of γ-Bi_2MoO_6 catalyst on the membrane surface, the conversion of propylene significantly increased with production of acrolein, even at OCV. In contrast to the previous experiment without γ-Bi_2MoO_6 catalyst, the acrolein production decreases with the current density. By this study, and although the role of oxygen species provided by $Bi_{25.75}Mo_{10}O_{68.625}$ is difficult to explain, it has been demonstrated that combining a decoupling redox operation, by using the CDMR with oxide ion conducting BiMoO membrane, and the catalyst Bi_2MoO_6 allows to operate continuously in reduction conditions. In these conditions the selectivity to acrolein is higher that that obtained in a conventional reactor which is fed by both hydrocarbon and gaseous oxygen

Electrocatalysis is a wide field which is applied industrially. This is a preliminary study that would deserve far more numerous experiments to elucidate the phenomena. Anyway it seems that the application of a current to a catalyst/membrane system would be a powerful tool to modify the catalyst activity.

References

[1] N. Aishah, S. Amin, and S. E. Pheng, *Chem. Eng. J.*, 2006, **116**, 187–195.

[2] M. Rebeilleau-Dassonneville, S. Rosini, A. C. van Veen, D. Farrusseng, and C. Mirodatos, *Catal. Today*, 2005, **104**, 131–137.

[3] E. Santacesaria, M. Cozzolino, M. D. Serio, A. M. Venezia, and R. Tessera, *Appl. Catal. A: Gen.*, 2004, **270**, 177–192.

[4] L. M. Madeira, J. M. Herrmann, J. Disdier, M. F. Portela, and F. G. Freirec, *Appl. Catal. A: Gen.*, 2002, **235**, 1–10.

[5] P. Corbo and F. Migliardini, *Int. J. Hydrogen Energy*, 2007, **32**, 55–56.

[6] E. van der Heide, M. Zwinkels, A. Gerritsen, and J. Scholten, *Appl. Catal. A: Gen.*, 1992, **86**, 181–198.

[7] G. Centi, F. Cavani, and F. Trifiro, *Selective Oxidation by Heterogeneous Catalysis*, Kluwer Academic/Plenum, 2001.

[8] R. K. Grasselli and J. D. Burrington, *Adv. Catal.*, 1981, **30**, 133–163.

[9] P. Mars and D. van Krevelen, *Chem. Eng. Sci.*, 1954, **3**, 41–59.

[10] R. M. Contractor, Improved vapor phase catalytic oxidation of butane to maleic anhydride, 1987.

[11] T. T. Tsotsis, A. M. Champagnie, R. G. Minet, and H.-G. Liu, *Computer Aided Design of Catalysts*, Marcel Dekker, 1993.

[12] R. Ramos, M. Menéndez, and J. Santamaría, *Catal. Today*, 2000, **56**, 239–245.

[13] G. Saracco and V. Specchia, *Catal. Rev.-Sci. Eng.*, 1994, **36**, 305–384.

[14] R. N. Vannier, G. Mairesse, F. Abraham, and G. Nowogrocki, *J. Solid State Chem.*, 1996, **122**, 394–406.

[15] R. N. Vannier, F. Abraham, G. Nowogrocki, and G. Mairesse, *J. Solid State Chem.*, 1999, **142**, 294–304.

[16] G. Fafilek and P. Kurek, *Solid State Ionics*, 2003, **157**, 171–176.

[17] M. Malys, G. Fafilek, C. Pirovano, and R. N. Vannier, *Solid State Ionics*, 2005, **176**, 1769–1773.

[18] L. Holmes, L. Peng, I. Heinmaa, L. A. O'Dell, M. E. Smith, R.-N. Vannier, and C. P. Grey, *Chem. Mater.*, 2008, **20**, 3638–3648.

[19] F. C. Fonseca, M. C. Steil, R. N. Vannier, G. Mairesse, and R. Muccillo, *Solid State Ionics*, 2001, **140**, 161–171.

[20] A. Löfberg, S. Boujmiai, E. Capoen, M. C. Steil, C. Pirovano, R. N. Vannier, G. Mairesse, and E. Bordes-Richard, *Catal. Today*, 2004, **91-92**, 79–83.

[21] M. Mori, T. Abe, H. Itoh, O. Yamamoto, Y. Takeda, and T. Kawahara, *Solid State Ionics*, 1994, **74**, 157–164.

[22] H. Bodet *Céramiques denses comme réacteur membranaire pour l'oxydation ménagée des hydrocarbures* PhD thesis, University Lille 1, 2007.

[23] E. Capoen *Etude de composés oxydes conducteurs mixtes, anioniques et électroniques, pour leur utilisation en tant que matériaux membranaires pour la séparation sélective de l'oxygène de l'air* PhD thesis, University Lille 1, 2002.

[24] E. Capoen, M. Steil, G. Nowogrock, M. Malys, C. Pirovano, A. Lofberg, E. Bordes-Richard, J. Boivin, G. Mairesse, and R. Vannier, *Solid State Ionics*, 2006, **177**, 483–488.

[25] H. Bodet, A. Löfberg, C. Pirovano, M. Steil, R. Vannier, and E. Bordes-Richard, *Catal. Today*, 2009, **141**, 260–263.

[26] Z. Wu and M. Liu, *Solid State Ionics*, 1996, **93**, 65–84.

[27] H. J. M. Bouwmeester and A. J. Burggraaf, *The CRC Handbook of Solid State Electrochemistry, Chapter 14, Dense ceramic membranes for oxygen separation.*, CRC Press, Inc., 1997.

[28] A. Löfberg, H. Bodet, C. Pirovano, M. Steil, R. Vannier, and E. B. Richard, *Catal. Today*, 2006, **118**, 223–227.

[29] H. Bouwmeester, H. Kruidhof, A. Burggraaf, and P. Gellings, *Solid State Ionics*, 1992, **53-56**, 460–468.

[30] M. Mogensen and S. Skaarup, *Solid State Ionics*, 1996, **86-88**, 1151–1160.

[31] A. Chetouani, B. Taouk, and E. Bordes-Richard, *Catal. Today*, 2004, **91-92**, 73–77.

APPENDIX

Appendix

1. LOW TEMPERATURE SEALING GLASS

According to the CDMR study with a $Bi_{25.75}Mo_{10}O_{68.625}$-Ag ***cermet*** membrane, a pyrex glass has been demonstrated to be an appropriate seal, providing a good gas-tightness between the LOP and HOP chambers, for the operating temperature range between 600 and 700°C. However, its sealing performance is moderate at lower temperature. Thereby, the investigation of a new seal for the SEMR applications, with operating temperatures below 600°C, was required.

One of the most important challenges for the development of intermediate-temperature SEMR was the development of a proper sealant that separates the LOP and HOP chambers and maintains the gas-tightness of the total system at operating temperatures. Seals are generally applied to the cell edges between the membrane and the ceramic tubes. Commonly used rubber O-ring seals are not suitable for these applications due to their resistance limits (<400°C). Only inorganic materials with high melting points can be employed for sealing at higher temperatures. Several CDMR, SEMR and oxygen permeation studies used soft and relatively inert metal, such as silver and gold, as a seal [1, 2, 3]. In our study, the only metal which could be used was gold in order to avoid the alloy formation that would occur between the gold electrodes and other metal seals. In this technique, the gas-tightness is achieved by exerting a compression force on the metal ring. However, the system can be sustained under thermally-induced stress because of the use of compression force and difference in thermal expansion coefficients between the metal seal, tubes and ceramic membrane. Another main drawback of gold sealant is its high sealing temperature should be at 800°C for one night [4] which is close to the melting point of $Bi_{25.75}Mo_{10}O_{68.625}$.

Therefore the utilization of glass based seals was considered. In this case a glass paste or ring is placed between membrane and ceramic tubes. The glass softens at high temperature, filling the gap of the joint, and the temperature is then lowered to solidify the seal for application. The glass based seals have a better spreading properties and thermal compatibility with the ceramic components, as compared with the metal seals. However, a good glass seal should fulfill the following requirements: it should have a good wettability and thermal expansion compatibility with both membrane and supporting tubes; it should also have a suitable viscosity and should be chemically inert in the operating temperature range [5]. The thermal expansion coefficients of the membrane material, seals and some commonly used support materials are listed in Table 1.

Table 1 Thermal properties of the membrane material, seals and some commonly used support materials.

Materials	Membrane $Bi_{25.75}Mo_{10}O_{68.625}$	Alumina (Al_2O_3)	Mullite ($3Al_2O_3.2SiO_2$)	Quartz (SiO_2)	Gold	Borosilicate Glass [6] (SiO_2-B_2O_3)
Melting/softening point (°C)	976	2045	1870	1470	1063	440-840
Thermal expansion coefficient ($10^{-6}.K^{-1}$)	10	9.2	6.5	0.6	15.2	2-14

From Table 1, it is clear that glass has thermal expansion coefficient range covering both support and membrane material. Moreover, the thermal expansion coefficient of $Bi_{25.75}Mo_{10}O_{68.625}$ is closer to that of alumina than that of mullite and quartz, indicating that alumina is likely the most appropriate material to be used as a support tubes in our reactor.

After some literature reviews, five glass families were chosen. The main criterion to select sealant materials is their thermal expansion coefficient (TEC), which must be compatible to that of membrane and support materials. ZnO-Sb_2O_3-P_2O_5 glasses and Barium-containing glass system, including Ba alluminoborosilicate, BaCa borosilicate, BaMg borosilicate and BaZn borosilicate with TEC values of approximately $8x10^{-6}$ to $12x10^{-6}$ K^{-1} and Tg in the temperature range of 400-650°C are promising for our applications. Their compositions are given in Table 2. The glasses were prepared according to the experimental procedure described in the corresponding paper. In order to evaluate the sealing performance, a series of tests were performed. Pressed powder pellets of each glass composition were placed between the dense membrane and alumina pellets. Later, they were heated to the sealing temperature and then cooled down. The results of these tests showed that only AlBaSi glass had the best sealing performance. It had a good viscosity, wettability and binding strength with the $Bi_{25.75}Mo_{10}O_{68.625}$ membrane and alumina.

Table 2 Glass compositions.

Glass	Composition (mol%)
Sb20 [7]	40% ZnO, 20% Sb_2O_3, 40% P_2O_5
Sb40 [7]	20% ZnO, 40% Sb_2O_3, 40% P_2O_5
CaBaSi [8]	36.21% BaO, 9.4% B_2O_3, 35.33% SiO_2, 5.18% Al_2O_3, 12.64% CaO, 1.23% ZrO_2
AlBaSi [9]	66.81% BaO, 15.66% B_2O_3, 3.13% SiO_2, 14.40% Al_2O_3,
MgBaSi [10]	27% BaO, 15% B_2O_3, 40% SiO_2, 18% MgO
SchottBi*	1-10% B_2O_3, 0.1-1% SiO_2, 0.1-1% Al_2O_3, 10-50% ZnO, > 50% Bi_2O_3

*Industrial glass distributed by Schott.

Prior to application of AlBaSi glass seal for the CDMR applications, a rigorous thermal characterization of this composition has been investigated. A DT analysis was performed during the heating process from room temperature to 1300°C. It is worth noticing that there is no significant modification observed in the DTA curve for the temperature range from room temperature to 400°C, subsequently only the thermal evolution from 400°C to 1300°C is presented in Fig. 1.

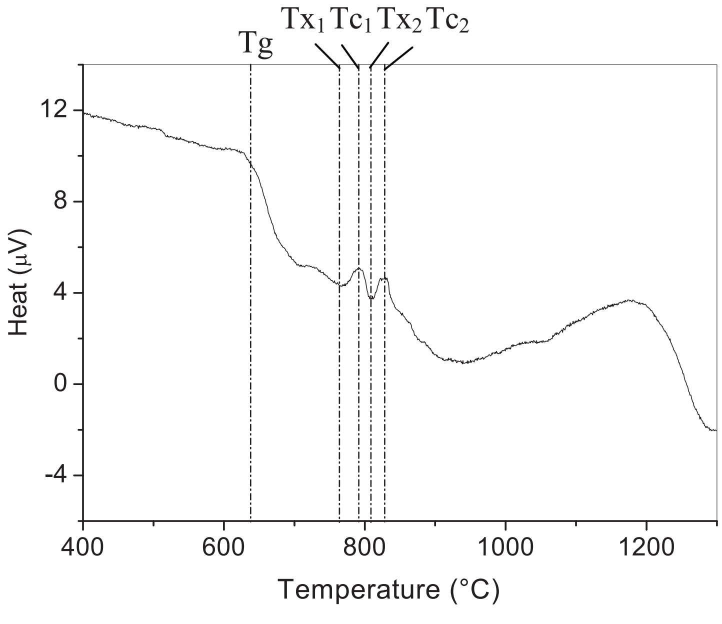

Fig. 1 DT analysis of AlBaSi glass heated from room temperature to 1300°C.

From Fig. 1, the characteristic temperatures of AlBaSi glass: the transformation temperature (Tg=638°C), the temperatures of beginning of crystallization (Tx_1= 766°C and Tx_2= 808°C) and the crystallization temperatures (Tc_1=791°C and Tc_2=829°C) were evidenced.

For the sealing applications, it is necessary to determine the sealing temperature. According to Pacual et *al*. [10], the viscosity of glasses, which is known to vary with temperature, influences considerably the binding property between glass and other components. It has been found that the appropriate sealing viscosity should be around 10^5 dPa.S, which is located between two characteristic temperatures: maximum shrinkage and half ball temperatures [11].

In order to determine these characteristic temperatures, a Hot-Stage Microscope (HSM) with image analysis used to fellow the softening of a cylindrical sample of glass powder. In this study, the sample was heated from room temperature to the flow point (or melting point) with a 10°C/min heating rate and an image of the sample was recorded every 10°C. From the sample shape, characteristic temperatures were deduced. These results are reported in Fig. 2. The characteristic temperatures: first shrinkage (FS=560°C), maximum shrinkage temperature (MS=657°C), sphere temperature (R=685°C), hemisphere temperature (HS=753°C) and flow temperature (F=791°C) were evidenced. The appropriate sealing temperature of AlBaSi glass was finally determined to be around 680°C.

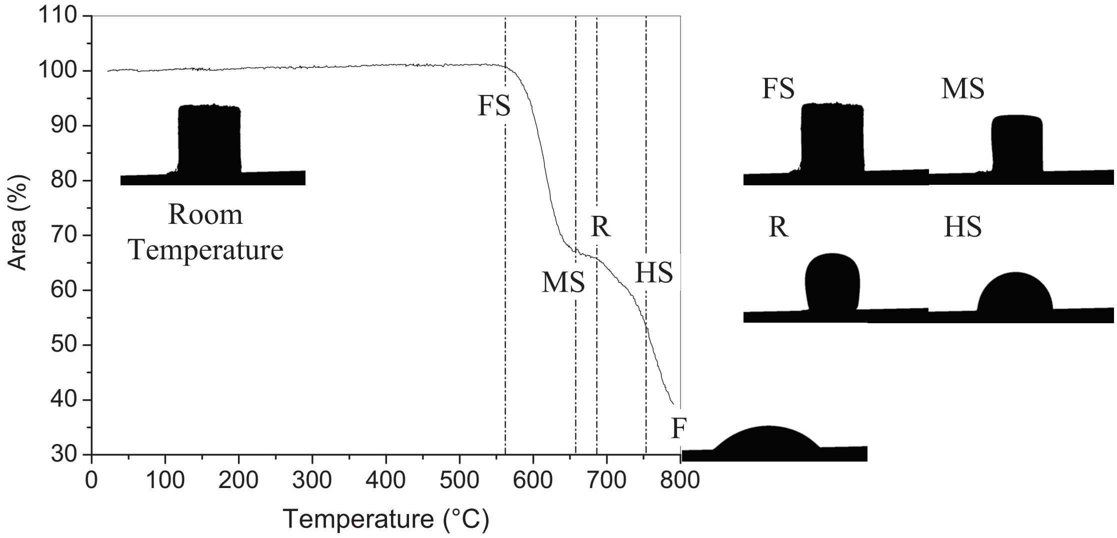

Fig. 2 The characteristic temperatures of AlBaSi glass: first shrinkage (FS=560°C), deformation temperature (MS=657°C), sphere temperature (R=685°C), hemisphere temperature (HS=753°C) and flow temperature (F=791°C) obtained by HSM and alumina substrate.

In good agreement with the conditions of use of the SEMR we wanted to develop, this composition of sealant (AlBaSi) was finally chosen for our application.

2. CATALYTIC RESULTS

2.1. Catalytic Results of Reactions in a Catalytic Dense Membrane Reactor

Table 3 Distribution of product pressures at different current density using a $Bi_{25.75}Mo_{10}O_{68.625}$ membrane with $Bi_{25.75}Mo_{10}O_{68.625}$-Au *cermet* electrodes (500°C, 1% C_2H_6/He in LOP, air in HOP).

3rd*	Gas & Voltage/I(mA)	avant HC	0	10	20	30	0	sans HC
O_2 Permeation	Voltage (mV)	-102	-	855	-	1593	-	-
	PO_2 of gas outlet (Pa)	6.0	-	65.2	-	195.4	-	-
Reaction	Voltage (mV)	-95.00	-349.00	845.00	1228.00	1609.00	-347.00	-217.00
	PO_2 (Pa)	0.53	0.21	12.30	31.20	47.10	0.31	0.38
	PH_2 (Pa)	0.00	95.84	66.70	56.70	50.90	60.40	2.08
	PCO_2 (Pa)	0.00	0.00	8.68	11.80	16.80	0.00	0.00
	PCO (Pa)	1.19	1.61	3.88	4.57	5.26	1.36	1.33
	Pethylene (Pa)	0.00	0.00	4.57	5.88	7.80	0.00	0.00
	Paccrolein (a.u.)	0.10	0.28	3.30	4.14	5.84	0.26	0.00
	PH_2O (a.u.)	2.01	22.40	60.10	69.90	87.10	20.30	0.00
	Conversion (%)	-	0.37	4.02	3.02	2.58	0.86	-

Table 4 Distribution of product pressures at different current density using a $Bi_{25.75}Mo_{10}O_{68.625}$ membrane with $Bi_{25.75}Mo_{10}O_{68.625}$-Au *cermet* electrodes (525°C, 1% C_2H_6/He in LOP, air in HOP).

4th*	Gas & Voltage/I(mA)	avant HC	0	10	20	30	40	0	sans HC
O_2 Permeation	Voltage (mV)	-107	-	738	-	1381	-	-	-
	PO_2 of gas outlet (Pa)	4.4	-	66.1	-	193.2	-	-	-
Reaction	Voltage (mV)	-101.00	-355.00	697.00	1027.00	1365.00	1652.00	-349.00	-204.00
	PO_2 (Pa)	0.49	0.18	5.98	22.10	34.10	44.50	0.25	0.40
	PH_2 (Pa)	0.00	78.60	60.80	52.20	47.40	45.40	55.70	1.32
	PCO_2 (Pa)	0.00	0.00	11.20	15.80	25.10	33.10	0.00	0.00
	PCO (Pa)	1.15	1.53	4.90	5.63	6.40	7.55	1.26	1.29
	Pethylene (Pa)	0.00	0.00	6.96	7.38	13.00	16.10	0.64	0.00
	Paccrolein (a.u.)	0.00	0.27	4.72	5.45	7.75	9.88	0.26	0.00
	PH_2O (a.u.)	1.54	19.60	68.30	82.20	111.0	138.0	18.60	0.21
	Conversion (%)	-	1.09	2.83	3.64	4.63	6.72	0.18	-

Table 5 Distribution of product pressures at different current density using a $Bi_{25.75}Mo_{10}O_{68.625}$ membrane with $Bi_{25.75}Mo_{10}O_{68.625}$-Au *cermet* electrodes (550°C, 1% C_2H_6/He in LOP, air in HOP).

1st*	I(mA)/ Gas & Voltage	avant HC	0	10	20	30	40	50	0	sans HC
O_2 Permeation	Voltage (mV)	-124	-	600	-	1115	-	-	-	-
	PO_2 of gas outlet (Pa)	4.3	-	84.2	-	224.6	-	-	-	-
Reaction	Voltage (mV)	-104.0	-327.0	500.0	811.0	1082.0	1334.0	1562.0	-354.0	-213.0
	PO_2 (Pa)	0.55	0.00	0.36	3.79	10.30	19.80	32.90	0.19	0.35
	PH_2 (Pa)	0.00	18.30	73.30	59.20	49.50	43.50	38.80	48.80	0.85
	PCO_2 (Pa)	0.00	0.00	13.30	24.70	35.30	43.60	51.70	0.00	0.00
	PCO (Pa)	1.31	1.34	5.96	7.69	8.80	9.57	9.97	1.19	1.44
	Pethylene (Pa)	0.00	0.00	12.30	17.10	20.90	23.20	24.80	0.36	0.00
	Paccrolein (a.u.)	0.00	0.39	7.34	10.70	12.30	13.70	14.30	0.38	0.00
	PH_2O (a.u.)	1.24	15.90	78.30	118.0	150.0	179.0	199.0	18.80	-2.51
	Conversion (%)	-	4.30	6.09	5.98	7.86	8.77	9.56	2.31	-

Table 6 Distribution of product pressures at different current density using a $Bi_{25.75}Mo_{10}O_{68.625}$ membrane with $Bi_{25.75}Mo_{10}O_{68.625}$-Au *cermet* electrodes (565°C, 1% C_2H_6/He in LOP, air in HOP).

2nd*	I(mA)/ Gas & Voltage	avant HC	0	10	20	30	40	50	0	sans HC
O_2 Permeation	Voltage (mV)	-149	-	552	-	1042	-	-	-	-
	PO_2 of gas outlet (Pa)	0.0	-	67.8	-	213.5	-	-	-	-
Reaction	Voltage (mV)	-149.00	-363.00	450.00	749.00	1005.00	1245.00	1471.00	-359.00	-161.00
	PO_2 (Pa)	0.41	0.13	0.28	3.83	11.20	21.50	35.80	0.29	0.40
	PH_2 (Pa)	0.51	76.40	51.50	44.40	38.80	36.40	35.40	50.20	0.24
	PCO_2 (Pa)	0.26	0.00	12.90	25.10	35.30	45.10	52.20	0.00	0.00
	PCO (Pa)	1.40	1.10	7.11	9.06	10.20	11.40	12.30	1.62	1.27
	Pethylene (Pa)	0.00	0.00	8.00	13.40	16.60	18.70	20.40	1.37	0.00
	Paccrolein (a.u.)	0.00	0.35	7.02	10.00	11.50	12.90	13.50	0.46	0.20
	PH_2O (a.u.)	0.20	13.50	74.90	115.0	147.0	176.0	199.0	16.10	0.38
	Conversion (%)	-	0.00	4.94	7.07	9.54	10.40	11.50	3.10	-

Table 7 Distribution of product pressures at different current density using the $Bi_{25.75}Mo_{10}O_{68.625}$ membrane with $Bi_{25.75}Mo_{10}O_{68.625}$-Au *cermet* electrodes and a Bi_2MoO_6 catalyst powder (500°C, 1% C_2H_6/He in LOP, air in HOP).

5^{th}*	Gas & Voltage/I(mA)	avant HC	0	10	20	30	0	sans HC
O_2 Permeation	Voltage (mV)	-94	-	877	-	1626	-	-
	PO_2 of gas outlet (Pa)	2.65	-	60.98	-	205.18	-	-
Reaction	Voltage (mV)	-89.00	-621.00	868.00	1236.00	1618.00	-616.00	-578.00
	PO_2 (Pa)	0.40	0.20	0.28	0.33	0.34	0.07	0.10
	PH_2 (Pa)	0.00	83.40	76.10	68.40	62.40	60.30	0.76
	PCO_2 (Pa)	0.00	35.50	39.80	38.60	31.80	15.50	0.00
	PCO (Pa)	0.08	3.79	4.83	5.75	5.51	0.00	0.00
	Pethylene (Pa)	0.15	89.40	60.90	40.90	29.50	58.50	0.20
	Paccrolein (a.u.)	0.00	40.00	27.20	16.90	11.80	26.80	0.00
	PH_2O (a.u.)	-4.68	241.0	213.0	186.0	160.0	10.30	0.00
	Conversion (%)	-	14.20	11.10	8.49	7.56	10.30	-

* Experiment order.

2.2. Catalytic Results of Reactions in a Conventional Reactor

The temperature programmed reactions and co-feed reactions were performed on the Bi_2MoO_6 and $Bi_{25.75}Mo_{10}O_{68.625}$ powder in a conventional reactor in order to better understand the behavior of these materials for propylene oxidation. Experiments were carried out in reductive conditions (1% propylene in inert gas) similar to those of the LOP compartment of CDMR or in more classical co-feed conditions (1% propylene +1% oxygen). The evolution of partial pressures and conversion versus time/temperature of these reactions are shown in Fig. 3-Fig. 5.

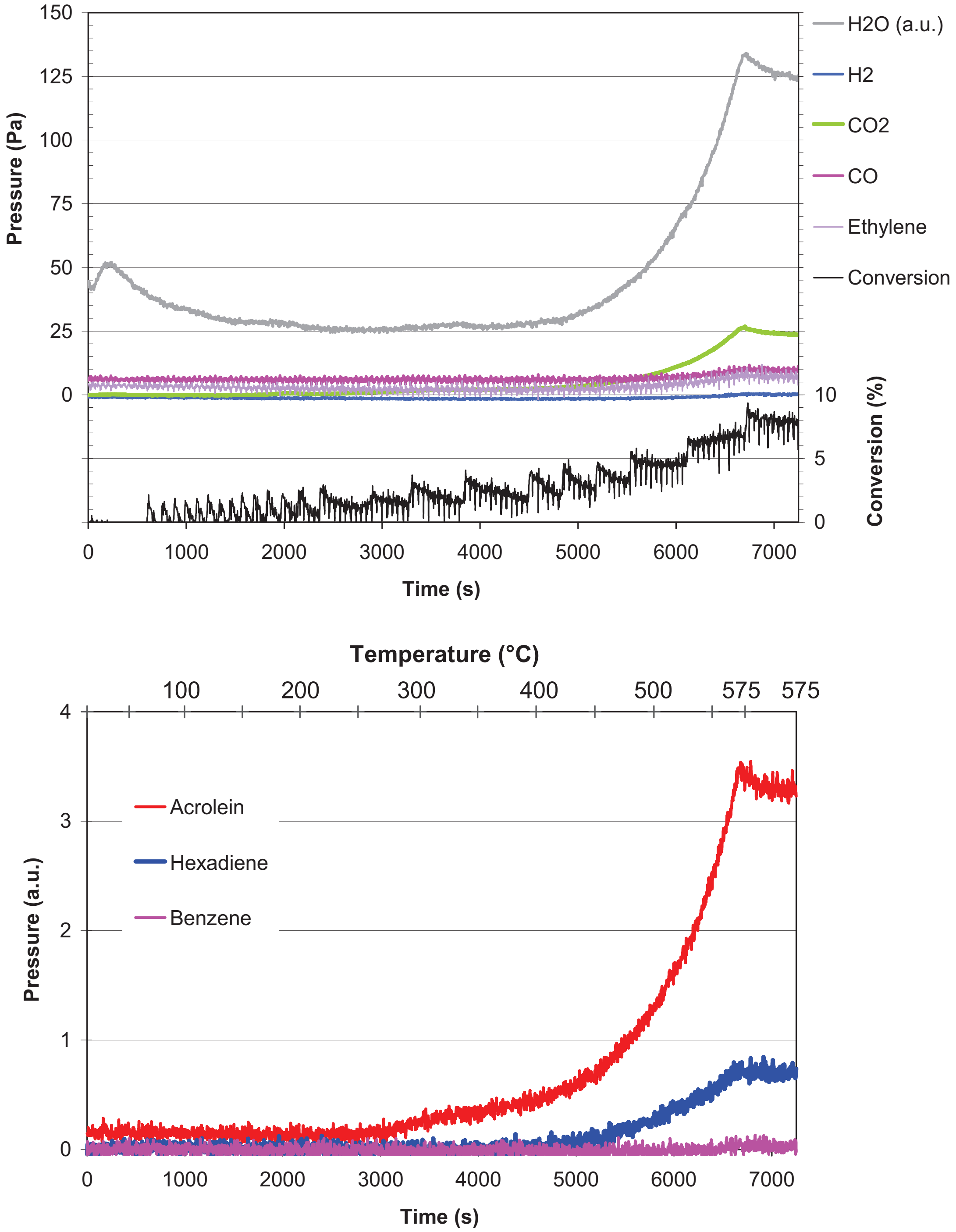

Fig. 3 Distribution of product pressures vs. time and temperature for the co-feed reaction of Bi_2MoO_6 catalyst with 50 ml/min Ar, 48 ml/min He, 1 ml/min C_3H_6 and 1 ml/min O_2 in a conventional reactor.

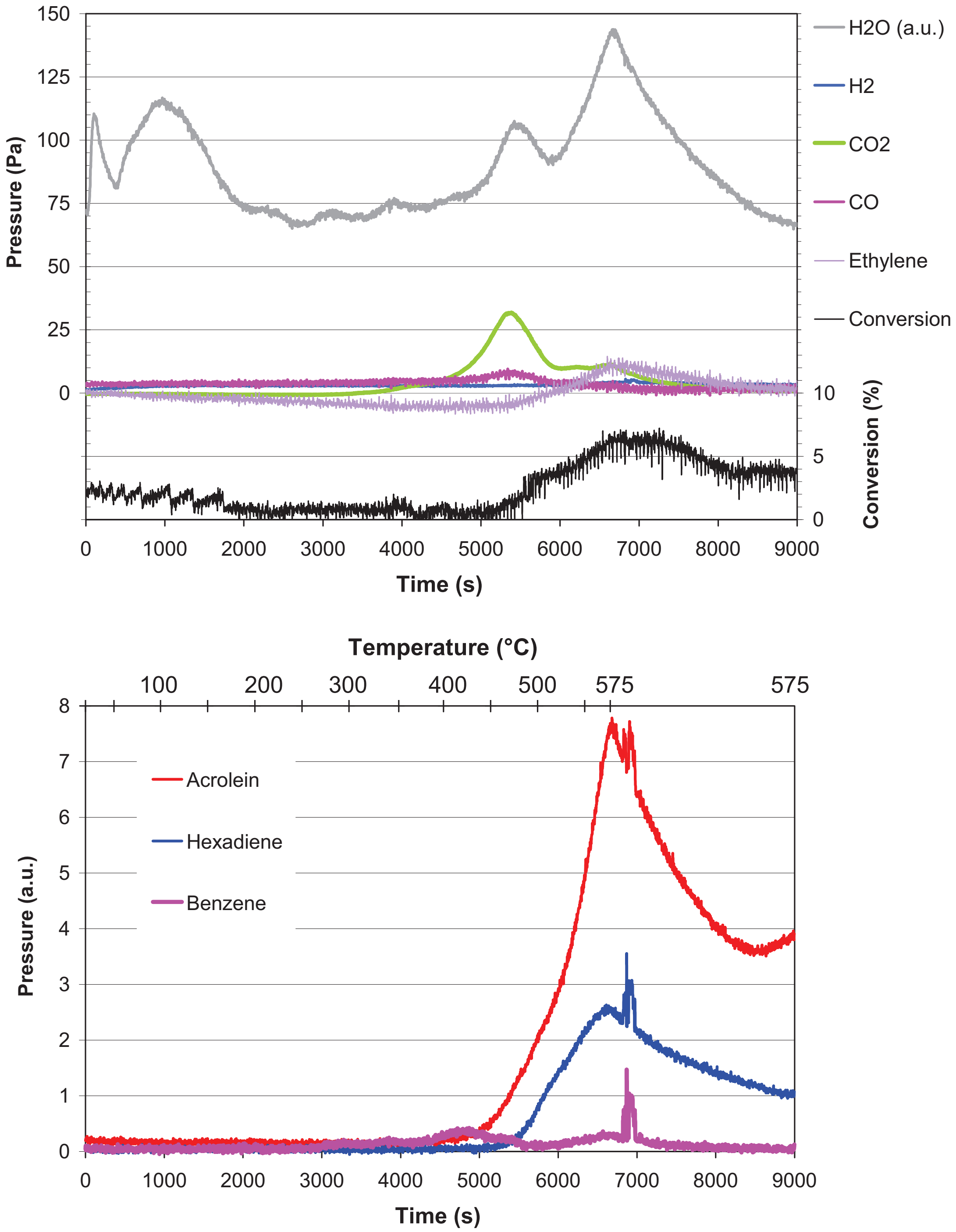

Fig. 4 Distribution of product pressures vs. time and temperature for the Temperature-Program Reduction (TPR) of $Bi_{25.75}Mo_{10}O_{68.625}$ with 75 ml/min Ar, 24 ml/min He and 1 ml/min C_3H_6 in a conventional reactor.

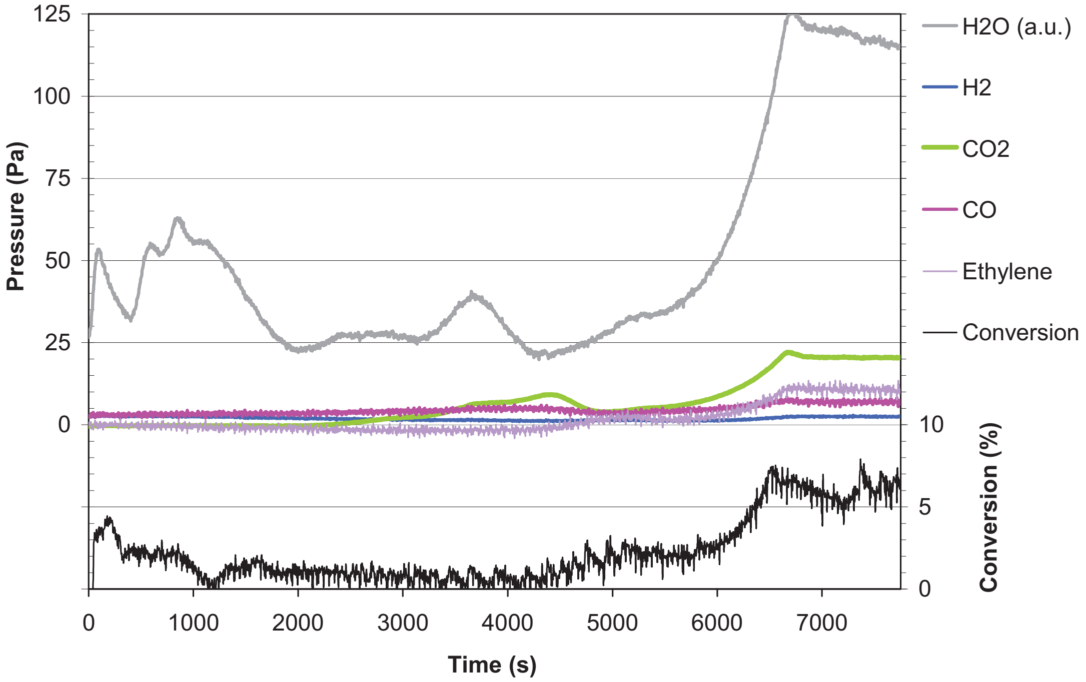

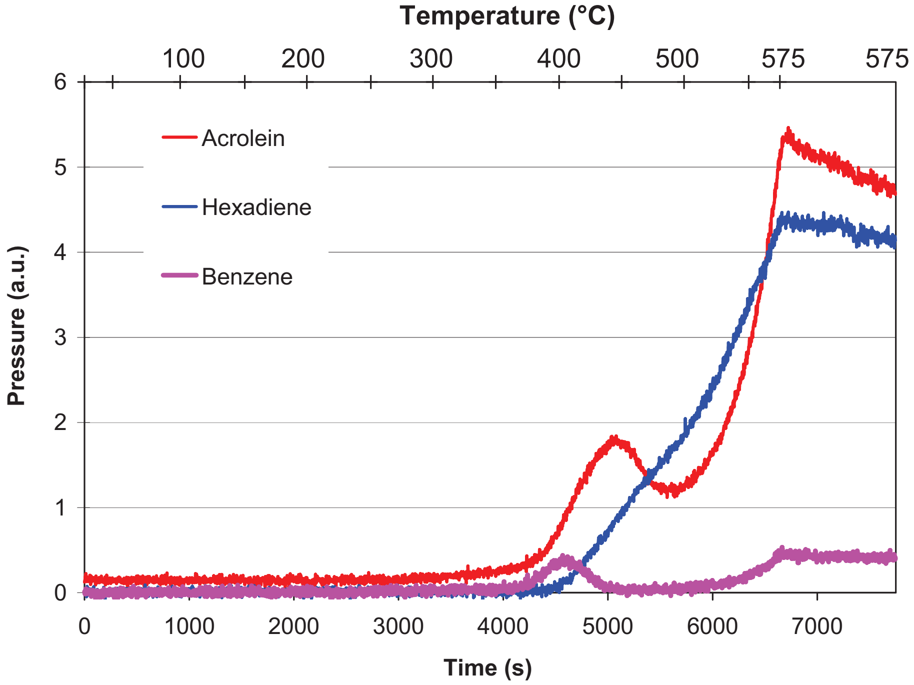

Fig. 5 Distribution of product pressures vs. time and temperature for the cofeed reaction of $Bi_{25.75}Mo_{10}O_{68.625}$ with 50 ml/min Ar, 48 ml/min He, 1 ml/min C_3H_6 and 1 ml/min O_2 in a conventional reactor.

References

[1] J. A. Lane, S. J. Benson, D. Waller, and J. A. Kilner, *Solid State Ionics*, 1999, **121**, 201–208.

[2] W. Zhu, W. Han, G. Xiong, and W. Yang, *Catal. Today*, 2005, **104**, 149–153.

[3] Q. Li, X. Zhu, and W. Yang, *J. Memb. Sci.*, 2008, **325**, 11–15.

[4] M. Rebeilleau-Dassonneville, S. Rosini, A. C. van Veen, D. Farrusseng, and C. Mirodatos, *Catal. Today*, 2005, **104**, 131–137.

[5] X. Qi, F. T. Akin, and Y. S. Lin, *J. Memb. Sci.*, 2001, **193**, 185–193.

[6] I. W. Donald, *J. Mater. Sci.*, 1993, **28**, 2841–2886.

[7] B. Zhang, Q. Chen, L. Song, H. Li, F. Hou, and J. Zhang, *J. Non-Crystalline Solids*, 2008, **354**, 1948–1954.

[8] S. Ghosh, A. D. Sharma, P. Kundu, S. Mahanty, and R. N. Basu, *J. Non-Crystalline Solids*, 2008, **354**, 4081–4088.

[9] N. Laorodphan, P. Namwong, W. Thiemsorn, M. Jaimasith, A. Wannagon, and T. Chairuangsri, *J. Non-Crystalline Solids*, 2009, **355**, 38–44.

[10] M. J. Pascual, A. Guillet, and A. Durán, *J. Power Sources*, 2007, **169**, 40–46.

[11] M. J. Pascual, A. Duran, and M. O. Prado, *Phys. Chem. Glasses*, 2005, **46**, 512–520.